Optical property of rare earth based scheelite materials: Fundamental research and applications

Thesis submitted by
Nibedita Haldar

Doctor of Philosophy (Science)

School of Materials Science and Nanotechnology

Faculty of Interdisciplinary Studies, Law and Management

Jadavpur University

Kolkata-700032, India

2023

INDEX No. D-7/ISLM/34/2020

1. Title of the thesis:

Optical property of rare earth based scheelite materials: Fundamental research and applications

2. Name Designation & Institution of the Supervisor:

Dr. Chandan Kumar Ghosh

Assistant Professor

School of Material science and Nanotechnology

Jadavpur University

Kolkata-700032, India

e-mail: chandu_ju@yahoo.co.in

CERTIFICATE FROM SUPERVISORS

This is to certify that the thesis entitled "**Optical property of rare earth based scheelite materials: Fundamental research and applications**" submitted by **Ms. Nibedita Haldar (Reg. No. D-7/ISLM/34/2020)**, who got her name registered on **02.12.2020** for the award of **Ph.D. (Science)** degree of **Jadavpur University** is absolutely based upon her own work under the supervision of **Dr. Chandan Kumar Ghosh, Jadavpur University**.

Signature of supervisor

CKGhosh 29/09/2023

Dr. Chandan Kumar Ghosh, Assistant Professor,
School of Material Science and Nanotechnology,
Jadavpur University, Kolkata

(Signature of the supervisor, date with official seal)

Dr. Chandan Kumar Ghosh
Assistant Professor
School of Materials Science
& Nanotechnology,
Jadavpur University
Kolkata - 700 032

Statement of Originality

I, **Nibedita Haldar** registered on **02.12.2020** do hereby declare that this thesis entitled "**Optical property of rare earth based scheelite materials: Fundamental Research and applications**" contains literature survey and original research work done by the undersigned candidate as part of Doctoral studies.

All information in this thesis have been obtained and presented in accordance with existing academic rules and ethical conduct. I declare that, as required by these rules and conduct, I have fully cited and referred all materials and results that are not original to this work.

I also declare that I have checked this thesis as per the "Policy on Anti Plagiarism, Jadavpur University, 2019", and the level of similarity as checked by iThenticate software is **1%**.

Signature of Candidate: Nibedita Haldar

Date : 29.09.2023

Certified by

Supervisor(s): 29/09/2023

(Signature with date, seal)

Dr. Chandan Kumar Ghosh
Assistant Professor
School of Materials Science
& Nanotechnology,
Jadavpur University
Kolkata - 700 032

Dedicated to

My mother, Mrs. Nilima Haldar

My father, Mr. Sujit Kumar Haldar

My Husband, Mr. Tanmoy Mondal

Acknowledgements

At the onset, I express my sincere thanks to my supervisor, **Dr. Chandan Kumar Ghosh**, Assistant Professor, School of Material Sciences & Nanotechnology, Jadavpur University, Kolkata for giving me the opportunity to work on the present problem and for their invaluable guidance. I would like to thank him particularly for giving me the freedom to explore the areas that excited me most.

The constant enthusiasm and leadership of Dr. Ghosh not only provided almost an infinite source of encouragements every morning during the entire period of my work but also kept me moving in the most stressful times. He always acted as a philosopher and friend besides providing the scientific guidance. I am also grateful to him for making me aware about the potential application of nanotechnology for mechanical characterization that was totally unknown to me, and for providing me a wonderful opportunity for independent, creative contribution towards cutting edge research. I am also really thankful to him for the scientific inputs and guidance from the subject areas.

I express my deep sense of gratitude to Dr. Mrinal pal (scientist of CSIR-Central Glass and Ceramic Research Institute, Kolkata – 700032) and, Debabrata Sarkar (Assistant professor of Applied NanoPhysics Laboratory, Department of Physics and Nanotechnology, SRM Institute of Science and Technology, Kattankulathur – 603203, India) for helping me by using their infrastructural facilities.

I deeply appreciate the kind help and supports as well as stimulating interaction with Mr. Tanmoy Mondal, who is my Colleague in our research group entire the time of work. I shall fail in my duties if I do not mention the tremendous supports. I am also thankful to Ms. Tanushree Das, my Colleague, CSIR-CGCRI, Kolkata for her kind help and valuable suggestions. I am also grateful to Dr. Sudipta Goswami, Research Associate of our research group, not only for her valuable suggestions but also for her delightful presence.

It is now my turn to thank the people who were involved behind the curtain for completion of my thesis works. First of all, I am really grateful to my beloved parents, **Mrs. Nilima Haldar and Mr. Sujit Kumar Haldar.** I am eternally thankful towards my family and dedicate this dissertation to them. Special thanks are due to **Mr. Tanmoy Mondal**, for her unconditional love, encouragement and supports during the course of the present thesis work. Last but not the least; I heartily acknowledge the financial supports received in terms of a Junior Research Fellowship in **Joint UGC-CSIR Net JRF [F.No. 16-9(June 2017)/2018(NET/CSIR)]**. Without this deep supports it would possibly not have been possible at all to complete this thesis work.

Nibedita Haldar

Nibedita haldar 29.09.2023

September, 2023

Abstract

Rare earth-based scheelite materials exhibit unique optical properties that make them highly attractive for various applications. This abstract provides an overview of the optical properties of rare earth-based scheelite materials and highlights their diverse applications in optoelectronics, lighting, sensing, and photonics. The optical properties of rare earth-based scheelite materials are primarily governed by the presence of rare earth ions within their crystal lattice. The energy levels and electronic transitions of these ions lead to distinctive optical behaviors, including absorption, emission, and luminescence. The choice of rare earth elements enables the tailoring of optical properties, such as emission wavelengths and lifetimes, making these materials versatile for specific applications.

In the field of optoelectronics, rare earth-based scheelite materials find application in light-emitting diodes (LEDs) and phosphors. The unique luminescent properties of these materials allow for efficient light emission in a wide range of wavelengths, facilitating the development of energy-efficient and high-performance lighting devices. Additionally, their ability to emit light under high temperatures makes them ideal for solid-state lighting applications.

Rare earth-based scheelite materials also show promise in sensing applications. Their sensitivity to various environmental factors, such as temperature, pressure, and chemical species, enables their use as optical sensors. By utilizing their luminescent properties, these materials can be employed for detecting and monitoring specific analytes or environmental changes, providing valuable information for diverse sensing platforms.

Moreover, the optical properties of rare earth-based scheelite materials make them highly desirable for various applications in optoelectronics, lighting, sensing, and photonics. Ongoing research focuses on further understanding their optical behavior, developing new synthesis techniques, and exploring their integration into emerging technologies, including quantum photonics and integrated optical circuits. The continued exploration of rare earth-based scheelite materials' optical properties is expected to drive innovation and enable the development of advanced optical devices with enhanced performance and functionality.

Publications

1) Haldar, N., Mondal, T., Das, T., Sarkar, D., Pal, M. and Ghosh, C.K., 2023. Hydrothermal synthesis of defect-induced pristine α-$NaCe(WO_4)_2$: a novel material for solid state lighting and gas sensing. CrystEngComm. DOI: 10.1039/D3CE00312D (Paper) CrystEngComm, 2023, 25, 3514-3527.

2) Haldar, N., Mondal, Dutta, A., Sarkar, D., Ghorai, U.K. and Ghosh, C.K., An ab initio modelling for pristine and defects induced emissions from $NaCe(WO_4)_2$: a potential material for solid state lighting application. Applied Physics A (2023) 129:708 https://doi.org/10.1007/s00339-023-06898-2

3) Raha, J., Haldar, N. and Ghosh, C.K., 2021. Intense orange emission from hydrothermally synthesized ZnO flower-like structure: effect of charge carrier—LO phonon interaction on emission characteristics. Applied Physics A, 127, pp.1-8.

4) Mondal, T., Haldar, N., Mondal, D. and Ghosh, C.K., 2022. Oxygen vacancy in GdOF: generation of reactive oxygen species under dark. Applied Physics A, 128(8), p.698.

5) Mondal, T., Haldar, N., Paul, B. and Ghosh, C.K., 2022. Morphology controllable synthesis of GdOF nanocrystals and application in theranostic purpose. Materials Today: Proceedings, 69, pp.47-55.

6) Mallick, A., Haldar, N., Nandy, S. and Ghosh, C.K., 2023. Fabrication of Graphene, Graphene Oxide, Reduced Graphene Oxide, Fullerene (C60) and Carbon Nanotube Thin Film By Langmuir–Blodgett Method. In Handbook of Porous Carbon Materials (pp. 21-38). Singapore: Springer Nature Singapore.

7) Haldar, N., Choudhury, D; Mondal, T. and Ghosh, C.K. Scheelite materials in cell imaging and bioanalysis. CRC Press. (Accepted).

8) Haldar, N., Mondal, T. and Ghosh, C.K Carbon-based coatings: Synthesis and applications. Elsevier. (Accepted).

9) Haldar, N., Mondal, T., Das, T., Sarkar, D., Pal, M. and Ghosh, C.K., 2023. Truncated octahedra $NaCe(MoO_4)_2$ nanostructure: role of defects on photoluminescence, electron – phonon interaction and gas sensing property. ACS Applied Optical materials. (Under progress)

10) Haldar, N., Mondal, T., Das, T., Sarkar, D., Pal, M. and Ghosh, C.K., 2023. Influence of alkali metal ions on the defect induced photoluminescence properties of double tungstate compounds $ACe(WO_4)_2$ (A = Li, Na, K): Experimental and *ab initio* theoretical study. Crystal growth and design. (Under progress).

Contents

Chapter 1:	Page No.
1. Introduction	1- 40
1.1. Background and motivation of the work	1-2
1.2. Beauty of Nanotechnology	2-4
1.3 Application of nanotechnology	4-7
1.3.1. Electronics and Computing	4
1.3.2. Medicine and Healthcare	5
1.3.3. Energy and Environment	5
1.3.4. Materials and Manufacturing	6
1.3.5. Environmental and Structural Monitoring	6
1.3.6. Food and Agriculture	6 - 7
1.3.7. Water Purification and Desalination	7
1.3.8. Consumer Products	7
1.4. An overview of scheelite materials	7- 10
1.4.1. Physical Properties	8
1.4.2. Appearance	8
1.4.3. Occurrence	8
1.4.4. Uses	9 - 10
1.5. Why rare earth based scheelite nanomaterials?	10 - 11
1.6. What we want to do ……	12 -13

1.7. An overview of optical property 13 - 36

1.7.1. UV-VIS Absorption spectra 15 - 17

1.7.2. Transition probabilities and selection rules 18 - 19

1.7.3. Frank- Condon principle 19 - 21

1.7.4. Direct and indirect band gap 21 - 23

1.7.5. Luminescence 23 - 37

1.7.5.1. Chemiluminescent 28 - 30

1.7.5.2. Crystalloluminescent 31 -33

1.7.5.3. Radio luminescent 33 - 35

1.7.5.4. Thermo luminescent 35 - 37

References 37 - 40

Chapter 2:

1. Literature Review 41 - 68

1.1 Synthesis strategies of rare earth based scheelite type Micro/Nano structured materials 41 - 52

1.1.1. Hydro(solvo) thermal technique 43 - 44

1.1.2. Microwave assisted hydrothermal technique 44 - 46

1.1.3. Sol gel synthesis method 46 - 47

1.1.4. Combined sol–gel synthesis and electrospinning 47

1.1.5. Solid state reaction 48 - 49

1.1.6. Molten salt synthesis 49 - 50

Table 1: Synthesis procedures of rare earth based scheelite nanomaterials 51 - 52

1.2 Particle growth mechanism 53 - 64

1.2.1 The influence of organic ligands 54 - 57

1.2.2 The influence of pH 57 - 58

1.2.3 The influence of reaction temperature 59 - 60

1.2.4 The influence of reaction time 60 - 62

1.2.5 The influence of the rare earth source 62 - 64

1.2.6 The influence of tungstate/molybdate amount 64

1.3. Applications of $NaCe(MO_4)_2$ (M = W/Mo) nanomaterials 65 - 68

1.3.1. Luminescent Materials 65

1.3.2. Phosphors for Solid-State Lighting 65

1.3.3. Gas sensing 65 - 67

1.3.4. Solid-State Lasers 67

1.3.5. Scintillator Materials 67 - 68

1.4. Scope of the present work 68 - 69

1.5. Objective of the present work 69 - 70

References 70 - 73

Chapter 3:

Hydrothermal Synthesis of defect induced pristine α-$NaCe(WO_4)_2$: a novel material for solid state lightening and gas sensing

1. Introduction 74 - 76

2. Experimental section 76 - 78

2.1 Materials and synthesis procedure of α-NCWO 76

2.2 Characterizations 76 - 77

2.3: Gas-sensing properties measurement of α-NCWO nanomaterials 77 - 78

2.4: Band structure calculation using ab initio density functional theory 78

3. Result and discussion 78 – 101

3.1 Phase and structure analyses of the as-prepared Samples 78 - 82

3.2 Investigations of defects in α-NCWO nanostructures by FTIR, Raman and x-ray photoelectron spectroscopies 83 - 87

3.3 Investigations of optical properties of α-NCWO nanostructures by UV-Visible, steady state photoluminescence spectroscopies 88 - 92

3.4 Investigations of gas sensing properties of α-NCWO nanostructures 92 - 96

3.5 Ab initio calculation of electronic structure of α-NCWO: modelling of defects induced modification in band structure and density of states 96 - 100

4. Conclusion 101

APPENDIX-I 101 - 106

References 106 - 109

Chapter 4:

An *ab initio* modelling for pristine and defects induced emissions from $NaCe(WO_4)_2$: a potential material for solid state lighting application

1. Introduction	**110 - 112**
2. Experimental section	**112 - 114**
2.1 Materials and synthesis	**112 - 113**
2.2 Characterizations	**113**
2.3: Band structure calculation using ab initio density functional theory	**113 - 114**
3. Result and discussion	**114 - 135**
3.1 Phase and local structure analyses of the samples	**114 - 118**
3.2 Investigations of local structure by FTIR, Raman and x-ray photoelectron spectroscopies	**118 - 125**
3.3 Optical properties of the as-prepared $NaCe(WO_4)_2$ samples by UV-Vis, steady state and time – dependent photoluminescence spectroscopy	**125 - 130**
3.4 DFT calculation of $NaCe(WO_4)_2$: modelling of distortion induced emissions	**131 - 135**
4. Conclusion:	**135**
APPENDIX-II	**136 - 138**
References	**138 - 142**

Chapter 5:

Truncated octahedra $NaCe(MoO_4)_2$ nanostructure: role of defects on photoluminescence, electron – phonon interaction and gas sensing property

1. Introduction	**143 - 146**
2. Experimental Section	**146 - 149**
2.1 Materials and synthesis	**146 - 147**
2.2 Characterization and Gas sensing properties	**147 - 148**
2.3 Calculation of band structure and investigation of gas sensing mechanism using *ab initio* density functional theory	**148 - 149**
3. Result and discussion	**149 - 169**
3.1 Structural and morphological studies by XRD, FESEM and TEM	**149 - 152**
3.2 Investigations of local structure by FTIR, Raman and x-ray photoelectron spectroscopies	**152 - 156**
3.3 Optical properties of the as-prepared NCMO samples by UV-Vis, photoluminescence spectroscopy	**157 - 162**
3.4 Investigations of gas sensing properties of NCMO nanostructures	**162 - 165**
3.5 Density functional theory (DFT) calculation of NCMO	**165 - 169**
4. Conclusion	**169**
APPENDIX-III	**169 - 180**
References	**181 - 184**

Chapter 6:

Influence of alkali metal ion on the defect induced photoluminescence property of double tungstate compounds $ACe(WO_4)_2$ (A = Li, Na, K): Experimental and *ab initio* theoretical study

1. Introduction 185 - 187

2. Experimental section 187 - 189

2.1 Materials and synthesis 187

2.2 Measurement and Characterization 187 - 188

2.3 Ab-Initio Density Functional Theory 188 - 189

3. Result and discussion 189 - 207

3.1 Phase and crystal structure analyses of the samples by XRD, FESEM, TEM 189 - 199

3.2 Investigations of defects in ACWO nanostructures by FTIR, Raman and x-ray photoelectron spectroscopies 199 - 197

3.3 Optical properties of the as-prepared ACWO samples by UV-Vis, photoluminescence spectroscopy 198 - 202

3.4 Density functional theory (DFT) calculation of ACWO 202 - 206

4. Conclusions 207

APPENDIX-IV 207- 215

References 216 - 219

Chapter 7:

Overall conclusion and future prospects 220 - 223

LIST OF TABLES:

Chapter 2

Table 1: Synthesis procedures of rare earth based scheelite nanomaterials. **51 - 52**

Chapter 3

Table 1: Refined structural parameters and the reliability factors from the Rietveld fitting of α-NCWO structure. **80 - 81**

Chapter 3 (APPENDIX- I)

Table A1: Coordination environment of triclinic NCWO structure. **101- 102**

Table A2: The details of the deconvolution of the FTIR bands. **102 - 103**

Chapter 4

Table 1: Refined structural parameters and the reliability factors from Rietveld refinement of $NCWO_{1:1}$ and $NCWO_{1:2}$. **116 - 117**

Chapter 5 (APPENDIX- III)

Table A1: Refined structural parameters and the reliability factors from the Rietveld fitting of NCMO samples **169 - 170**

Table A2: Calculated energy (from DFT) for Acetone adsorption of NCMO samples **170 - 171**

Chapter 6 (APPENDIX- IV)

Table A1: Coordination environment of triclinic ACWO nanostructures. **207 - 208**

Table A2: Refined structural parameters and the reliability factors from Rietveld refinement of ACWO nanostructures. **208 - 209**

Table A3: The details of the deconvolution of the FTIR bands of ACWO nanostructures. **209 - 210**

Table A4: Lattice parameters of ACWO nanostructures from DFT calculation. **210**

Table A5: The contributed orbitals for different emissions of ACWO nanostructures from defect states (DFT). **210 - 211**

LIST OF FIGURES:

Chapter 1

Figure 1: Schematic diagram of optical (radiative and non-radiative) transitions. **15**

Figure 2: Schematic representation of Franck-Condon principle. **21**

Figure 3: Schematic picture of Direct and Indirect band gap. **23**

Chapter 2

Figure 1: SEM morphologies of the products (A) no additive reagents; (B) adding 0.05 g of 0.01 mol/L n-dodecanethiol; (C) adding 0.04 g of 0.01 mol/L â-cyclodextrin; (D) adding 0.015 g of 0.01 mol/L ethylenediamine; (E) adding 0.044 g of 0.01 mol/L L-ascorbic acid; (F) adding 0.0075 g of polyformaldehyde **56**

Figure 2: SEM images of the as-prepared hydroxyl sodium yttrium molybdate samples formed in the presence of (A) AO, (B) PVP, (C) EDTA and (D) Na_2tar **57**

Figure 3: FESEM images of $BiVO_4$ powders prepared at different pH values: (a) 0.59, (b) 0.70, (c) 1.21, (d) 2.55, (e) 3.65, (f) 4.26, (g) 7.81, (g) 9.50, (h) 9.76, (i) 10.44, (j) 10.55, (k) 12.59 and (l) 12.93 **58**

Figure 4: SEM images of the as-prepared hydroxyl sodium yttrium molybdate samples at 180 °C for different reaction times: (A) 0.5 h, (B) 3 h, (C) 6 h and (D) 12 h. **61**

Figure 5: SEM morphologies of the products at different reaction times (A) 1 h; (B) 4 h; (C) 6 h; (D) 10 h. **62**

Chapter 3

Figure 1: XRD patterns of the $NaCe(WO_4)_2$ samples (a) $NCWO_{120^oC}$, (b) $NCWO_{140^oC}$, (c) Triclinic unit cell's structure of the $NaCe(WO_4)_2$ nanostructures. **80**

Figure 2: FESEM image of NCWO nano/micro structures (a) $NCWO_{120^oC}$ and (b) $NCWO_{140^oC}$, (c) TEM images and (d) corresponding SAED pattern of $NCWO_{140^oC}$. **82**

Figure 3: Deconvolution of the FTIR bands 660 – 717, 718-777 and 778 – 910 cm^{-1} of $NCWO_{120^oC}$ (a, b, c) and $NCWO_{140^oC}$ (d, e, f) respectively. **84**

Figure 4: Raman spectra of $NCWO_{120^oC}$ and $NCWO_{140^oC}$ **85**

Figure 5: (a, b) XPS W4f and (c, d) XPS Ce3d core level spectra of $NCWO_{120^oC}$ and $NCWO_{140^oC}$ respectively. **87**

Figure 6: (a, b) XPS O1s core level spectra and (c, d) valence band edge of $NCWO_{120^oC}$ and $NCWO_{140^oC}$ respectively. **87**

Figure 7: Photoluminescence spectra of (a) $NCWO_{120^oC}$ and (b) $NCWO_{140^oC}$ respectively. (c) Normalized PL intensity ratio of emission wavelengths (d) The CIE chromaticity diagram of the NCWO phosphors. **91**

Figure 8: Schematic diagram of oxygen vacancies of CeO_8 polyhedra unit. **92**

Figure 9: (a, b) Response of $NCWO_{120^oC}$ and $NCWO_{140^oC}$ based sensors to ammonia, acetone and ethanol gasses measured at different operating temperatures, respectively. (c)Temperature calibration curve of $NCWO_{120^oC}$ and $NCWO_{140^oC}$ for 10 ppm ammonia and acetone, respectively. (d, e) Dynamic response curve of $NCWO_{120^oC}$ sensor at 350 °C and $NCWO_{140^oC}$ sensor at 300 °C to different concentrations of acetone and ammonia, respectively. (f, g) Calculation of response and recovery time of $NCWO_{120^oC}$ (350°C) and $NCWO_{140^oC}$ (300°C) for 10ppm acetone and for 10ppm ammonia, respectively. (h) Stability in 10ppm ammonia and 10 ppm acetone sensing data of $NCWO_{120^oC}$ and $NCWO_{140^oC}$ at 350°C and 300°C temperature, respectively, for 100 days. **95 - 96**

Figure 10: (a) Band structure and (b) spin polarised TDOS and PDOS of (c) Na, (d) Ce, (e) W and (f) O of NCWO. **98**

Figure 11: (a) Band structure and (b) spin polarised TDOS and PDOS of (c) Na, (d) Ce, (e) W and (f) O of NCWO – $V_O^{\bullet}$. **99**

Figure 12: (a) Band structure and (b) spin polarised TDOS and PDOS of (c) Na, (d) Ce, (e) W and (f) O of NCWO – $2V_O^{\bullet}$. **100**

Figure 13: Schematic diagram of photoluminescence transitions. **100**

APPENDIX-I

Figure A1: The elemental mapping of $NCWO_{120^oC}$. **104**

Figure A2: The elemental mapping of $NCWO_{140^oC}$ **104**

Figure A3: FTIR spectra of $NCWO_{120^oC}$ and $NCWO_{140^oC}$. **105**

Figure A4: XPS wide spectrum of Ce-3d, W-4f, O-1s, **105**
Na-1s of (a) $NCWO_{120^oC}$ and (b)$NCWO_{140^oC}$
respectively.

Figure A5: UV spectra (a, b) and corresponding band gap **106**
calculation (c, d) of $NCWO_{120^oC}$ and $NCWO_{140^oC}$
respectively.

Chapter 4

Figure 1: XRD patterns of the $NaCe(WO_4)_2$ samples(a) **116**
$NCWO_{1:1}$ and (b) $NCWO_{1:2}$, (c) Tetragonal
unit cell's structure of the $NaCe(WO_4)_2$ nanostructures.

Figure 2: FESEM image of $NaCe(WO_4)_2$ nano/micro **118**
structures (a) $NCWO_{1:1}$ and (b) $NCWO_{1:2}$, (c)
TEM images and (d) corresponding SAED
pattern of NCWO tetragonal structure.

Figure 3: (a) Deconvoluted FTIR bands 660 – 717, 718-777 **120**
and 778 – 910 cm^{-1} of $NCWO_{1:1}$ (a, b, c) and $NCWO_{1:2}$
(d, e, f) respectively.

Figure 4: Raman spectra of $NCWO_{1:1}$ and $NCWO_{1:2}$. **122**

Figure 5: (a, b) XPS W 4f and (c, d) XPS Ce 3d core level **124**
spectra of $NCWO_{1:1}$ and $NCWO_{1:2}$ respectively.

Figure 6: (a, b) XPS O1s core level spectra and (c, d) **125**
valence band edge of $NCWO_{1:1}$ and $NCWO_{1:2}$ respectively.

Figure 7: Photoluminescence spectra of (a) $NCWO_{1:1}$ and (b) $NCWO_{1:2}$ **130**
(c) Normalized P intensity ratio of emission wavelengths
(d) The CIE chromaticity diagram of the NCWO.

Figure 8: Schematic diagram of oxygen vacancies of CeO_8 **130**
polyhedra unit.

Figure 9: (a) Band structure and (b) spin polarised TDOS and **132**
PDOS of (c) Na, (d) Ce, (e) W and (f) O of NCWO.

Figure 10: (a) Band structure and (b) spin polarised TDOS and **134**
PDOS of (c) Na, (d) Ce, (e) W and (f) O of NCWO – $V_O^{\bullet}$.

Figure 11: (a) Band structure and (b) spin polarised TDOS and **134**
PDOS of (c) Na, (d) Ce, (e) W and (f) O of NCWO – $2V_O^{\bullet}$.

Figure 12: Schematic diagram of photoluminescence transitions. **135**

APPENDIX- II

Figure A1: EDX spectra of (a) $NCWO_{1:1}$ and (b) $NCWO_{1:2}$ **136**
respectively.

Figure A2: FTIR spectra of $NCWO_{1:1}$ and $NCWO_{1:2}$. **136**

Figure A3: XPS wide spectrum of Ce-3d, W-4f, O-1s, Na-1s of **137**
(a) $NCWO_{1:1}$ and (b) $NCWO_{1:2}$ respectively.

Figure A4: UV spectra and corresponding band gap of **137**
$NCWO_{1:1}$ (a, c) and $NCWO_{1:2}$ (b, d) respectively.

Figure A5: PLE spectra of $NCWO_{1:1}$ (a) and $NCWO_{1:2}$ **138**
(b) respectively.

Chapter 5

Figure 1: XRD patterns of the $NaCe(MoO_4)_2$ samples (a) $NCMO_{0.00}$, (b) $NCMO_{0.50}$, (c) $NCMO_{0.78}$ and (d) $NCMO_{1.00}$ respectively. **151**

Figure 2: FESEM images NCMO samples (a) $NCMO_{0.00}$, (b) $NCMO_{0.50}$, (c) $NCMO_{0.78}$ and (d) $NCMO_{1.00}$, (e) and (f) TEM image and SAED pattern of $NCMO_{1.00}$. **152**

Figure 3: Schematic diagram of oxygen vacancies of CeO_8 polyhedral unit. **156**

Figure 4: Photoluminescence spectra of (a) $NCMO_{0.00}$, (b) $NCMO_{0.50}$, (c) $NCMO_{0.78}$ and (d) $NCMO_{1.00}$ respectively (e) Normalized PL intensity ratio of emission wavelengths (f) The CIE chromaticity diagram of the NCMO phosphors. **161**

Figure 5: (a) Temperature calibration curve of $NCMO_{0.00}$, $NCMO_{0.50}$, $NCMO_{0.78}$ and $NCMO_{1.00}$, respectively. (b) Selectivity of $NCMO_{0.00}$, $NCMO_{0.50}$, $NCMO_{0.78}$ and $NCMO_{1.00}$ sensors measured at 300°C operating temperature. (c) Linear fitting of logarithm of sensitivity and logarithm of acetone concentration data of all samples. (d)Dynamic acetone response curve of $NCMO_{1.00}$ sensor to acetone concentration from 1 – 100 ppm at 300°C. (e) Response and recovery time of $NCMO_{1.00}$ based sensor for 1 ppm acetone at 300°C. (f) Long term stability of $NCMO_{1.00}$ based sensor in 1 ppm acetone sensing measured over 90 days. **165**

Figure 6: (a) Band structure and (b) spin polarised TDOS of NCMO. **167**

Figure 7: Schematic picture of luminescent transitions within different CeO_8 polyhedra involving different orbitals. **169**

APPENDIX-III

Figure A1: Schematic representation of reaction procedure. **171**

Figure A2: Atomic structure of acetone molecule adsorption on NCMO (112) surface. **171**

Figure A3: Structure of the NCMO (Tetragonal) nanostructure. **172**

Figure A4: FTIR spectra of NCMO nanostructures. **172**

Figure A5: Deconvoluted FTIR bands 660-750 and 750-960 of $NCMO_{0.00}$ (a, b), $NCMO_{0.50}$ (c, d), $NCMO_{0.78}$ (e, f) and $NCMO_{1.00}$ (g, h) respectively. **173**

Figure A6: Raman spectra of NCMO nanostructures. **174**

Figure A7: XPS wide spectrum of Ce-3d, W-4f, O-1s, Na-1s of (a) $NCMO_{0.00}$, (b) $NCMO_{0.50}$, (c) $NCMO_{0.78}$ and (d) $NCMO_{1.00}$ respectively. **174**

Figure A8: XPS Mo 3d of (a) $NCMO_{0.00}$, (b) $NCMO_{0.50}$, (c) $NCMO_{0.78}$ and (d) $NCMO_{1.00}$ respectively. **175**

Figure A9: XPS Ce 3d core level spectra of (a) $NCMO_{0.00}$, (b) $NCMO_{0.50}$, (c) $NCMO_{0.78}$ and (d) $NCMO_{1.00}$ respectively. **175**

Figure A10: XPS O1s core level spectra of (a) $NCMO_{0.00}$, (b) $NCMO_{0.50}$, (c) $NCMO_{0.78}$ and (d) $NCMO_{1.00}$ respectively. **176**

Figure A11: UV spectra and corresponding band gap of (a, b) $NCMO_{0.00}$, (c, d) $NCMO_{0.50}$, (e, f) $NCMO_{0.78}$ and (g, h) $NCMO_{1.00}$ respectively. **177**

Figure A12: PLE spectra of (a) $NCMO_{0.00}$, (b) $NCMO_{0.50}$, (c) $NCMO_{0.78}$ and (d) $NCMO_{1.00}$ respectively. **178**

Figure A13: Schematic representation of luminescent transitions of NCMO. **178**

Figure A14: (a) Sensitivity vs acetone concentration (1-100 ppm) curve for $NCMO_{0.00}$, $NCMO_{0.50}$, $NCMO_{0.78}$ and $NCMO_{1.00}$ at 300°C, (b) Cyclic response-recovery curves of $NCMO_{1.00}$ sensor to 5 ppm acetone for six consecutive cycles of measurement at 300°C. Dynamic acetone response curve of (c) $NCMO_{0.00}$, (d) $NCMO_{0.50}$ and (e) $NCMO_{0.78}$ sensor to acetone concentration from 1 – 100 ppm at 300°C, respectively. **179**

Figure A15: PDOS of (a) Na, (b) Ce, (c) Mo and (d) O of NCMO. **179**

Figure A16: (a) Band structure and (b) spin polarised TDOS and PDOS of (c) Na, (d) Ce, (e) Mo and (f) O of NCMO – $V_O^{\bullet}$. **180**

Figure A17: (a) Band structure and (b) spin polarised TDOS and PDOS of (c) Na, (d) Ce, (e) Mo and (f) O of NCMO – $2V_O^{\bullet}$. **180**

Chapter 6

Figure 1: XRD patterns (a, b, c) and triclinic unit cell's structure (d, e, f) of LCWO, NCWO, KCWO respectively. **191**

Figure 2: (a)-(c) FESEM image of LCWO, NCWO, KCWO respectively. **192**

Figure 3: TEM image, HRTEM image and corresponding SAED pattern of LCWO (a)-(c), NCWO (d)-(f), KCWO (g)-(i) respectively. **192**

Figure 4: (a) Deconvoluted curves of the FTIR bands 660 – 717, 718-777 and 778 – 910 cm^{-1} of LCWO (a, b, c), NCWO (d, e, f) and KCWO (g, h, i) respectively. **195**

Figure 5: Raman spectra of ACWO nanostructures. **195**

Figure 6: (a, b, c) XPS W4f, (d, e, f) XPS Ce 3d, (g, h, i) XPS O1s core level spectra of LCWO, NCWO, KCWO respectively. **197**

Figure 7: Photoluminescence spectra of (a) LCWO, (b)NCWO and (c) KCWO respectively. (d) Normalized PL intensity ratio of emission wavelengths (e) The CIE chromaticity diagram of the ACWO. **202**

Figure 8: (a) Band structure and (b) spin polarised TDOS and PDOS of (c) Li, (d) Ce, (e) W and (f) O of pristine - LCWO. **204**

Figure 9: (a) Band structure and (b) spin polarised TDOS and PDOS of (c) Na, (d) Ce, (e) W and (f) O of pristine - NCWO. **204**

Figure 10: (a) Band structure and (b) spin polarised TDOS and PDOS of (c) K, (d) Ce, (e) W and (f) O of pristine - KCWO. **205**

Figure 11: Schematic representation of photoluminescence transitions of ACWO nanomaterial involving different orbitals. **206**

APPENDIX-IV

Figure A1: FTIR of ACWO nanostructures. **211**

Figure A2: XPS wide spectrum of (a)LCWO, (b)NCWO and (c)KCWO respectively. **211**

Figure A3: UV spectra and corresponding band gaps for (a, b) LCWO, (c, d) NCWO and (e, f) KCWO respectively. **212**

Figure A4: PLE spectra for (a)LCWO, (b)NCWO and (c)KCWO respectively. **212**

Figure A5: (a) Band structure and (b) spin polarised TDOS and PDOS of (c) Li, (d) Ce, (e) W and (f) O of LCWO – $V_O^{\bullet}$. **213**

Figure A6: (a) Band structure and (b) spin polarised TDOS and PDOS of (c) Na, (d) Ce, (e) W and (f) O of NCWO – $V_O^{\bullet}$. **213**

Figure A7: (a) Band structure and (b) spin polarised TDOS and PDOS of (c) K, (d) Ce, (e) W and (f) O of KCWO – $V_O^{\bullet}$. **214**

Figure A8: (a) Band structure and (b) spin polarised TDOS and PDOS of (c) Li, (d) Ce, (e) W and (f) O of LCWO – $2V_O^{\bullet}$. **214**

Figure A9: (a) Band structure and (b) spin polarised TDOS and PDOS of (c) Na, (d) Ce, (e) W and (f) O of NCWO – $2V_O^{\bullet}$. **215**

Figure A10: (a) Band structure and (b) spin polarised TDOS and PDOS of (c) K, (d) Ce, (e) W and KCWO – $2V_O^{\bullet}$. **215**

Introduction

1. Introduction

1.1. Background and motivation of the work

Indeed, nanotechnology has emerged as a highly influential field of research, attracting attention from scientists and researchers worldwide. The ability to manipulate and control materials at the nanoscale (1 to 100 nanometers) has opened up new avenues for developing materials with improved properties and exploring alternative precursors. Over the past decade, nanotechnology has made significant advancements in various areas. Researchers have focused on nanoparticles and powders, developing methods to synthesize and utilize nanoscale particles with unique properties. Nanolayers and coatings have also been a major area of research, aiming to enhance the performance and functionality of surfaces through nanoscale modifications. Nanotechnology has also revolutionized the development of electrical, optical, and mechanical nanodevices. By harnessing the properties of materials at the nanoscale, researchers have been able to create highly efficient and miniaturized devices with improved performance. Furthermore, the field has expanded into nanostructured biological materials, exploring the applications of nanotechnology in the biomedical and healthcare sectors.

The term "nanotechnology" was coined by Nori Taniguchi in 1974, and since then, it has grown into a multidisciplinary field. Researchers from physics, chemistry, material science, engineering, and other cross-disciplinary sciences contribute to the progress of nanotechnology. Collaboration between these

fields has led to breakthroughs in sample preparation, device fabrication, and the exploration of new physical properties at the nanoscale. Nanotechnology is expected to continue exerting a significant influence on various scientific and technological domains for the next two to three decades. Its potential impact spans fields such as electronics, energy, medicine, environmental science, and more. As researchers delve deeper into nanoscience and nanotechnology, new discoveries and innovations are anticipated, further pushing the boundaries of what is possible at the nanoscale. A significant amount of research is being conducted on various types of nanoparticles worldwide. These nanoparticles include semiconductor quantum dots, insulating nanoparticles, nanowires, nanotubes, nanopowders etc. Researchers employ diverse methods to prepare nanoparticles using materials such as insulators, semiconductors, ceramics, metallic alloys, carbon nanotubes. The physical properties of nanomaterials, including their structural, electrical, magnetic, linear, and nonlinear optical properties, are often described in the context of quantum size effects. These effects arise due to the confinement of electrons within the nanoscale dimensions, leading to unique and size-dependent phenomena. Overall, research in these areas aims to explore and understand the properties and behaviors of nanoparticles, leveraging their unique characteristics for a wide range of applications in fields such as electronics, materials science, energy, and medicine.

1.2. Beauty of Nanotechnology

Nanotechnology is a fascinating field that explores the manipulation and control of matter at the nanoscale, which is approximately 1 to 100 nanometers in size. The beauty of nanotechnology lies in its incredible potential to revolutionize various aspects of our lives. Here are some key aspects highlighting the beauty of nanotechnology:

- **Miniaturization:** Nanotechnology enables the miniaturization of devices and systems. By manipulating and arranging atoms and molecules at the nanoscale, scientists can create materials and structures with unique properties and functionalities. This has led to the development of smaller, more efficient electronic devices, such as nanoscale transistors, sensors, and memory devices.
- **Enhanced Properties:** At the nanoscale, materials can exhibit enhanced properties compared to their bulk counterparts. For example, nanoparticles can have improved strength, higher reactivity, increased electrical conductivity, or enhanced optical properties. This allows for the creation of new materials with superior characteristics, such as stronger and lighter materials for aerospace applications or more efficient catalysts for chemical reactions.
- **Medical Breakthroughs:** Nanotechnology has the potential to revolutionize medicine. Nanoscale drug delivery systems can target specific cells or tissues in the body, improving the efficacy and reducing side effects of therapeutic treatments. Nano sensors can detect disease markers at an early stage, enabling early diagnosis and intervention. Furthermore, nanomaterial can be used for tissue engineering, regenerative medicine, and the development of artificial organs.
- **Environmental Impact:** Nanotechnology offers promising solutions for environmental challenges. For example, nanomaterials can be used to develop more efficient and cost-effective solar cells, leading to renewable energy sources. Nanoparticles can also be employed in water treatment processes to remove pollutants and improve water quality. Additionally, nanotechnology plays a crucial role in developing energy-efficient and lightweight materials for vehicles, reducing fuel consumption and carbon emissions.

- **Consumer Applications:** Nanotechnology is gradually finding its way into various consumer products, enhancing their functionality and performance. Examples include nanocoatings that provide stain resistance or waterproofing properties, nanofabrics with improved durability and breathability, and nanoelectronics used in smart devices. These advancements improve our everyday lives and highlight the beauty of nanotechnology's impact on society.
- **Scientific Exploration:** Nanotechnology has opened up new avenues for scientific exploration and understanding of the fundamental principles governing matter. Researchers can now observe and manipulate phenomena at the nanoscale, uncovering new properties and behaviors. This knowledge not only expands our understanding of the natural world but also provides insights for the development of future technologies.

The beauty of nanotechnology lies in its ability to transform and innovate across various disciplines, offering solutions to complex problems and unlocking new possibilities. As scientists continue to push the boundaries of nanoscale science and engineering, the potential for further advancements and discoveries is both exciting and awe-inspiring.

1.3 Application of nanotechnology

Nanotechnology has a wide range of applications across various fields, and its potential impact is significant. Here are some areas where nanotechnology is being applied:

1.3.1. Electronics and Computing:

- Nanoscale transistors and memory devices have revolutionized the electronics industry by enabling faster and more efficient computer chips [1].

- Carbon nanotubes and graphene, with their exceptional electrical properties, are being explored as potential replacements for traditional silicon-based components [2].

1.3.2. Medicine and Healthcare:

- Nanoscale drug delivery systems offer targeted delivery of therapeutic agents, improving efficacy and reducing side effects. They can deliver drugs to specific cells or tissues, such as cancer cells [3].
- Nanosensors provide real-time monitoring of patient health by detecting biomarkers and providing information on vital signs. They have potential applications in wearable devices and point-of-care diagnostics [4].
- Nanomaterials are used in tissue engineering and regenerative medicine to develop artificial organs, scaffolds, and wound dressings that promote tissue regeneration [5].

1.3.3. Energy and Environment:

- Nanomaterials are utilized in the development of more efficient solar cells, such as perovskite solar cells, to harness renewable energy. These cells offer high power conversion efficiency and can be fabricated using low-cost processes [6].
- Nanocatalysts enhance the efficiency of chemical reactions, enabling cleaner and more sustainable industrial processes, such as catalytic converters for vehicle exhaust systems [7].
- Nanoparticles are employed in water treatment technologies, including filtration and adsorption, to remove pollutants and improve water quality. They have applications in wastewater treatment and desalination processes [8].

1.3.4. Materials and Manufacturing:

- Nanocomposites, which combine nanoparticles with conventional materials, exhibit enhanced mechanical, electrical, and thermal properties. These materials find applications in aerospace, automotive, and construction industries, leading to stronger, lighter, and more durable products [9].
- Nanomanufacturing techniques, such as atomic layer deposition and self-assembly, enable precise control over the fabrication of nanostructures and devices. This allows for the production of nanoscale components with high precision and scalability [10].

1.3.5. Environmental and Structural Monitoring:

- Nanosensors are utilized for environmental monitoring to detect and measure pollutants, gases, and chemicals in the environment. They provide real-time data for pollution control and environmental management [11].
- Structural health monitoring using nanosensors allows for the continuous monitoring of buildings, bridges, and infrastructure. It provides early warning signs of potential failures, ensuring the safety and integrity of structures [12].

1.3.6. Food and Agriculture:

- Nanosensors are employed in food safety to detect foodborne pathogens and contaminants. They can help ensure the safety and quality of food products by providing rapid and sensitive detection methods [13].
- Nanoencapsulation techniques are used for controlled release of nutrients, flavors, and preservatives in food products. This enhances food quality, extends shelf life, and improves delivery of bioactive compounds [14].

- Nanomaterials have the potential to enhance crop productivity by delivering targeted fertilizers and pesticides, reducing environmental impact, and improving resource efficiency [15].

1.3.7. Water Purification and Desalination:

- Nanotechnology offers innovative solutions for water purification. Nanomaterials, such as graphene oxide membranes and carbon nanotubes, selectively filter out contaminants, providing clean drinking water [16].
- Nanofiltration and reverse osmosis techniques utilizing nanomaterials can make desalination more efficient and cost-effective, addressing water scarcity issues in water-stressed regions [17].

1.3.8. Consumer Products:

- Nanocoatings provide various functionalities in consumer products, such as stain resistance, scratch resistance, and UV protection. They are used in products like clothing, eyewear, and electronics [18].
- Nanoparticles are used in sunscreens to provide effective UV protection by scattering and absorbing UV radiation [19].
- Nanotechnology enables the development of flexible and lightweight displays for electronic devices, enhancing their portability and user experience [20].

These applications demonstrate the vast potential of nanotechnology across various fields. Properly citing the references ensures accuracy and credibility of the information provided.

1.4. An overview of scheelite materials

Scheelite is a calcium tungstate mineral with the chemical formula $CaWO_4$. It belongs to the scheelite group of minerals, which also includes minerals such as stolzite and powellite. Scheelite is the most important ore of tungsten, a rare metal that is widely used in various industrial applications. In the early 20th century, efforts were made to synthesize scheelite materials for industrial applications, particularly in the field of lighting. Scheelite's ability to fluoresce when exposed to ultraviolet (UV) light made it suitable as a phosphor material in fluorescent lamps.

The synthesis of scheelite phosphors involved various methods, including solid-state reactions, precipitation, and high-temperature techniques. The doping of scheelite with different activators, such as rare earth elements, allowed for the tuning of its optical properties. One of the earliest references to the synthesis of scheelite phosphors can be found in a patent by Adolf Meyer and Gottfried Vitt, filed in 1919, which describes the preparation of calcium tungstate phosphors. Over the years, scheelite phosphors have been extensively used in applications such as fluorescent lamps, X-ray screens, cathode-ray tubes, and scintillation detectors.

1.4.1. Physical Properties: Scheelite has a tetragonal crystal structure and typically forms as prismatic or tabular crystals. It has a hardness of 4.5 to 5.5 on the Mohs scale, which means it is relatively hard. The mineral has a high specific gravity ranging from 5.9 to 6.1, making it dense compared to many other minerals.

1.4.2. Appearance: Scheelite exhibits a range of colors, including white, yellow, orange, brown, and sometimes green. The color variation is due to impurities present in the mineral, with the most common impurities being molybdenum and iron. The transparency of scheelite can vary from transparent to translucent [21].

1.4.3. Occurrence: Scheelite is found in a variety of geological environments. It commonly occurs in contact metamorphic deposits associated with granitic intrusions. It can also be found in hydrothermal veins and skarn deposits formed during the contact metamorphism of carbonate rocks. Scheelite is often found in association with other minerals such as quartz, fluorite, molybdenite, and wolframite.

1.4.4. Uses: The primary use of scheelite is as a source of tungsten metal. Tungsten has exceptional strength and high melting point, making it valuable in various applications. Some significant uses of tungsten include:

- **Tungsten Production:** Scheelite is the most important ore of tungsten, a metal known for its high melting point and excellent hardness. Tungsten is widely used in various industries, including aerospace, electronics, defense, and manufacturing. Scheelite serves as a primary source for tungsten extraction due to its high tungsten content.
- **Fluorescent Lighting:** Scheelite's unique fluorescence property under UV light makes it a valuable material for fluorescent lighting applications. It is used as a phosphor material in fluorescent lamps, where it converts UV light into visible light, thereby producing the desired illumination[22].
- **X-ray and Gamma-ray Detection:** Scheelite is used in the manufacturing of scintillation detectors for X-ray and gamma-ray detection. Its high density and efficient light emission make it an ideal scintillator material for detecting and measuring ionizing radiation.
- **Ceramic Industry:** Scheelite's high melting point and refractory nature make it suitable for use in the ceramic industry. It is used as a component in the production of ceramic glazes, enamels, and pigments, adding desirable colors and effects to ceramic products [23].

- **Gemstone and Jewellery:** Scheelite's vibrant colors, particularly the blue fluorescence under UV light, make it a popular gemstone for collectors and jewellery enthusiasts. It is faceted and cut into various shapes for use in gemstone jewellery, where its unique optical properties are highly valued[24].

1.5. Why rare earth based scheelite nanomaterials?

Rare earth-based scheelite nanomaterials are chosen for several reasons due to their unique properties and advantages. Elaborated below are some of the key reasons, supported by properly cited references, for choosing rare earth-based scheelite nanomaterials:

- **Enhanced Luminescence Properties:** Rare earth ions, such as europium (Eu), neodymium (Nd), and ytterbium (Yb), when incorporated into the scheelite lattice, exhibit strong luminescence properties. This makes rare earth-based scheelite nanomaterials suitable for applications in optoelectronics, lighting, and display technologies [25].
- **Tunable Emission Spectra:** The emission spectra of rare earth-based scheelite nanomaterials can be tuned by adjusting the concentration and composition of the rare earth dopants. This tunability allows for the customization of their luminescent properties to meet specific requirements [26].
- **Efficient Energy Transfer:** Rare earth ions in scheelite nanomaterials possess unique energy transfer processes, such as Förster resonance energy transfer (FRET) and cross-relaxation. These processes enable efficient energy transfer between different rare earth ions within the material, resulting in enhanced luminescence efficiency [27].
- **Optical Sensing Applications:** The luminescent properties of rare earth-based scheelite nanomaterials make them suitable for optical sensing

applications, such as chemical and biological sensing, due to their high sensitivity and selectivity [28]. They can be used as luminescent probes for detecting and monitoring specific analytes with high precision and accuracy.

- **Biomedical Imaging:** Rare earth-based scheelite nanomaterials have shown promise in biomedical imaging applications, including fluorescence imaging, bioimaging, and diagnostics. Their strong luminescence and tunable emission spectra make them valuable tools for visualizing biological structures and processes at the cellular and molecular level [29].
- **Energy Storage:** Rare earth-based scheelite nanomaterials, particularly those doped with cerium (Ce) and europium (Eu) ions, have demonstrated potential for energy storage applications, including solar energy conversion and photovoltaics. Their ability to absorb and emit light efficiently makes them suitable for harnessing and converting solar energy into electricity [30].

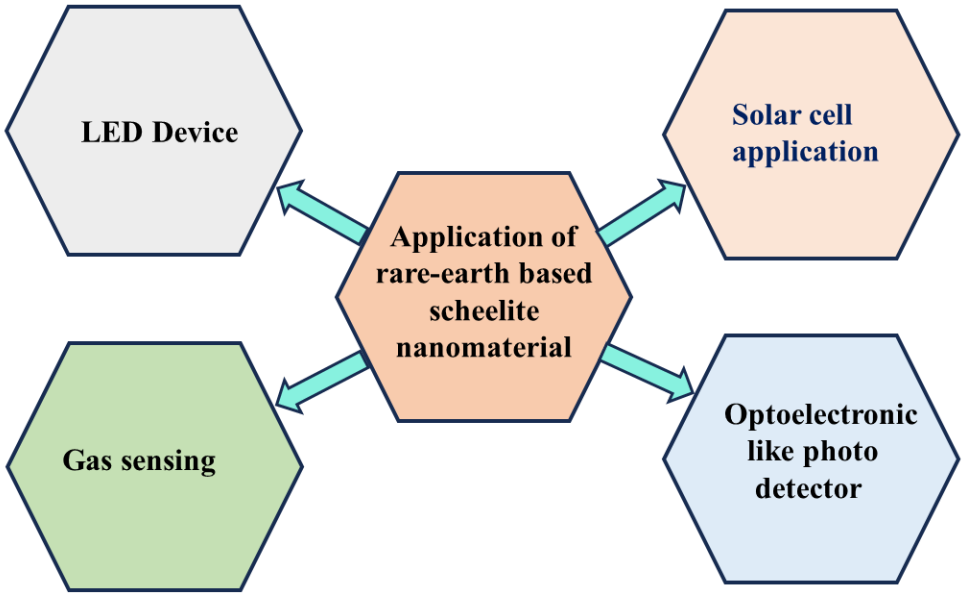

Applications of rare earth based scheelite nanomaterials

1.6. What we want to do ……

- Synthesis of various rare earth based scheelite material like $ACe(MO_4)_2$ (A= Li/Na/K; M = W/Mo) materials having different morphology by changing processing parameters and techniques will be attempted following extensive literature survey.

- Characterization of those rare earth based scheelite materials by X-ray Diffraction (XRD) technique, electron microscopic techniques (Field Emission Scanning Electron Microscopy (FE-SEM) and Transmission Electron Microscopy (TEM) etc.), Fourier-transform infrared spectroscopy (FTIR), Raman spectroscopy, x-ray photoelectron spectroscopies (XPS), Absorption spectroscopy (UV-VIS), photoluminescence spectroscopy will be done.

- The dependencies of micro/nano structure on the processing conditions and process parameters etc. will be investigated and effort will be made to examine if the variations in reaction temperature, precursors of reactants, precursors of organic additives, concentration of organic additives have any role in governing the nucleation and growth of the rare earth based scheelite materials.

- The dependencies of nanostructure and photoluminescence property on the processing conditions and process parameters etc. will be investigated and attempt will be made to optimize the processing condition for achieving great luminescent property.

- Attempt will be made to optimize the defect in the nanostructures and luminescent property of rare earth based scheelite material.

- Proof of concept demonstration through utilization of the synthesized rare earth based scheelite material for solid state lightening application and gas sensing and identification of the possible photoluminescence mechanisms will be attempted.

1.7. An overview of optical property

The optical properties of semiconducting materials are of great significance in various applications, including optoelectronics, photovoltaic and lasers. These properties arise from the unique electronic band structure of semiconductors and their ability to absorb, emit, and manipulate light. Some key optical properties of semiconducting materials include:

- **Bandgap:** One of the most crucial optical properties of semiconductors is their bandgap energy. The bandgap is the energy difference between the highest occupied energy level (valence band) and the lowest unoccupied energy level (conduction band). Photons with energies equal to or higher than the bandgap energy can excite electrons from the valence band to the conduction band, creating electron-hole pairs and enabling various optical processes [31].
- **Absorption:** Semiconducting materials can absorb light at specific wavelengths corresponding to the energy levels of the bandgap. When photons with energies equal to or higher than the bandgap energy are incident on the semiconductor, they can be absorbed, leading to electron excitation across the bandgap and the generation of electron-hole pairs [32].

- **Emission:** Semiconductors can emit light when electron-hole pairs recombine. There are two main types of emissions: spontaneous emission, where the electron-hole recombination occurs naturally, and stimulated emission, which leads to lasing when the emission is amplified by stimulated emission [33].
- **Photoluminescence:** When semiconductors are excited by photons, they can emit light at longer wavelengths than the excitation light. This phenomenon is known as photoluminescence and is widely used in various luminescence-based applications such as LED technology, display devices, and fluorescence imaging [34].
- **Refractive Index:** The refractive index of a semiconductor determines the speed of light as it propagates through the material. It plays a crucial role in optical devices such as lenses, waveguides, and photonic crystals, where light manipulation is essential [35].
- **Optical Gain:** Optical gain refers to the increase in the intensity of light when it passes through a semiconductor medium. This property is fundamental to the operation of lasers and amplifiers, where stimulated emission leads to an increase in the number of photons [36].
- **Nonlinear Optical Properties:** Semiconductors can exhibit nonlinear optical effects when intense light interacts with them. These effects include second-harmonic generation, sum-frequency generation, and optical parametric amplification. Nonlinear optical properties are utilized in various applications, such as frequency conversion and ultrafast optics [37].

The optical properties of semiconducting materials are extensively studied and engineered to create efficient and advanced optoelectronic devices, making them essential components of modern technology.

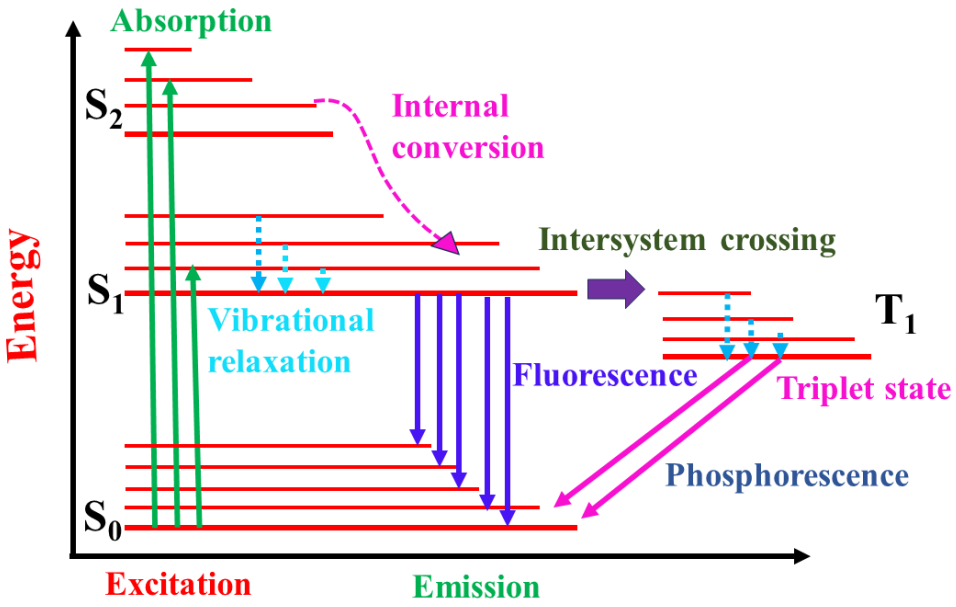

Figure 1: Schematic diagram of optical (radiative and non-radiative) transitions.

1.7.1. UV-VIS Absorption spectra

Absorption spectra refer to the measurement of the absorption of light by a substance as a function of wavelength or frequency. They provide valuable information about the interaction between light and matter and are widely used in various fields, including chemistry, physics, materials science, and biology.

When light passes through a substance, it can be absorbed by the material, leading to a reduction in the intensity of the transmitted light. The absorption of light occurs when photons with energy matching the energy levels of the material are absorbed, causing electronic or vibrational transitions within the substance. The absorbed energy is typically converted into heat or used to excite the electrons to higher energy levels. The absorption spectrum is typically represented as a plot of the absorbance (or sometimes transmittance) of the substance as a function of the wavelength or frequency of the incident light. It provides valuable information about the electronic and molecular structure of

the material, as well as the energy levels and transitions that occur within it [38].

Absorption spectra can be understood and analyzed using the Lambert-Beer's Law, which describes the relationship between the concentration of an absorbing species, the path length of light through the sample, and the absorbance of light. The Lambert-Beer's Law can be stated as follows:

$A = \varepsilon \cdot c \cdot l$

Where:

A is the absorbance of the sample, ε is the molar absorptivity (also known as the extinction coefficient), which represents the substance's ability to absorb light at a specific wavelength, c is the concentration of the absorbing species in the sample, typically measured in moles per liter (Molar concentration), l is the path length of light through the sample, typically measured in centimeters,

According to the Lambert-Beer's Law, absorbance is directly proportional to the concentration of the absorbing species and the path length of light through the sample. Therefore, by measuring the absorbance of a sample at different wavelengths, it is possible to obtain an absorption spectrum that reveals the substance's characteristic absorption behaviour [39].

When light passes through a sample, it interacts with the absorbing species present in the material. The absorbing species can absorb specific wavelengths of light, leading to a decrease in the intensity of the transmitted light. The amount of light absorbed is related to the concentration of the absorbing species and the path length of light through the sample. By measuring the absorbance of a sample at different wavelengths, it is possible to construct an absorption spectrum. The spectrum displays the absorbance as a function of wavelength or frequency, and it provides information about the substance's absorption

characteristics [40]. The shape and features of an absorption spectrum can reveal important characteristics of the substance. For example:

- Absorption Peaks: Peaks in the absorption spectrum indicate specific wavelengths or energy levels at which the material strongly absorbs light. The position and intensity of these peaks can provide information about the electronic structure, energy band gaps, and presence of specific molecular groups or chromophores within the material.
- Absorption Bands: Broad regions of the absorption spectrum, often observed in complex materials or molecules, are known as absorption bands. These bands can arise from the overlapping of multiple electronic or vibrational transitions within the material.
- Absorption Edge: The abrupt increase in absorption at a specific wavelength or energy is called the absorption edge. It indicates the onset of absorption when the energy of the incident photons matches or exceeds the energy required to excite electrons across a particular energy band or transition.

Absorption spectra are widely used in various fields. In chemistry, they are used to identify compounds, determine their concentration, and study chemical reactions. In physics, absorption spectra provide insights into the behavior of materials and the electronic structure of solids. In biology, they are employed to analyse biomolecules, such as proteins and pigments. In conclusion, absorption spectra are essential tools for studying the interaction of light with matter. They provide valuable insights into the electronic and molecular properties of materials and are widely employed in scientific research, analysis, and various practical applications.

1.7.2. Transition probabilities and selection rules

Transition probabilities and selection rules are fundamental concepts in the field of quantum mechanics that govern the likelihood and allowed transitions between energy levels in atomic or molecular systems. These concepts help to understand the emission, absorption, and scattering of electromagnetic radiation by matter. Let's explore transition probabilities and selection rules in more detail:

- **Transition Probabilities:** Transition probabilities describe the likelihood of a quantum system undergoing a transition from an initial state to a final state. In the context of atomic or molecular systems, transition probabilities are typically associated with the emission or absorption of photons, which correspond to electromagnetic radiation. The probability of a transition depends on several factors, including the interaction between the system and the electromagnetic field, the initial and final states' energy difference, and the properties of the system itself. Transition probabilities are expressed in terms of transition dipole moments and are related to the square of the matrix elements of the relevant quantum operators.
- **Selection Rules:** Selection rules are a set of constraints or conditions that determine which transitions are allowed or forbidden in a given system. They arise from the conservation laws that govern physical processes, such as energy, angular momentum, and parity conservation. The selection rules specify the changes in quantum numbers that must occur for a transition to be allowed. Quantum numbers, such as the principal quantum number (n), orbital angular momentum (l), total angular momentum (j), and spin (s), provide a way to characterize the states of atomic or molecular systems. For example, the selection rules for electric dipole transitions in atoms state that the change in the principal quantum

number (Δn) must be ±1, the change in the orbital angular momentum quantum number (Δl) must be ±1, and the change in the total angular momentum quantum number (Δj) must be 0 or ±1.

The selection rules provide valuable insights into the optical properties of atoms and molecules, as they determine the allowed transitions in absorption, emission, and scattering processes. By considering the selection rules, one can predict the spectral lines observed in atomic or molecular spectra. It is important to note that selection rules can be relaxed or violated under certain conditions, such as in highly excited states, in the presence of external fields, or in systems with strong interactions. In such cases, additional factors or perturbations may come into play, leading to the relaxation of the selection rules and the occurrence of otherwise forbidden transitions.

1.7.3. Frank- Condon principle

The Franck-Condon principle is a fundamental concept in molecular spectroscopy that describes the distribution of molecular electronic states during a molecular transition, such as electronic excitation or vibrational relaxation. The principle is named after the scientists James Franck and Edward Condon, who proposed it in the 1920s based on their studies of gas-phase molecular spectra.

- The Franck-Condon principle states that during a molecular transition, such as electronic excitation or relaxation, the nuclear motion (vibrational modes) of the molecule remains relatively unchanged. In other words, the transition occurs so rapidly compared to the time scale of nuclear motion that the nuclei are essentially stationary during the transition. The principle is based on the fact that electronic transitions occur much faster than nuclear vibrations. When a molecule absorbs or emits a photon, promoting or de-exciting an electron to a higher or lower energy level,

the electronic transition occurs almost instantaneously. However, the nuclei in the molecule continue to vibrate and can adopt different positions and energies at different electronic states.

- The Franck-Condon principle allows us to understand the intensity distribution of vibrational bands in molecular spectra. It states that the intensity of a vibrational transition in a molecular spectrum is directly related to the overlap between the initial and final vibrational wave functions of the molecule.
- In spectroscopy, the Franck-Condon principle is used to interpret and analyse electronic spectra, such as electronic absorption or emission spectra. It helps to explain the relative intensities of vibrational bands and the progression of vibrational levels in the excited electronic state compared to the ground state.

The Franck-Condon principle has significant applications in various areas of chemistry and spectroscopy. It is particularly relevant in understanding the spectroscopic properties of polyatomic molecules, such as in studies of electronic transitions in organic compounds, gas-phase molecular spectra, and photochemical processes.

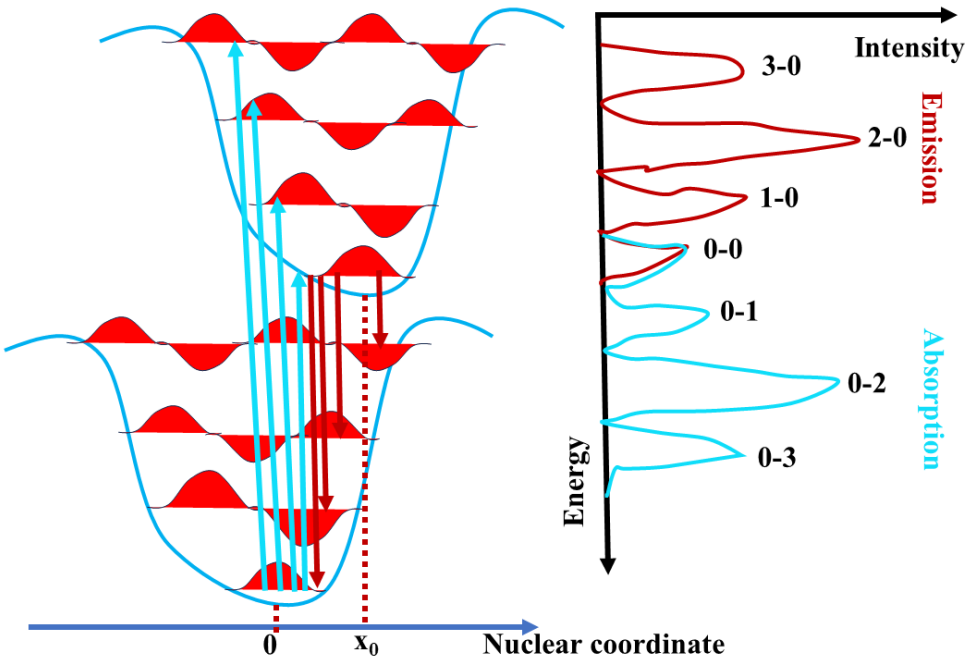

Figure 2: Schematic representation of Franck-Condon principle.

1.7.4. Direct and indirect band gap

In solid-state physics, the band gap is an important concept that characterizes the electronic properties of materials. It refers to the energy difference between the top of the valence band (the highest energy level filled with electrons) and the bottom of the conduction band (the lowest empty energy level) in the electronic band structure of a material. The band gap determines whether a material is an insulator, semiconductor, or conductor. There are two types of band gaps: direct and indirect. Let's explore these concepts in more detail:

- **Direct Band Gap:** In materials with a direct band gap, the maximum energy of the valence band occurs at the same momentum (k-point) as the minimum energy of the conduction band in the reciprocal lattice (k-space). This means that electrons can easily transition between the valence and conduction bands with the emission or absorption of photons without a change in momentum. The process is highly efficient since there is no need for additional momentum to be provided or removed.

Direct band gap materials are favorable for optoelectronic applications, such as light-emitting diodes (LEDs) and lasers. When an electron in the conduction band recombines with a hole (electron vacancy) in the valence band, it emits a photon directly, resulting in efficient light emission.

- **Indirect Band Gap:** In materials with an indirect band gap, the maximum energy of the valence band does not align with the minimum energy of the conduction band in k-space. As a result, electron transitions between the valence and conduction bands require a change in momentum, in addition to the emission or absorption of photons.

  Indirect band gap materials have lower optical transition probabilities and, thus, are less efficient in emitting light compared to direct band gap materials. The recombination of an electron and a hole typically involves an additional scattering event with phonons (lattice vibrations) to conserve momentum, making the process less likely and less efficient in terms of light emission. Indirect band gap materials are commonly used in electronic devices such as transistors, where electrical rather than optical properties are the primary concern.

In terms of optical properties, direct band gap materials typically exhibit a sharp absorption edge in their optical absorption spectra, corresponding to the energy required for electrons to make a direct transition across the band gap. In contrast, indirect band gap materials have a less pronounced absorption edge due to the additional momentum conservation requirement. The distinction between direct and indirect band gaps has significant implications for the design and performance of electronic and optoelectronic devices. Direct band gap materials are more efficient for light emission and absorption processes, making them suitable for applications such as solar cells and photodetectors. On the other hand, indirect band gap materials are often used in electronic devices such

as transistors and integrated circuits, where efficient light emission is not a primary requirement.

It is important to note that the direct or indirect nature of the band gap depends on the specific electronic band structure of a material, which can be influenced by factors such as crystal structure, symmetry, and chemical composition.

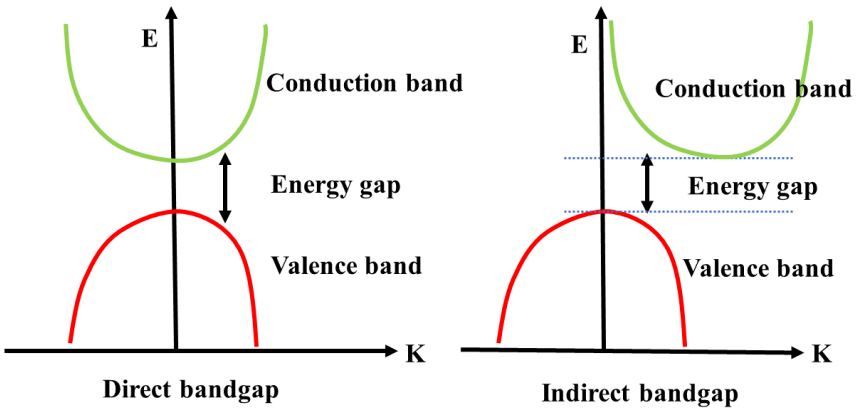

Figure 3: Schematic picture of Direct and Indirect band gap.

1.7.5. Luminescence

Luminescent emission is the process by which a material emits light after being excited by an external energy source. The emission of light occurs as a result of the relaxation of excited states in the material. Understanding the luminescent emission process involves considering the steps involved in the absorption of energy, excitation of electrons, and subsequent emission of light. Here is an overview of the luminescent emission process:

- **Absorption of Energy:** The luminescent emission process begins with the absorption of energy by the material. This energy can be in the form of photons (light), electrons, or other forms of excitation energy. When the material absorbs the energy, it promotes some of its electrons from

their ground state to higher energy levels. The absorption process follows the principles of quantum mechanics, where the energy of the absorbed photons or particles must match the energy difference between the electronic states.

- **Excitation of Electrons:** The absorbed energy causes the electrons to transition to higher energy levels, creating excited states within the material. The excited states are temporary energy levels where the electrons are in higher energy orbits around the atomic or molecular nucleus. The excitation can involve different mechanisms, such as electronic transitions in atoms, or energy transfer processes in molecules or semiconductors.
- **Relaxation Processes:** After excitation, the excited electrons in the material undergo relaxation processes to return to lower energy levels. These relaxation processes involve the release of excess energy, which can occur through various mechanisms, depending on the specific material and its properties. The relaxation processes can be categorized into two main types:

a. **Radiative Relaxation:** In radiative relaxation, the excited electrons return to lower energy levels by emitting photons of light. The emitted photons carry the excess energy that was absorbed during excitation. The emitted light can have different characteristics, such as wavelength, intensity, and duration, depending on the specific luminescent properties of the material.

b. **Non-Radiative Relaxation:** In non-radiative relaxation, the excess energy is dissipated through non-radiative processes, such as thermal energy transfer or interaction with other particles in the material. Non-radiative relaxation pathways do not result in the emission of light. Instead, the excess energy is converted into other forms, such as heat.

- **Emission of Light:** In the case of radiative relaxation, the excess energy is released as photons, resulting in the emission of light. The emitted light can have different characteristics, including the wavelength (color), intensity, and polarization, which depend on the specific luminescent properties of the material. The emitted light carries information about the energy levels and electronic transitions occurring within the material. The processes of emiting light are discussed below:

a. **Fluorescence:** Fluorescence is a phenomenon in which a substance absorbs light at a specific wavelength and then emits light at a longer wavelength. It is a type of luminescence that involves the absorption of photons by a molecule, followed by the subsequent release of photons as the excited molecule returns to its ground state. When a molecule absorbs photons, it undergoes an electronic transition from the ground state to an excited state. This excited state is typically short-lived, and the molecule quickly returns to the ground state through various relaxation processes. One of these relaxation pathways involves the emission of a photon with lower energy than the absorbed photon, resulting in fluorescence.

   It is extensively employed in techniques such as fluorescence spectroscopy, fluorescence microscopy, flow cytometry, immunoassays, and molecular imaging. Fluorescent molecules, or fluorophores, can be natural or synthetic compounds specifically designed for fluorescence applications. They can exhibit different emission colors, allowing for multiplexing and simultaneous detection of multiple targets. Fluorescence techniques offer high sensitivity, selectivity, and versatility, making them valuable tools for studying molecular interactions, detecting and quantifying analytes, visualizing biological processes, and developing diagnostic and imaging tools.

b. Phosphorescence: Phosphorescence is a luminescent phenomenon similar to fluorescence, but with a key distinction. While fluorescence

involves the immediate emission of light upon absorption of photons, phosphorescence is characterized by a delayed emission of light after the cessation of excitation. In phosphorescence, a molecule absorbs photons and undergoes an electronic transition to an excited state. However, unlike in fluorescence, the excited state has a longer lifetime and persists even after the excitation source is removed. This long-lived excited state is referred to as a triplet state. The delay in light emission during phosphorescence arises from a phenomenon called intersystem crossing. Instead of directly returning to the ground state, the excited molecule undergoes a spin-forbidden transition from the singlet excited state to the triplet excited state. This intersystem crossing process is relatively slow, resulting in a delayed emission of light. The emitted light in phosphorescence occurs at a longer wavelength than the absorbed light, similar to fluorescence. The wavelength of the emitted light is determined by the energy difference between the triplet excited state and the ground state. Phosphorescent materials can exhibit various emission colors, depending on the specific molecular structure and composition.

Phosphorescence finds applications in various fields, including lighting, displays, security features, and optical sensing. It is particularly valuable in situations where long-lived emission and sensitivity to external factors are desired. Phosphorescent materials can be engineered to exhibit specific emission colors, making them versatile for diverse applications in research, industry, and everyday products.

The luminescent emission process is influenced by various factors, including the nature of the material, its crystal structure, impurities, defects, and external environmental conditions. By studying and understanding the luminescent emission process, scientists can explore the optical properties of materials,

design luminescent materials for specific applications, and develop technologies such as lighting, displays, sensors, and biomedical imaging.

- **Crystal defects:** Crystal defects can have significant effects on the optical properties of semiconducting materials. These defects can arise from various sources, such as vacancies, interstitials, impurities, dislocations, or grain boundaries. The presence of defects introduces localized energy levels within the bandgap of the semiconductor, leading to alterations in its optical behavior. Here are a few ways in which crystal defects can affect the optical properties of semiconducting materials:

a. **Absorption and transmission:** Crystal defects can introduce additional energy levels within the bandgap, resulting in the absorption of light at specific wavelengths. These defects act as intermediate states for photon absorption, broadening the absorption spectrum of the material. The presence of defects can also affect the material's transmission properties by either increasing or reducing its transparency to specific wavelengths.

b. **Photoluminescence:** Defects can significantly impact the emission of light from semiconducting materials. Certain defects, such as dopants or impurities, can act as luminescent centers that emit light when excited. This emission can occur as fluorescence or phosphorescence, and the energy levels associated with the defects determine the emitted light's wavelength. Defects can introduce new energy levels for radiative recombination, influencing the material's photoluminescent properties.

c. **Non-radiative recombination:** Defects can facilitate non-radiative recombination processes, where electrons and holes recombine without emitting photons. These non-radiative pathways can lead to the loss of optical efficiency and reduced emission intensity in semiconducting materials. Defects with deep energy levels or trap states can act as

recombination centers, competing with radiative recombination and diminishing the material's overall optical performance.

d. **Scattering and refraction:** Crystal defects, such as dislocations or grain boundaries, can cause light scattering within the material. This scattering effect can alter the transmission and reflection of light, leading to reduced optical clarity and increased diffuse reflection. Additionally, defects can influence the refractive index of the semiconductor, affecting the way light is refracted as it passes through the material.
e. **Quantum confinement:** Defects can interact with quantum confinement effects in nanostructured semiconductors. The presence of defects can modify the confinement potential and energy levels within quantum dots, nanowires, or other nanostructures. This alteration can result in changes in the material's energy band structure, optical absorption, and emission properties.

Controlling and minimizing crystal defects in semiconducting materials is crucial for optimizing their optical properties. Defect engineering techniques, such as defect passivation or annealing processes, can be employed to reduce the concentration and impact of defects on the material's optical behavior. By understanding and manipulating crystal defects, researchers can tailor the optical properties of semiconducting materials to meet specific requirements in optoelectronic devices, photovoltaics, light-emitting diodes (LEDs), and other optical applications.

1.7.5.1. Chemiluminescent

Chemiluminescence is a fascinating phenomenon in which light is emitted as a result of a chemical reaction, without the need for an external energy source such as heat or electricity. It involves the conversion of chemical energy into light energy. Chemiluminescent reactions typically involve the formation of

excited states or electronically excited molecules that subsequently relax and emit photons of light. Here is an overview of chemiluminescence:

- **Mechanism of Chemiluminescence:** Chemiluminescent reactions involve the conversion of chemical energy into light energy through a series of chemical reactions. In these reactions, certain reactant molecules undergo chemical transformations that result in the formation of excited states or electronically excited molecules. These excited states or molecules are unstable and subsequently return to their ground state by releasing energy in the form of light.
- **Chemiluminescent Systems:** Chemiluminescence can occur in various systems, ranging from simple chemical reactions to complex biological processes. Some examples of chemiluminescent systems include:

a. **Organic Compounds:** Certain organic compounds, known as luminophores or luminogens, are capable of undergoing chemiluminescent reactions. These compounds often contain specific functional groups, such as peroxides or dioxetanes, which can undergo chemical transformations leading to the release of light.

b. **Bioluminescent Reactions:** Bioluminescence is a type of chemiluminescence exhibited by living organisms, such as fireflies, jellyfish, and bacteria. It involves the production and emission of light through biochemical reactions. For example, in fireflies, the enzyme luciferase catalyzes the oxidation of a substrate called luciferin, resulting in the emission of light.

- **Analytical Chemiluminescence:** Chemiluminescence is also widely used in analytical chemistry for detection and analysis. Analytical chemiluminescence methods involve the use of specific chemical reactions that produce light as a result of target analytes present in a sample. These methods are sensitive, selective, and can be employed for

various applications, including environmental monitoring, forensic analysis, and clinical diagnostics.

- **Applications of Chemiluminescence:** Chemiluminescence has found numerous applications in various fields. Some notable applications include:

a. **Lighting and Illumination:** Chemiluminescent compounds are used in light sticks, emergency lighting, glow-in-the-dark products, and safety signage. These applications rely on chemiluminescent reactions for reliable and portable light sources.

b. **Biological and Medical Imaging:** Chemiluminescence-based imaging techniques, such as Western blotting and immunoassays, are widely used in biological and medical research. These techniques employ chemiluminescent labels to detect and visualize specific biomolecules.

c. **Environmental Monitoring:** Chemiluminescence can be utilized for the detection and quantification of certain environmental pollutants, such as reactive oxygen species and nitrogen oxides, which are involved in atmospheric and water pollution.

d. **Forensic Science:** Chemiluminescence techniques are employed in forensic investigations for the detection of trace evidence, such as bloodstains or fingerprints. Luminol, a chemiluminescent compound, is commonly used for these applications.

e. **Security and Authentication:** Chemiluminescent materials are employed for security purposes, including document verification, anti-counterfeiting measures, and tamper-evident labels.

Chemiluminescence is a captivating phenomenon that has both scientific and practical significance. It offers unique opportunities for studying chemical reactions, developing sensitive detection methods, and creating self-contained light sources for various applications.

1.7.5.2. Crystalloluminescent

Crystalloluminescence is a phenomenon in which certain crystalline materials emit light when subjected to mechanical stress or deformation. Unlike other forms of luminescence, such as fluorescence or phosphorescence, crystalloluminescence does not involve the absorption and subsequent relaxation of excited states. Instead, it relies on the mechanical interactions within the crystal lattice to generate light emission. Here is an overview of crystalloluminescence:

- **Mechanism of Crystalloluminescence:** Crystalloluminescence occurs due to the piezoelectric effect and the generation of electric charges within certain crystalline materials under mechanical stress. When a crystalline material is subjected to stress or deformation, the crystal lattice experiences a change in symmetry and structure, resulting in the generation of electric charges or dipoles. These induced charges and dipoles then give rise to an electric field, which can interact with the electrons within the material and lead to the emission of light.
- **Types of Crystalloluminescence:** Crystalloluminescence can be divided into two main types based on the emitted light:
    a. **Triboluminescence:** Triboluminescence refers to the emission of light when a crystalline material is fractured, crushed, or scratched. When mechanical stress is applied to the crystal lattice, the resulting electric field excites the electrons, causing them to transition to higher energy levels. As the electrons return to their ground state, they emit photons of light. Common examples of triboluminescent materials include quartz, sugar, and certain minerals.
    b. **Mechanoluminescence:** Mechanoluminescence is the emission of light resulting from mechanical deformation, such as bending,

twisting, or compressing a crystalline material. The mechanical stress induces the generation of electric charges or dipoles, which in turn interact with the electrons, leading to light emission. Mechanoluminescence is observed in various materials, including certain inorganic crystals, organic compounds, and polymers.

- **Applications and Significance:** Crystalloluminescence has intrigued scientists and researchers due to its unique properties and potential applications. Some of the applications and significance of crystalloluminescence include:

a. **Material Characterization:** Crystalloluminescence can provide valuable information about the structural and mechanical properties of crystalline materials. By studying the intensity, wavelength, and kinetics of the emitted light, researchers can gain insights into the material's behavior under stress or deformation.

b. **Sensing and Detection:** Crystalloluminescent materials have been explored for potential sensing and detection applications. Their light emission can be used as an indicator or probe for mechanical stress, deformation, or structural changes. This makes them promising for stress sensors, impact detection, and structural health monitoring.

c. **Fundamental Research:** Crystalloluminescence serves as a platform for studying the underlying mechanisms of light emission and charge generation in materials under mechanical stress. The understanding gained from these studies contributes to the broader field of luminescence and material science.

Crystalloluminescence is a fascinating area of study that offers insights into the interactions between mechanical stress, electric fields, and light emission in crystalline materials. Further research in this field may lead to advancements in

material characterization, sensing technologies, and fundamental understanding of luminescent phenomena.

1.7.5.3. Radio luminescent

Radio luminescence, also known as radio-luminescence, is a phenomenon in which certain materials emit light when exposed to ionizing radiation. Unlike other forms of luminescence, radio luminescence does not involve the absorption and subsequent relaxation of excited states. Instead, it occurs when ionizing radiation interacts with the material, causing the emission of photons. Here is an overview of radio luminescence:

- **Mechanism of Radio Luminescence:** Radio luminescence is primarily driven by the excitation of electrons within the material through ionizing radiation. Ionizing radiation, such as alpha particles, beta particles, or gamma rays, possesses sufficient energy to ionize atoms or molecules in the material. When ionization occurs, electrons are ejected from their orbitals, creating electron vacancies or ionized states. The recombination of these ionized states with free electrons results in the emission of light in the form of photons.
- **Types of Radio Luminescent Materials:** Various materials exhibit radio luminescence when exposed to ionizing radiation. Some common examples include:

a. **Phosphors:** Phosphors are materials that exhibit luminescence under different excitation sources, including ionizing radiation. These materials contain activator ions that absorb the energy from ionizing radiation and subsequently emit light. Phosphors are widely used in applications such as radiation detectors, luminescent paints, and luminous safety signs.

b. **Crystals:** Certain crystals, such as alkali halides and rare-earth doped crystals, can exhibit radio luminescence. These crystals contain impurity ions or defects that play a role in the light emission process. Radio

luminescent crystals have applications in radiation dosimetry and radiation therapy.

c. **Polymers:** Some polymers exhibit radio luminescence when exposed to ionizing radiation. These polymers contain fluorescent dyes or other luminescent materials that emit light upon interaction with ionizing radiation. Radio luminescent polymers find applications in radiation dosimetry and imaging.

- **Applications of Radio Luminescence:** Radio luminescent materials and techniques have several practical applications, including:

a. **Radiation Dosimetry:** Radio luminescent materials are commonly used in radiation dosimeters, which are devices used to measure and monitor radiation exposure. The emitted light intensity or color can be correlated to the radiation dose received, providing valuable information for radiation safety and medical applications.

b. **Radiation Detection and Imaging:** Radio luminescent materials are utilized in radiation detectors and imaging systems. These materials can convert ionizing radiation into visible light signals, allowing for the detection and visualization of radiation sources.

c. **Radiation Therapy:** In radiation therapy, radio luminescent materials can be employed to verify and measure the dose distribution delivered to the target tissues. This helps ensure accurate and effective treatment in cancer therapy.

d. **Nuclear Power and Industry:** Radio luminescent materials play a role in radiation safety and monitoring in nuclear power plants, industrial settings involving radioactive materials, and environmental radiation monitoring.

Radio luminescence is an important phenomenon that enables the detection, measurement, and imaging of ionizing radiation. The development of radio

luminescent materials and techniques continues to advance radiation-related technologies and enhance radiation safety practices.

1.7.5.4. Thermo luminescent

Thermo luminescence is a phenomenon in which certain materials emit light when heated after being previously exposed to ionizing radiation. The term "thermo luminescence" combines the words "thermo" (referring to heat) and "luminescence" (referring to the emission of light). This process occurs due to the trapping and subsequent release of charge carriers within the material's crystal lattice. Here is an overview of thermo luminescence:

- **Mechanism of Thermo luminescence:** When a material is exposed to ionizing radiation, such as X-rays or gamma rays, some of the electrons within the material are excited to higher energy levels or ejected from their orbitals. As a result, electron-hole pairs are created, and some of the electrons become trapped in energy levels or defects within the crystal lattice.
- **Trapping and Excitation:** During the exposure to ionizing radiation, the trapped electrons accumulate in specific energy levels or defects, forming metastable states. These trapped charge carriers are stabilized by the surrounding lattice structure. The number and energy distribution of the trapped electrons depend on factors such as the type and energy of the ionizing radiation, the properties of the material, and the temperature during irradiation.
- **Heating and Light Emission:** When the thermo luminescent material is subsequently heated, the trapped electrons gain enough thermal energy to overcome the energy barriers that trap them. As they are released from the traps, the electrons recombine with the trapped holes, and the excess energy is emitted as visible light. The emitted light intensity is

proportional to the amount of charge carriers released, which, in turn, depends on the radiation dose absorbed by the material.

- **Applications of Thermo luminescence:** Thermo luminescence has various practical applications, including:

a. **Radiation Dosimetry:** Thermo luminescent materials are commonly used in radiation dosimetry to measure the absorbed dose of ionizing radiation. The emitted light intensity is correlated with the radiation dose, providing valuable information for radiation safety, medical diagnostics, archaeological dating, and environmental monitoring.

b. **Dating Techniques:** Thermo luminescence dating is a method used to determine the age of archaeological artifacts, pottery, and geological materials. By measuring the accumulated radiation dose through thermo luminescence, the time since the material was last heated or exposed to sunlight can be estimated.

c. **Radiation Detection and Monitoring:** Thermo luminescent materials are used in radiation detectors for personal dosimetry, environmental monitoring, and radiation protection. These detectors can provide accurate and reliable measurements of ionizing radiation in various settings, including medical facilities, nuclear power plants, and research laboratories.

d. **Material Characterization:** Thermo luminescence can be utilized to study the properties of materials, including their defects, impurities, and structural changes. By analysing the thermo luminescence characteristics, researchers can gain insights into the behavior and stability of materials under different environmental conditions.

Thermo luminescence is a valuable technique for radiation dosimetry, dating, and material characterization. It has found widespread use in fields such as

radiation protection, archaeology, geology, and materials science, providing important information about the interaction of materials with ionizing radiation.

References:

[1] Passian, A. and Imam, N., 2019. Nanosystems, edge computing, and the next generation computing systems. *Sensors*, *19*(18), p.4048.

[2] Geim, A.K. and Novoselov, K.S., 2007. The rise of graphene. *Nature materials*, *6*(3), pp.183-191.

[3] Torchilin, V.P., 2014. Multifunctional, stimuli-sensitive nanoparticulate systems for drug delivery. *Nature reviews Drug discovery*, *13*(11), pp.813-827.

[4] Jain, K.K., 2005. Nanotechnology in clinical laboratory diagnostics. *Clinica chimica acta*, *358*(1-2), pp.37-54.

[5] Hoffman, A.S., 2012. Hydrogels for biomedical applications. *Advanced drug delivery reviews*, *64*, pp.18-23.

[6] Wang, Y.P., Li, H.C., Huang, Y.C. and Tan, C.S., 2023. Synthesis and Applications of Halide Perovskite Nanocrystals in Optoelectronics. *Inorganics*, *11*(1), p.39.

[7] Rodriguez, J.A., Ma, S., Liu, P., Hrbek, J., Evans, J. and Perez, M., 2007. Activity of CeO x and TiO x nanoparticles grown on Au (111) in the water-gas shift reaction. *Science*, *318*(5857), pp.1757-1760.

[8] Gehrke, I., Geiser, A. and Somborn-Schulz, A., 2015. Innovations in nanotechnology for water treatment. *Nanotechnology, science and applications*, pp.1-17.

[9] Cuppoletti, J. ed., 2011. *Nanocomposites and polymers with analytical methods*. BoD–Books on Demand.

[10] Okoli, J.U., Briggs, T.A. and Major, I.E., 2013. Application of nanotechnology in the manufacturing sector: A review. *Nigerian Journal of Technology*, *32*(3), pp.379-385.

[11] Coussens, C. and Goldman, L. eds., 2005. Implications of nanotechnology for environmental health research.

[12] Song, G., Wang, C. and Wang, B., 2017. Structural health monitoring (SHM) of civil structures. *Applied Sciences*, *7*(8), p.789.

[13] He, X. and Hwang, H.M., 2016. Nanotechnology in food science: Functionality, applicability, and safety assessment. *journal of food and drug analysis*, *24*(4), pp.671-681.

[14] He, X. and Hwang, H.M., 2016. Nanotechnology in food science: Functionality, applicability, and safety assessment. *journal of food and drug analysis*, *24*(4), pp.671-681.

[15] Qu, X., Alvarez, P.J. and Li, Q., 2013. Applications of nanotechnology in water and wastewater treatment. *Water research*, *47*(12), pp.3931-3946.

[16] Park, J., Bazylewski, P. and Fanchini, G., 2016. Porous graphene-based membranes for water purification from metal ions at low differential pressures. *Nanoscale*, *8*(18), pp.9563-9571.

[17] Theron, J., Walker, J.A. and Cloete, T.E., 2008. Nanotechnology and water treatment: applications and emerging opportunities. *Critical reviews in microbiology*, *34*(1), pp.43-69.

[18] Mondal, B., Mac Giolla Eain, M., Xu, Q., Egan, V.M., Punch, J. and Lyons, A.M., 2015. Design and fabrication of a hybrid superhydrophobic–hydrophilic surface that exhibits stable dropwise condensation. *ACS applied materials & interfaces*, *7*(42), pp.23575-23588.

[19] Vujovic, M. and Kostic, E., 2019. Titanium Dioxide and Zinc Oxide Nanoparticles in Sunscreens: A Review of Toxicological Data. *Journal of cosmetic science*, *70*(5), pp.223-234.

[20] Hontañón, E. and Vallejos, S., 2021. One-dimensional metal oxide nanostructures for chemical sensors. *21st Century Nanostructured Materials-Physics, Chemistry, Classification, and Emerging Applications in Industry, Biomedicine, and Agriculture*.

[21] Kupka, N. and Rudolph, M., 2018. Froth flotation of scheelite–A review. *International Journal of Mining Science and Technology*, *28*(3), pp.373-384.

[22] Jiao, W., Zhang, Z. and Jingtai, Z., 2015. Luminescence properties of Eu3+-doped new scheelite-type compounds. *Journal of Rare Earths*, *33*(12), pp.1241-1245.

[23] Harran, I., Chen, Y., Wang, H., Li, H., Li, Y. and Tao, L., 2017. High-pressure induced phase transition of FeS2: Electronic, mechanical and thermoelectric properties. *Journal of Alloys and Compounds*, *710*, pp.267-273.

[24] Stumm, W., 1992. *Chemistry of the solid-water interface: processes at the mineral-water and particle-water interface in natural systems*. John Wiley & Son Inc..

[25] Pavel, C.C., Marmier, A., Tzimas, E., Schleicher, T., Schüler, D., Buchert, M. and Blagoeva, D., 2016. Critical raw materials in lighting applications: Substitution opportunities and implication on their demand. *physica status solidi (a)*, *213*(11), pp.2937-2946.

[26] Cao, C., Zhang, Z., Wei, S., Xie, A., Noh, H.M. and Jeong, J.H., 2020. Synthesis, optical properties, energy transfer, thermal behavior, and LED package of Eu3+ doped lutetium tungsten oxide phosphors. *Optical Materials*, *101*, p.109753.

[27] Eliseeva, S.V. and Bünzli, J.C.G., 2010. Lanthanide luminescence for functional materials and bio-sciences. *Chemical Society Reviews*, *39*(1), pp.189-227.

[28] Mahata, P., Mondal, S.K., Singha, D.K. and Majee, P., 2017. Luminescent rare-earth-based MOFs as optical sensors. *Dalton Transactions*, *46*(2), pp.301-328.

[29] Probst, J., Dembski, S., Milde, M. and Rupp, S., 2012. Luminescent nanoparticles and their use for in vitro and in vivo diagnostics. *Expert review of molecular diagnostics*, *12*(1), pp.49-64.

[30] Liang, S., Wang, H., Li, Y., Qin, H., Luo, Z., Huang, B., Zhao, X., Zhao, C. and Chen, L., 2020. Rare-earth based nanomaterials and their composites as electrode materials for high performance supercapacitors: a review. *Sustainable Energy & Fuels*, *4*(8), pp.3825-3847.

[31] Sze, S.M. and Ng, K.K., 2006. LEDs and lasers. *Physics of Semiconductor Devices*, *3*, pp.601-657.

[32] Streetman, B.G. and Banerjee, S., 2000. *Solid state electronic devices* (Vol. 4). New Jersey: Prentice hall.

[33] Liang, S., Wang, H., Li, Y., Qin, H., Luo, Z., Huang, B., Zhao, X., Zhao, C. and Chen, L., 2020. Rare-earth based nanomaterials and their composites as electrode materials for high performance supercapacitors: a review. *Sustainable Energy & Fuels*, *4*(8), pp.3825-3847.

[34] Hecht, E.E., Robins, D.L., Gautam, P. and King, T.Z., 2017. Intranasal oxytocin reduces social perception in women: Neural activation and individual variation. *Neuroimage*, *147*, pp.314-329.

[35] Yeh, P. and Hendry, M., 1990. Optical waves in layered media. *Physics Today*, *43*(1), p.77.

[36] Coldren, L.A., Corzine, S.W. and Mashanovitch, M.L., 2012. *Diode lasers and photonic integrated circuits*. John Wiley & Sons.

[37] Boyd, R.W. and Masters, B., 2008. Nonlinear Optics 3rd edn (New York: Academic).

[38] Skoog, D.A., Holler, F.J. and Crouch, S.R., 2017. *Principles of instrumental analysis*. Cengage learning.

[39] Silverstein, R.M. and Bassler, G.C., 1962. Spectrometric identification of organic compounds. *Journal of Chemical Education*, *39*(11), p.546.

[40] Reddy, K.K., Grossman, L. and Rogers, G.S., 2013. Common complementary and alternative therapies with potential use in dermatologic surgery: risks and benefits. *Journal of the American academy of dermatology*, *68*(4), pp.e127-e135.

Chapter 2: Literature Review.....

1. Literature Review

1.1 Synthesis strategies of rare earth based scheelite type Micro/Nano structured materials

The synthesis of rare earth-based scheelite materials can be accomplished using various methods, including hydrothermal techniques, sol-gel methods, solid-state reactions, and more. Here, I'll provide a general overview of the synthesis process for rare earth-based scheelite materials:

- **Precursor Selection:** Choose suitable precursor materials based on the desired composition of the scheelite material. Rare earth metal salts (such as chlorides, nitrates, or carbonates) and a tungstate source (such as sodium tungstate) are commonly used.

- **Precursor Preparation:** Prepare the precursor materials by dissolving the rare earth metal salts and the tungstate source in appropriate solvents or through solid-state mixing, depending on the synthesis method.
- **Mixing and Homogenization:** Thoroughly mix the precursor materials to ensure a uniform distribution of rare earth and tungstate ions. This step is crucial for achieving a homogeneous scheelite material.
- **Synthesis Method Selection:** Choose a specific synthesis method based on the desired properties and applications of the scheelite material.
- **Reaction or Processing Conditions:** The specific reaction conditions, including temperature, pressure, duration, and any additional additives or catalysts, will depend on the chosen synthesis method.
- **Product Isolation and Post-Treatment:** Once the reaction or processing is complete, the resulting scheelite material needs to be isolated from the reaction mixture. This can involve processes like filtration, centrifugation, or solvent evaporation. Further post-treatment steps, such as washing, drying, and grinding, may be necessary to obtain the final product with desired characteristics.
- **Characterization:** Characterize the synthesized scheelite material using various techniques to evaluate its composition, crystal structure, morphology, and physical properties. Common characterization methods include X-ray diffraction (XRD), scanning electron microscopy (SEM), transmission electron microscopy (TEM), energy-dispersive X-ray spectroscopy (EDS), and spectroscopic techniques (e.g., FTIR, UV-Vis).

It's important to note that the specific synthesis procedures and conditions may vary depending on the rare earth elements used, the tungstate source, the desired properties of the scheelite material, and the chosen synthesis method. Consulting scientific literature, research papers, or experts in the field can provide more detailed and tailored synthesis protocols for specific rare earth-

based scheelite materials. Also the photoluminescence properties of scheelite nanomaterials are closely connected to their preparative methods. The nanoparticle size, morphology, and corresponding microstructure of luminescent materials depend on their different preparation method, which can affect their application in diversified directions. The synthesis of rare earth-based scheelite materials can be accomplished using various methods, including hydrothermal techniques, sol-gel methods, solid-state reactions, and more.

1.1.1. Hydro(solvo) thermal technique:

The synthesis of rare earth-based scheelite materials by the hydrothermal technique involves the formation of scheelite-type crystals using a hydrothermal reaction at elevated temperatures and pressures. Here's a general outline of the synthesis process:

- **Precursor Preparation:** Start by preparing the precursor materials, which typically consist of rare earth metal salts (e.g., rare earth chlorides or nitrates) and a source of tungstate ions (e.g., sodium tungstate). These materials should be of high purity to ensure the quality of the final product.
- **Solution Preparation:** Dissolve the rare earth metal salts and the tungstate source in an appropriate solvent. Typically, deionized water or other aqueous solutions are used. The concentration of the precursor materials will depend on the desired composition of the final scheelite material.
- **Reactor Setup:** Transfer the precursor solution to a hydrothermal reactor, which is a high-pressure vessel capable of withstanding elevated temperatures and pressures. The reactor is usually made of materials such as stainless steel or Teflon.
- **Reaction Conditions:** Seal the reactor and heat it to the desired reaction temperature, which can range from around 140°C to several hundred

degrees Celsius. The pressure inside the reactor is controlled by the amount of solvent and any additional gas phase introduced. The reaction time can vary from a few hours to several days, depending on the specific synthesis parameters and the desired properties of the scheelite material.

- **Cooling and Isolation:** After the reaction is complete, the reactor is cooled down to room temperature. The resulting product is then isolated by filtration or centrifugation. Washing the product with a suitable solvent and drying it under controlled conditions may be necessary to remove any residual impurities.
- **Characterization:** The synthesized scheelite material should be characterized using various techniques to confirm its composition, crystal structure, and physical properties. Techniques such as X-ray diffraction (XRD), scanning electron microscopy (SEM), energy-dispersive X-ray spectroscopy (EDS), and Fourier-transform infrared spectroscopy (FTIR) can provide valuable information about the material's structure and properties.

1.1.2. Microwave assisted hydrothermal technique:

The synthesis of rare earth-based scheelite materials using the microwave-assisted hydrothermal method involves utilizing microwave radiation to enhance the hydrothermal reaction. This technique offers advantages such as reduced reaction time and improved product yield. Here's a general procedure for synthesizing rare earth-based scheelite materials using the microwave-assisted hydrothermal method:

- **Precursor Preparation:** Start by preparing the precursor materials, including rare earth metal salts (e.g., rare earth chlorides or nitrates) and a

source of tungstate ions (e.g., sodium tungstate). Ensure that the precursors are of high purity to obtain a high-quality final product.

- **Solution Preparation:** Dissolve the rare earth metal salts and the tungstate source in an appropriate solvent. Deionized water or other aqueous solutions are commonly used. Adjust the concentration of the precursor materials based on the desired composition of the scheelite material.
- **Reactor Setup:** Transfer the precursor solution to a suitable reaction vessel that is microwave transparent, such as a Teflon-lined autoclave. Ensure that the vessel is compatible with microwave radiation.
- **Microwave-Assisted Hydrothermal Reaction:** Seal the reaction vessel and place it in a microwave reactor. Apply microwave radiation to the vessel at the desired power and frequency. The reaction conditions, including temperature and time, can be controlled by adjusting the microwave power and reaction duration.
- **Cooling and Isolation:** After the reaction is complete, cool the reaction vessel to room temperature. Carefully open the vessel and isolate the synthesized product. Filtration or centrifugation can be used to separate the product from the solvent. Wash the product with a suitable solvent and dry it under controlled conditions to remove any residual impurities.
- **Characterization:** Characterize the synthesized scheelite material using various techniques to confirm its composition, crystal structure, and physical properties. X-ray diffraction (XRD), scanning electron microscopy (SEM), energy-dispersive X-ray spectroscopy (EDS), and Fourier-transform infrared spectroscopy (FTIR) are commonly employed for characterization.

It is important to note that microwave-assisted hydrothermal synthesis parameters (such as microwave power, temperature, and time) should be

optimized based on the specific rare earth elements, tungstate source, and desired properties of the scheelite material.

1.1.3. Sol gel synthesis method:

The synthesis of rare earth-based scheelite materials can also be achieved through the sol-gel method, combined with sol-gel synthesis and electrospinning. Here's a general procedure for synthesizing rare earth-based scheelite materials using this combined approach:

- **Precursor Preparation:** Start by preparing precursor solutions by dissolving rare earth metal salts (e.g., rare earth chlorides or nitrates) and a source of tungstate ions (e.g., sodium tungstate) in suitable solvents. The concentrations of the precursors should be adjusted based on the desired composition of the scheelite material.
- **Mixing and Stabilization:** Mix the precursor solutions together, ensuring thorough homogenization. To stabilize the precursor mixture, an appropriate chelating agent or complexing agent can be added. This helps in controlling the gel formation and subsequent crystallization.
- **Gel Formation:** Allow the precursor mixture to undergo gelation by aging the solution at a controlled temperature for a specific duration. This step results in the formation of a gel, which contains a network of interconnected nanoparticles.
- **Drying and Calcination:** Dry the gel to remove the solvent, typically by evaporating it under controlled conditions. The dried gel is then subjected to calcination at elevated temperatures. Calcination helps in converting the gel into a crystalline scheelite structure by eliminating organic residues and inducing crystallization.

- **Characterization:** Characterize the synthesized scheelite material using techniques such as X-ray diffraction (XRD), scanning electron microscopy (SEM), energy-dispersive X-ray spectroscopy (EDS), and Fourier-transform infrared spectroscopy (FTIR) to confirm its composition, crystal structure, and physical properties.

1.1.4. Combined sol–gel synthesis and electrospinning

In this approach, the sol-gel method is combined with electrospinning to create fibrous structures of scheelite materials.

- **Sol-Gel Preparation:** Follow the steps outlined above for the sol-gel synthesis to prepare the precursor gel.
- **Electrospinning Solution Preparation:** Dissolve a suitable polymer, such as polyvinylpyrrolidone (PVP), in a solvent to form an electrospinning solution. Add the precursor gel to the electrospinning solution and ensure proper mixing.
- **Electrospinning:** Load the electrospinning solution into a syringe with a fine needle or nozzle. Apply a high voltage to the solution while simultaneously extruding it from the nozzle. The electric field causes the solution to form a charged jet that stretches into fine fibers as it moves towards a grounded collector.
- **Drying and Calcination:** Collect the electrospun fibers on a suitable collector and dry them to remove the solvent. Proceed with the calcination step to convert the fibers into crystalline scheelite structures.
- **Characterization:** Characterize the electrospun scheelite fibers using techniques such as XRD, SEM, EDS, and FTIR to analyze their composition, crystal structure, and physical properties.

1.1.5. Solid state reaction:

The synthesis of rare earth-based scheelite materials through the conventional solid-state reaction involves the direct reaction between rare earth metal oxides or carbonates and a source of tungstate ions at high temperatures. Here's a general procedure for synthesizing rare earth-based scheelite materials using this method:

- **Precursor Preparation:** Start by preparing the precursor materials, which typically include rare earth metal oxides or carbonates and a source of tungstate ions. Ensure that the precursors are of high purity to obtain a high-quality final product.
- **Weighing and Mixing:** Weigh the appropriate amounts of the rare earth metal oxide or carbonate and the tungstate source based on the desired stoichiometry of the scheelite material. Thoroughly mix the powders in a mortar and pestle or a ball mill to ensure homogeneity.
- **Grinding and Homogenization:** Grind the mixture using a mortar and pestle or a ball mill to further homogenize the powders and enhance the reaction kinetics. This step promotes intimate mixing of the precursors and facilitates the solid-state reaction.
- **Pellet Formation:** Press the powdered mixture into pellets or tablets using a hydraulic press. The applied pressure ensures good compaction and uniformity of the pellet shape and size.
- **Heat Treatment:** Place the pellets in a suitable high-temperature furnace. Heat the furnace to the desired reaction temperature, typically ranging from several hundred to over a thousand degrees Celsius. Maintain the temperature for a specified duration, which can vary depending on the specific synthesis parameters and desired properties of the scheelite material.

- **Cooling and Isolation:** After the heat treatment, cool the furnace to room temperature. Retrieve the synthesized scheelite material, which may be in the form of pellets or compacted powders.
- **Grinding and Sieving (Optional):** If necessary, grind the synthesized material into fine powder using a mortar and pestle or a ball mill. Sieve the powder to obtain a desired particle size range.
- **Characterization:** Characterize the synthesized scheelite material using techniques such as X-ray diffraction (XRD), scanning electron microscopy (SEM), energy-dispersive X-ray spectroscopy (EDS), and Fourier-transform infrared spectroscopy (FTIR) to confirm its composition, crystal structure, and physical properties.

1.1.6. Molten salt synthesis:

The synthesis of rare earth-based scheelite materials by the molten salt method involves the use of high-temperature molten salt as a reaction medium. This technique enables the reaction between rare earth metal oxides or carbonates and a source of tungstate ions at elevated temperatures. Here's a general procedure for synthesizing rare earth-based scheelite materials using the molten salt method:

- **Precursor Preparation:** Start by preparing the precursor materials, which typically include rare earth metal oxides or carbonates and a source of tungstate ions. Ensure that the precursors are of high purity to obtain a high-quality final product.
- **Salt Preparation:** Select a suitable molten salt as the reaction medium. Commonly used molten salts include alkali metal carbonates (e.g., potassium carbonate) or mixtures of alkali metal carbonates and halides (e.g., potassium carbonate/potassium chloride). The molten salt should

have a sufficiently high melting point and good solubility for the precursor materials.

- **Reaction Setup:** Mix the rare earth metal oxide or carbonate and the tungstate source with the molten salt in an appropriate molar ratio. The mixture is typically heated in a crucible or reaction vessel made of materials resistant to high temperatures and chemical reactivity, such as platinum or graphite.
- **Reaction Conditions:** Heat the reaction mixture to a high temperature, typically above the melting point of the chosen molten salt (usually several hundred degrees Celsius). Maintain the reaction temperature for a specified duration, which can range from hours to days, depending on the specific synthesis parameters and desired properties of the scheelite material.
- **Cooling and Isolation:** After the reaction is complete, cool the reaction mixture to room temperature. The product can be isolated by dissolving the cooled reaction mixture in water or an appropriate solvent. Filtration or centrifugation can be used to separate the solid product from the solution. Wash the product with a suitable solvent and dry it under controlled conditions to remove any residual impurities.
- **Characterization:** Characterize the synthesized scheelite material using various techniques to confirm its composition, crystal structure, and physical properties. X-ray diffraction (XRD), scanning electron microscopy (SEM), energy-dispersive X-ray spectroscopy (EDS), and Fourier-transform infrared spectroscopy (FTIR) are commonly employed for characterization.

To synthesis rare earth based scheelite type materials, precursors materials, reaction conditions are shown in Table 1. Other synthesis methods, including

microwave assisted hydrothermal reaction, molten salt synthesis method are also discussed for comparison.

Table 1: Synthesis procedures of rare earth based scheelite nanomaterials

Method	Precursors materials	Reaction condition	Synthesized materials	References
Hydro(solvo)thermal reaction	A rare earth nitrate/chloride salt and a sodium/ammonium tungstate or molybdate salt.	120–200^{o}C for 1–72 hours, calcination at 800^{o}C for 2-5 hours.	$La_2(MoO_4)_3$, $NaCe(MoO_4)_2$, $NaCe(WO_4)_2$, $NaY(MoO_4)_2$, $NaLa(WO_4)_2$, Tm^{3+} and Yb^{3+} co-doped $NaGd(WO_4)_2$.	[1-8]
Microwave assisted hydrothermal reaction	A rare earth nitrate salt and a sodium tungstate or molybdate salt	Temperature 200^{o}C with 90 W power of a microwave irradiation.	$NaY(WO_4)_2$, $NaLa(MoO_4)_2$.	[9,10]

Combined sol–gel synthesis and electrospinning	A rare earth nitrate salt and an ammonium tungstate or molybdate salt	The gel can be dried under critical conditions or by evaporation. Then calcined at high temperature.	$Gd_2(MoO_4)_3$, Gd_2MoO_6, $Tb_2(WO_4)_3$.	[11,12]
Conventional solid-state reaction	A rare earth oxide and tungstate or molybdate oxide and alkali carbonates	1073K for 12 hours at a rate 250k per hour.	$LiCe(WO_4)_2$, $NaCe(WO_4)_2$, $KCe(WO_4)_2$, $Gd_2(MoO_4)_3$, $NaEu(WO_4)_2$.	[13-15]
Molten salt synthesis	Rare earth oxides and tungstate or molybdate oxides, NaCl and KCl as reaction salt as well as solvent.	950^oC for 6 hours.	Gd_2WO_6, Gd_2MoO_6	[16,17]

1.2. Particle growth mechanism

The particle growth mechanism refers to the processes by which particles, such as crystals or nanoparticles, increase in size during their formation. It is essential to understand particle growth mechanisms to control and tailor the properties of the resulting materials for various applications. The growth of particles can be influenced by factors such as temperature, reaction time, concentration of reactants, and the presence of different species in the reaction medium. Several common particle growth mechanisms are described below:

- **Nucleation and Growth:** Nucleation is the initial stage of particle formation, where atoms, ions, or molecules come together to form small clusters called nuclei. Nuclei can be critical in determining the size, structure, and properties of the final particles. After nucleation, these nuclei continue to grow through the addition of more atoms or molecules, resulting in the formation of larger particles.
- **Ostwald Ripening:** Ostwald ripening is a particle growth mechanism that occurs in systems where particles are in contact with a surrounding solution or medium. In this process, smaller particles dissolve, and their constituent species re-deposit onto larger particles, leading to an increase in the size of larger particles and a decrease in the size of smaller ones. Ostwald ripening tends to promote the growth of larger, more stable particles.
- **Aggregation and Coalescence:** In some cases, particles can aggregate or come together to form larger assemblies. Aggregation occurs when individual particles weakly interact or adhere to each other due to van der Waals forces or other attractive interactions. Coalescence, on the other

hand, involves the fusion of two or more particles to form a single, larger particle.

- **Surface Diffusion:** Surface diffusion refers to the movement of atoms or molecules across the surface of a growing particle. During particle growth, atoms or molecules from the surrounding medium may attach to the surface of the particle and then migrate across the surface until they find a suitable site to incorporate into the particle's crystal lattice. Surface diffusion plays a crucial role in determining the shape and crystallinity of the growing particle.
- **Template-Mediated Growth:** In template-mediated growth, a pre-existing template or scaffold guides the formation and growth of particles with specific shapes or structures. The template can be a biomolecule, a surfactant, or a solid substrate. The particles' growth occurs preferentially in specific directions dictated by the template's geometry, resulting in well-defined morphologies.
- **Phase Transformation:** Particle growth can also involve phase transformations, where a material changes from one crystal structure to another as it grows. The transformation may occur due to changes in temperature, pressure, or composition during the synthesis process.

Understanding the particle growth mechanism is essential for controlling the size, shape, and properties of the particles, as well as optimizing their performance for various applications, including catalysis, drug delivery, electronics, and energy storage. Researchers and engineers use this knowledge to design and engineer materials with tailored properties suited to specific needs.

1.2.1 The influence of organic ligands

Hydrothermal and microwave-assisted synthesis are widely utilized methods for preparing rare earth tungstate/molybdate nano/micro-materials. During this synthetic process, organic ligands are introduced into the reaction to form complexes with rare earth metal ions. This complex formation slows down the nucleation and growth of crystals and leads to the binding of functional groups on the material's surface, influencing the growth rate of specific crystal facets [18]. Numerous organic ligands have been employed to control the reaction in the preparation of tungstate/molybdate materials. Commonly used ligands include cetyltrimethyl ammonium bromide, polyvinylpyrrolidone, ethylenediaminetetraacetic acid, trisodium citrate, ammonium oxalate, disodium tartrate, and others.

For instance, $NaCe(WO_4)_2$ rods and hierarchical spindles were synthesized by Dirany et al. through an EDTA-assisted hydrothermal reaction at 200°C for 24 hours, followed by calcination at 800°C for 5 hours [3]. In another hydrothermal synthesis, $NaLa(MoO_4)_2$ was prepared using a combination of oleic acid (OA) and oleylamine (OL) as mixed surfactants at 140°C for 6 hours [19]. The use of organic additives like n-dodecanethiol, a-cyclodextrin, ethylenediamine, L-ascorbic acid, and polyformaldehyde instead of eggshell templates resulted in various nanostructures with different morphologies, such as flower-like, double-taper-like, anchor-like, sphere-like, and fasciculus-like shapes [21]. The addition of trisodium citrate led to the formation of 3D urchin-like microarchitectures, while polyvinylpyrrolidone resulted in irregular microcrystals. Ammonium oxalate produced irregular microplates, disodium tartrate yielded nanoparticles, and ethylenediaminetetraacetic acid resulted in irregular nanoplates (Figure 1). Additionally, the formation of $Y_2(WO_4)_3$ nano/microcrystals in a hydrothermal reaction using sodium dodecyl benzenesulfonate (SDBS) as an organic solvent at 200°C for 20 hours and subsequent calcination at 800°C for 2 hours was reported [22]. The amount of

SDBS was found to play a crucial role in controlling the crystal's shape. Varying the amount of SDBS influenced the formation of bowknot-shaped microstructures, bowknot-like structures, and nanosheet building blocks with 3D micro flower structures.

Furthermore, the presence of ethylenediaminetetraacetic acid (EDTA) affected the formation of 3D flower-like architectures during the synthesis of $Y_2(WO_4)_3$ nano/microcrystals [23]. Other organic additives such as AO, PVP, EDTA, and Na_2tar also influenced the morphologies of the formed $NaY(MoO_4)_2$ nanocrystals, resulting in irregular microplates or nanoparticles (figure 2)[30]. These results demonstrate the significant impact of organic ligands on the size, shape, and morphology of the reaction products.

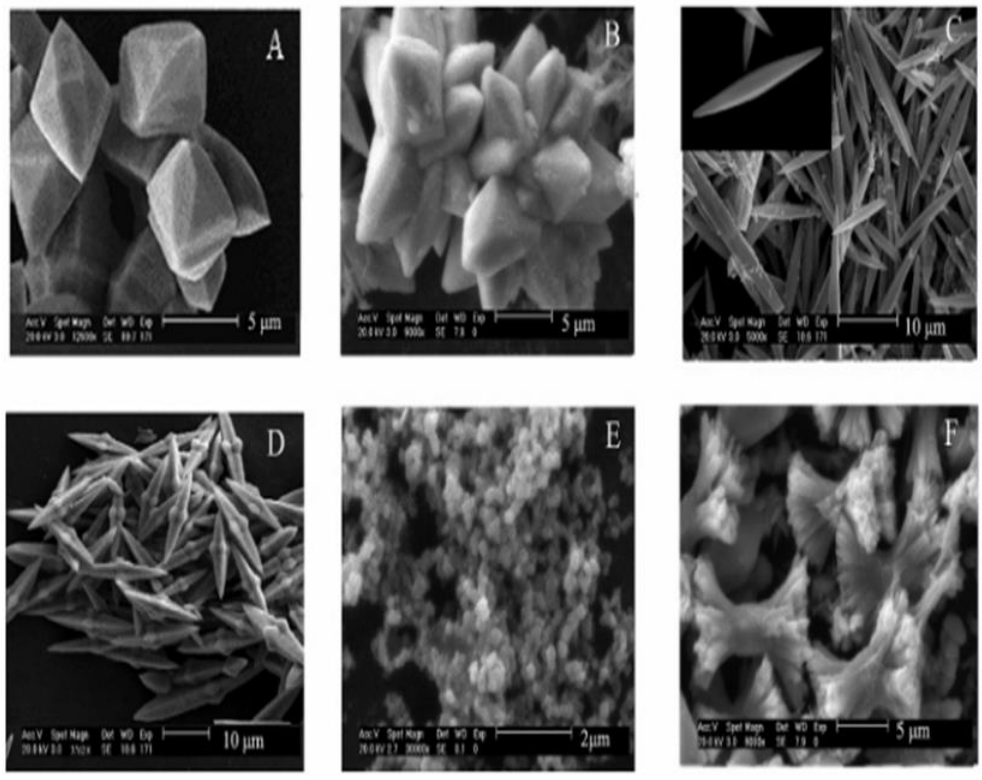

Figure 1: SEM morphologies of the products (A) no additive reagents; (B) adding 0.05 g of 0.01 mol/L n-dodecanethiol; (C) adding 0.04 g of 0.01 mol/L â-cyclodextrin; (D) adding 0.015 g of 0.01 mol/L ethylenediamine; (E) adding

0.044 g of 0.01 mol/L L-ascorbic acid; (F) adding 0.0075 g of polyformaldehyde [21].

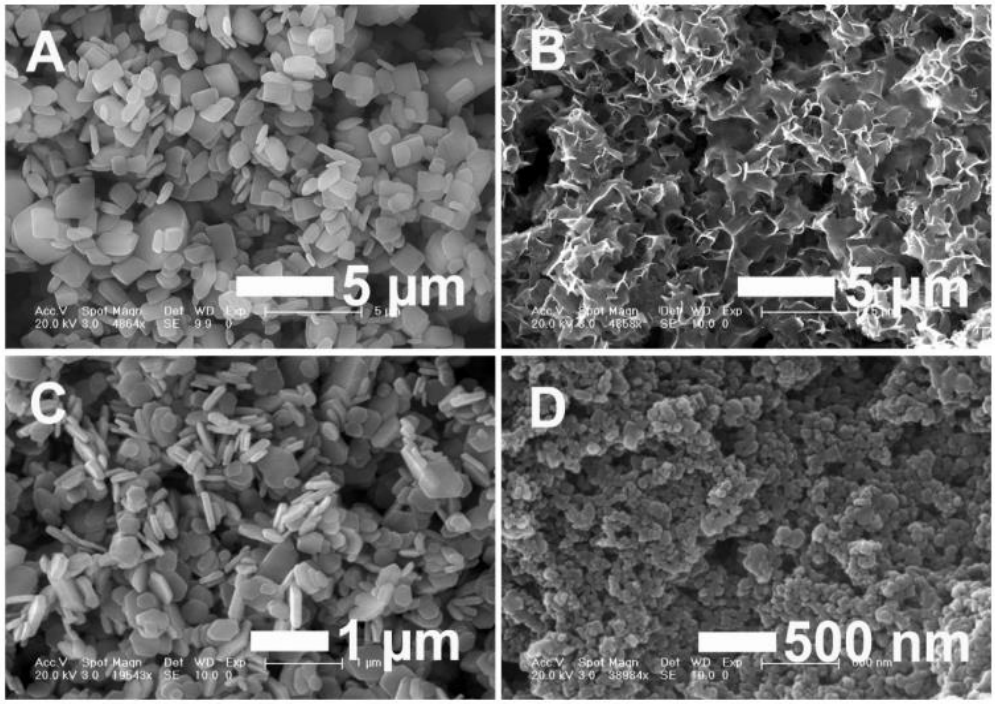

Figure 2: SEM images of the as-prepared hydroxyl sodium yttrium molybdate samples formed in the presence of (A) AO, (B) PVP, (C) EDTA and (D) Na_2tar [30].

1.2.2 The influence of pH

According to literature reports, the pH of the reaction mixture plays a significant role in determining the size and morphology of the final reaction product. For example, in the hydrothermal synthesis process of $NaY(MoO_4)_2$ microcrystals, altering the pH of the initial reaction solution resulted in different morphologies [24]. When the molar ratio of $Y(NO_3)_3$ to Na_2MoO_4 was 1:7 and the pH was adjusted to 4, rectangular plate-like microcrystals were observed. Maintaining the pH between 5 and 6 led to the formation of rhombic morphologies, while increasing the pH to 7 resulted in the synthesis of sheet-like microcrystals. This logical conclusion emphasizes the significant influence

of pH on the size, shape, and morphology of the final reaction product. Similarly, in the microwave hydrothermal reaction for producing $BiVO_4$ powders, varying the pH of the reaction medium led to the generation of diverse morphologies [25]. Figure 3 shows the different morphologies achieved at different pH conditions. In the case of $NaCe(WO_4)_2$ nanomaterial synthesis, adjusting the pH of the solution also produced various morphologies, including micro spindles, microspheres, or micro flowers of self-assembled nanoparticles [26]. Specifically, when 0.3 g of EDTA was present in a neutral environment at pH 7, spindle-like structures were obtained. Increasing the pH to 8 under unchanged reaction conditions led to the formation of homogenous and self-assembled 3D hierarchical microspheres.

These findings highlight that pH manipulation in the reaction medium is an effective strategy to control and tune the size, shape, and morphology of various nanomaterials, enabling the tailoring of their properties for specific applications.

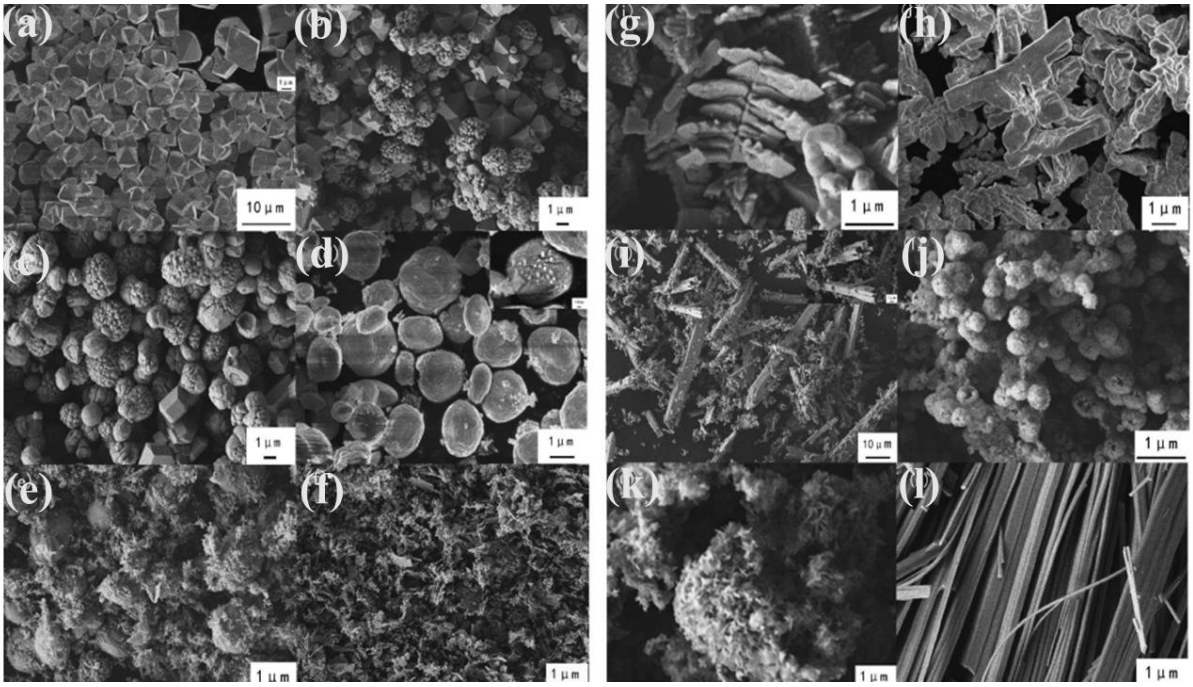

Figure 3: FESEM images of $BiVO_4$ powders prepared at different pH values: (a) 0.59, (b) 0.70, (c) 1.21, (d) 2.55, (e) 3.65, (f) 4.26, (g) 7.81, (g) 9.50, (h) 9.76, (i) 10.44, (j) 10.55, (k) 12.59 and (l) 12.93 [25].

1.2.3 The influence of reaction temperature

Numerous studies in the literature have established that the formation of rare earth tungstate/molybdate materials is highly dependent on the reaction temperature. For instance, in the hydrothermal synthesis of $NaEu(MoO_4)_2$ nano/microcrystals in the presence of EDTA, different morphologies were obtained by varying the reaction temperature [27]. At 120°C, regular rhombic nanosheets with sizes ranging from 200 to 500 nm were observed. Increasing the temperature to 140°C resulted in the formation of irregular nanospindles with an average length of 3 mm and a width of 500 nm. Further raising the temperature to 180°C led to the synthesis of microrugbies with lengths ranging from 0.4 to 1.3 mm.

In the case of $NaLa(MoO_4)_2$ nano/microcrystals, a microwave-assisted synthesis process was employed without any organic ligands, with reactions conducted at different temperatures for 10 minutes under magnetic stirring [28]. The variation in reaction temperature led to the observation of various morphologies. At 100°C or 120°C, octahedral bipyramidal-shaped particles were obtained. Increasing the temperature to 140°C or 160°C resulted in the formation of microcrystals with dendrite shapes.

Similarly, the formation of $Gd_2(WO_4)_3$ microstructures was investigated by Zeng et al. using a hydrothermal reaction without the presence of organic ligands, and the reaction was carried out for 36 hours [29]. At 120°C, belt-like structures with dimensions of 400–700 nm in length and an average thickness of 80 nm were obtained. Raising the reaction temperature to 160°C led to the formation of star-like structures with a thickness of about 50 nm and a length of

approximately 3 mm. These star-like structures were constructed from several leaf-like sheets with a common centre.

The results from these studies emphasize the crucial role of reaction temperature in controlling the size, shape, and morphology of rare earth tungstate/molybdate materials. Adjusting the reaction temperature allows for the tailored synthesis of desired nano/microstructures, which is essential for various applications in nanotechnology and materials science.

1.2.4 The influence of reaction time

The reaction time is a crucial factor in determining the morphology of nanomaterials during the preparation process. In a microwave-assisted hydrothermal process for $NaY(MoO_4)_2$ synthesis, different morphologies of nano/microstructures were obtained by varying the reaction time [30]. After a 1-hour completion of the reaction, the product consisted of large irregular-shaped and twisted pieces. Extending the reaction time to 3 hours resulted in the formation of rugged nanostrips assembled in a radiating and adhering manner. A reaction time of 6 hours led to the generation of nanoflakes and more aggregates. Further increasing the reaction time to 12 hours transformed the products into a uniform urchin-like morphology, as shown in Figure 4. In the synthesis of $BaWO_4$ crystals using novel supramolecule templates such as eggshell and different organic additives under mild conditions, the reaction time played a crucial role in tuning the morphologies with varying shapes and sizes of the crystals [21]. In the presence of polyformaldehyde, different time intervals yielded various types of morphologies, as represented in Figure 5.

The ability to control the reaction time allows researchers to tailor the morphology and structure of nanomaterials to suit specific applications in diverse fields, such as ceramics and luminescence materials. These findings

underscore the significance of optimizing the reaction time to achieve desired nanomaterial properties for various technological applications.

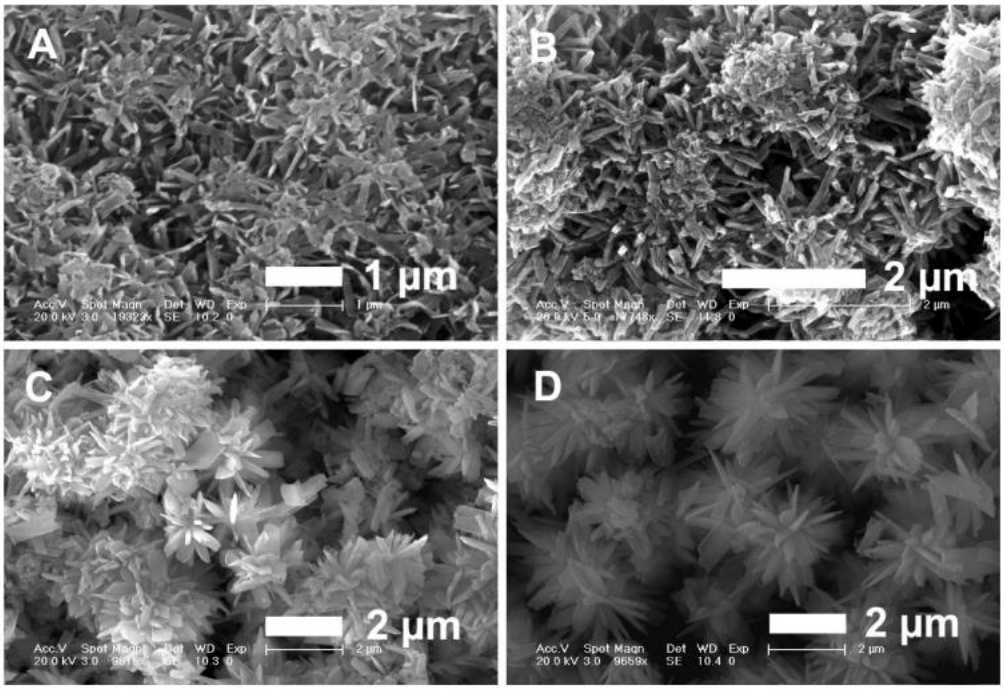

Figure 4: SEM images of the as-prepared hydroxyl sodium yttrium molybdate samples at 180 °C for different reaction times: (A) 0.5 h, (B) 3 h, (C) 6 h and (D) 12 h. [30]

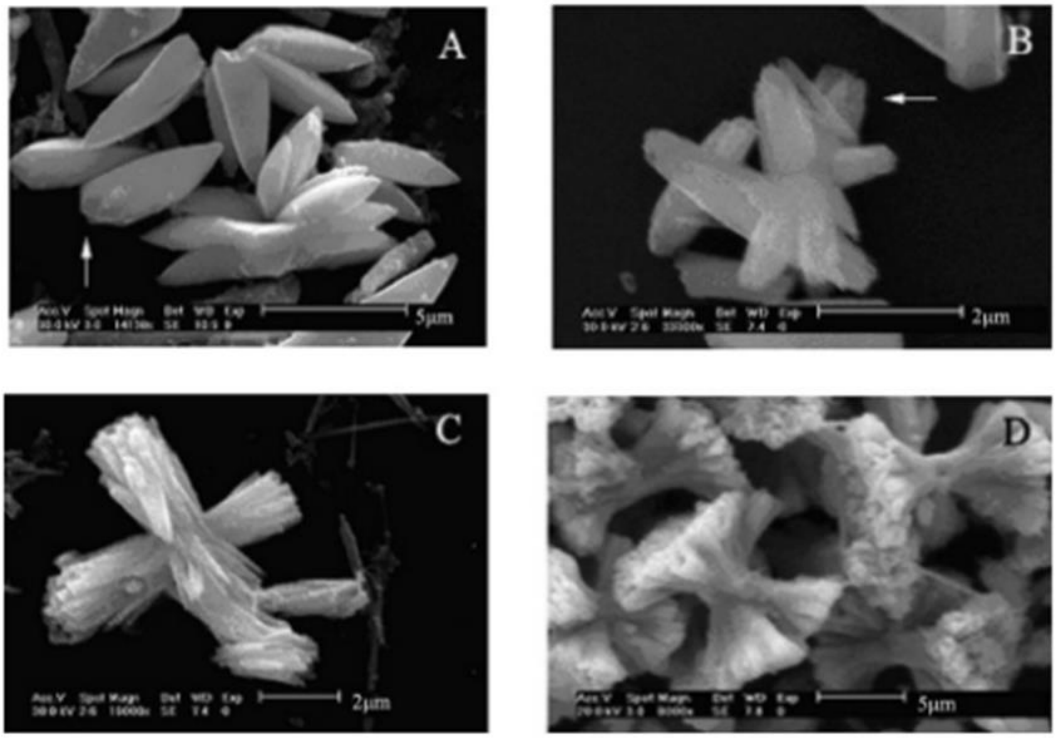

Figure 5: SEM morphologies of the products at different reaction times (A) 1 h; (B) 4 h; (C) 6 h; (D) 10 h. [21]

1.2.5 The influence of the rare earth source

From the majority of reported literature, the synthesis of scheelite-type tungstates/molybdates materials often involves the use of nitrate salts of rare earth elements in the reaction. However, there have been a few investigations exploring the influence of the rare earth source on the formation of such materials. Kaczmarek et al. conducted a study to investigate the effect of using nitrates and acetate salts of rare earth elements in a DSS (deep eutectic solvent) assisted hydrothermal process for the formation of $Y(WO_3)_2(OH)_3$ and $La_2(WO_4)_3$ nano/microstructures.

In the case of $Y(WO_3)_2(OH)_3$ synthesis using $Y(NO_3)_3$ as the yttrium source, the reaction initially resulted in irregular nanoparticles. After 3 hours of reaction time, nanorods with lengths of 300–500 nm were obtained, and these nanorods assembled into bundle-like aggregates. Increasing the reaction time led to the further development of these bundles, forming spherical microstructures. When the reaction time was extended to 24 hours, spherical microstructures in the range of 4–5 mm were achieved.

On the other hand, using $Y(OAc)_3$ as the yttrium source, the reaction initially produced amorphous particles, which served as the parent materials for the evolution of shrubby-like structures built from nanorods radiating from the central 'trunk'. With increasing reaction time, these shrubby-like structures aggregated to grow microstructures with a comparable size and shape as those obtained from $Y(NO_3)_3$. This indicates that the source of rare earth has a significant effect on the size and shape of the nano building blocks. Microstructures obtained from acetate salts showed tight packing of the nano building blocks compared to nitrate salts, as evidenced by almost no nitrogen absorption.

In another study by Liu et al., the synthesis of $NaY(MoO_4)_2$ nano/microcrystals was achieved using $Y(OH)_3$ nanorods as the yttrium source. The resulting product exhibited high crystallinity without the need for calcination. Various shapes, sizes, and morphologies were obtained, including sheaf-like structures, nanoflakes, cubes, truncated rhombic polyhedra, tetragonal bipyramids, and perfect bipyramids [32].

These investigations demonstrate that the choice of rare earth source can significantly influence the size, shape, and morphology of the nano/microstructures obtained, highlighting the importance of carefully

selecting the precursor salts for tailoring the desired properties of the synthesized materials.

1.2.6 The influence of tungstate/molybdate amount

Indeed, the amount of tungstate/molybdate source used in the reaction plays a significant role in determining the size, shape, and morphology of the synthesized materials. In the synthesis of $NaY(MoO_4)_2$ materials using excess amounts of Na_2MoO_4 in a hydrothermal process, researchers observed interesting effects on the crystal growth. Researchers reported that MoO_4^{2-} ions preferentially adsorb on a specific plane, the (001) plane, of $NaY(MoO_4)_2$ crystal nuclei. This preferential adsorption leads to changes in the thickness of the $NaY(MoO_4)_2$ crystals, resulting in the transformation of micro-sized to nano-sized particles [33]. By utilizing different amounts of Na_2MoO_4 (ranging from 4 to 14 mmol) in the synthesis, they achieved varying final products. Using 4 mmol of Na_2MoO_4, the final products exhibited uniform octahedra enclosed by (101) facets. Increasing the amount of Na_2MoO_4 to 6 mmol resulted in octahedrons truncated by (001) planes, transforming the morphology to quasi-cubes. At 8 mmol of Na_2MoO_4, the synthesized materials appeared as tetragonal prisms. Further increasing the amount of Na_2MoO_4 to 10 mmol led to the formation of thin plates with a thickness of approximately 150 nm.

This study demonstrates that the amount of tungstate/molybdate source used in the synthesis of $NaY(MoO_4)_2$ materials has a remarkable influence on the size, shape, and morphologies of the final products. The preferential adsorption of MoO_4^{2-} ions on specific crystal planes governs the crystal growth and results in a range of diverse morphologies, highlighting the importance of precise control over the reactant stoichiometry for tailoring the desired properties of the synthesized materials.

1.3. Applications of nano $NaCe(MO_4)_2$ (M = W/Mo) materials

The scheelite-type $NaCe(WO_4)_2$ and $NaCe(MoO_4)_2$ materials have several applications due to their unique properties. Here, I will elaborate on some of the applications that can be relevant for a thesis work:

1.3.1. Luminescent Materials: Rare earth double tungstates or molybdates, including $NaCe(WO_4)_2$ and $NaCe(MoO_4)_2$, are known for their luminescent properties. The incorporation of cerium (Ce) ions as activators within the crystal lattice enables these materials to emit light when excited. This luminescence makes them suitable for applications in solid-state lighting, optoelectronics, and display technologies. Your thesis work could focus on studying and optimizing the luminescent properties of these materials, including their emission spectra, efficiency, and potential applications in lighting or display devices.

1.3.2. Phosphors for Solid-State Lighting: Phosphors are materials that can absorb energy and re-emit it as visible light. Rare earth double tungstates or molybdates, with their luminescent properties, can be used as phosphors in solid-state lighting applications. $NaCe(WO_4)_2$ and $NaCe(MoO_4)_2$, doped with suitable rare earth ions, can emit light in specific colors, contributing to the overall color quality and efficiency of solid-state lighting devices. Your thesis work could focus on optimizing the phosphor properties of these materials, investigating their emission characteristics, color rendering index (CRI), and their potential applications in solid-state lighting systems.

1.3.3. Gas sensing: Alkali rare earth-based scheelite materials have also been explored for gas sensing applications, offering unique properties and potential advantages in certain cases. These materials typically involve the combination of alkali metals (such as sodium, potassium) and rare earth elements (such as cerium, yttrium) with tungsten oxide (WO_3). The incorporation of alkali and rare earth elements into the scheelite structure can modify the properties of

tungsten trioxide and enhance its gas sensing capabilities. Here are some key aspects of alkali rare earth-based scheelite materials in gas sensing:

a. **Enhanced sensitivity:** Alkali rare earth doping can increase the sensitivity of tungsten trioxide to specific gases. By altering the electronic structure and surface properties of WO_3, these dopants can improve the interaction between the gas molecules and the sensing material, leading to higher sensitivity and lower detection limits.
b. **Selectivity improvement:** Alkali rare earth doping can also enhance the selectivity of WO_3-based gas sensors. The introduction of specific dopants can alter the surface chemistry and adsorption characteristics of the material, enabling it to selectively respond to target gases while minimizing interference from other gases present in the environment.
c. **Operating temperature optimization:** Alkali rare earth doping can influence the operating temperature range of gas sensors based on scheelite materials. The addition of specific dopants can lower the operating temperature, enabling the sensor to function effectively at lower energy consumption. This can be advantageous for practical applications that require low power consumption and fast response times.
d. **Stability and durability:** Similar to undoped WO_3, alkali rare earth-based scheelite materials generally offer good stability and durability. However, the specific doping elements and concentrations can impact the material's long-term stability, and optimization is required to ensure reliable and consistent performance over extended periods.

Gas sensing devices based on alkali rare earth-doped scheelite materials follow the same operating principles as conventional gas sensors. The interaction between the target gas and the sensing material leads to measurable changes in electrical properties, such as resistance or conductivity, which can be detected and quantified to determine gas concentration.

It's important to note that the performance and suitability of alkali rare earth-based scheelite materials in gas sensing applications depend on several factors, including the choice of doping elements, their concentrations, and the specific target gases of interest. Careful optimization and characterization are necessary to design and develop gas sensors that exhibit the desired sensitivity, selectivity, and stability for specific gas sensing applications.

1.3.4. Solid-State Lasers: Rare earth double tungstates or molybdates are utilized as laser gain media due to their excellent optical properties. These materials can provide laser emissions in the visible or near-infrared regions when pumped with suitable energy sources. $NaCe(WO_4)_2$ and $NaCe(MoO_4)_2$ can serve as host lattices for rare earth dopants, such as neodymium (Nd), allowing the creation of solid-state lasers with specific emission wavelengths. Your thesis could involve the design, fabrication, and characterization of laser devices based on these materials, exploring their laser performance and potential applications in areas like laser machining, communications, or medical applications.

1.3.5. Scintillator Materials: Scintillators are materials that can convert high-energy radiation, such as X-rays or gamma rays, into detectable light signals. Rare earth double tungstates or molybdates have shown promising scintillation properties, making them suitable for radiation detection and imaging applications. $NaCe(WO_4)_2$ and $NaCe(MoO_4)_2$, with the incorporation of cerium as a luminescent dopant, can be investigated for their scintillation efficiency,

energy resolution, and other relevant characteristics. Your thesis could involve the synthesis and characterization of scintillator materials based on these compounds, exploring their potential in radiation detection systems or medical imaging.

These are just a few potential applications of scheelite-type $NaCe(WO_4)_2$ and $NaCe(MoO_4)_2$ materials. Depending on your specific interests and research objectives, you can explore these applications in greater detail, including material synthesis, characterization techniques, performance optimization, and potential device integration.

1.4. Scope of the present work

Based on the literature review presented above the scope of the present thesis emerges as a sequence of questions as given below.

1. What is the effect on crystalline structure of using different organic additives for the preparation of rare earth based scheelite materials by the hydrothermal technique and the molar concentrations of the reactants?

2. Does the morphology of rare earth based scheelite materials change with the change of organic additives of the precursor? If so what is the reason for that?

3. What is the role of the reactants in the hydrothermal technique?

4. Is there any relation between the microstructure of the rare earth based scheelite materials and the molar concentration of the precursor solutions?

5. What is the effect of the molar concentration of the precursor solutions on the photoluminescence properties of rare earth based scheelite materials?

6. Can the rare earth based scheelite materials be used for solid state lightening?

7. How the photoluminescence properties of rare earth based scheelite materials is related to solid state lightening?

8. Can the rare earth based scheelite material be used for gas sensing?

9. How the gas sensing is related with photoluminescence property of rare earth based scheelite material?

The aforesaid scope thus defines the objective of the present work as given below.

1.5. Objective of the present work

1. To examine if the crystalline structure of rare earth based scheelite materials change in using different organic additives for the preparation of by the hydrothermal technique and the molar concentrations of the reactants, different reaction temperature and if so to find out the reason for the same.

2. To understand the role of the reactants in the hydrothermal technique.

3. To understand the role of reaction temperature to control the morphology and photoluminescence property of rare earth based scheelite materials.

4. To find out the relation between the microstructure of the rare earth based scheelite materials and the molar concentration of the precursor solutions.

5. To check out if the rare earth based scheelite materials can be used for solid state lightening.

6. To critically study how the photoluminescence property of rare earth based scheelite materials is related to solid state lightening.

7. To verify if the rare earth based scheelite materials be used for gas sensing.

8. To understand how the photoluminescence property is related with gas sensing.

9. To study explicitly the gas sensing is related with photoluminescence property of rare earth based scheelite materials.

10. To summarize the results to attain a reasonable conclusion which may aid in future growth of technological application of rare earth based scheelite materials.

References:

1) Yi G, Sun B, Yang F, Chen D, Zhou Y, Cheng J (2002) Synthesis and Characterization of High-Efficiency Nanocrystal Up-Conversion Phosphors: Ytterbium and Erbium Codoped Lanthanum Molybdate. Chem. Mater. 14: 2910.

2) Xu L, Yang X, Zhai Z, Gu D, Pang H, Hou W (2012) Self-assembled 3D architectures of $NaCe(MoO_4)_2$ and their application as absorbents. Cryst Eng Comm 14: 7330.

3) Dirany N , Arab M, Moreau , Valmalette CJ , Gavarri RJ (2016) Hierarchical design and control of $NaCe(WO_4)_2$ crystals: structural and optical properties. Cryst Eng Comm 18: 6579–6593

4) Liu J, Xu .B, Song C, Luo H, Zou X, Han L, Yu X (2012) shape-controlled synthesis of monodispersed nano-/micro-$NaY(MoO_4)_2$(doped with Eu^{3+}) without capping agents via a hydrothermal process. Cryst Eng Comm 14: 2936.

5) Liu X, Hou H, Yang X, Liang J (2014) Morphology controllable synthesis of $NaLa(WO_4)_2$: the morphology dependent photoluminescent properties and single-phased white light emission of $NaLa(WO_4)_2$: $Eu^{3+}/Tb^{3+}/Tm^{3+}$. Cryst Eng Comm 16: 1268–1276

6) Huang S , Wang D , Li C, Wang L, Zhang X, Wan Y, Yang P (2012) Controllable synthesis, morphology evolution and luminescence properties of $NaLa(WO_4)_2$ microcrystals. Cryst Eng Comm 14: 2235–2244.

7) Wang Z, Li Y, Jiang Q, Zeng H, Ci Z, Sun L (2014) Graphene quantum dots: versatile photoluminescence for energy, biomedical, and environmental applications. J. Mater. Chem. C 2: 4495–4501.

8) Bilecka I, Niederberger M (2010) Microwave chemistry for inorganic nanomaterials synthesis Nanoscale 2: 1358.

9) Tian Y, Chen B, Hua R, Yu N, Liu B, Sun J, Cheng L, Zhong H, Li X, Zhang J, Tian B, Zhong H (2012) Lanthanide dopant-induced phase transition and luminescent enhancement of EuF_3nanocrystals. Cryst Eng Comm 14: 1760.

10) Zhang J, Wang X, Zhang X, Zhao X, Liu X and Peng L (2011) Microwave synthesis of $NaLa(MoO_4)_2$ microcrystals and their near-infrared luminescent properties with lanthanide ion doping (Er^{3+}, Nd^{3+}, Yb^{3+}). Inorg. Chem. Commun 14: 1723.

11) Pan Y, Zhang Q, Zhao C, Jiang Z (2007) Luminescent properties of novel Ho^{3+} and Tm^{3+} doped gadolinium molybdate nanocrystals synthesized by the Pechini method. Solid State Commun 142: 24.

12) Hou Z, Cheng Z, Li G, Wang W, Peng C, Li C, Ma P, Yang D, Kang X, Lin J (2011) Electrospinning-derived $Tb_2(WO_4)_3$:Eu^{3+}nanowires: energy transfer and tunable luminescence properties. Nanoscale 3: 1568.

13) Shimumera T, Sawaguchi N, Saski M (2017) Structure and light emission of scheelite-type $ACe(WO_4)_2$ (A = Li, Na, or K). Journal of the Ceramic Society of Japan 125: 150-154.

14) He X, Zhou J, Lian N, Sun J, Guan M (2010) Sm^{3+}-activated gadolinium molybdate: an intense red-emitting phosphor for solid-state lighting based on InGaN LEDs. J. Lumin 130: 743.

15) Huang J, Xu J, Luo H, Yu X, Li Y (2011) Effect of Alkali-Metal Ions on the Local Structure and Luminescence for Double Tungstate Compounds $AEu(WO_4)_2$ (A = Li, Na, K). Inorg. Chem. 50: 11487–11492.

16) Lei F, Yan B (2009) Molten Salt Synthesis, Characterization, and Luminescence Properties of Gd_2MO_6:Eu^{3+} (M=W, Mo) Phosphors. J. Am. Ceram. Soc 92:1262.

17) Lei F, Yan B, Chen HH (2008) Solid-state synthesis, characterization and luminescent properties of Eu^{3+}-doped gadolinium tungstate and molybdate phosphors: $Gd_{(2-x)}MO_6:Eu_x^{3+}$ (M=W, Mo). J. Solid State Chem 181: 2845.

18) Tian Y, Chen B, Hua R, Yu N, Liu B, Sun J, Cheng L, Zhong H, Li X, Zhang J (2012) Self-assembled 3D flower-shaped $NaY(WO_4)_2:Eu^{3+}$ microarchitectures: Microwave-assisted hydrothermal synthesis, growth mechanism and luminescent properties. Cryst Eng Commun 14: 1760–1769.

19) Bu W, Chen Z, Chen F, Shi J (2009) Oleic Acid/Oleylamine Cooperative-Controlled Crystallization Mechanism for Monodisperse Tetragonal Bipyramid $NaLa(MoO_4)_2$ Nanocrystals. J. Phys. Chem. C 113: 12176.

20) Preda P, Multigner M, Venta J, Garcia AM, Ruiz-Gonzalez L (2006) Structural and magnetic characterization of oleic acid and oleylamine-capped gold nanoparticles. J. Appl. Phys 100: 123915.

21) Liu J, Wu Q, Ding Y (2005) Controlled Synthesis of Different Morphologies of $BaWO_4$ Crystals through Biomembrane/Organic-Addition Supramolecule Templates. Cryst. Growth Des 5[2]: 445–449.

22) Huang S, Zhang X, Wang L, Bai L, Xu J, Li C, Yang P (2012) Controllable synthesis and tunable luminescence properties of $Y_2(WO_4)_3:Ln^{3+}$ (Ln = Eu, Yb/Er, Yb/Tm and Yb/Ho) 3D hierarchical architectures. Dalton Trans 41: 5634.

23) Xu L, Shen J, Lu C, Chen Y, Hou W (2009) Self-Assembled Three-Dimensional Architectures of $Y_2(WO_4)_3$:Eu: Controlled Synthesis, Growth Mechanism, and Shape-Dependent Luminescence Properties. Cryst. Growth Des 9: 3129.

24) Li Y, Wang G, Qu K, Liu S, Feng L (2013) Formation and down/up conversion luminescence of Ln^{3+} doped $NaY(MoO_4)_2$ microcrystals. Dalton Trans 42: 3366.

25) Tan G, Zhang L, Ren H, Wei S, Huang J, Xia A (2013) Effects of pH on the Hierarchical Structures and Photocatalytic Performance of $BiVO_4$ Powders Prepared via the Microwave Hydrothermal Method. ACS Appl. Mater. Interfaces 5: 5186−5193.

26) Dirany N , Arab M, Moreau B , Valmalette JC , Gavarri JR (2016) Hierarchical design and control of $NaCe(WO_4)_2$ crystals: structural and optical properties. Cryst Eng Comm 18:6579–6593.

27) Xu L, Yang X, Zhai Z, Chao X, Zhang Z and Hou W (2011) EDTA-mediated hydrothermal synthesis of $NaEu(MoO_4)_2$ microrugbies with tunable size and enhanced luminescence properties. Cryst. Eng Comm 13: 4921.

28) Zhang J, Wang X, Zhang X, Zhao X, Liu X, Peng L (2011) Microwave synthesis of $NaLa(MoO_4)_2$ microcrystals and their near-infrared luminescent properties with lanthanide ion doping (Er^{3+} , Nd^{3+} , Yb^{3+}). Inorg. Chem. Commun 14: 1723.

29) Zeng Y, Li Z, Wang L, Xiong Y (2012) Controlled synthesis of $Gd_2(WO_4)_3$ microstructures and their tunable photoluminescent properties after Eu^{3+} /Tb^{3+} doping. Cryst. Eng Comm 14: 7043.

30) Xu Z, Li C, Li G, Chai R, Peng C, Yang D, Lin J (2010) Self-Assembled 3D Urchin-Like $NaY(MoO_4)_2$:Eu^{3+}/Tb^{3+} Microarchitectures: Hydrothermal Synthesis and Tunable Emission Colors. J. Phys. Chem. C 114: 2573–2582.

31) Kaczmarek AM, Liu YY, Van Der Voort P, Van Deun R (2013) Tuning the architecture and properties of microstructured yttrium tungstate oxide hydroxide and lanthanum tungstate. Dalton Trans 42: 5471.

32) Liu J, Xu .B, Song C, Luo H, Zou X, Han L, Yu X (2012) shape-controlled synthesis of monodispersed nano-/micro-$NaY(MoO_4)_2$ (doped with Eu^{3+}) without capping agents via a hydrothermal process. Cryst. Eng Comm 14: 2936.

33) Liu SS, Yang DP, Ma DK, Wang S, Tang TD, Huang SM (2011) Single-crystal $NaY(MoO_4)_2$ thin plates with dominant {001} facets for efficient photocatalytic degradation of dyes under visible light irradiation. Chem. Commun 47: 8013.

Chapter 3

Hydrothermal Synthesis of defect induced pristine α-$NaCe(WO_4)_2$: a novel material for solid state lightening and gas sensing

1. Introduction

Over the past few years, rare earth (RE) based optical materials have drawn considerable attention in the field of display technology, solid-state laser, thermometry optical fibre and few other optoelectronic devices due to their durable 4f - 5d transitions [1-3]. Among them, particularly alkali RE double tungstates with general formula $ALn(WO_4)_2$ (A^+ = Na^+, K^+, etc.; Ln^{3+} = Y^{3+}, Ce^{3+}, Gd^{3+}, Eu^{3+}, etc.), have emerged as an promising materials due to their favourable physical and chemical properties, high quantum yield etc.[4]. $ALn(WO_4)_2$ exhibits minimal photobleaching effect, narrow emission bands etc. in contrast to oxide, fluoride based luminescent materials, wherein 4f - 5d transitions and related optical properties like Stoke – shift, radiative and non-radiative lifetime etc. distinctively depend on the crystalline field of Ln^{3+} [5]. It has been noted that $ALn(WO_4)_2$ correspondences two different crystal structures e.g. tetragonal $ALn(WO_4)_2$ (β-phase) and triclinic $ALn(WO_4)_2$ (α-phase). In the β-phase of $ALn(WO_4)_2$, A^+ and Ln^{3+} are statistically distributed over *4b* sites which primarily depends on synthesis condition. It has been investigated by several researchers including us that the optical properties of this β-$ALn(WO_4)_2$ significantly depends on this statistical distribution, hence it appears that the optical properties are not robust which limits real field applications. In contrast,

α-$ALn(WO_4)_2$ possesses great advantage over distribution over cations as no such phenomenon arises here. In this connection, it can be said that whereas several studies on β-$ALn(WO_4)_2$ have been conducted, but relatively less work has been done to comprehend the various optoelectronic features of α-$ALn(WO_4)_2$, specifically of α-$NaCe(WO_4)_2$. To the best of our knowledge, though, for instance, Shimemura *et al*. analysed the optical emissions from $ACe(WO_4)_2$ with A = Na, Li, and K [4], whereas Munirathnappa *et al*. only recently synthesized $NaCe(WO_4)_2$ *via* template-free solvothermal approach, and they found a correlation between distorted noncentrosymmetric structure and optical nonlinear second harmonic generation [5]. Dirany *et al*. investigated the variation of optical absorption with regard to morphology [6]. Also many researchers investigated optical transitions of various rare earth based scheelite materials [7-9]. However, dependence of the spectrum characteristics of Ce^{3+} on crystallographic parameters, defects etc. has not been studied for α-$NaCe(WO_4)_2$.

Herein, it may be stated that we have already synthesized β- $NaCe(WO_4)_2$ through cetyltrimethyl ammonium bromide (CTAB) assisted facile hydrothermal reaction at 160^{o}C and have investigated its optical emission. By reducing the reaction temperature, presently we have noticed the formation of α-$NaCe(WO_4)_2$ and have investigated the optical emissions of this phase for first time. Herein, we have also observed that α-$NaCe(WO_4)_2$ contains oxygen vacancies (V_O) which depend on the reaction temperature and these vacancies regulates formation of CeO_7 and CeO_6, which function as active luminous centres for emissions of blue and green emissions. It is reported in literature that V_Os play important role in gas sensing properties of metal oxides and scheelite material (c.a. $NaBi(MoO_4)_2$) has the potency of gas sensing activity.

Taking this background into account, we have also examined the potentiality of α-$NaCe(WO_4)_2$ as gas sensor. Herein, it may be stated that we couldn't find any gas sensing activity from β-$NaCe(WO_4)_2$, while α-$NaCe(WO_4)_2$ possesses this.

An in-depth examination of the experimental data, we have also computed *ab initio* band structure of α-$NaCe(WO_4)_2$ for first time illustrating that Ce's $5d_z^2$, $5d_{yz}$, and $5d_{xz}$ orbitals contribute to the 5d – 4f transition with CeO_7 and CeO_6, formed due to V_O and $2V_O$ and produce blue and green emissions from α-$NaCe(WO_4)_2$.

2. Experimental section

2.1 Materials and synthesis procedure of α-NCWO

Currently, α-NCWO has been synthesized through a facile hydrothermal process, followed by calcination. Briefly, 0.34 mmol (0.124 gm) of cetyltrimethyl ammonium bromide [CTAB, Merck, Germany] as surfactant was mixed with 60 ml of DI water containing 0.17 mmol (0.074 gm) of cerium nitrate [$Ce(NO_3)_3.6H_2O$, Merck, Germany]. After 3 h of vigorous stirring at room temperature, the solution turned milky white, and then 20 ml of aqueous solution containing 0.34 mmol (0.112 gm) of sodium tungstate ($Na_2WO_4.H_2O$, Merck, Germany) was added dropwise. After stirring for another 30 minutes, the mixture was delivered to the Teflon autoclave for hydrothermal treatment, carried out for 20 h. The final product was obtained after cooling the autoclave to room temperature, centrifugation, and washing with DI water and ethanol, followed by calcination at 800^{o}C for 5 h. In order to examine the effect of temperature during hydrothermal reaction, we did the reaction at 120^{o}C and 140^{o}C and accordingly samples were designated as $NCWO_{120^oC}$ and $NCWO_{140^oC}$ respectively.

2.2 Characterizations

X-ray diffraction (XRD) pattern, collected on Rigaku Ultima III, Japan powder diffractometer equipped with CuK_α radiation (λ = 1.5406 Å), was adopted to examine the phase purity and crystal structure of the as-prepared samples. Rietveld refinement was performed on MAUD platform to determine structural

and microstructural parameters. Herein, backdrop of each pattern was fitted with a fourth order polynomial function, while experimental profiles were fitted using the best possible pseudo-Voigt analytical function with asymmetry. The samples' morphology was examined using a field emission scanning electron microscope (FESEM; Hitachi S4800, operated at 5 kV), while higher resolution microscopic images and selected area electron diffraction (SAED) were taken by transmission electron microscope (TEM-2100 Plus Electronmicroscope, 200 kV). Alpha 300, Wintec was adopted to measure Raman spectra using a 530 nm laser (3 mW output and a 2 m spot size), while infrared spectra (400 and 4000 cm^{-1}) was captured on IR Prestige. With the help of the PHI Versa Probe III Scanning XPS with Al K source, the X-ray photoelectron spectra were gathered to determine chemical states of the elements. Optical properties were measured on UV-Vis (V-630, JACSO) and photoluminescence (FP-8300, JASCO, equipped with a 100W Xe lamp) spectrophotometers. The study of gas sensing performance of the prepared materials was conducted using Agilent 34461A digital multimeter.

2.3: Gas-sensing properties measurement of α-NCWO nanomaterials

To measure gas sensing properties, Taguchi type sensor module was fabricated by thick coating of the materials on hollow α-alumina tube substrates. Electrodes were added to the modules by using conducting gold paste and Pt wire at the two ends. Ni-Cr wire was used as heating coil to control the temperature of the sensor by changing the voltage applied across it. Gas cylinders balanced in air were used for sensing measurement studies. Detailed study on the sensing characteristics of the materials was carried out by exposing the sensors to different VOCs viz. acetone, ammonia and ethanol. The sensing property of the as synthesised materials was studied by measuring the resistance of the sensors in air (R_{air}) and its change after exposure to the target analyte

(R_{gas}). The sensitivity (S) of the sensors were calculated using the following relation, S= $\frac{R_{gas}}{R_{air}}$. The optimum operating temperatures of the sensors were determined by measuring the sensitivity of the sensors towards a fixed concentration of target analyte at different operating temperatures ranging from 200 ºC to 400 ºC.

2.4: Band structure calculation using ab initio density functional theory

We have computed the total density of states (TDOS), projected density of state (PDOS), and the spin polarised electronic band structure for each atom. Herein, we have used Perdew-Bruke-Ernzerh (PBE) exchange correlation ultra-soft potentials and plane-wave pseudo potential (PAW) approach as implemented in the VASP simulation software for *ab initio* calculations. We have considered valence electrons of the following atoms Na atom ($1s^2$ $2s^2$ $2p^6$ $3s^1$), Ce atom ($5s^2$ $5p^6$ $4f^1$ $5d^1$ $6s^2$), W atom ($5p^6$ $6s^2$ $5d^{10}$), O atom ($2s^2$ $2p^4$). Prior to calculation, structure was optimized at lowest single point ground state energy using the 4 × 4 × 4 Monkhorst - Pack k point at cut off energy 520 eV, while band structure was calculated at different symmetry points (Γ to R, R to Z, Z to Γ). Each atom was subjected to a Hellmann-Feynman force of 0.01 eV, with the maximum atomic displacement ~ 5×10^{-4} Å and stress ~ 0.02 GPa. For this calculation, EDIFF and force EDIFG parameters were set to 10^{-6} eV and 10^{-3} eV respectively for high accuracy convergence.

3. Result and discussion

3.1 Phase and structure analyses of the as-prepared samples

XRD patterns of both samples (shown in Figure 1 (a) and (b)) match well with scheelite-type triclinic α-NCWO (ICSD card: 200520, pace group: P-1(2), [10], wherein absence of any other peak confirms phase purity of the samples. Crystallographic parameters, obtained from Rietveld refinement which was

carried out until convergence of χ^2, R_p and R_{wp} reached to acceptable ranges, are presented in Table 1 and Table A1 of APPENDIX-I, [11]. It is understood from refinement that W, Ce and Na atoms are connected via O atoms forming a cage like structure where Ce is coordinated with eight O atoms to form regular CeO_8 polyhedra, Na is coordinated with four O atoms to form NaO_4 tetrahedra, while each NaO_4 shares one edge with WO_6 octahedra and connects to CeO_8 polyhedra via O atoms (shown in Figure 1(c)). Rietveld analyses also reveals that W atoms exhibit inversion symmetry and lead edge sharing octahedra forming W_4O_{16} as a tetramer via W_2O_2 bridged O atom. Herein, lower lattice parameters, unit cell volume, Na – O and Ce – O bond lengths, Na – O – W, Ce – O – W and O – W – O bond angles of $NCWO_{120^oC}$ are attributed to oxygen vacancy (V_O) induced distortion within CeO_8 polyhedra and WO_6 octahedra [10]. Very briefly, we have evaluated degree of CeO_8 polyhedron distortion (K) ~ 0.96, 0.93 for $NCWO_{120^oC}$ and $NCWO_{140^oC}$ from the relation $K = \frac{d1(Ce-O)}{d2(Ce-O)}$ where d_1(Ce – O) and d_2(Ce – O) denote two different bond lengths and WO_6 octahedron distortion (N) ~ 0.86 and 0.79 using the relation $N = \frac{\alpha1(O-W-O)}{\alpha2(O-W-O)}$ where α_1(O – W – O) and α_2(O – W – O) represent two different bond angles corroborating higher V_O induced distortion [12]. We have also noticed a decrease of c/a ratio in $NCWO_{140^oC}$ with respect to $NCWO_{120^oC}$ which according to Li *et al.* indicates the influence of dipole – dipole interactions on short-range disorder due to charge entrapment at V_O site.

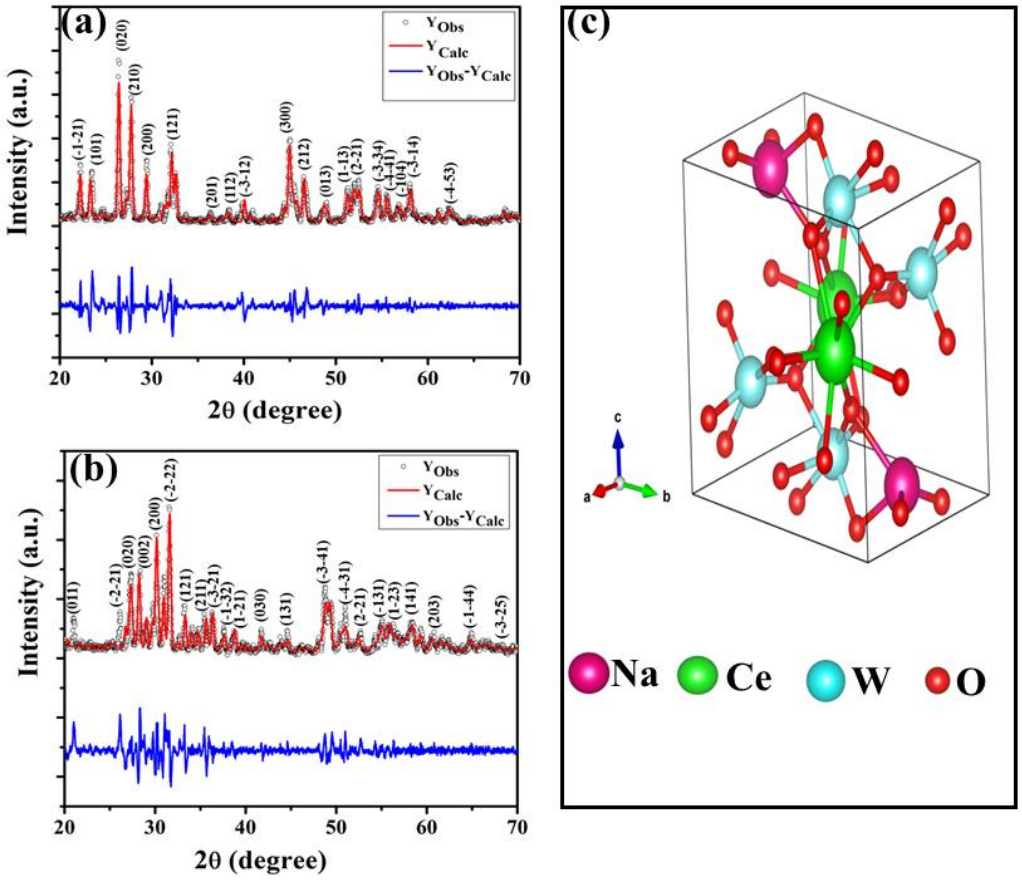

Figure 1: XRD patterns of the $NaCe(WO_4)_2$ samples (a) $NCWO_{120^oC}$, (b) $NCWO_{140^oC}$, (c) Triclinic unit cell's structure of the $NaCe(WO_4)_2$ nanostructures.

Table 1: Refined structural parameters and the reliability factors from the Rietveld fitting of α-NCWO structure

Properties		$NCWO_{140^oC}$	$NCWO_{120^oC}$
Lattice parameter (A^0) (errors)	a	7.453(0.0007)	7.439(0.0004)
	b	8.048(0.0006)	8.121(0.0006)
	c	7.017(0.0006)	7.164(0.0005)

Unit cell volume $(A^0)^3$		340.092(0.0002)	353.100(0.0002)
Bond length (A^0) (errors)	Na-O	2.30(0.007)	2.33(0.004)
	Ce-O	2.42(0.009)	2.45(0.005)
	W-O	1.97(0.005)	2.01(0.009)
Bond angle (in degree) (errors)	Na-O-W	106.460(0.0003)	105.400(0.0003)
	Na-O-Ce	105.540(0.0003)	105.620(0.0003)
	O-Ce-O	83.166(0.0007)	77.152(0.0002)
	Ce-O-W	109.549(0.0003)	109.118(0.0004)
	O-Na-O	65.958(0.0005)	75.107(0.0004)
	O-W-O	93.110(0.0004)	94.870(0.0005)
Density of the component		14.299	13.317
Crystallite size(nm)		64.70(0.002)	74.14(0.004)
R_p (%)		10.10	13.20
R_{wp} (%)		12.80	18.20
R_{exp} (%)		8.80	9.33
χ^2		2.12	3.82

Morphologies of the samples (shown in Figure 2(a) and (b)), as obtained from FESEM, are found in agglomerated, ascribed to calcination effect at 800°C. Morphology (Figure 2(c)), analysed further by transmission electron microscopy (TEM), also shows irregular shape and size of the samples, while selected area diffraction (SAED) pattern (Figure 2(d)) consists of diffraction spots from $(\bar{3}\bar{2}5)$, (203), (030), (200) and (011) planes illustrating good crystallinity of the samples. The elemental mapping of α-NCWO clusters are shown APPENDIX-I (figure A1 and A2).

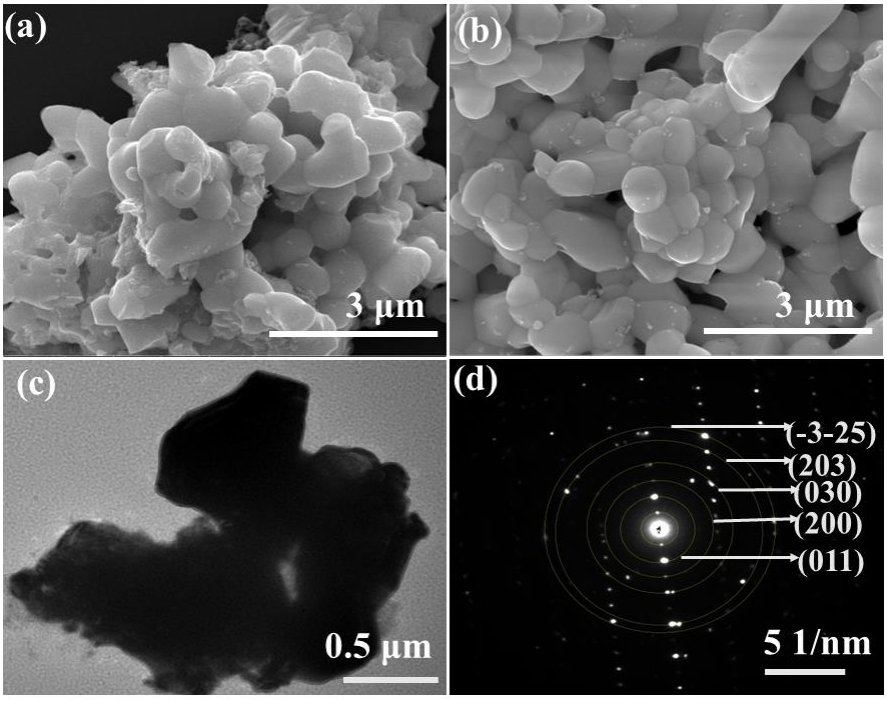

Figure 2: FESEM image of NCWO nano/micro structures (a) $NCWO_{120^oc}$ and (b) $NCWO_{140^oc}$, (c) TEM images and (d) corresponding SAED pattern of $NCWO_{140^oc}$.

3.2 Investigations of defects in α-NCWO nanostructures by FTIR, Raman and x-ray photoelectron spectroscopies

FTIR and Raman spectroscopies were adopted to gain information about short-range distortion associated with structural defect due to V_O. Four absorption bands (shown in Figure A3, APPENDIX-I), found in the FTIR spectra, can readily be assigned to four internal vibrations of WO_6 [13,14]. It has been studied that within distorted scheelite materials, WO_6 either form regular octahedra (W^RO_6) with 2i site symmetry or distorted WO_6 octahedra (W^DO_6) due to V_O within WO_6 octahedra. In general, vibration (Γ_{Oh}) of W^RO_6 is represented by $\Gamma_{Oh}= 36A_u$, as symmetry gets changed in W^DO_6 indicating different lattice vibrational energies. Presently, deconvolution (shown in Figure 3) of two bands (778 – 910 and 660 – 717 cm^{-1}) reveals three peaks (c.a. 669, 681, 700 cm^{-1} and 814, 853, 881 cm^{-1}). The details of the deconvolution of the FTIR bands are shown in the APPENDIX-I (Table A2). Peaks at 700 and 881 cm^{-1} are assigned to the stretching vibration (→ O → W → O →) of W^DO_6 and W^RO_6 octahedra respectively, while other deconvoluted peaks correspond to asymmetric stretching of two-oxygen bridged W_2O_2 of W^RO_6 and W^DO_6 octahedra [15,16]. Similarly, deconvoluted peaks (Figure 3) at 738 and 754 cm^{-1} yield W – O bending vibration of W^DO_6 and W^RO_6 respectively [17] and from area under the curves we have calculated weighted percentage of W^DO_6 ~ 40 and 32% for $NCWO_{120^oC}$ and $NCWO_{140^oC}$ respectively, indicating more V_O in $NCWO_{120^oC}$. Raman spectra of both samples (represented in Figure 4) consist of one sharp peak at 474 cm^{-1} which can be attributed to A_g symmetric stretching mode of W_2O_2 unit, while other peaks at 348, 391 and 583 cm^{-1} are assigned to asymmetric and symmetric bending vibration of O – W – O of A_g mode and asymmetric stretching mode of W_2O_2 unit [17,18].

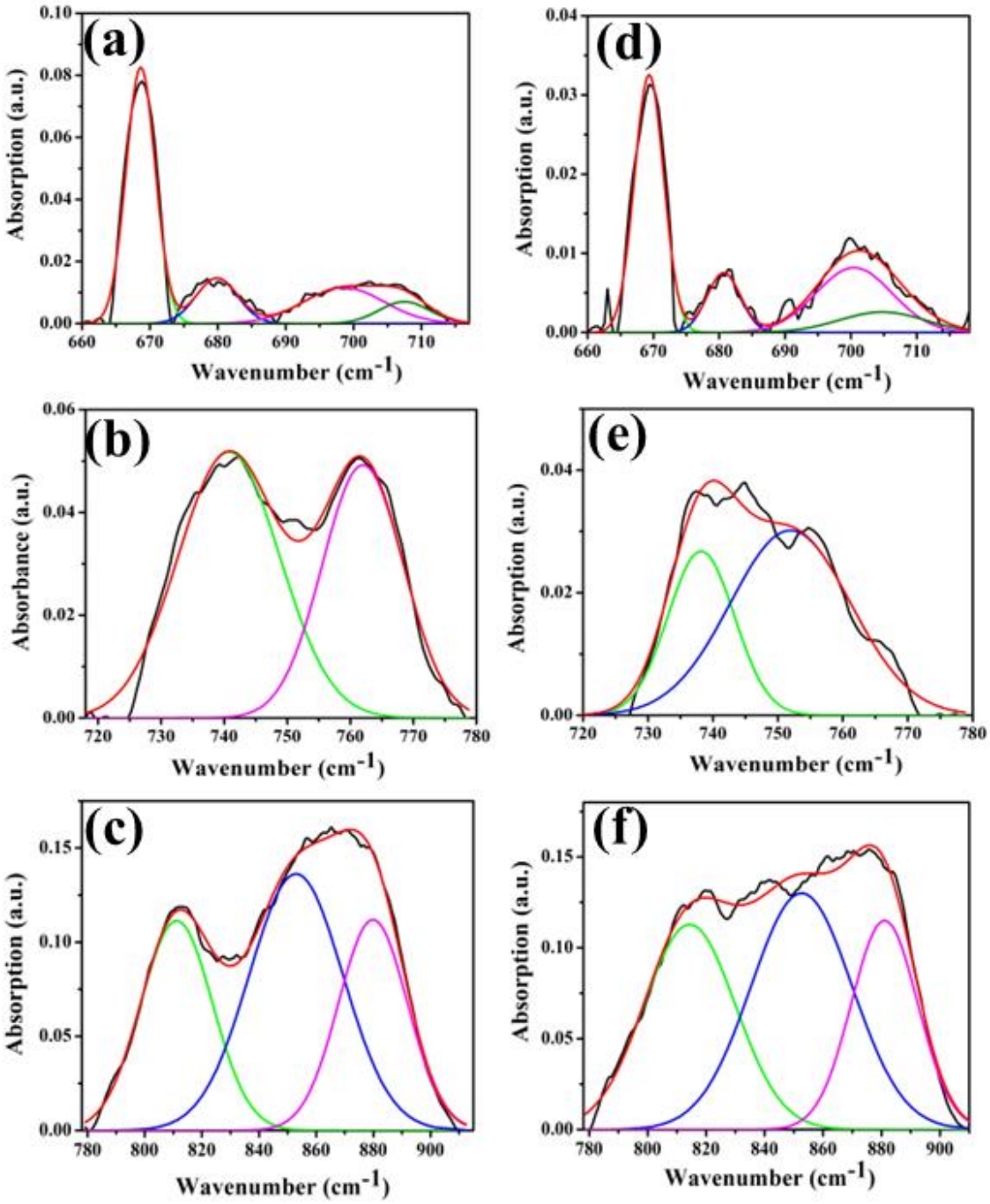

Figure 3: Deconvolution of the FTIR bands 660 – 717, 718-777 and 778 – 910 cm^{-1} of $NCWO_{120^oC}$ (a, b, c) and $NCWO_{140^oC}$ (d, e, f) respectively.

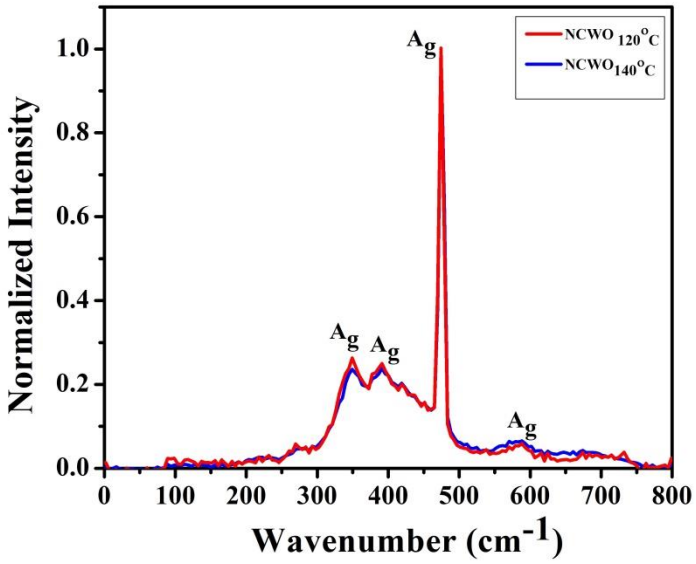

Figure 4: Raman spectra of $NCWO_{120^oC}$ and $NCWO_{140^oC}$

As V_O induced disorder has significant impact on local electronic environment which in consequence affects valance states of the constituent elements and valence band edges, hence to gain more insight about V_O induced effects on electronic structure, we have employed XPS to examine chemical states of Na, Ce, W and O. Obtained data for all elements were adjusted to account C1s, which is caused by adventitious C that comes during atmospheric exposure and has a binding energy of 284.6 eV. For both samples, the survey scan reflecting the core binding energies of Na, Ce, W, and O is shown (Figure A4, APPENDIX-I) in the range of 0 to 1100 eV, while Figures 5 and 6 show high resolution spectra of W, Ce, and O and band edges. Very briefly, Figures 5(a) and 5(b) illustrate two asymmetric peaks at 35.4 and 37.4 eV due to spin-orbit splitted $4f_{7/2}$ and $4f_{5/2}$ orbitals of W^{6+} [19], while deconvolution results four peaks c.a. W_a, W_b, W_c, and W_d at 35.0, 35.7, 37.0, and 37.7 eV, Currently, W_b and W_d correspond to $4f_{7/2}$ and $4f_{5/2}$ states of the W^RO_6, whereas W_a and W_c represent $4f_{7/2}$ and $4f_{5/2}$ states of W^DO_6 [20]. On the basis of electronegativity difference between W (~ 2.36) and O (~3.50), it can be stated that W – O bond is ionic, thus electrons are mostly located on O. Therefore, V_O increases the effective charge on W enhancing electron – electron repulsion on W; hence

binding energies of $4f_{7/2}$ and $4f_{5/2}$ states get reduced in W^DO_6. From area under the curve, we have estimated W^DO_6 ~ 44 and 35% within $NCWO_{120^oC}$ and $NCWO_{140^oC}$ corroborating FTIR studies. As presented in Figures 5(c) and (d), two asymmetric peaks in the ranges 877 – 891 eV and 895 – 910 eV characterise of Ce 3d [21]. Careful deconvolution of the $3d_{5/2}$ peak yields three peaks c.a. 882.0, 884.6, and 886.9 eV, named as Ce_a, Ce_b, and Ce_c, respectively, and they can be associated with Ce of three different electronic environment. Ce_c is assigned to CeO_8, whereas Ce_a and Ce_b are assigned to CeO_7 and CeO_6 containing V_O and $2V_O$ respectively. Herein, it may be stated that CeO_7 and CeO_6 refer deformed CeO_8 polyhedra with nearby one and two W^DO_6 subunits (schematically shown in Figure 8). The high covalent nature of the Ce – O bond, caused by the low electronegativity difference between Ce and O, has a major impact on the binding energies of the highly localised $3d_{5/2}$ and $3d_{3/2}$ orbitals. Here, V_O shortens Ce – O bond length that enhances electron-electron repulsion at the Ce site and lowering the binding energies of the $3d_{5/2}$ and $3d_{3/2}$ orbitals [22]. Careful analysis shows decrease (21 to 17%) of Ce_a in $NCWO_{140^oC}$ indicating suppression of V_O, hence the result highly corroborates previous observation. XPS of O 1s, shown in Figure 6(a) and (b) for $NCWO_{120^oC}$ and $NCWO_{140^oC}$, is highly symmetric indicating absence of surface adsorbed or interstitial O [23]. Valence band energy as shown in Figure 6(c) and (d) are measured to be ~ 2.36 and 2.13 eV for $NCWO_{120^oC}$ and $NCWO_{140^oC}$ respectively and is assigned to the influence of V_O on O 2p – W 5d bonding energy (discussed later).

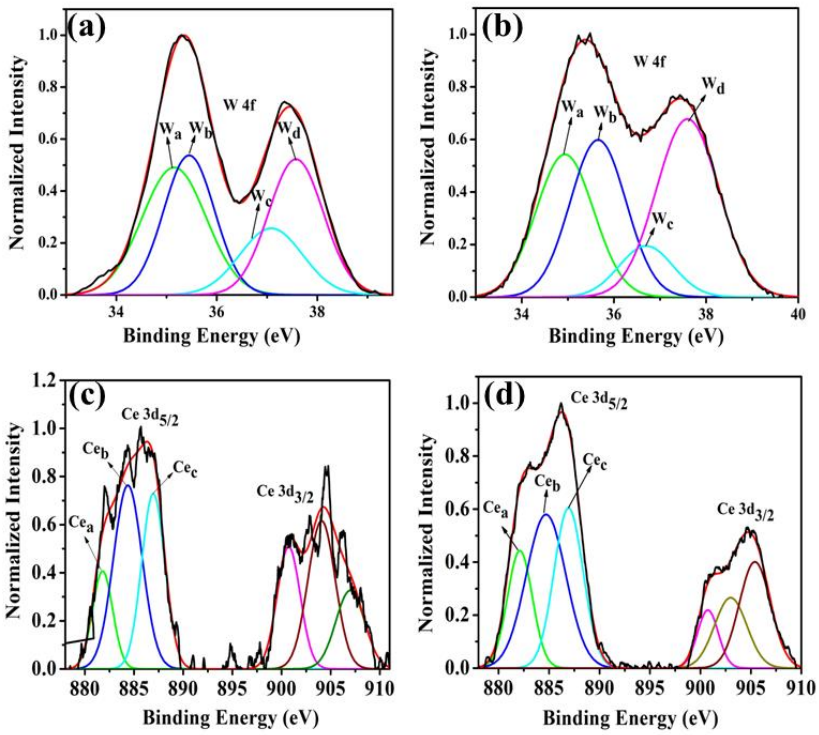

Figure 5: (a, b) XPS W4f and (c, d) XPS Ce3d core level spectra of $NCWO_{120^oC}$ and $NCWO_{140^oC}$ respectively.

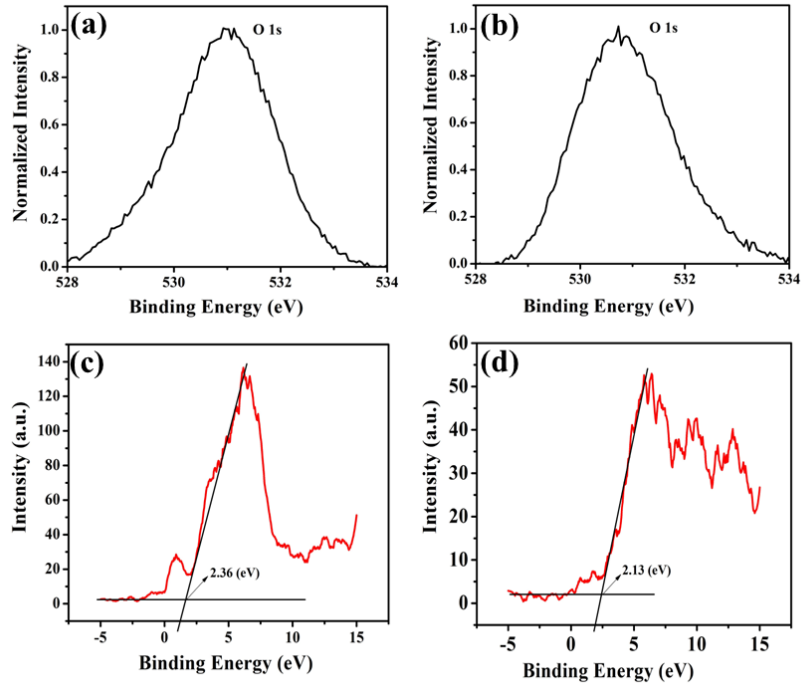

Figure 6: (a, b) XPS O1s core level spectra and (c, d) valence band edge of $NCWO_{120^oC}$ and $NCWO_{140^oC}$ respectively.

3.3 Investigations of optical properties of α-NCWO nanostructures by UV-Visible, steady state photoluminescence spectroscopies

The UV – Vis absorption spectra reveals optical band gap (E_g) ~ 3.07 and 3.17 eV for $NCWO_{120^oC}$ and $NCWO_{140^oC}$ respectively (shown in Figure A5, APPENDIX-I). Less E_g of $NCWO_{120^oC}$, ascribed to its higher valance band (VB) energy as identified by XPS, can also be explained as follows: DFT based *ab initio* calculation (discussed later) illustrates that VB of NCWO comprises of O 2p – W 5d hybridization, while W – 5d, Ce – 4f and O – 2p contribute to conduction band (CB) wherein V_O reduces O 2p – W 5d overlap in W^DO_6 (discussed later) resulting blue shift of VB [24]. Figures 7(a) and (b) illustrate luminescence characteristics of both the samples upon excitation at 380 nm. One strong peak at 434 nm (blue I, 23,042 cm^{-1}) and two peaks in the blue peaks at 460 (blue II, 21,739 cm^{-1}) and 488 nm (blue III, 20,492 cm^{-1}) and green emission at 520 nm (19,231 cm^{-1}) have been noticed in the visible region. It has been studied earlier that emissions from scheelite materials mostly comes from 5d to 4f transitions within lanthanides, however proper understanding of the mechanism is still under debate as several parameters such as crystal field, polarizability etc. have significant influence on the emission characteristics [25]. As an example, two emissions from $LiCe(WO_4)_2$, recorded at 390 and 412 nm, were attributed to $^5D_0$ - $^2F_{5/2}$ and $^5D_0$ - $^2F_{7/2}$ transitions within Ce^{3+}, while Dorenbos *et al.* had measured them at 451 and 485 nm [26,27]. Presently, we have adopted equation (1), provided by van Uitert *et al.*, to understand the emission wavelength (λ) from α-NCWO [28], where 5d – 4f transition within Ce^{3+} within regular CeO_8 dodecahedron is given by:

$$\frac{1}{\lambda} = \frac{Q^*}{hc}\left[1 - \left(\frac{V}{4}\right)^{\frac{1}{V}} 10^{\frac{-(nrE_a)}{80}}\right] \qquad (1)$$

where, Q*, V, 'n', E_a and 'r' represent the energy of 5d band edge of free Ce^{3+} ion (= 200 nm), valance of the Ce^{3+}, number of anions in the immediate shell around Ce^{3+}, electron affinity of the atoms forming anions, and r is the radius of the host cation replaced by the Ce^{3+} ion. Herein, we have calculated λ = 435 nm is well correlated with our 434 nm experimental blue I emission. According to earlier studies including us, we know that V_O defects within E_g act as luminescence centres leading various emission characteristics. As an illustration, Korzhik *et al.* [29] had attributed green emission from scheelites with WO_3 centres, while green-red emission was assigned with WO_3•$\ddot{V}_O$ oxygen-deficient complexes by Sokolenko *et al.* [30]. Sienelnikov *et al.* have proposed that W^DO_6 stimulates creation of which, as a result, acts as a hub for green emission [31]. Since the XPS study confirms the presence of CeO_7 and CeO_6 within our synthesized samples, hence a similar calculations using equation (1) with CeO_7 and CeO_6 configuration reveal $\lambda \sim$ 472.9 and 520.4 nm respectively. Most importantly, these match very well with our experimentally observed green and blue III emissions (Schematically represented in figure 8). Briefly, it can be stated that V_O alters energy of 5d orbitals Ce^{3+} of these CeO_7 and CeO_6 causing different emissions. For better understanding, we have calculated centroids of the d-orbitals (ε_{cfs} (1, 3 +, A)) of Ce^{3+} in CeO_7 and CeO_6 according to Dorenbos's which is given by equation (2) [32]:

$$\varepsilon_{cfs}\,(1, 3+, A) = \beta R_{av}^{-2} \qquad (2)$$

where, β = 1.35 × 10^9 pm^2 cm^{-1} for Ce^{3+} and $R_{av} = \frac{1}{N}\sum_{i=1}^{N}(R_i - 0.6\Delta R)$; R_i denotes bond lengths to the N coordinating anions in strained lattice. Given that our calculations produce $\varepsilon_{cfs} \sim$ 5.92 and 5.34 eV for CeO_7 and CeO_6, it is inferred that V_O significantly influences ε_{cfs} which determines 'λ' for 5d – 4f transition within CeO_7 and CeO_6 while their formation can be understood by Kröger-Vink notation as follows: as electrons are released into the host matrix,

V_O and $2V_O$ lead ionised defects states c.a. $V_O^{\bullet}$ and $2V_O^{\bullet}$, which can be written by equation 3(a) and (b):

$$[CeO_8]^x + \left[CeO_7 \bullet V_O^X\right] \rightarrow [CeO_8]' + [CeO_7 \bullet V_O^{\bullet}] \qquad 3(a)$$

$$[CeO_8]^x + \left[CeO_6 \bullet 2V_O^X\right] \rightarrow [CeO_8]'' + [CeO_6 \bullet 2V_O^{\bullet}] \qquad 3(b)$$

where $[CeO_8]'$ and $[CeO_8]''$ denote electron donors and $[CeO_7 \bullet V_O^{\bullet}]$ and $[CeO_6 \bullet 2V_O^{\bullet}]$ are the electron acceptors those exhibit blue II and green emission. It has been noted from previous literature that the difference between $^5D_0$- $^2F_{5/2}$ and $^5D_0$-$^2F_{7/2}$ transitions within Ce^{3+} is ~ 2,000 cm^{-1}, however this difference i.e. the difference between blue I and blue II emissions is ~ 1,303 cm^{-1}. Hence, it may be stated that blue I emission cannot be ascribed to $^5D_0$-$^2F_{7/2}$ transition within regular CeO_8 dodecahedra. In this context, it is important to note that CeO_6 forms two distinct ε_{cfs}s. Our DFT calculation leads two different ε_{cfs} within E_g, hence blue II emission could be assigned to other ε_{cfs}. The intensity ratio of blue II and green with respect to blue I emission are seen in figure 7(c) to be higher, while that of blue III emission is constant.

Commission International De I'Eclairage (CIE) coordinates (shown in Figure 7(d)) are calculated to be (0.18, 0.14) and (0.17, 0.15) for $NCWO_{120^oC}$ and $NCWO_{140^oC}$ [33]. The coordinates illustrates blue emission from synthesized samples, while variation in the coordinates are ascribed to different contribution from blue II and III. Colour purity ~ 95% has been estimated for both samples from equation (4) [34,35] :

$$\text{Color purity} = \frac{\sqrt{(x-x_i)^2+(y-y_i)^2}}{\sqrt{(x_d-x_i)^2+(y_d-y_i)^2}} \times 100\% \qquad (4)$$

where (x, y) represents the color coordinates of the phosphor; (x_i, y_i) is the illuminant point of the 1931 CIE Standard Source with the colour coordinates of (0.3101, 0.3162); (x_d, y_d) refers to colour coordinates of the dominant wavelength and the correlated colour temperatures (CCTs) ~ 7340 and 7715 K for $NCWO_{120^oC}$ and $NCWO_{140^oC}$ have been calculated from McCamy's relation as given in equation (5) [36],

$$CCT = 449n^3 + 3525n^2 + 6823.3n + 5520.3 \quad (5)$$

where $n = \frac{(x-0.3320)}{(0.1858-y)}$ and (x, y) represents the chromaticity co-ordinates. Herein, it may be stated α-NCWO can be a potential material for cold blue lighting applications.

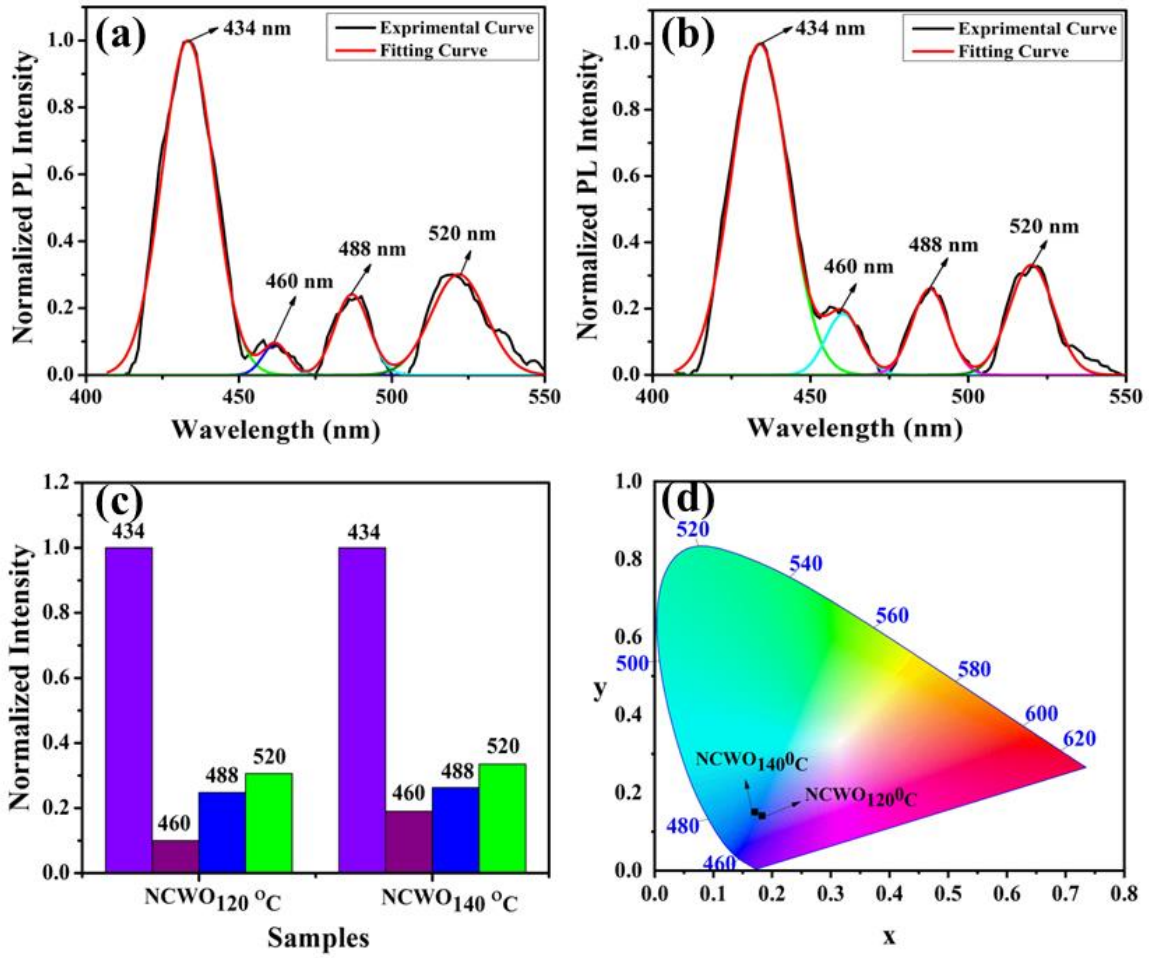

Figure 7: Photoluminescence spectra of (a) $NCWO_{120^oC}$ and (b) $NCWO_{140^oC}$ respectively. (c) Normalized PL intensity ratio of emission wavelengths (d) The CIE chromaticity diagram of the NCWO phosphors.

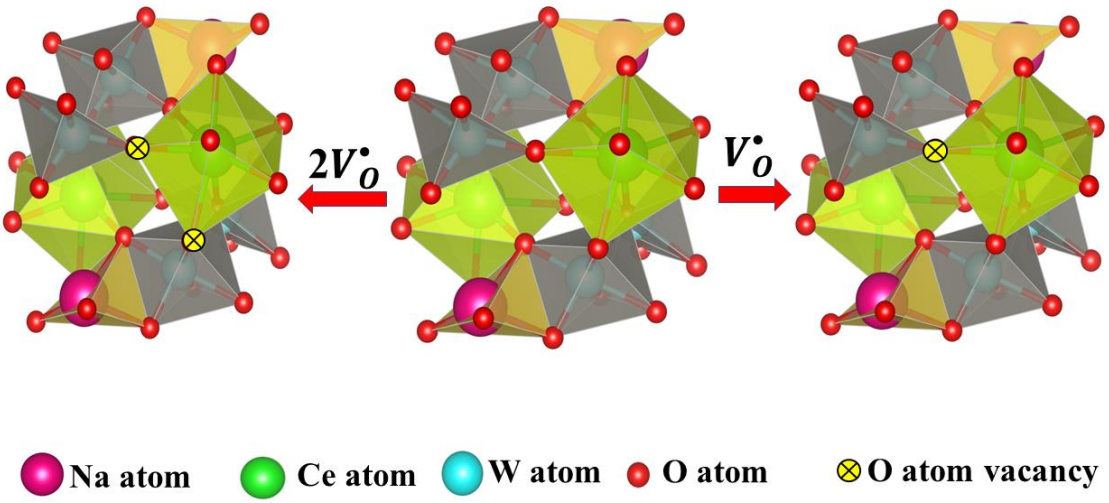

Figure 8: Schematic diagram of oxygen vacancies of CeO_8 polyhedra unit.

3.4 Investigations of gas sensing properties of α-NCWO nanostructures

Most common gas-sensing mechanism of metal oxides is determined by solid – gas interfacial reaction, in which adsorption and desorption of the targeted gas molecules on the surface sensing materials produces an intense change in resistance. Hence, it is accepted that adsorption and desorption of the target molecules on the surface of the materials is most crucial in its gas sensing activity [37,38]. In recent past, a significant effort has been made to examine the influence of morphology, surface area, surface defects etc. on the sensing properties. Very briefly it can be stated that among various defects, V_O plays very crucial role in as they increase the ability to adsorb molecular oxygen as described by equation (6):

$$O_2(\text{gas}) + e^- \leftrightarrow O_2^-(\text{ads}) \qquad (6)$$

And in turn gas sensing properties get enhanced through a better interaction with targeted gas molecules. From our previous experiments, we have observed that our samples contain V_O, $2V_O$ defects, which may act potential center for adsorption of molecular O_2 and lead sensing activity. From literature, we know

that upon exposure to ammonia (NH_3) or acetone (C_3H_6O) or ethanol (CH_3CH_2OH), the following reactions take place in the presence of $O_2^-(ads)$

$$4NH_3(gas) + 3O_2^-(ads) \leftrightarrow 6H_2O(gas) + 2N_2(gas) + 3e^- \quad (7a)$$

$$C_3H_6O(gas) + 8O_2^-(ads) \leftrightarrow 3H_2O(gas) + 3CO_2 + 16e^- \quad (7b)$$

$$CH_3CH_2OH(gas) + O_2^-(ads) \leftrightarrow H_2O(gas) + C_2H_4O + 2e^- \quad (7c)$$

Hence, it may be stated that α-NCWO may be a potential sensor material for volatile organic compounds (VOCs) viz. NH_3, acetone, ethanol. In order to verify this, we have carried out a set of measurements by exposing the $NCWO_{120^oC}$ and $NCWO_{140^oC}$ based sensors to different target analytes (NH_3, acetone, ethanol) at different operating temperatures in the range 200^0C-400^0C. Highest acetone sensitivity from $NCWO_{120^oC}$ (measured at operating temperature 350 ^{0}C) is observed, while $NCWO_{140^oC}$ possesses highest sensitivity to ammonia (measured at operating temperature 300 ^{0}C), (shown in Figure 9 (a)-(b)). Sensitivity performance of $NCWO_{120^oC}$ and $NCWO_{140^oC}$ has been further examined from temperature calibration curve (Figure 9 (c)) in the presence of 10 ppm acetone and 10 ppm ammonia, respectively. It can be inferred from figure that $NCWO_{120^oC}$ and $NCWO_{140^oC}$ exhibit highest sensitivity at ~ 350^0C and 300^0C, hence they may be ascribed as the optimum operating temperature for acetone and NH_3 respectively as target analyte. Dynamic response characteristics of $NCWO_{120^oC}$ and $NCWO_{140^oC}$ against respective analyte are represented in Figure 9 (d)-(e). Herein, we have calculated sensitivity ($= \frac{R_{gas}}{R_{air}}$) of $NCWO_{120^oC}$ ~ 1.69, 1.71 and 1.90 against 10, 50 and 100 ppm of acetone, respectively, while $NCWO_{140^oC}$ exhibits sensitivity ~ 1.52, 1.68, 1.76 against 10, 50 and 100 ppm of NH_3. Presently, we have measured response and recovery time ~ 1.9s/29.0s and 3.7s/79.0s for acetone and NH_3 by the respective sensor (shown in Figure 9 (f)-(g)). Figure 9 (h) displays the long-term stability of the sensors measured for 100 days. Both of $NCWO_{120^oC}$ and $NCWO_{140^oC}$ based sensors showed excellent stability.

Equation (3) indicates the presence of $[CeO_8]'$ and $[CeO_8]''$ as electron donors within our synthesized samples. Hence, it may be approximated that electrons from $[CeO_8]'$ and $[CeO_8]''$ may be transferred to the O_2 molecule, adsorbed on the surface of α-NCWO nanostructures which will convert O_2 molecule to oxygen ions (as given in equation (6)) through depletion of electrons from host matrix.

However, the gas-sensing mechanism of NCWO is mainly depends on amount of defect. Both nanomaterials exhibited remarkable sensing property towards volatile organic compounds (VOCs). Study of sensing performance of $NCWO_{140^oC}$ revealed that the sensor exhibited better response towards ammonia gas compared to acetone and ethanol. Moreover, acetone is known for having large dipole moment for which the selectivity of $NCWO_{120^oC}$ to acetone may be attributed to the strong interaction between acetone molecules and $NCWO_{120^oC}$ compared to other target analytes such as ammonia and ethanol [39]. The future prospect of NCWO based sensor is that, even though the difference between the response of the sensors to acetone, ammonia and ethanol is not very large, these sensors can be incorporated into a sensor array to detect different volatile organic compounds simultaneously.

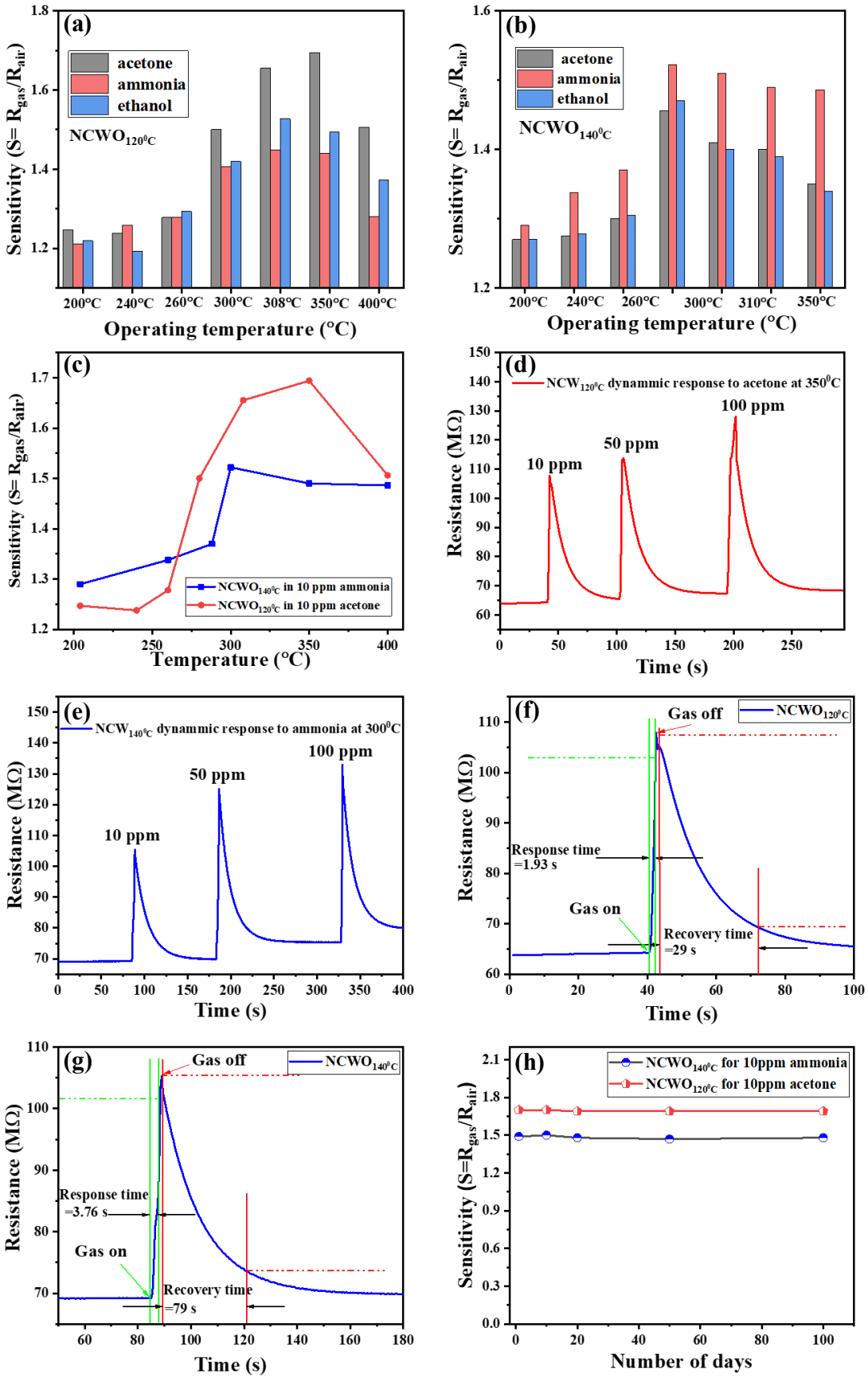
(a)
acetone
ammonia
ethanol
NCWO120°C
Sensitivity (S= Rgas/Rair)
200°C 240°C 260°C 300°C 308°C 350°C 400°C
Operating temperature (°C)
(b)
acetone
ammonia
ethanol
NCWO140°C
Sensitivity (S= Rgas/Rair)
200°C 240°C 260°C 300°C 310°C 350°C
Operating temperature (°C)
(c)
Sensitivity (S= Rgas/Rair)
NCWO140°C in 10 ppm ammonia
NCWO120°C in 10 ppm acetone
Temperature (°C)
(d)
NCW120°C dynammic response to acetone at 350°C
10 ppm
50 ppm
100 ppm
Resistance (MΩ)
Time (s)
(e)
NCW140°C dynammic response to ammonia at 300°C
10 ppm
50 ppm
100 ppm
Resistance (MΩ)
Time (s)
(f)
Gas off
NCWO120°C
Response time
=1.93 s
Gas on
Recovery time
=29 s
Resistance (MΩ)
Time (s)
(g)
Gas off
NCWO140°C
Response time
=3.76 s
Gas on
Recovery time
=79 s
Resistance (MΩ)
Time (s)
(h)
NCWO140°C for 10ppm ammonia
NCWO120°C for 10ppm acetone
Sensitivity (S=Rgas/Rair)
Number of days

Figure 9: (a, b) Response of $NCWO_{120^oC}$ and $NCWO_{140^oC}$ based sensors to ammonia, acetone and ethanol gasses measured at different operating temperatures, respectively. (c) Temperature calibration curve of $NCWO_{120^oC}$ and $NCWO_{140^oC}$ for 10 ppm ammonia and acetone, respectively. (d, e) Dynamic response curve of $NCWO_{120^oC}$ sensor at 350 °C and $NCWO_{140^oC}$ sensor at 300 °C to different concentrations of acetone and ammonia, respectively. (f, g) Calculation of response and recovery time of $NCWO_{120^oC}$ (350°C) and $NCWO_{140^oC}$ (300°C) for 10ppm acetone and for 10ppm ammonia, respectively. (h) Stability in 10ppm ammonia and 10 ppm acetone sensing data of $NCWO_{120^oC}$ and $NCWO_{140^oC}$ at 350 °C and 300 °C temperature, respectively, for 100 days.

3.5 Ab initio calculation of electronic structure of α-NCWO: modelling of defects induced modification in band structure and density of states

In order to understand above mentioned experimental findings, electronic band structures, total densities of states (TDOS) and angular momentum projected partial densities of states (PDOS) of pure and CeO_7, CeO_6 containing NCWO have been calculated along several high-symmetry points within the Brillouin zones using ab-initio DFT. We have modelled CeO_7 and CeO_8 by removing one O (c.a. V_O) and two O atoms (c.a. $2V_O$) from the unit cell of NCWO as these defects serve as a foundation for the interpretation of the luminescence property mentioned above. Prior to calculating the band structure, we have optimised the NCWO unit cell and our calculation reveals lattice parameters a ~ 7.115 Å, b~ 7.348 Å, c ~ 7.271 Å, angles α ~ 114.232, β ~ 115.779, γ ~ 90.692 degree and bond lengths Na – O ~ 2.366 Å, Ce – O ~ 2.421 Å, and W – O ~ 1.787 Å. Herein, it may be stated that these parameters closely match with our

experimental results, demonstrating the accuracy of our calculations, including choice of exchange correlation function. Presently, we have set top of the valence band maxima (VBM) at zero energy level. Herein, we have found that VBM at Γ point, while the conduction band minimum (CBM) is situated along R line (Figure 10(a)) demonstrating an indirect $E_g \sim 3.10$ eV e of α-NCWO. The curvature at CBM suggests low effective mass for electron, while that of VBM is relatively low indicating high effective mass for hole. Hence, it is anticipated that α-NCWO will have high electron mobility, providing electrons a higher opportunity to have longer mean free paths. Our calculation also demonstrates spin polarized CB, but VB is not spin polarized. A careful examination of the PDOS on Na, Ce, W, and O atoms (shown in Figure 10(b) - (f)) reveals that the upper part of the valence band (VB) is predominated by O - $2p_x$, $2p_y$ and $2p_z$ orbitals, with minor contributions from Ce - 4f, W - $5d_{xy}$, $5d_{yz}$, $5d_{x^2-y^2}$, and Na - 3s orbitals. Hence, low curvature of VB can be ascribed to unmixing of O 2p with Ce – 4f, W – 5d and Na – 3s. It is also visible from our calculation that O - $2p_x$, $2p_y$, and $2p_z$ combine mostly with W - $5d_{xy}$, $5d_{yz}$, $5d_{zx}$, and $5d_{x^2-y^2}$ in the lower half of the VB. CBM mostly originates from Ce - $4f_{xyz}$, $4f_{yz^2}$, 4_{fz^3}, $4f_{zx^2}$, $4f_{x^3}$, and $4f_{y^3x^2}$ with relatively minor contribution from O - $2p_x$, $2p_y$, and $2p_z$ and provide higher curvature. Therefore, it may be stated that VB primarily is constructed of WO_6 octahedra, but CB is sensitive to both WO_6 octahedra and CeO_8 dodecahedra and band to band transition takes place from O ↔ Ce charge transfer process.

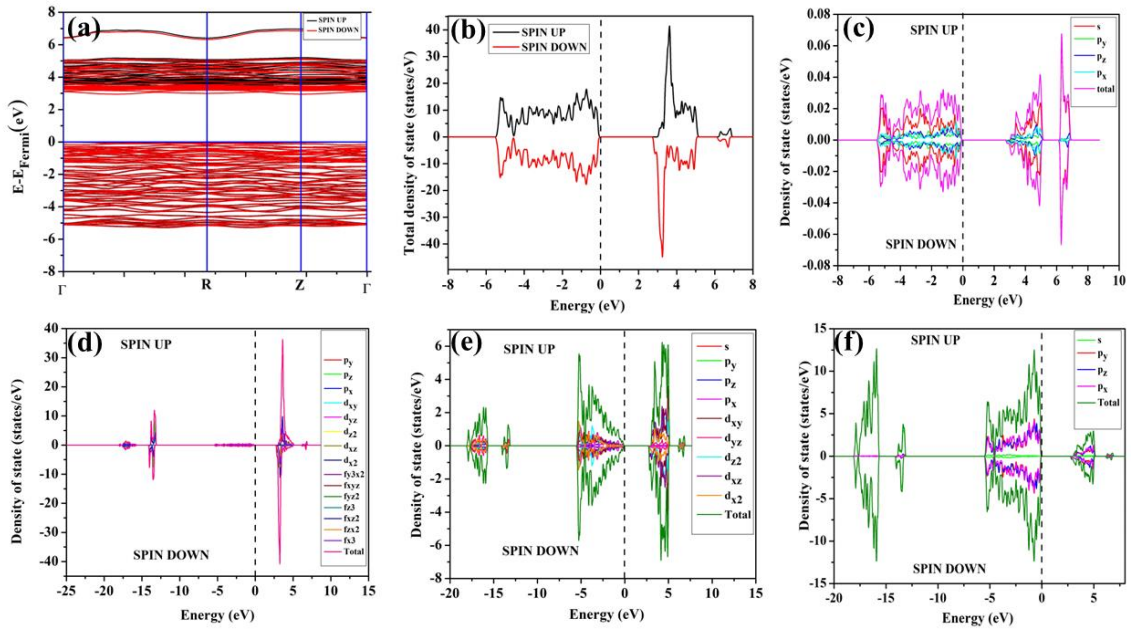

Figure 10: (a) Band structure and (b) spin polarised TDOS and PDOS of (c) Na, (d) Ce, (e) W and (f) O of NCWO.

Band structure, TDOS, and PDOS of V_O and $2V_O$ contained α-NCWO sample, named as α-NCWO – V_O and α-NCWO – $2V_O$, are represented in Figure 11 and 12 respectively. It is clearly visible from Figure 11(a) and 12(a) that VBM of α-NCWO – V_O remains unchanged at the Γ -point while that of α-NCWO – $2V_O$ shifts to R-point. In a similar fashion, CBM remains fixed at Γ point, while it moves along Γ – R line for α-NCWO – $2V_O$. In both samples, E_g is found to be monotonically lowering with regard to NCWO (2.97 and 2.30 eV respectively), hence it may be stated that $NCWO_{120}{}^oC$ contains more oxygen vacancies with reference to $NCWO_{140}{}^oC$. Herein, calculations of TDOS (Figures 11(b) and 12(b)) and PDOS (Figures 11(c)-(f) and 12(c)-(f)) reveal that VB width greatly increases in α-NCWO – $2V_O$ due to more delocalization of O 2p. It is also observed that the curvature of VBM as well as CBM significantly get enhanced in α-NCWO – V_O and α-NCWO – $2V_O$, which may be attributable increase in the orbital overlap suggesting that carrier mobility can be easily tuned by oxygen vacancies. It is also important to note that α-NCWO – $2V_O$ exhibits at

1.50 and 2.30 eV above VBM, whereas α-NCWO – V_O possesses only one defect state at 2.34 eV above VBM. While contributions from other Ce 4f orbitals, O 2p and W 5d orbitals have been identified, a comprehensive investigation of TDOS and PDOS reveals that among all 5d orbitals, Ce $5d_{xz}$ and $5d_{x^2-y^2}$ orbitals dominate in these defect states. Here, our calculations show that, among other Ce 5d orbitals, the Ce $5d_{z^2}$ and $5d_{x^2-y^2}$ orbitals, contribute the most to defect states at 1.50 and 2.30 eV. Hence from above discussion, it may be stated institutively that blue III emission originates from Ce $5d_{xz}$, $5d_{x^2-y^2} \rightarrow$ 4f transitions within deformed CeO_7 polyhedra, while blue II and green emissions comes from Ce $5d_{z^2} \rightarrow$4f and $5d_{x^2-y^2} \rightarrow$4f transitions within CeO_6 polyhedra respectively as schematically shown in Figure 13.

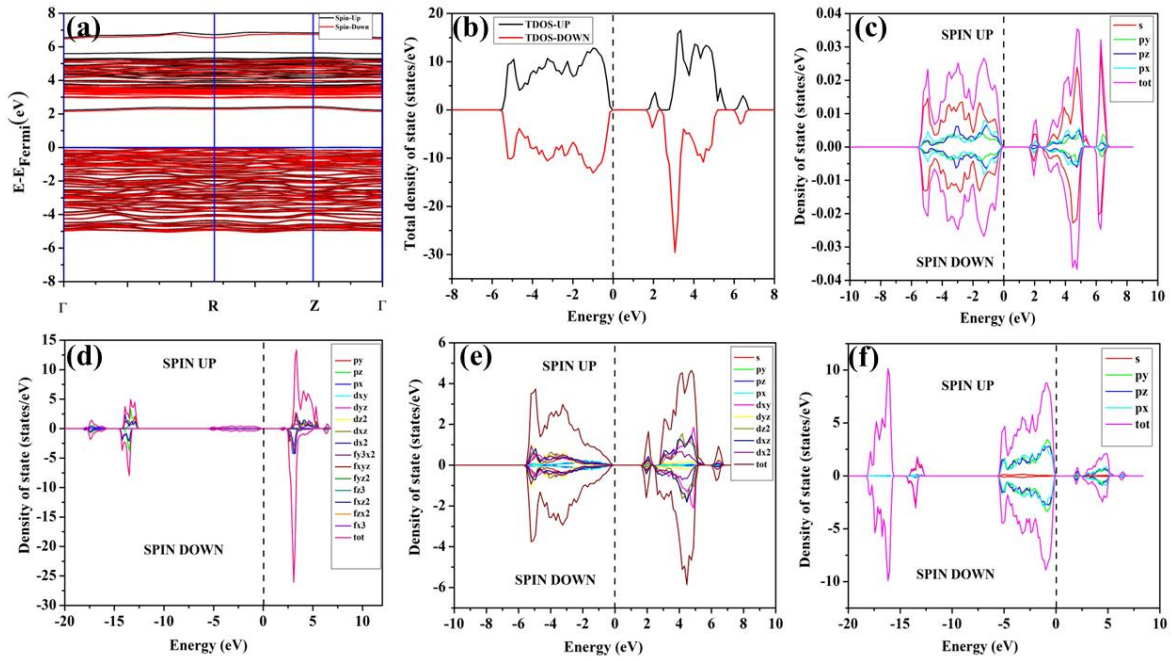

Figure 11: (a) Band structure and (b) spin polarised TDOS and PDOS of (c) Na, (d) Ce, (e) W and (f) O of NCWO – $V_O^{\bullet\bullet}$.

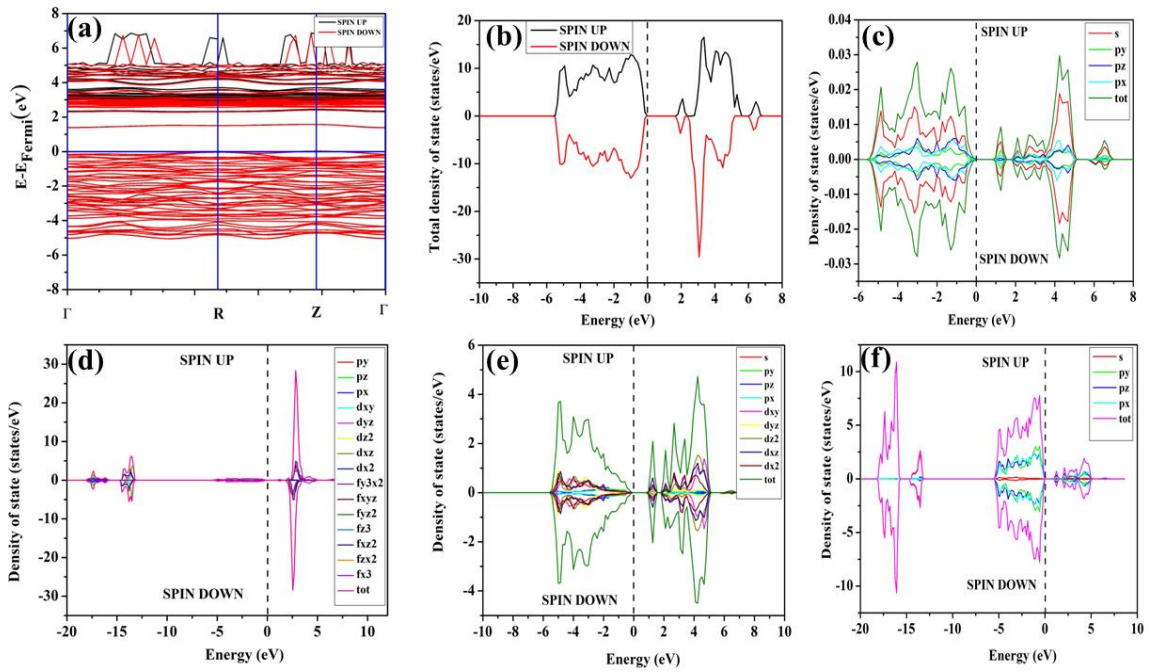

Figure 12: (a) Band structure and (b) spin polarised TDOS and PDOS of (c) Na, (d) Ce, (e) W and (f) O of NCWO – $2V_O^{\bullet}$.

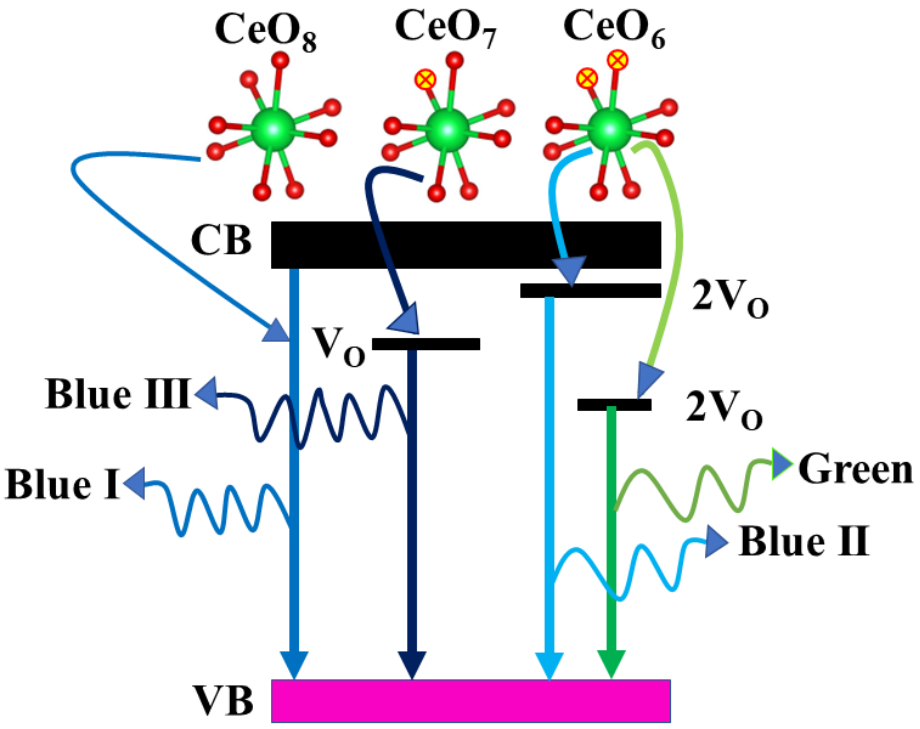

Figure 13: Schematic diagram of photoluminescence transitions.

4. Conclusion:

Pristine α-NCWO clusters have been synthesized with varying oxygen monovacancy by a facile CTAB assisted hydrothermal technique. This is the first time we are reporting intense blue I and comparatively low intense blue II, blue III and green emissions from α-NCWO. Our detailed experimental and theoretical studies reveal that all these transitions are related with 5d → 4f transition of Ce, but in different CeO_8 polyhedral configuration. More specifically, blue I and blue III emissions originate from CeO_8 and CeO_7, while CeO_6 provides blue II and green emissions indicating that from α-NCWO has the potentiality for blue emitting device application. We have also identified first time gas sensing properties of from α-NCWO, which is attributable to oxygen vacancies related with CeO_7 and CeO_6. Herein, it may be stated that this study will be helpful for better understanding of the optoelectronic properties of pristine as well as oxygen vacancy contained α-NCWO, wherein our calculation demonstrates that valence and conduction bands comprises of O 2p and O 2p – Ce 5d orbitals respectively and they are highly sensitive of oxygen vacancies, hence these may be used to tune optical and gas sensing applications of α-NCWO. Hence, it may be finally concluded that α-NCWO may be a potential material for light emitting and sensing applications.

APPENDIX- I

Table A1: Coordination environment of triclinic NCWO structure.

Coordinates atoms	x	y	Z	Occupancy	Site occupancy	symmetry
Na1	0.2815	0.7733	0.1567	1.0	1a	1
Na2	0.7184	0.2266	0.8432	1.0	1a	1
Ce1	0.1740	0.2878	0.4547	1.0	1a	1
Ce2	0.2860	0.7121	0.5452	1.0	1a	1

O1	0.1823	0.3500	0.7987	1.0	1a	1
O2	0.8176	0.6500	0.2012	1.0	1a	1
O3	0.4619	0.6413	0.2627	1.0	1a	1
O4	0.5380	0.4586	0.7372	1.0	1a	1
O5	0.8659	0.0119	0.1955	1.0	1a	1
O6	0.1340	0.9880	0.8044	1.0	1a	1
O7	0.7074	0.0107	0.4898	1.0	1a	1
O8	0.2925	0.9893	0.5101	1.0	1a	1
O9	0.1740	0.6339	0.5530	1.0	1a	1
O10	0.8259	0.3660	0.4469	1.0	1a	1
O11	0.4847	0.8316	0.0074	1.0	1a	1
O12	0.5152	0.1683	0.9925	1.0	1a	1
O13	0.0578	0.3132	0.1062	1.0	1a	1
O14	0.9421	0.6868	0.8937	1.0	1a	1
O15	0.3906	0.1712	0.2675	1.0	1a	1
O16	0.6093	0.8287	0.7324	1.0	1a	1
W1	0.2753	0.2990	0.0396	1.0	1a	1
W2	0.7246	0.7009	0.9603	1.0	1a	1
W3	0.6569	0.1086	0.2887	1.0	1a	1
W4	0.3430	0.8913	0.7112	1.0	1a	1

Table A2: The details of the deconvolution of the FTIR bands

Samples	Peak position (cm^{-1})		Area (cm^2)	FWHM	χ^2
	660-717	668.644	0.446	5.089	3.24
		679.572	0.112	7.247	
		698.572	0.172	13.993	
		707.462	0.065	8.798	

$NCWO_{120^0C}$	718-777	742.568 762.311	0.477 0.614	15.444 14.002	3.30
	778-910	811.177 852.943 879.857	3.500 5.599 3.377	29.541 38.620 28.367	2.1
$NCWO_{140^0C}$	660-717	669.343 680.665 700.475 704.758	0.181 0.047 0.118 0.042	5.242 5.993 13.643 15.349	2.24
	718-777	738.186 751.922	0.342 0.700	12.033 21.808	3.81
	778-910	814.374 852.670 881.042	4.428 5.636 3.264	36.893 40.724 26.692	2.43

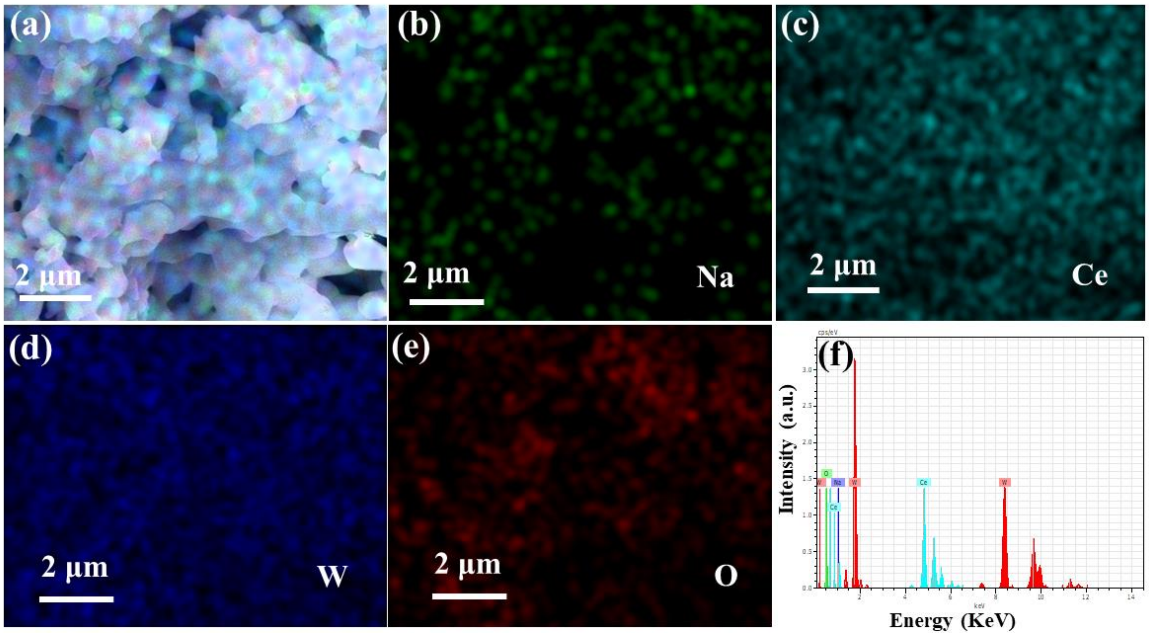

Figure A1: The elemental mapping of $NCWO_{120^oc}$.

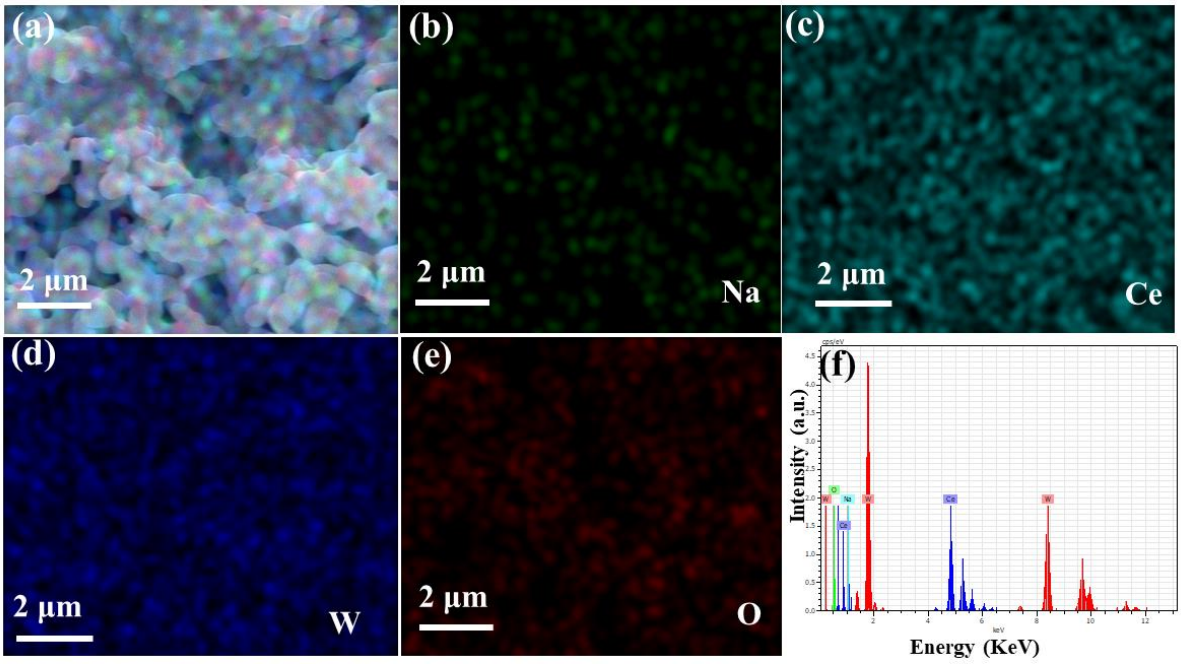

Figure A2: The elemental mapping of $NCWO_{140^oc}$

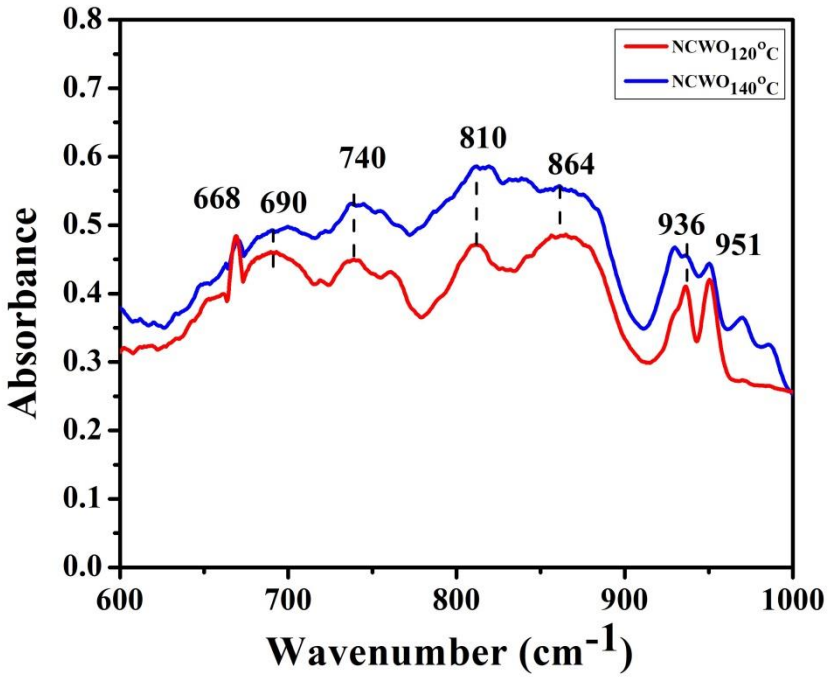

Figure A3: FTIR spectra of $NCWO_{120^oc}$ and $NCWO_{140^oc}$.

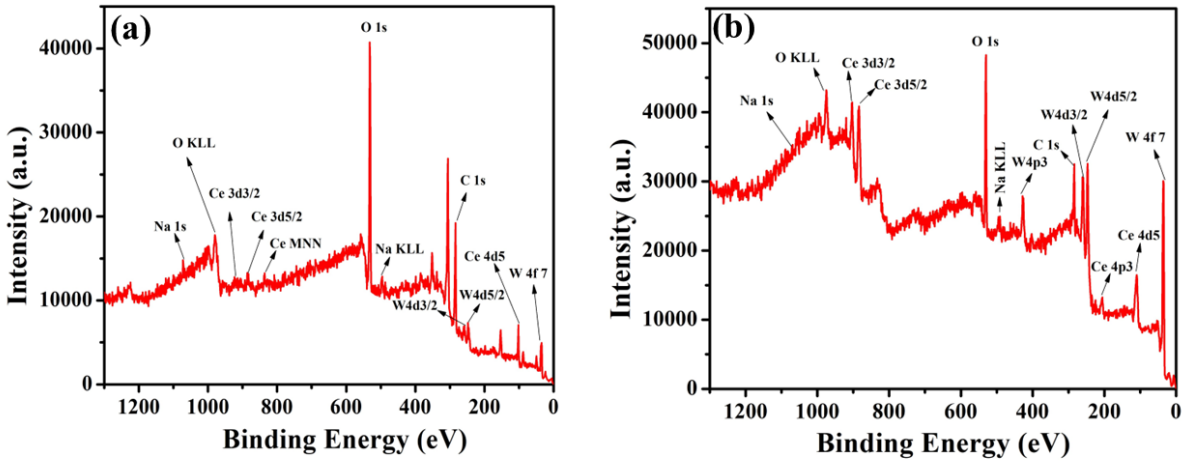

Figure A4: XPS wide spectrum of Ce-3d, W-4f, O-1s, Na-1s of (a) $NCWO_{120^oc}$ and (b) $NCWO_{140^oc}$ respectively.

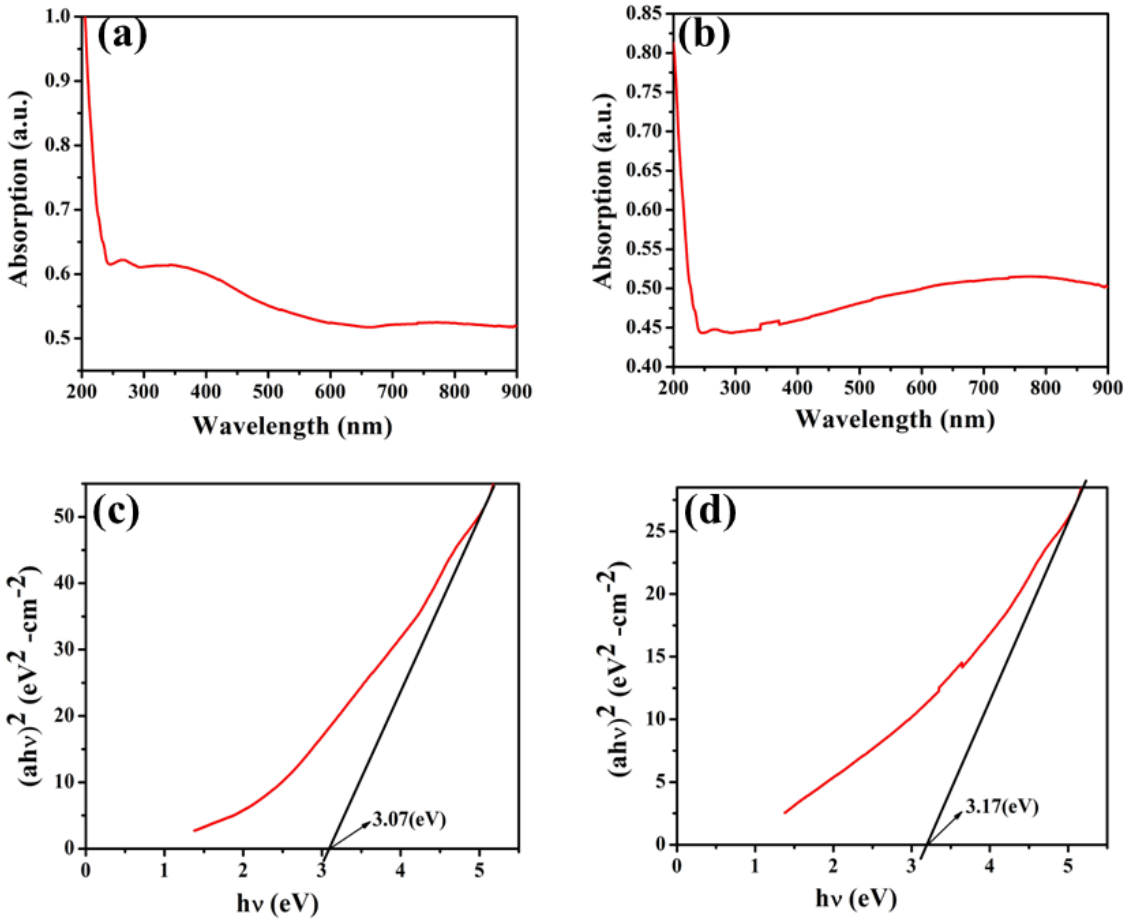

Figure A5: UV spectra (a, b) and corresponding band gap calculation (c, d) of $NCWO_{120^oC}$ and $NCWO_{140^oC}$ respectively.

References

1. G. Bemoît, J. Véroniue, A. Arnaud and G. Alain, *Sol. State Sci.*, 2011, **13**, 460467

2. H. Yang, F. Peng, Q. Zhang, W. Liu, D. Sun, Y. Zhao and X. Wei, *Opt. Mater.*, 2013, **35**, 23382342

3. J. Moraes, S. Baldochi, L. Soares, V. Mazzocchi, C. Parente and L. Courol, *Mater. Res. Bull.*, 2012, **47**, 744749

4. T. Shimemura, N. Sawaguchi and M. Sasaki, *J. Ceram Soc. Japan*, 2017, **125**, 150-154

5. A.K. Munirathnappa, V.C. Petwal, J. Dwivedi and N.G. Sundaram, *New J. Chem*., 2018, **42**, 2726-2732

6. N. Dirany, M. Arab, A. Moreau, J.C. Valmalette and J.R. Gavarri, *CrystEngComm*., 2016, **18**, 6579-6593

7. Y. Tian, B. Chen, R. Hua, J. Sun, L. Cheng, H. Zhong, X. Li, J. Zhang, Y. Zheng, T. Yu and L. Huang, *J. Appl. Phys*., 2011, **109**, 053511

8. Y. Tian, B. Chen, R. Hua, J. Sun, L. Cheng, H. Zhong, X. Li, J. Zhang and B. Tian, *CrystEngComm*., 2012, **14**, 1760-1769

9. H. Zheng, B. Chen, H. Yu, J. Zhang, J. Sun, X. Li, M. Sun, B. Tian, S. Fu, H. Zhong and B. Dong, *J. colloid and interface sci*., 2014, **420**, 27-34

10. A.K. Munirathnappa, D. Dwibedi, J. Hester, P. Barpanda, D. Swain, C. Narayana and N.G. Sundaram, *J. Phys. Chem. C*, 2018, **123**, 1041-1049

11. W.R. Liu, C.W. Yeh, C.H. Huang, C.C. Lin, Y.C. Chiu, Y.T. Yeh and R.S. Liu, *J. Mater. Chem.*, 2011, **21**, 3740-3744

12. R.L. Andrews, A.M. Heyns and P.M. Woodward, *Dalton Trans*., 2015, **44**, 10700-10707

13. Pushpendra, R.K. Kunchala, S.N. Achary and B.S. Naidu, *ACS Appl. Nano Mater*., 2019, **2**, 5527-5537

14. F. Esteban-Betegón, C. Zaldo and C. Cascales, *Chem. Mater*., 2010, **22**, 2315-2324

15. M. Gancheva, A. Naydenov, R. Iordanova, D. Nihtianova and P. Stefanov, *J. Mater. Sci*., 2015, **50**, 3447-3456

16. A.H. Ahmad and A.K. Arof, *Ionics*, 2004, **10**, 200-205

17. L. Macalik, J. Hanuza and A.A. Kaminskii, *J. Mol. Struct*., 2000, **555**, 289-297

18. A. Jayaraman, S.K. Sharma and S.Y. Wang, *J. Raman spectrosc*., 1998, **29**, 305-312

19. S.D. Ramarao and V.R.K. Murthy, *Dalton Trans*., 2015, **44**, 2311-2324

20. C. Zhang, D. Guo, W. Xu, C. Hu and Y. Chen, *J. Phys. Chem. C*, 2016, **120**, 12218-12225

21. A.K. Munirathnappa, J.C. Neuefeind, P. Yanda, A. Sundaresan, I.V. Kityk, K. Ozga, J. Jedryka, A. Rao and N.G. Sundaram, *Cryst. Growth Des*., 2019, **19**, 6082-6091

22. S. Mandal, C.K. Ghosh, D. Sarkar, U.N. Maiti and K.K. Chattopadhyay, *Sol. state sci*., 2010, **12**, 1803-1808

23. B.P. Singh and R.A. Singh, *New J. Chem*., 2015, **39**, 4494-4507

24. L.S. Cavalcante, F.M.C. Batista, M.A.P. Almeida, A.C. Rabelo, I.C. Nogueira, N.C. Batista, J.A. Varela, M.R.M.C. Santos, E. Longo and M.S. Li, *RSC Adv*., 2012, **2**, 6438- 6454

25. G. Li, Y. Tian, Y. Zhao and J. Lin, *Chem. Soc. Rev*., 2015, **44**, 8688-8713

26. T. Shimemura, N. Sawaguchi and M. Sasaki, *J. Ceram Soc. Japan*, 2016, **124**, 938-942

27. P. Dorenbos, *ECS J. Sol. State Sci. Technolo*., 2012, **2**, 3001

28. Y. Zhu, Y. Liang, M. Zhang, M. Tong, G. Li and S. Wang, *RSC Adv*., 2015, **5**, 98350-98360

29. M.V Korzhik, V.B. Pavlenko, T.N. Timoschenko, V.A. Katchanov, A.V. Singovskii, A.N. Annenkov, V.A. Ligun, I.M. Solskii and J.P. Peigneux, *physica status solidi (a)*, 1996, **154**, 779-788

30. E.V. Sokolenko, V.M. Zhukovskii, E.S. Buyanova and Y.A. Krasnobaev, *Inorg. Mater*., 1998, **34**, 499-502

31. B.M., Sinel'nikov, E.V. Sokolenko and V. ZVEKOV, *Inorg Mater*., 1996, **32**, 999-1001

32. A. Lecointre, A. Bessière, A.J.J. Bos, P. Dorenbos, B. Viana and S. Jacquart, *J. Phys. Chem. C*, 2011, **115**, 4217-4227

33. S. Das, C.K. Ghosh, R. Dey and M. Pal, *RSC Adv*., 2016, **6**, 236-244

34. Y. Shi, Y. Wen, M. Que, G. Zhu and Y. Wang, *Dalton Trans*., 2014, **43**, 2418-2423

35. Q. Wang, G. Zhu, Y. Li and Y. Wang, *Opt. Mater*., 2015, **42**, 385-389

36. M. Rai, G. Kaur, S. K. Singha and S. B. Rai, *Dalton Trans*., 2015, **44**, 6184

37. Z. Wang, X. Qiu, W. Xi, M. Tang, J. Liu, H. Jiang and L. Sun, *Sen. Act. B Chem.*, 2021, **345**, 130417.

38. Z. Wang, X. Qiu, W. Xi, M. Tang, J. Liu, H. Jiang and L. Sun, *Sen. Act. B Chem.*, 2023, **376**, 132936

39. C.N. Wang, M.X. Peng, L.J. Yue, X.Y. Yang and Y.H. Zhang, *Sens. Act. A Phys*., 2022, **342**, 113650

Chapter 4

An *ab initio* modelling for pristine and defects induced emissions from $NaCe(WO_4)_2$: a potential material for solid state lighting application

1. Introduction

During last few years, increasing demand of rare earth (RE) based optical materials have attracted researchers as they exhibit wide range of applications in the field of display systems, solid-state laser, thermometry, optoelectronic devices, optical fibers, scintillators etc., owing to their robust 4f – 5d transitions [1]. Among various RE consisting optical materials, alkaline rare-earth double tungstates with generic formula $ALn(WO_4)_2$ (A^+ = Na^+, K^+ etc. Ln^{3+} = Y^{3+}, Ce^{3+}, Gd^{3+}, Eu^{3+} etc.) have shown their candidature as promising material due to good physical and chemical characteristics, high quantum yield etc. [2]. In contrast to conventional oxide, fluoride luminescent materials such as organic fluorescent dyes, oxide semiconductors, $ALn(WO_4)_2$ possesses low photobleaching, narrow emission bands etc. Mostly, $ALn(WO_4)_2$ crystalizes in the tetragonal scheelite structure where W atoms are surrounded by four O atoms and A/Ln atoms are eight coordinated, each A/LnO_8 polyhedron shares with eight adjacent WO_4 tetrahedra making [⋯O – W – O⋯] – [⋯O – A/Ln – O⋯] bonds. It has been examined earlier that the versatility of the crystalline field due to statistically distributed A and Ln makes 4f – 5d transitions very unique with characteristic features of large stoke shift, sharp and abundant emission colours, broad near-UV charge transfer band (CTB) etc. [3]. It has been observed that $ALn(WO_4)_2$ possesses wide range of structural versatility

due to cationic distribution that primarily depends on synthesis condition. In consequence, it has been noted that the variation in cationic distribution occurs at short range modifying electronic band structure of tungstates; hence it has a great influence on luminescence properties [3]. In this context, it may be stated that several investigations have been carried out to investigate these phenomenon and modelled it. As an example, Arakcheeva *et al.* have proposed a structural model on the basis of clustering of rare-earth ions [4] and the study yields that the variation of composition in $A_xLn_{(2-x)/3}WO_4$ leads a modulated structure with respect to fully ordered distributed structure involving Ln^{3+} cations resulting unusual luminescence property as lattice symmetry of the system gets changed in modulated structures.

In this context, it may be stated that though several investigations have been carried out on $ALn(WO_4)_2$, but very less efforts had been given to understand various optoelectronic properties of $NaCe(WO_4)_2$. However, to the best of our knowledge, only three reports are available on cerium-based double tungstate. For instance, variation of optical absorption with respect to morphology has been studied by Dirany *et al.* [5], while Shimemura *et al.* have compared optical emissions from $ACe(WO_4)_2$ with A = Na, Li and K [6]. Very recently, noncentrosymmetry in the local structure of $NaCe(WO_4)_2$, synthesized using template free solvothermal method, has been examined by Munirathnappa *et al.* and a correlation between distorted noncentrosymmetric structure with optical nonlinear second harmonic generation has been established [7]. However, spectral properties of the Ce^{3+} were not clear by either study. As we know that surfactant plays a major role in crystal growth and distortion of the unit cell depending on its interaction with functional groups of the reactant and use of different surfactant makes easy technique to tune distortion and related optical emission [8]. As there exists no report on cetyltrimethyl ammonium bromide (CTAB) assisted hydrothermal synthesis of $NaCe(WO_4)_2$, hence we have adopted CTAB in order to investigate its role on distortion and optical

emissions from $NaCe(WO_4)_2$. Herein, it may be stated that CTAB tunes CeO_7, CeO_6 those act as active luminescent centers for blue and green emissions respectively. A rigorous analysis of the experimental results and *ab initio* band structure calculation demonstrate that the $5d_z^2$, $5d_{yz}$ and $5d_{xz}$ orbitals of Ce lead to the 5d – 4f transition within CeO_7 and CeO_6 resulting blue and green emissions from $NaCe(WO_4)_2$.

2. Experimental section

2.1 Materials and synthesis

Presently, $NaCe(WO_4)_2$ (NCWO) has been synthesized by a facile hydrothermal method, followed by calcination. Briefly, 0.17 mmol (0.074 g) of cerium nitrate [$Ce(NO_3)_3.6H_2O$, Merck, Germany] and 0.17 (0.062 g) and 0.34 mmol (0.124 g) cetyltrimethyl ammonium bromide [CTAB, Merck, Germany] as surfactant were dissolved in 60 ml of DI water. After continuous magnetic stirring at room temperature for 3 hours, solution became milky white which was added dropwise with another 20 ml aqueous solution containing 0.34 mmol (0.112 g) of sodium tungstate [$Na_2WO_4.H_2O$, Merck, Germany]. After through mixing of the above two solutions for 30 minutes, final mixture turned in pale green colour which was transferred into the Teflon autoclave for hydrothermal treatment. After 20 hours of reaction at 160^{o}C, followed by cooling down at room temperature, centrifugation and washing with DI water and ethanol, final product was obtained after calcination at 800^{o}C for 5 hours. Previous literature reports reveal the organization of [CeO_8], [WO_4] clusters depending on experimental variables such as temperature, surfactant ratio, reaction time etc. may lead to the formation or reduction of structural defects (oxygen vacancies, distortion of the bonds, stress, strain on the crystalline lattice) those in consequence lead to various tuneable properties [9]. Hence, to investigate the role of CTAB on optical emissions of NCWO, we have synthesized at two

$Ce(NO_3)_3.6H_2O$: CTAB ratio (1:1 and 1:2) and respective samples were nomenclatured as $NCWO_{1:1}$ and $NCWO_{1:2}$ respectively.

2.2 Characterizations

Phase purity and crystal structure of the as-prepared samples were investigated by X-ray diffraction (XRD), collected on Rigaku Ultima III, Japan powder diffractometer, equipped with CuK_α radiation (λ = 1.5404 Å). Rietveld refinement was carried out by least-square fitting method to obtain structural and microstructural refinement parameters on MAUD platform. Experimental profiles were fitted with most suitable pseudo-Voigt analytical function with asymmetry, while background of each pattern was fitted with fourth order polynomial function. Morphology of the as prepared samples was analysed by field emission scanning electron microscope (FESEM; Hitachi S4800, operated at 5 kV). Raman measurements were carried out on alpha 300, Wintec with a 530 nm laser (power 3 mW and spot size: 2 μm), while infrared spectra were taken on IR Prestige in the range between 400 and 4000 cm^{-1}. The X-ray photoelectron spectra were collected using the PHI Versa Probe III Scanning XPS Microprobe with Al Kα source. Band gap of the as-prepared samples was determined from UV-Vis absorption spectra, taken on UV-Vis spectrophotometer (V – 630, JACSO), while photoluminescence emission spectra were recorded on FP-8300, JASCO having 100W Xe lamp at room temperature.

2.3: Band structure calculation using ab initio density functional theory

We had calculated spin polarized electronic band structure, total density of state (TDOS), and projected density state of each atom. Herein, we had used plane-wave pseudo potential (PAW) method as implemented in VASP simulation package and had adopted Perdew-Bruke-Ernzerh of (PBE) exchange correlation

ultra-soft potentials. For this calculation we took valence electron of Na atom ($1s^2\ 2s^2\ 2p^6\ 3s^1$), Ce atom ($5s^2\ 5p^6\ 4f^1\ 5d^1\ 6s^2$), W atom ($5p^6\ 6s^2\ 5d^{10}$), O atom ($2s^2\ 2p^4$). At first the structure with minimum single point ground state energy using 4 × 4 × 4 Monkhorst – Pack k point's supercell structure were optimized and for band structure calculation (Γ to X, X to H_1, H_1 to C, C to H, H to Y, Y to Γ) symmetry point were taken. A plane wave cut off energy (520 eV) was placed after checking the converging energy from 220 to 620 eV. Hellmann-Feynman forces applied on each atom were 0.01 eV/Å, while maximum displacement of each atom and stress were fixed at 5×10^{-4} Å and 0.02 GPa respectively. For high accuracy converging of this calculation, EDIFF and force EDIFG were set to 10^{-6} eV and $<10^{-3}$ eV/Å.

3. Result and discussion

3.1 Phase and local structure analyses of the samples

X-ray diffraction pattern (shown in Figure 1(a) and (b)) of $NCWO_{1:1}$ and $NCWO_{1:2}$ can readily be indexed with crystalline, structurally long-range ordered tetragonal β phase of NCWO (space group $I4_1/a$, ICSD card: 00-050-0348, [10]. Herein, absence of any peak other than β-NCWO confirms phase purity of the synthesized samples. As diffraction pattern is highly dependent on local environment, thus Rietveld refinements have been carried out to assess short-range ordered local structure of the as-prepared samples. During refinement, atom position, fraction factors, thermal vibration etc. were set free until convergence of χ^2, R_p and R_{wp} reached acceptable ranges [11]. Refinement yields plausible structural parameters e.g. lattice constants, unit cell volume, bond length, bond angles, crystallite size, strain etc. as listed in Table – 1. Most importantly, unit cell (shown in Figure 1(c)) adequately matches well with reported cell structure of scheelite materials indicating reliability of the refinement process. Very briefly, unit cell of NCWO contains statistically distributed Na^+ and Ce^{3+} over 4*b* site, coordinated to eight O^{2-} with two different

bond lengths forming edge shared $(Na/Ce)O_8$ polyhedra which is connected with WO_4 (W occupies 4*a* site) tetrahedron through O^{2-} of 16*f* sites. Herein, 'c'-parameter, unit cell volume and Na/Ce – O bond lengths are higher in $NCWO_{1;1}$ with respect to $NCWO_{1;2}$, whereas Na/Ce-O-W and O-W-O bond angles exhibit opposite trend indicating different levels of order-disorder and/or distortions within $(Na/Ce)O_8$ polyhedra and WO_4 tetrahedral unit [12]. In this regard, degree of tetrahedral distortion (N), given by $N = \frac{\alpha_{1(O-W-O)}}{\alpha_{2(O-W-O)}}$, where $\alpha_{1(O-W-O)}$ and $\alpha_{2(O-W-O)}$ represent two different bond angles, and degree of polyhedral distortion (K), calculated using the relation $K= \frac{d_{1(Na,Ce-O)}}{d_{2(Na,Ce-O)}}$, where $d_{1(Na,Ce-O)}$ and $d_{2(Na,Ce-O)}$ denote two different bond lengths, are ~ 1.054, 1.055 and 1.011, 1.013 for $NCWO_{1:1}$ and $NCWO_{1:2}$ respectively [13]. Higher tetrahedral distortion (> 10^{-3}) with respect to octahedral distortion represents the condition where cooperative tilting of rigid polyhedra starts to break [14]; hence, our samples correspondence highly distorted structure. Presently, we have observed decrease of c/a ratio which according to Li *et al.* indicates the influence of dipole – dipole interactions on short-range order due to charge entrapment, whereas variability of bond lengths, bond angles can be assigned to distortion, specifically assumed to be oxygen vacancies [15]. Hence, it might be stated that our samples have oxygen vacancies those may entrap charge carriers. As radius of oxygen vacancy is smaller than that of oxygen ion, hence decrease of c/a ratio is highly consistent with our results. In addition, it can also be stated that electrical charge neutrality of oxygen deficient sample should be maintained by the free carriers: $0 \rightarrow Ce_{Na}^{m\bullet} + V_O^{n\bullet}$ i.e. antisite defects of more occupancy of Ce at 4*b* sites and it would be more in sample having more oxygen vacancies [16].

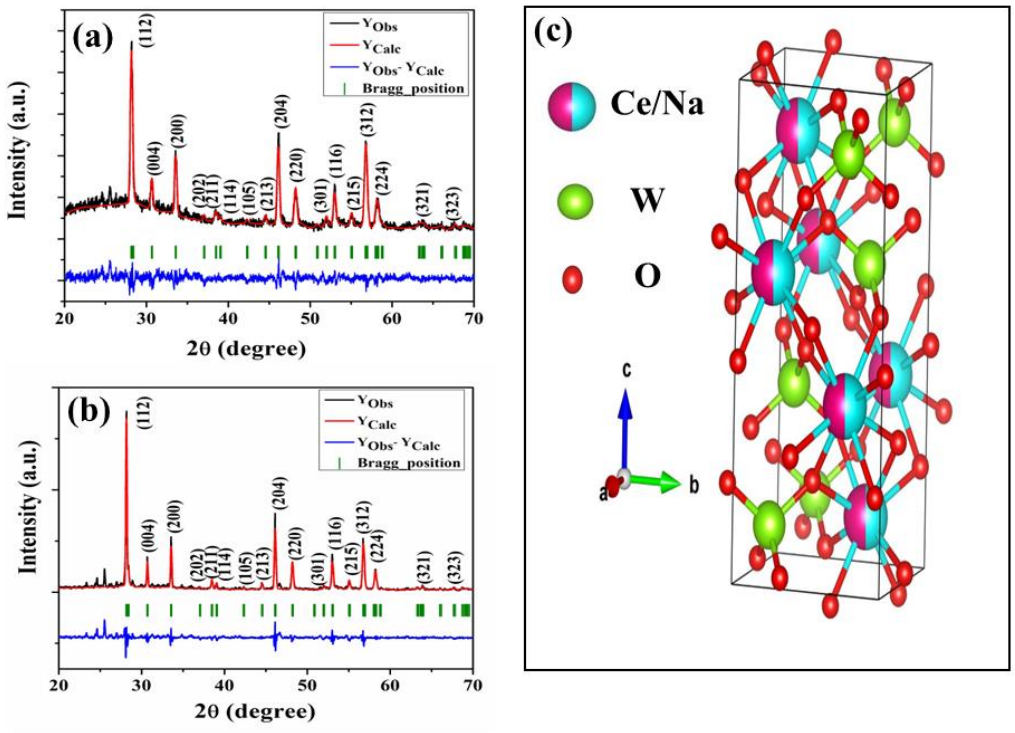

Figure 1: XRD patterns of the $NaCe(WO_4)_2$ samples (a) $NCWO_{1:1}$ and (b) $NCWO_{1:2}$, (c) Tetragonal unit cell's structure of the $NaCe(WO_4)_2$ nanostructures.

Table 1: Refined structural parameters and the reliability factors from Rietveld refinement

Properties		$NCWO_{1:1}$	$NCWO_{1:2}$
Lattice parameter (in A^0) (errors)	a = b	5.338 (0.0005)	5.338 (0.0002)
	c	11.662 (0.0001)	11.628 (0.0006)
Unit cell volume $(A^0)^3$		332.41 (0.002)	331.42 (0.009)
Bond length (in A^0) (errors)	Na/Ce-O	2.513 (0.0006)	2.455 (0.0007)
	W-O	1.810 (0.0007)	1.767 (0.0003)
Bond angle (in degree) (errors)	Na/Ce-O-Na/Ce	103.00 (0.003)	102.20 (0.008)

	Na/Ce-O-W	129.97 (0.005)	137.80 (0.003)
	O-W-O	107.72 (0.001)	108.50 (0.005)
Density of the component (g/cm^3)		5.623	5.640
Strain (in %) (errors)		0.19 (0.006)	0.04 (0.007)
Crystallite size (in nm) (errors)		61.2 (0.03)	63.1 (0.02)
R_p (%)		10.9	15.30
R_{wp} (%)		14.2	20.20
R_{exp} (%)		9.24	9.00
χ^2		2.35	5.03

Morphologies of the as-prepared nanostructures (shown in Figure 2(a) and (b)), as examined by FESEM, are found in agglomerated form (diameter ~ 0.4 – 0.8 μm) and can be ascribed to calcination effect at 800°C. Morphological analyses of the as-prepared samples have been further investigated by transmission electron microscopy (TEM). As shown in Figure 2(c), typical TEM images of $NCWO_{1:1}$ show irregular shape and size of the samples corroborating FESEM studies, while selected area diffraction (SAED) pattern (shown in Figure 2(d)) reveals diffraction spots corresponding to (101), (112), (200), (220) and (224) planes illustrating good crystallinity of the samples. Presently, EDX spectra of the NCWO nanostructures (Shown in APPENDIX-II, figure A1) reveal signals for Na, Ce, W and O in the as prepared samples.

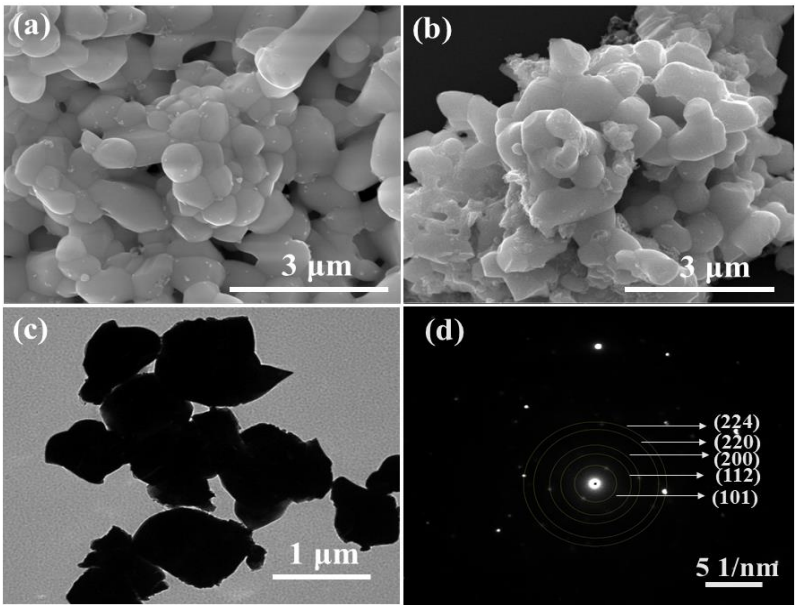

Figure 2: FESEM image of $NaCe(WO_4)_2$ nano/micro structures (a) $NCWO_{1:1}$ and (b) $NCWO_{1:2}$, (c) TEM images and (d) corresponding SAED pattern of NCWO tetragonal structure.

3.2 Investigations of local structure by FTIR, Raman and x-ray photoelectron spectroscopies

As FTIR, Raman spectroscopies give insight about short-range defect due to structural distortion; hence we have adopted these techniques to examine our samples. FTIR spectra consist of four absorption bands in between 500 – 1000 cm^{-1} (shown in Figure A2, APPENDIX-II) and they can readily be assigned to internal vibrations of WO_4 [17,18]. It has been studied that WO_4 either forms regular WO_4 tetrahedra (W^RO_4) with C_1 site symmetry or distorted WO_4 tetrahedra (W^DO_4) due to defects which may be in the form of antisite defect associated oxygen vacancy. In general, vibration (Γ_{Td}) of an isolated W^RO_4 can be represented by

$$\Gamma_{Td} = A_1 + E + 2F_2 \qquad (1)$$

However, its symmetry changes into S_4 in β-NCWO where $\nu_1(A_1)$, $\nu_2(E_1)$, $\nu_3(F_2)$, $\nu_4(F_2)$ modes, one free rotational mode $\nu_{f.r.}(F_1)$ and one

translational mode F_2 are IR active. Among them, antisymmetric stretching (→ O → W → O →) with $\nu_3(F_2)$ and $\nu_4(F_2)$ modes mostly dominates in β-NCWO [19]. In contrast to W^RO_4, Bravais cell of W^DO_4 (space group C_{2h}^6) has four formula units per crystallographic unit cell with following symmetries for the atoms: 2W(C_2), 4W(C_1), 4Ce(C_1) and 24O(C_1) [20]. Hence, vibrational modes get splitted due to lower site symmetry of W^DO_4. As per bond length – stretching frequency correlation, prescribed by Hardcastle *et al.,* two distinct bands at 917 and 966 cm^{-1} are assigned to $\nu_1(A_1)$ vibrational mode of W^DO_4 and W^RO_4 respectively [21]. Two bands in between 778 – 910 and 660 – 717 cm^{-1} are ascribed to $\nu_3(F_2)$ and $\nu_4(F_2)$ modes of vibration. Herein, careful deconvolution (shown in Figure 3) of these bands reveals three peaks (c.a. 668, 680 and 695 cm^{-1} and 810, 850 and 870 cm^{-1}). Third peaks of both bands are assigned to W^RO_4 tetrahedron, while first two peaks correspond to stretching vibration of (→ O → W(C_1) → O →) and (→ O → W(C_2) → O →) of W^DO_4 tetrahedra [22]. Similarly, two deconvoluted peaks at 740 and 760 cm^{-1} are attributed to $\nu_2(E)$ mode of W^DO_4 and W^RO_4 clusters (shown in Figure 3). Herein, weighted percentage of W^DO_4 is examined to be ~ 24 and 38% in $NCWO_{1:1}$ and $NCWO_{1:2}$ respectively indicating that $NCWO_{1:2}$ exhibits more distortion.

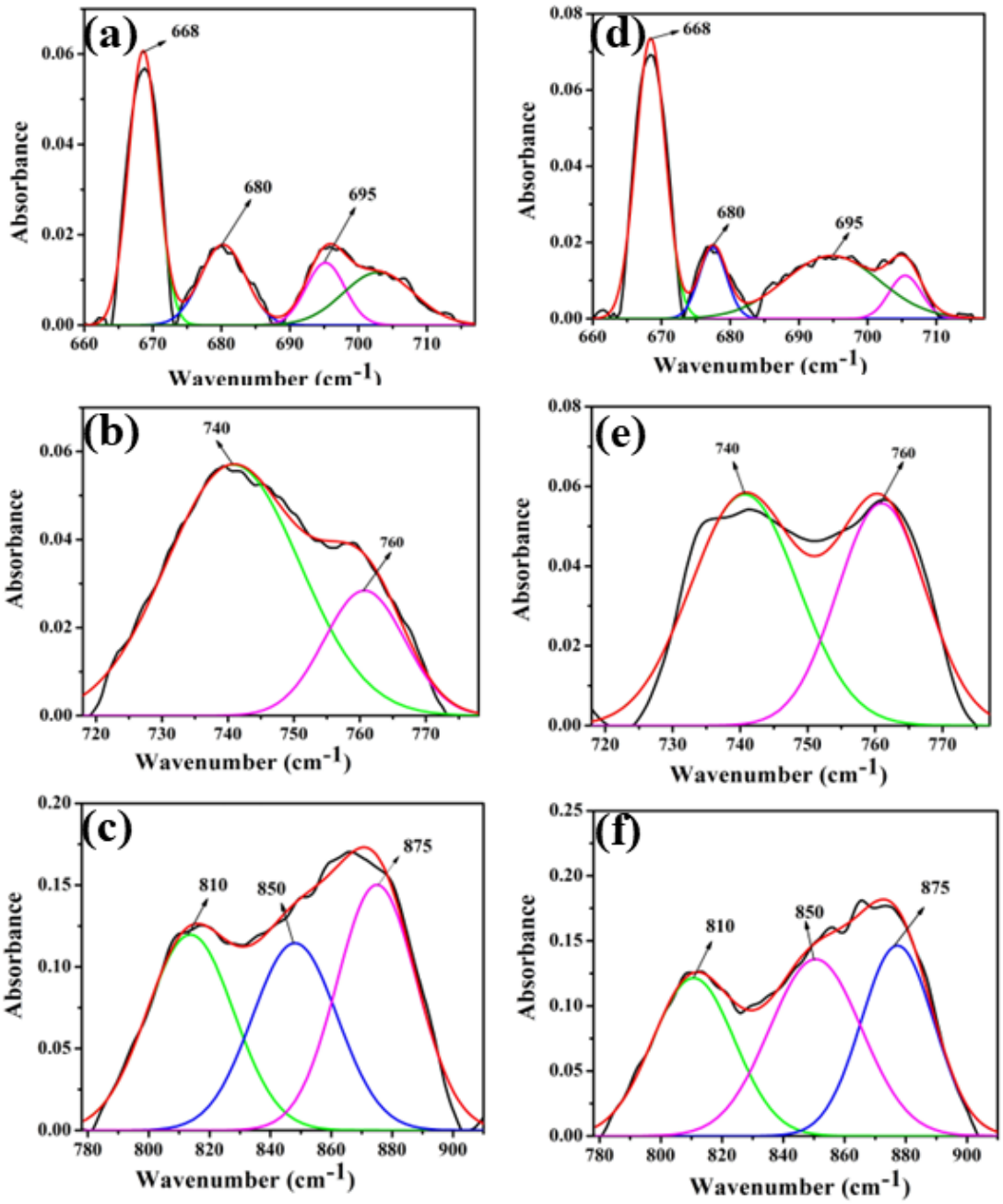

Figure 3: (a) Deconvoluted FTIR bands 660 – 717, 718-777 and 778 – 910 cm^{-1} of $NCWO_{1:1}$ (a, b, c) and $NCWO_{1:2}$ (d, e, f) respectively.

The Raman spectra show a sharp peak at 475 cm^{-1} and a broad band between 225 – 455 cm^{-1} (presented in Figure 4) owing to varied vibrational coupling within W^DO_4 and W^RO_4 [22]. In addition to above bands, $NCWO_{1:1}$ exhibits two more segment in between 650 – 870 and 870 – 980 cm^{-1} and can be explained as

follows: likewise other scheelites, Raman active modes of β-NCWO at Γ-point can be written as

$$\Gamma = 3A_g + 5B_g + 5E_g \qquad (2)$$

where A_g, B_g modes are non-degenerate and E_g is doubly degenerate corresponding to external and internal vibrations of WO_4 clusters [23, 24]. Herein, the dominating sharp peak directing the Raman active external mode of CeO_8 polyhedra matches well with previous report [25], while bands are designated as internal bending of WO_4 tetrahedra. A careful analysis of the band yields two peaks at 340 and 388 cm^{-1} in $NCWO_{1:1}$ and they can readily be ascribed to symmetric bending modes ($\nu_3(A_g)$) of O – W – O and antisymmetric bending modes $\nu_4(B_g)$ of O – W – O [26]. These peaks get blue shifted slightly and can be explained as follows: $\nu_3(A_g)$ and $\nu_4(B_g)$ significantly depend on the covalent interactions between WO_4 – CeO_8 [27], herein antisite defects in CeO_8 polyhedra increases covalence of the WO_4 – CeO_8 bonds which might be explained on the basis of electronegativity of the respective elements. Therefore, observed blue shift can specifically be attributed to the presence of more antisite defects in $NCWO_{1:2}$. Two Raman peaks at 805 and 918 cm^{-1} in $NCWO_{1:1}$ are attributed to antisymmetric $\nu_3(B_g)$ stretching mode (O → W → O) and symmetric stretching $\nu_1(A_g)$ mode (O ← W → O) within WO_4 tetrahedra [28, 29]. As intensity of the Raman peak significantly depends on symmetry of the crystal structure, hence much lower intensity of Raman peaks in $NCWO_{1:2}$ might be attributed with breaking of symmetry due to more oxygen vacancy associated with antisite defects; hence the results reveal more weighted percentage of W^DO_4 in $NCWO_{1:2}$ [30, 31].

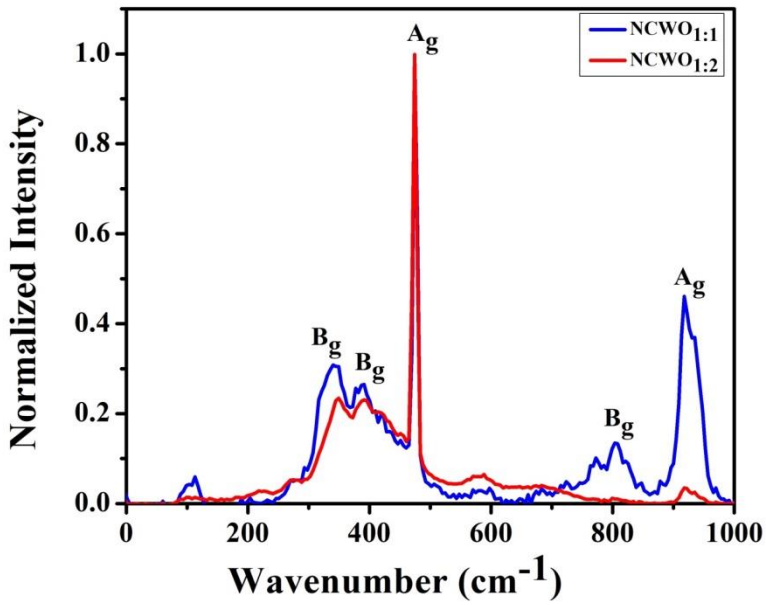

Figure 4: Raman spectra of $NCWO_{1:1}$ and $NCWO_{1:2}$.

In order to gain more insight about distortion induced changes in chemical bonding characteristics of the elements, we have employed XPS to examine valance states of constituting elements and valence band edges, as these two parameters significantly depend on local electronic environment. Herein, obtained data of all elements were corrected with reference to C1s appearing due to adventitious C, formed during atmospheric exposure and exhibits binding energy ~ 284.6 eV. The survey scan representing core binding energies of Na, Ce, W and O are represented (Figure A3, APPENDIX-II) in the range 0 – 1100 eV for both samples, while high resolution spectra of W, Ce and O are depicted in Figure 5 and Figure 6. As shown in Figure 5(a) and (b), XPS of W consists of two asymmetric peaks at 35.1 and 37.0 eV corresponding to spin-orbit splitted $4f_{7/2}$ and $4f_{5/2}$ orbitals of W^{6+} [32], while their deconvolution leads four peaks c.a. W_a, W_b, W_c and W_d having binding energy at 34.6, 35.6, 37.0 and 37.8 eV respectively. Presently, W_a and W_c are referred to $4f_{7/2}$ and $4f_{5/2}$ states of W^DO_4 tetrahedra [33], while W_b and W_d correspondence to $4f_{7/2}$ and $4f_{5/2}$ states of W^RO_4. Since W – O bond is highly ionic due to significant difference in electronegativity of the constituent elements; hence charge mostly resides on O.

Herein, oxygen vacancy enhances effective charge on W causing higher electron – electron repulsion on W, thus binding energies of $4f_{7/2}$ and $4f_{5/2}$ states get reduced. Analyses of the area under the peaks reveals higher weighted percentage of W^DO_4 in $NCWO_{1:2}$ (~ 38%) with reference to $NCWO_{1:1}$ (~ 24%), thus the observation highly corroborates with previous studies. In addition, it is visible that the energy difference between $4f_{7/2}$ and $4f_{5/2}$ states (~ 2.4 and 2.2 eV for W^RO_4 and W^DO_4) is more in $NCWO_{1:1}$ in comparison with $NCWO_{1:2}$ (~ 2.2 and 2.1 eV for W^RO_4 and W^DO_4) and it might be attributed to local electric field due to oxygen vacancies. As represented in Figure 5(c) and (d), XPS of Ce 3d consists of two significant asymmetric peaks in the range 877 – 891 and 895 – 910 eV which can be ascribed to spin-orbit splitted $3d_{5/2}$ and $3d_{3/2}$ orbitals of Ce^{3+} [34]. Herein, further deconvolution of $3d_{5/2}$ peak reveals three peaks c.a. Ce_a, Ce_b and $Ce_c$with binding energy 881.8, 883.3 and 885.8 eV respectively and they can readily be attributed with Ce of three different polyhedron configuration. Briefly, Ce_c is assigned for regular CeO_8, while Ce_b and Ce_a are assigned for CeO_7 and CeO_6 i.e. distorted CeO_8 polyhedra with one oxygen vacancy (V_O) and two oxygen vacancies ($2V_O$) respectively. In this context, it may be stated that distorted CeO_8 polyhedra having one W^DO_4 in its neighbourhood is referred CeO_7, while CeO_6 denotes distorted CeO_8 polyhedra which is surrounded by two W^DO_4 subunits. Due to low electronegativity difference between Ce and O, Ce – O bond is highly covalent; hence binding energies of highly localized $3d_{5/2}$ and $3d_{3/2}$ orbitals significantly depend on Ce – O hybridization. Herein, oxygen vacancy would reduce Ce – O bond length which in consequence would increase the electron – electron repulsion on Ce site resulting decrease of the binding energies of $3d_{5/2}$ and $3d_{3/2}$ orbitals [35]. A careful analyses illustrates that the area under Ce_a remains same for both samples (~ 20 %), while significant increase (27% to 45%) of Ce_b is associated with decrease of Ce_c (53 to 35%), hence it may be stated CeO_6 concentration remains same for both samples, while CeO_8 concentration is high in $NCWO_{1:2}$.

XPS of O 1s as shown in Figure 6(a) and (b) matches well with that of O^{2-}. Herein, peaks are found to be highly symmetric indicating neither surface adsorbed nor interstitial O are present in the samples [26]. In addition, we have also found Ce : Na ~ 1.00 : 0.91 and 1.00 : 0.74 which confirms vacancy induced antisite defects as described earlier and their respective compositions are tentatively found to be $Na_{0.91}Ce(W_{0.98}O_{3.94})_2$ and $Na_{0.74}Ce(W_{0.98}O_{3.88})_2$. Herein, valence band energy are ~ 2.54 and 2.68 eV for $NCWO_{1:1}$ and $NCWO_{1:2}$ respectively (shown in Figure 6(c) and (d)) and this change might be ascribed to higher O 2p – W 5d bonding energy due to V_O (discussed later).

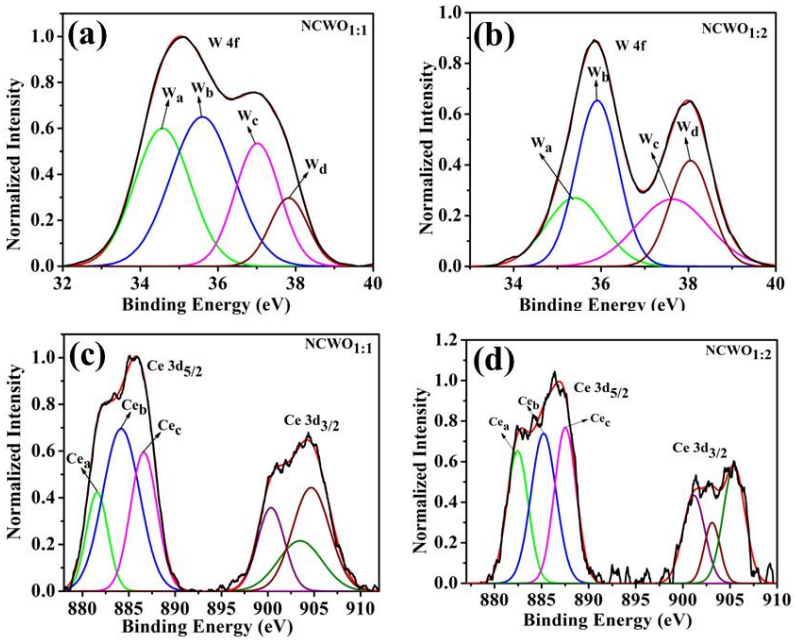

Figure 5: (a, b) XPS W 4f and (c, d) XPS Ce 3d core level spectra of $NCWO_{1:1}$ and $NCWO_{1:2}$ respectively.

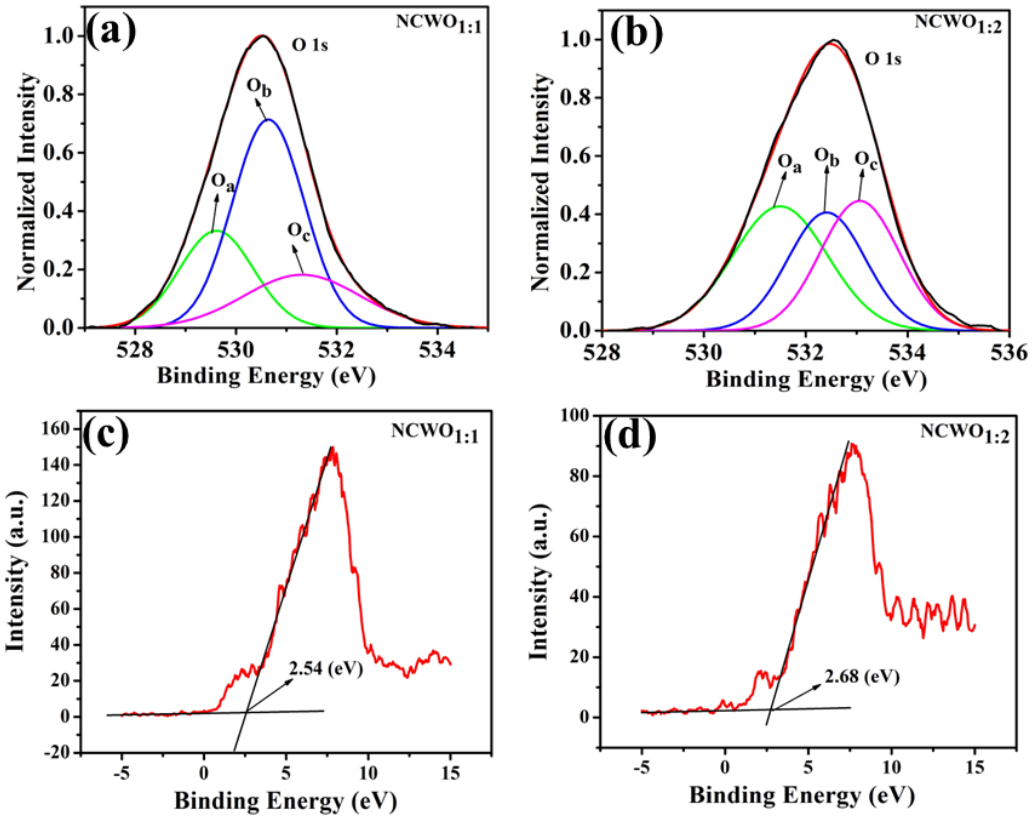

Figure 6: (a, b) XPS O1s core level spectra and (c, d) valence band edge of $NCWO_{1:1}$ and $NCWO_{1:2}$ respectively.

3.3 Optical properties of the as-prepared $NaCe(WO_4)_2$ samples by UV-Vis, steady state and time – dependent photoluminescence spectroscopy

Optical band gap (E_g) are calculated to be 3.28 and 3.25 eV for $NCWO_{1:1}$ and $NCWO_{1:2}$ respectively (shown in Figure A4, APPENDIX-II) from UV – Vis absorption spectra, while decrease is attributed to blue shift of the valance band as identified by XPS. Briefly, it can be explained as follows: as our band structure calculation using DFT (discussed later) reveals that valence band (VB) of NCWO comprises of O 2p – W 5d hybridization, while W – 5d, Ce – 4f and O – 2p contribute to conduction band (CB), hence V_O significantly reduce O 2p – W 5d overlap (discussed later) and consequently bonding state gets blue

shifted causing reduction of E_g [36, 37]; thus more weighted percentage of W^DO_4 clusters is ascertained for lower E_g in $NCWO_{1:2}$.

Luminescence properties of $NCWO_{1:1}$ and $NCWO_{1:2}$, recorded in visible region upon excitation at 380 nm, are shown in Figure 7 (a) and (b) respectively. For both samples, emission spectrum consist of one intense violet peak at 431 nm (~ 23,202 cm^{-1}) and two peaks in blue region at 451 (blue I, ~ 22,173 cm^{-1}) and 485 (blue II, ~ 20,618 cm^{-1}) nm and another peak in green region at 520 nm (~ 19,231 cm^{-1}) due to various electronic transitions. Usually, emissions from scheelites are assigned with lanthanides, however understanding of the emission is still very challenging as several factors like surrounding crystal field, symmetry, anion polarizability, covalence of the host crystal etc. significantly influence the 5d – 4f transition of Ce^{3+} [38]. As an example, two emission peaks of $LiCe(WO_4)_2$, measured at 390 and 412 nm, were attributed to $^5D_0 - {}^2F_{5/2}$ and $^5D_0 - {}^2F_{7/2}$ transitions within Ce^{3+} ions [39], while Dorenbos *et al.* had observed those emissions at 451 and 485 nm [40]. Presently, we have utilized equation (3), given by van Uitert *et al.* [41], to calculate emission wavelength (λ in nm) due to 5d → 4f transition in Ce^{3+} within regular CeO_8 polyhedron:

$$\frac{1}{\lambda} = \frac{Q^*}{hc}\left[1 - \left(\frac{V}{4}\right)^{\frac{1}{V}} 10^{\frac{-(nrE_a)}{80}}\right] \qquad (3)$$

where, Q*, V, 'n', E_a and 'r' represent the energy of 5d band edge of free Ce^{3+} ion (= 200 nm), valance of the Ce^{3+}, number of anions in the immediate shell around Ce^{3+}, electron affinity of the atoms forming anions (~ 2.27 eV), and r is the radius (= 0.99Å) of the host cation replaced by the Ce^{3+} ion. Herein, we have found λ = 435 nm which highly corroborates with our experimental violet emission at 431 nm. As per previous studies by various researchers including us, we know that oxygen vacancy creates defect states within band gap which in consequence acts as luminescence centers. This oxygen vacancy is found to play a significant role in emission characteristics of scheelite materials also. As an example, origin of green emission was assigned to WO_3 centers by Korzhik

et al. [42], while Sokolenko *et al.* had ascribed green-red emission with $WO_3 \bullet \ddot{V}_O$ oxygen-deficient complexes [43]. In this regard. Sienelnikov *et al.* had suggested that W^DO_4 facilitates formation of V_O which in consequence acts as green emission center [44]. Since XPS study illustrates the formation of CeO_7 and CeO_6, hence a similar calculation using equation (3) illustrates emissions at 472.9 and 520.4 nm from CeO_7 and CeO_6 respectively and most importantly they highly corroborate with wavelengths of blue II and green emissions (schematically represented in Figure 8). Herein, origin of these emissions might be attributed to the shift of the centroids of d-orbitals ($\varepsilon_{cfs}\ (1,3+,A)$) in CeO_7 and CeO_6. In this regard, we have calculated centroid shift $\varepsilon_{cfs}\ (1,3+,A)$, defined as $\varepsilon_{cfs}\ (1,3+,A)$ = 6.35 – $E^C(1,3+,A)$ eV, on the basis of vacuum referred binding energy diagram according to Dorenbos using the following relation [45]:

$$\varepsilon_{cfs}\ (1,3+,A) = \beta R_{av}^{-2} \qquad (4)$$

where, β = 1.35 × 10^9 pm^2 cm^{-1} for Ce^{3+} and $R_{av} = \frac{1}{N}\sum_{i=1}^{N}(R_i - 0.6\Delta R)$; R_i denotes individual bond lengths to the N coordinating anions in the un-relaxed lattice. Presently, our calculation yields ε_{cfs} ~ 5.93 and 5.39 eV for CeO_8 and CeO_6, hence it may be inferred that oxygen deficiencies have crucial role on ε_{cfs} which in consequence predominantly determines emission wavelength for 5d → 4f transition in Ce^{3+}. Mechanistically, emissions can be understood as follows: after releasing electrons into the host matrix, V_O and $2V_O$ lead ionized defects states (c.a. $V_O^{\bullet}$ and $2V_O^{\bullet}$) that can be described by Kröger – Vink notation

$$[CeO_8]^x + \left[CeO_7 \bullet V_O^X\right] \rightarrow [CeO_8]' + [CeO_7 \bullet V_O^{\bullet}] \qquad 5(a)$$

$$[CeO_8]^x + \left[CeO_6 \bullet 2V_O^X\right] \rightarrow [CeO_8]'' + [CeO_6 \bullet 2V_O^{\bullet}] \qquad 5(b)$$

where, $[CeO_8]'$ and $[CeO_8]''$ are electron donors, while $[CeO_7 \bullet V_O^{\bullet}]$ and $[CeO_6 \bullet 2V_O^{\bullet}]$ trap electrons and in consequence leads blue II and green emissions. Usually, emission Ce^{3+} possesses doublet character with a separation ~ 2,000 cm^{-1} between $^5D_0 \rightarrow {}^2F_{5/2}$ and $^5D_0 \rightarrow {}^2F_{7/2}$ transitions, however we have

found the difference between violet and blue I emissions ~ 1,029 cm^{-1} indicating that later can't be assigned to $^5D_0 \rightarrow {}^2F_{7/2}$ transition within CeO_8 dodecahedra. In this regard, it is to mention that two different ε_{cfs}s get formed in CeO_6 (discussed later), hence blue I emission is ascertained for other ε_{cfs}, formed within band gap. It has been studied earlier that low radial distribution (~ 38 pm from the nucleus) and filled $5p^6$ and $5s^2$ subshells of [Xe] electron configuration of Ce yield very narrow full width as half maxima (FWHM) for 5d → 4f transition in Ce^{3+}. However, we have obtained much broader FWHM of violet emission indicating significant influence of other orbitals on the transition [46, 47]. As represented in figure 7(c), intensity ratio of blue II and violet emission is noted to be higher in $NCWO_{1:2}$, while that of green emission is same. Hence these variations highly corroborate with previous XPS studies revealing the variation of weighted average of CeO_7 and CeO_6 within our samples.

In order gain more insight, we have measured excitation spectra (monitored emission at 431 nm) that consist of two intense Gaussian sub-bands with the peaks, located at 376 and 386 nm, and one weaker peak at 414 nm (shown in Figure A5, APPENDIX-II) and they can readily be ascribed to different polymorphism of excited state of Ce^{3+} in 4f orbital energy levels. Very briefly, it may be stated that different coordinated environment (c.a. CeO_8, CeO_7 and CeO_6) causes shift of the 5d centroids (nephelauxetic effect as described by equation (4)) and modifies 4f → 5d transition of Ce^{3+} giving three peaks in the excitation spectra [48,49]. In addition, different crystal field causes 5d manifold split of the Ce^{3+} excited states into certain widths leading broad excitation spectrum of Ce^{3+}. Hence, the results indicate presence of three Ce^{3+} centers, while no spectral overlap between excitation and emission spectra is likely to be assigned non-resonating energy transfer process i.e. Ce^{3+} acts as independent excitation centers [50].

The Commission International De I'Eclairage (CIE) coordinate that provides information about color purity of luminating material, has been calculated to be

(0.170, 0.148) and (0.180, 0.169) for sample $NCWO_{1:1}$, $NCWO_{1:2}$ (shown in Figure 7(d)) indicating blue emission from the samples [51]. The variation may be assigned to the presence of different contribution from blue I and blue II emissions to violet emission. Correlated color temperatures (CCT) of the samples are ~ 7854 and 6491K i.e. NCWO can be a potential material for solid state lighting application. Herein, we have calculated colour purity (CP) of our samples using equation (7)

$$CP = \frac{\sqrt{(x-x_i)^2+(y-y_i)^2}}{\sqrt{(x_d-x_i)^2+(y_d-y_i)^2}} \times 100\% \qquad (6)$$

where (x, y) represents the color coordinates; (x_i, y_i) is the illuminant point of the 1931 CIE Standard Source with the colour coordinates of (0.3101, 0.3162) and (x_d, y_d) refers to colour coordinates of the dominant wavelength. Herein, we have found CP ~ 97 and 90% for $NCWO_{1:1}$and $NCWO_{1:2}$ respectively, indicating excellent colour purity which is suitable for LEDs.

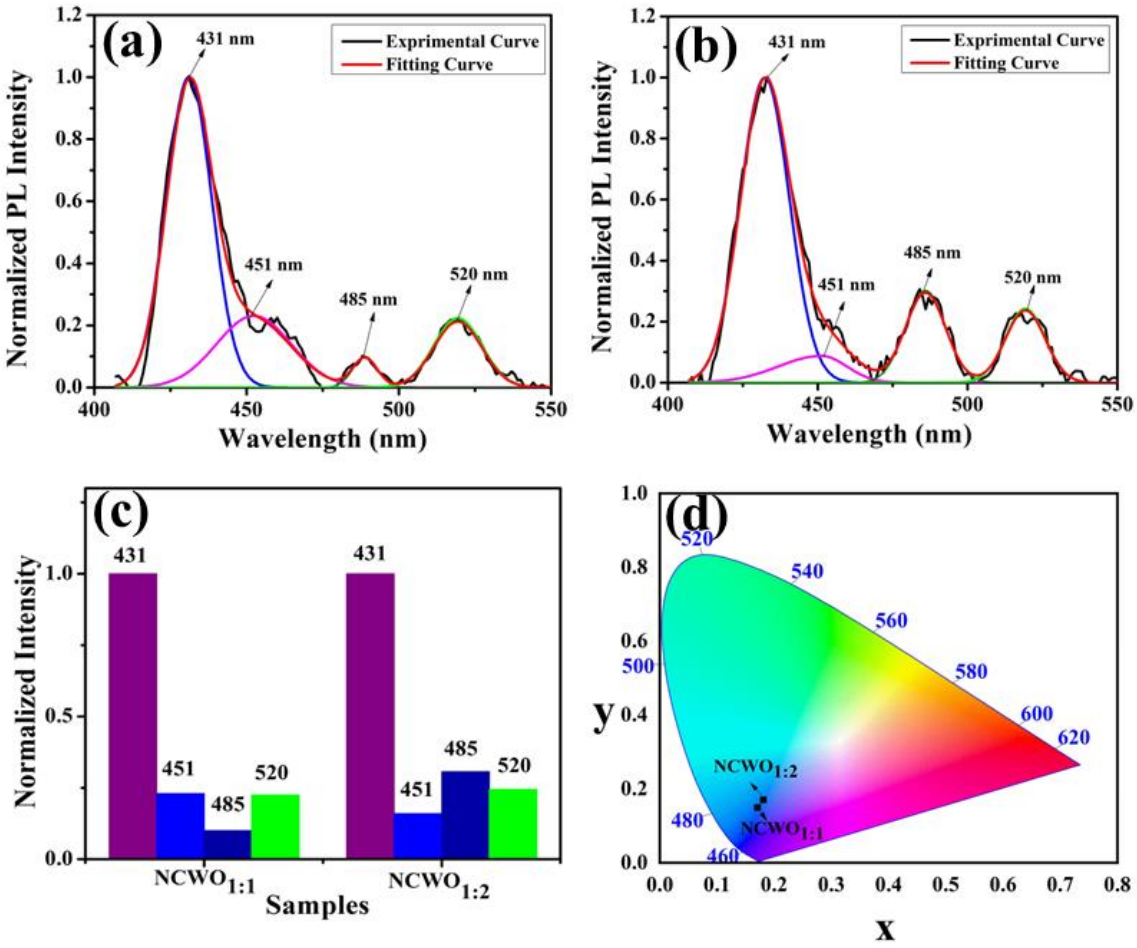

Figure 7: Photoluminescence spectra of (a) $NCWO_{1:1}$ and (b) $NCWO_{1:2}$ respectively. (c) Normalized PL intensity ratio of emission wavelengths (d) The CIE chromaticity diagram of the NCWO.

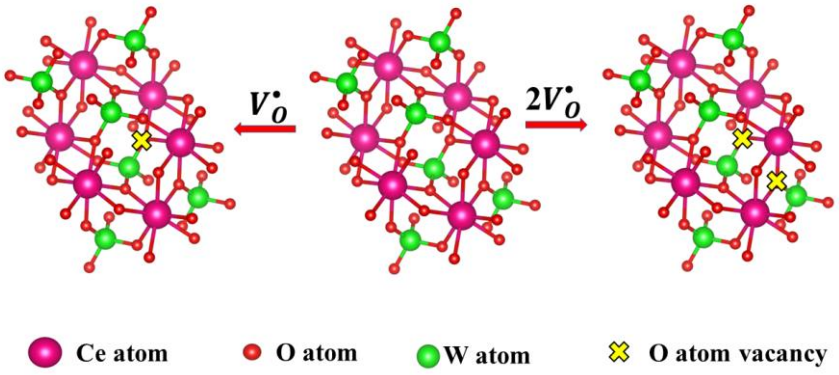

Figure 8: Schematic diagram of oxygen vacancies of CeO_8 polyhedra unit.

3.4 DFT calculation of $NaCe(WO_4)_2$: modelling of distortion induced emissions

To provide a basis for above mentioned interpretation of the luminescence property, we have calculated electronic band structures of pure and vacancy containing NCWO along several high-symmetry points accompanied by its Brillouin zone, total density of states (TDOS) and angular momentum projected partial density of states (PDOS) using ab-initio DFT. In order to simulate CeO_7 and CeO_6 associated on optical transition, we have built the structural distorted model, first by removing one O and two O atoms from unit cell of NCWO.

Prior to band structure calculation, we have optimized the unit cell of NCWO and have obtained a ~ 5.201 Å, c ~ 11.118 Å and Na/Ce – O ~ 2.450 Å and W – O ~ 1.800 Å. These unit cell parameters are very close with experimental results indicating good reliability of our calculation including choice of exchange correlation functions. Herein, top of the valence band maxima (VBM) is set to zero. Figure 9(a) clearly reveals that VBM is located at Γ point, while conduction band minima (CBM) lies along X – H_1 line indicating that NCWO behaves like an indirect band material with E_g ~ 3.42 eV which is higher than experimental E_g. The high curvature at CBM implies low effective electrons mass, while curvature at VBM is relatively low directing comparatively high effective hole mass. Therefore, the electron mobility of NCWO is expected to be high, providing greater scope for electrons to have longer mean free path. In addition, it is also realized that VBM of NCWO is spin unpolarized, whereas CB appears to be spin polarized. Careful analysis of PDOS on Na, Ce, W and O (shown in Figure 9(b) – (f)) illustrates that upper part of valence band (VB) is mostly predominated by O – $2p_x$, $2p_y$ and $2p_z$ orbitals along with minor contributions from Ce – 4f, W – $5d_{xy,}$ $5d_{yz}$, $5d_{zx}$, $5d_z^2$ and $5d_x^2$-$_y^2$ and Na – 3s orbitals that leads very low curvature. Lower part of VB is composed of O – $2p_x$, $2p_y$ and $2p_z$ orbitals mixing predominantly with W – $5d_{xy,}$ $5d_{yz}$, $5d_{zx}$, $5d_z^2$

and $5d_x^2$-$_y^2$ orbitals. For CBM, it is primarily occupied by Ce – $4f_{xyz}$, $4f_{yz}^2$, $4f_z^3$, $4f_{zx}^2$, $4f_{xz}^2$, $4f_x^3$ and $4f_y^3{}_x^2$ orbitals, hybridized with some O – $2p_x$, $2p_y$ and $2p_z$ and Ce 4f orbitals that gives higher curvature. Hence, during photo absorption process, the photo generated electrons can transfer from O atom to Ce due to internal field, created within CeO_8 dodecahedra. This could reduce electron – hole recombination rate endowing high radiative lifetime, hence NCWO can be a potential solid state lighting material. In contrast to WO_4 influenced of both VB and CB of $NaGd(MoO_4)_2$ [52], herein VB is mostly affected by WO_4 tetrahedra, whereas CB is sensitive to CeO_8 polyhedra as well as WO_4 tetrahedra.

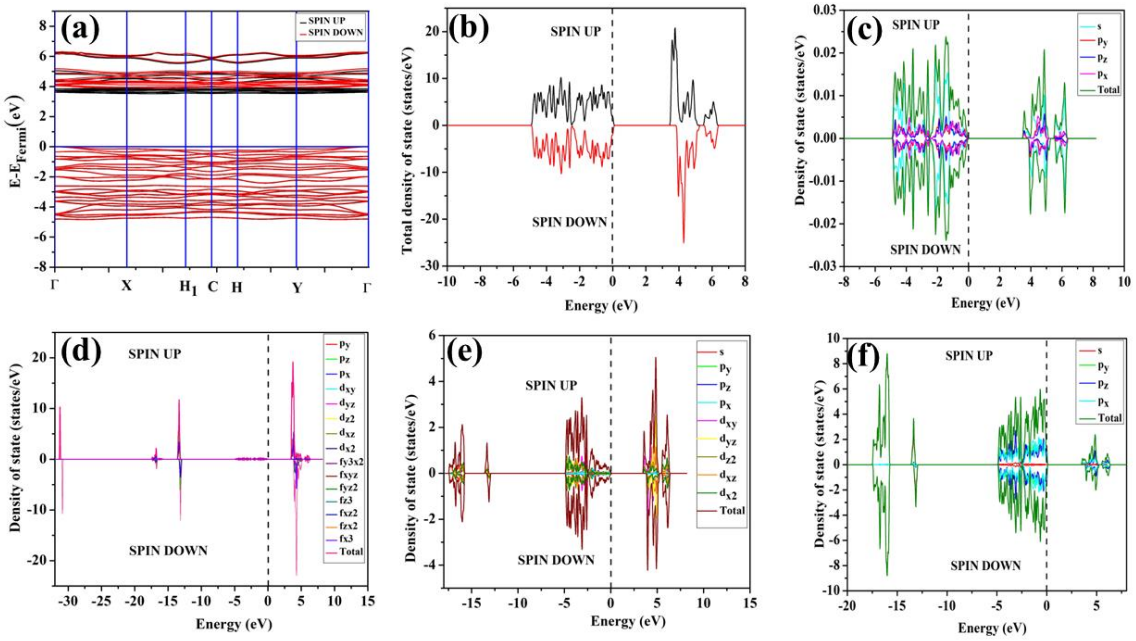

Figure 9: (a) Band structure and (b) spin polarised TDOS and PDOS of (c) Na, (d) Ce, (e) W and (f) O of NCWO.

Band structures, TDOS and PDOS of $V_O^{\bullet}$ and $2V_O^{\bullet}$ containing NCWO samples, designated as NCWO – $V_O^{\bullet}$ and NCWO – $2V_O^{\bullet}$, are represented in Figure 10 and 11 respectively. It is clear from figures (Figure 10(a) and 11(a)) that VBM of

NCWO – $V_O^{\bullet}$ remains unchanged at Γ-point, while that of NCWO – $2V_O^{\bullet}$ gets shifted into C-point. Similarly, respective CBMs are found along Γ – X line and at Γ-point. E_g is found to be decreasing monotonically in both samples (~ 3.4 and 3.36 eV respectively) with respect to NCWO, hence our result indicates that $NCWO_{1:2}$ exhibits more oxygen vacancies in comparison with $NCWO_{1:1}$. Herein TDOS (Figure 10(b) and 11(b)) and PDOS (Shown in Figure 10(c) – (f) and Figure 11(c) – (f)) calculations illustrate that VB width significantly gets increased in NCWO – $2V_O^{\bullet}$ that might be ascribed to delocalized O 2p orbitals. In addition, it can also be noted that the curvatures of VBM and CBM gets significantly enhanced in NCWO – $V_O^{\bullet}$ and NCWO – $2V_O^{\bullet}$ that may be attributed to increase of the orbitals overlapping. Hence, it may be inferred that carrier mobility can be tuned by oxygen vacancy defects. Most importantly, one defect state has been found in NCWO – $V_O^{\bullet}$ at 2.1 eV above VBM, while NCWO – $2V_O^{\bullet}$ exhibits two defect states at 1.42 and 3.01 eV above VBM. A careful analysis of TDOS and PDOS reveal that among all 5d orbitals, mostly Ce $5d_{xy}$ and $5d_z^2$ orbitals contribute to these defect states of NCWO – $V_O^{\bullet}$, while contribution from other Ce 4f orbitals, O 2p and W 5d orbitals have been observed. Herein, our calculations reveal that defect states at 1.42 and 3.01 eV are mostly contributed by Ce $5d_z^2$ and $5d_{yz,}$ $5d_{xz}$ orbitals respectively among other Ce 5d orbitals. Hence, we may ascribe blue II emission Ce $5d_{xy}$, $5d_z^2 \rightarrow$ 4f transitions within distorted CeO_7 polyhedra; while blue I and green emissions is assigned to Ce $5d_z^2 \rightarrow$ 4f and Ce $5d_{yz,}$ $5d_{xz} \rightarrow$ 4f transitions in CeO_6 polyhedra as schematically shown in Figure 12.

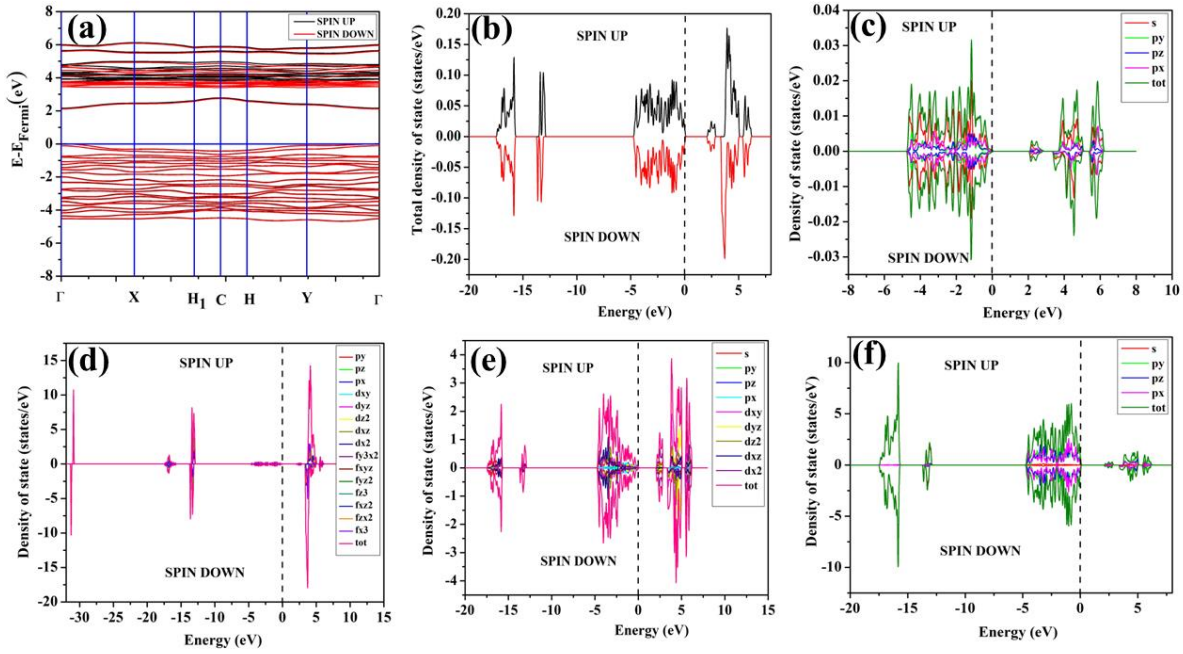

Figure 10: (a) Band structure and (b) spin polarised TDOS and PDOS of (c) Na, (d) Ce, (e) W and (f) O of NCWO – $V_O^{\bullet}$.

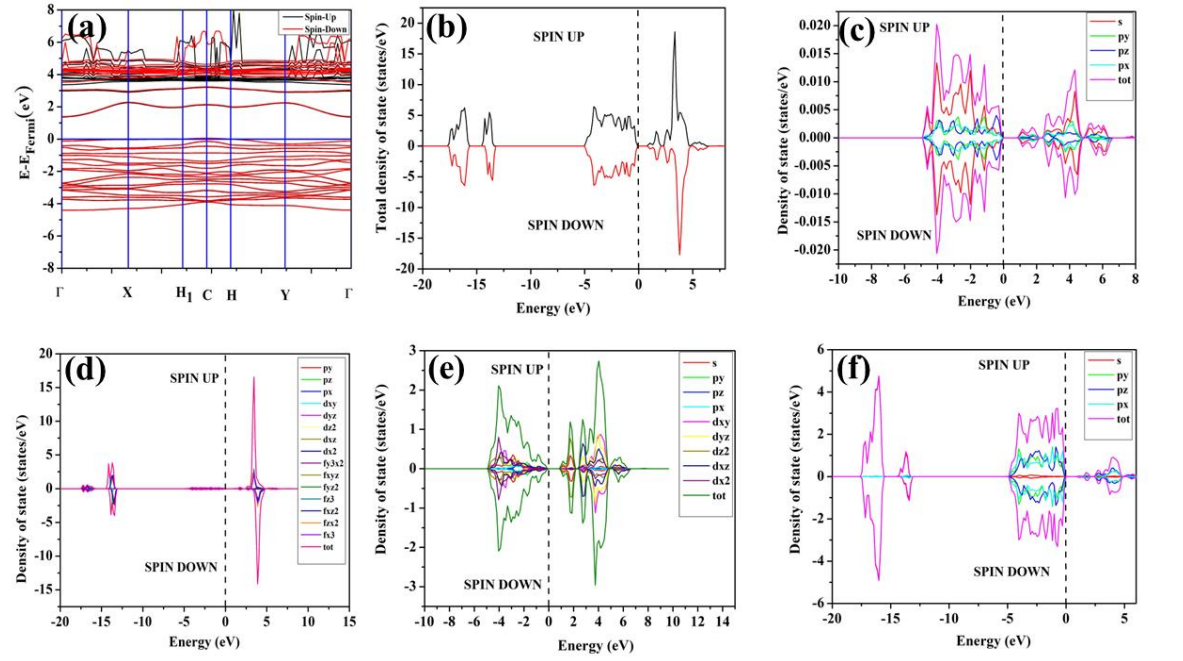

Figure 11: (a) Band structure and (b) spin polarised TDOS and PDOS of (c) Na, (d) Ce, (e) W and (f) O of NCWO – $2V_O^{\bullet}$.

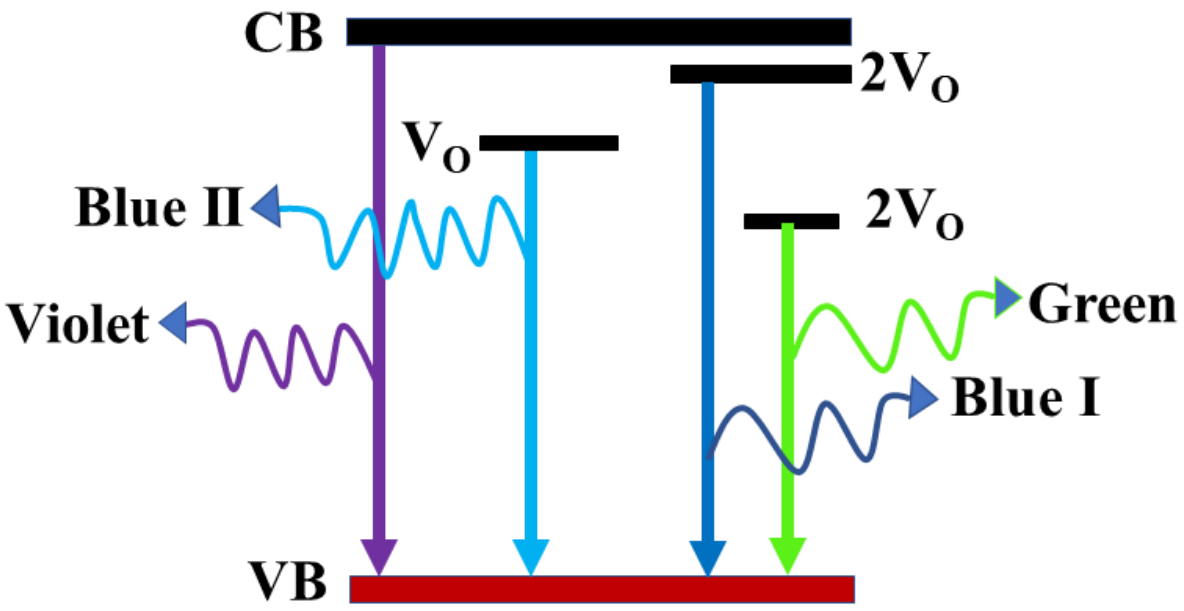

Figure 12: Schematic diagram of photoluminescence transitions.

4. Conclusion:

Pristine $NaCe(WO_4)_2$ samples with varying oxygen vacancy and vacancy cluster has been synthesized by a facile CTAB assisted hydrothermal technique. This is the first time we are reporting intense violet from $NaCe(WO_4)_2$ and blue I, blue II and green emission of relatively low intensity. Our detailed experimental and theoretical studies reveal that all these transitions are related with 5d → 4f transition of Ce, but in different CeO_8 dodecahedral configuration. More specifically, violet and blue II emissions originate from CeO_8 and CeO_7, while CeO_6 provides blue I and green emissions indicating that $NaCe(WO_4)_2$ may be a potential material for violet LED. Our calculation demonstrates that valence and conduction bands comprises of O 2p and O 2p – Ce 5d orbitals respectively are highly sensitive of defect states, hence these may be used to tune electronic properties of $NaCe(WO_4)_2$. Herein, it may be stated that this study will be helpful for better understanding of the optoelectronic properties of pristine as well as oxygen vacancy content $NaCe(WO_4)_2$.

APPENDIX- II

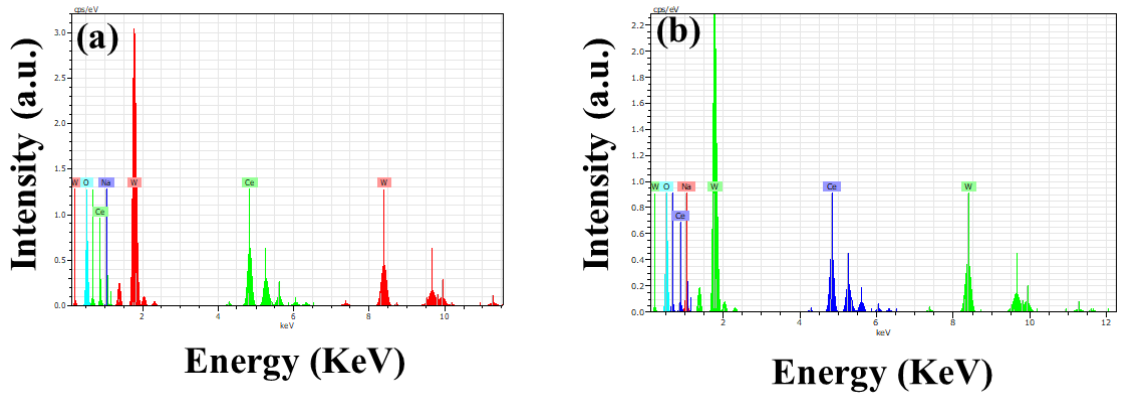

Figure A1: EDX spectra of (a) $NCWO_{1:1}$ and (b) $NCWO_{1:2}$ respectively.

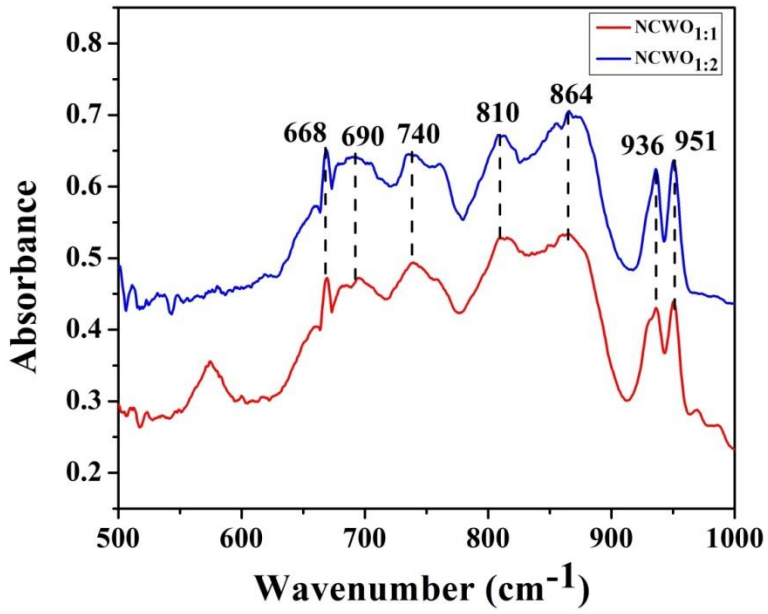

Figure A2: FTIR spectra of $NCWO_{1:1}$ and $NCWO_{1:2}$.

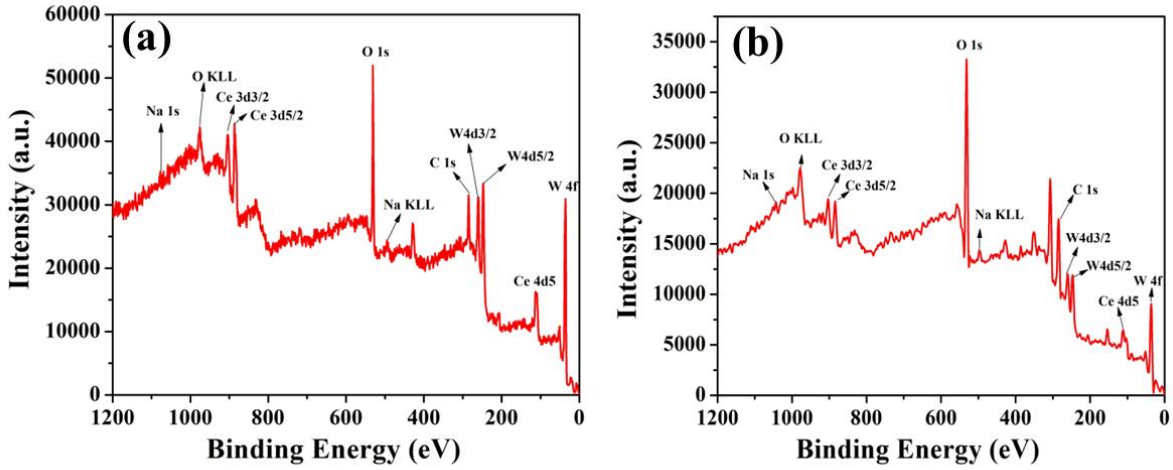

Figure A3: XPS wide spectrum of Ce-3d, W-4f, O-1s, Na-1s of (a) $NCWO_{1:1}$ and (b) $NCWO_{1:2}$ respectively.

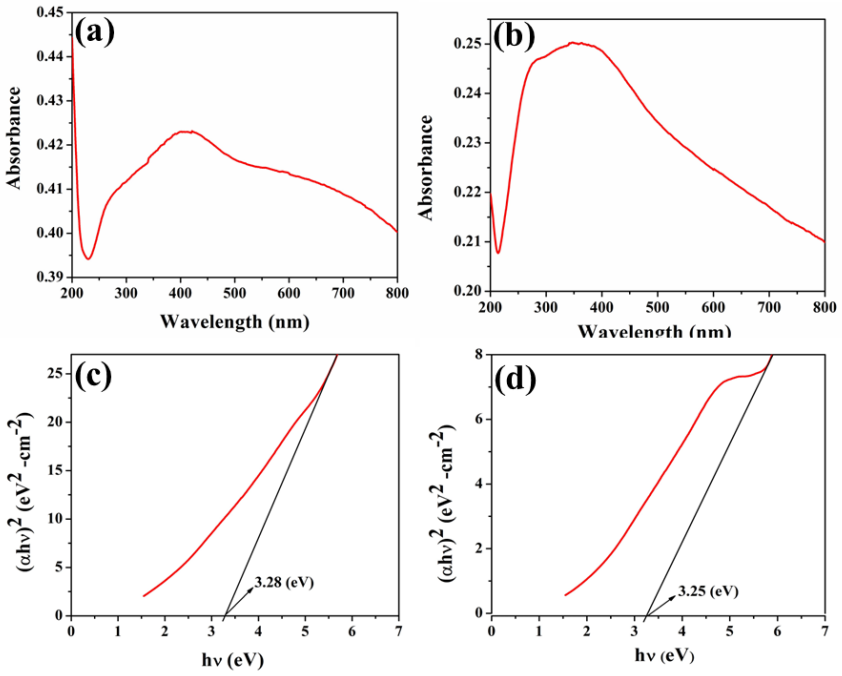

Figure A4: UV spectra and corresponding band gap of $NCWO_{1:1}$ (a, c) and $NCWO_{1:2}$ (b, d) respectively.

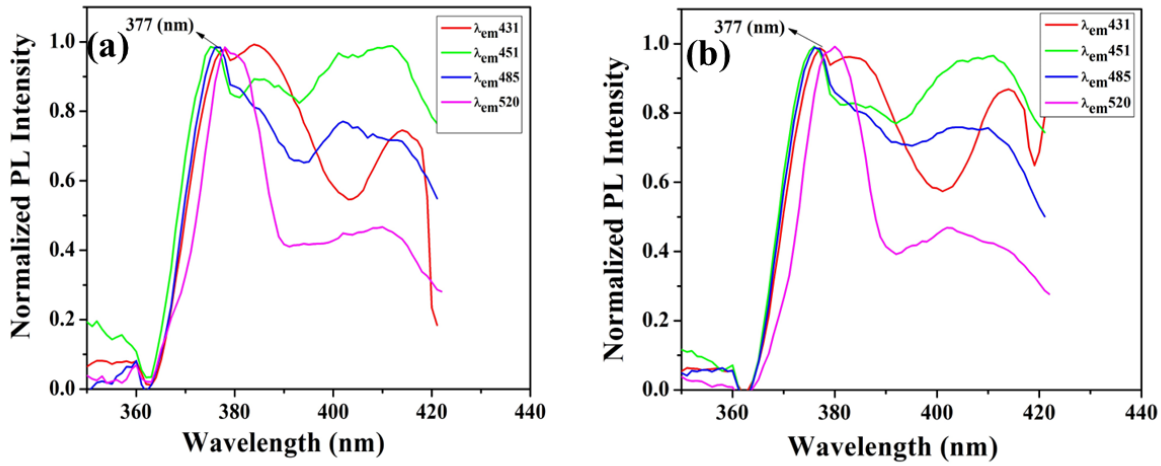

Figure A5: PLE spectra of $NCWO_{1:1}$ (a) and $NCWO_{1:2}$ (b) respectively.

REFERENCE

1) Y. Zhu, Y. Liang, M. Zhang, M. Tong, G. Li, S. Wang, RSC Adv. **5**, 98350-98360 (2015).

2) X. Zhang, J. Wu, P. Wang, J. Gao, F. Gao, D. Gao, Dalton Trans. **50**, 7826-7834 (2021).

3) A.K. Munirathnappa, V.C. Petwal, J. Dwivedi, N.G. Sundaram, New J. Chem. **42**, 2726-2732 (2018).

4) A. Arakcheeva, D. Logvinovich, G. Chapuis, V. Morozov, S.V. Eliseeva, J.C.G. Bünzli, P. Pattison, Chem. Sci. **3**, 384-390 (2012).

5) N. Dirany, M. Arab, A. Moreau, J.C. Valmalette, J.R. Gavarri, Cryst. Eng. Comm. **18**, 6579-6593 (2016).

6) T. Shimemura, N. Sawaguchi, M. Sasaki, J. Ceram. Soc. of Japan **125**, 150-154 (2017).

7) A.K. Munirathnappa, J.C. Neuefeind, P. Yanda, A. Sundaresan, I.V. Kityk, K. Ozga, J. Jedryka, A. Rao, N.G. Sundaram, Cryst. Grow. Des. **19**, 6082-6091 (2019).

8) X. Yang, Z. Fu, G. Liu, C. Zhang, Y. Wei, Z. Wu, T. Sheng, RSC Adv. **5**, 70220-70228 (2015).

9) R.F. Gonçalves, L.S. Cavalcante, I.C. Nogueira, E. Longo, M.J. Godinho, J.C. Sczancoski, V.R. Mastelaro, I.M. Pinatti, I.L.V. Rosa, A.P.A. Marques, Cryst. Eng. Comm. **17**, 1654-1666 (2015).

10) A.K. Munirathnappa, A.K. Sinha, N.G. Sundaram, Cryst. Grow. Des. **18**, 253-263 (2018).

11) W.R. Liu, C.W. Yeh, C.H. Huang, C.C. Lin, Y.C. Chiu, Y.T. Yeh, R.S. Liu, J. Mater. Chem. **21**, 3740-3744 (2011).

12) L.S. Cavalcante, F.M.C. Batista, M.A.P. Almeida, A.C. Rabelo, I.C. Nogueira, N.C. Batista, J.A. Varela, M.R.M.C. Santos, E. Longo, E. M.S. Li, RSC Adv. **2**, 6438-6454 (2012).

13) G.M. Kuzmicheva, A.V. Eremin, V.B. Rybakov, K.A. Subbotin, E.V. Zharikov, Russ. J. Inorg. Chem. **54**, 854-863 (2009).

14) R.L. Andrews, A.M. Heyns, P.M. Woodward, Dalton Trans. **44**, 10700-10707 (2015).

15) L. Li, Y. Su, G. Li, Appl. Phys. Lett. **90**, 054105 (2007).

16) G.M. Kuz'Micheva, I.A. Kaurova, V.B. Rybakov, P.A. Eistrikh-Geller, E.V. Zharikov, D.A. Lis, K.A. Subbotin, Cryst. Eng. Comm. **18**, 2921-2928 (2016).

17) Pushpendra, R.K. Kunchala, S.N. Achary, B.S. Naidu, ACS Appl. Nano Mater. **2**, 5527-5537 (2019).

18) F. Esteban-Betegón, C. Zaldo, C. Cascales, Chem. Mater. **22**, 2315-2324 (2010).

19) S. Basu, B.S. Naidu, B. Viswanadh, V. Sudarsan, S.N. Jha, D. Bhattacharyya, R.K. Vatsa, Rsc Adv. **4**, 15606-12 (2014).

20) W.G. Fateley, Krieger Publishing Company 1972.

21) J.A. Horsley, I.E. Wachs, J.M. Brown, G.H. Via, F.D. Hardcastle, J. Phys. Chem. **91**, 4014-4020 (1987).

22) Z. Xu, P. Du, Q. Zhu, X. Li, X. Sun, J.G. Li, Dalton Trans. **50**, 17703-17715 (2021).

23) D. Errandonea, J. Pellicer-Porres, M.C. Pujol, J.J. Carvajal, M. Aguiló, J. Allo. Comp. **638**, 14-20 (2015).

24) J. Hanuza, L. Macalik, Spectro. Acta Part A: Mol. Spec. **43**, 361-373 (1987).

25) N. Dirany, M. Arab, A. Moreau, J.C. Valmalette, J.R. Gavarri, Cryst. Eng. Comm. **18**, 6579-6593 (2016).

26) B.P. Singh, R.A. Singh, New J. Chem. **39**, 4494-4507 (2015).

27) F.F. Wu, D. Zhou, C. Du, S.K. Sun, L.X. Pang, B.B. Jin, Z.M. Qi, J. Varghese, Q. Li, X.Q. Zhang, J. Mater. Chem. C **9**, 9962-9971 (2021).

28) W. da Silva Pereira, M.M. Ferrer, G. Botelho, L. Gracia, I.C. Nogueira, I.M. Pinatti, I.L.V. Rosa, F.D.A. La Porta, J. Andres, E. Longo, Phys. Chem. Chem. Phys. **18**, 21966-21975 (2016).

29) P. Botella, R. Lacomba-Perales, D. Errandonea, A. Polian, P. Rodriguez-Hernandez, A. Munoz, Inorg. Chem. **53**, 9729-9738 (2014).

30) Y. Xiong, B. Wang, H. Zhuang, X. Jiang, G. Ma, Y. Yi, W. Hu, Y. Zhou, RSC Adv. **4**, 36738-36741(2014).

31) N. Dirany, E. McRae, M. Arab, Cryst. Eng. Comm. **19**, 5008-5021 (2017).

32) S.D. Ramarao, V.R.K.Murthy, Dalton Trans. **44**, 2311-2324 (2015).

33) C. Zhang, D. Guo, W. Xu, C. Hu, Y. Chen, J. Phys. Chem. C **120**¸12218-12225 (2016).

34) A.K. Munirathnappa, J.C. Neuefeind, P. Yanda, A. Sundaresan, I.V. Kityk, K. Ozga, J. Jedryka, A. Rao, N.G. Sundaram, Cryst. Grow. Des. **19**, 6082-6091 (2019).

35) S. Mandal, C.K. Ghosh, D. Sarkar, U.N. Maiti, K.K. Chattopadhyay, Solid state sci. **12**, 1803-1808 (2010).

36) L.S. Cavalcante, F.M.C. Batista, M.A.P. Almeida, A.C. Rabelo, I.C. Nogueira, N.C. Batista, J.A. Varela, M.R.M.C. Santos, E. Longo, M.S. Li, Rsc Adv. **2**, 6438-6454 (2012).

37) M. Anicete-Santos, E. Orhan, M.A.M.A. De Maurera, L.G.P. Simoes, A.G. Souza, P.S. Pizani, E.R. Leite, J.A. Varela, J. Andrés, A. Beltrán, E. Longo, Phys. Rev. B **75**, 165105 (2007).

38) G. Li, Y. Tian, Y. Zhao, J. Lin, Chem. Soc. Rev. **44**, 8688-8713 (2015).

39) T. Shimemura, N. Sawaguchi, M. Sasaki, J. Ceram. Soc. of Japan, **124**, 938-942 (2016).

40) P. Dorenbos, ECS J. Solid State Sci. Tech. **2**, 3001-3011 (2013).

41) Y. Zhu, Y. Liang, M. Zhang, M. Tong, G. Li, S. Wang, RSC Adv. **5**, 98350-98360 (2015).

42) M.V. Korzhik, V.B. Pavlenko, T.N. Timoschenko, V.A. Katchanov, A.V, Singovskii, A.N. Annenkov, V.A. Ligun, I.M. Solskii, J.P. Peigneux, physica status solidi (a) **154**, 779-788 (1996).

43) E.V. Sokolenko, V.M. Zhukovskii, E.S. Buyanova, Y.A. Krasnobaev, Inorg. mater. **34**, 499-502 (1998).

44) B.M. Sinel'nikov, E.V. Sokolenko, V. ZVEKOV, Inorg. Mater. **32**, 999-1001 (1996).

45) A. Lecointre, A. Bessière, A.J.J. Bos, P. Dorenbos, B. Viana, S. Jacquart, J. Phys. Chem. C **115**, 4217-4227 (2011).

46) X. Mi, J. Sun, P. Zhou, H. Zhou, D. Song, K. Li, M. Shang, J. Lin, J. Mater. Chem. C **3**, 4471-4481 (2015).

47) M. Li, J. Zhang, J. Han, Z. Qiu, W. Zhou, L. Yu, Z. Li, S. Lian, Inorg. Chem. **56**, 241-251(2017).

48) M. Yu, B. Wang, Y.G. Liu, L. Wang, Y. Xia, Z. Huang, M. Fang, In IOP Conference Series: Mater. Sci. Eng. **678**, 012085 (2019).

49) X. Wang, Y. Wang, The J. Phys. Chem. C **119**, 16208-16214 (2015).

50) W.Y. Huang, F. Yoshimura, K. Ueda, Y. Shimomura, H.S. Sheu, T.S. Chan, C.Y. Chiang, W. Zhou, R.S. Liu, Chem. Mater. **26**, 2075-2085 (2014).

51) S. Das, C.K. Ghosh, R. Dey, M. Pal, RSC Adv. **6**, 236-244 (2016).

52) X. Yu, Y. Jiang, X. Li, Z. Song, X. Zhang, H. Liu, B. Zhao, T. Ye, L. Duan, J. Fan, Cryst. Eng. Comm. **24**, 805-817 (2022).

Chapter 5

Truncated octahedra $NaCe(MoO_4)_2$ nanostructure: role of defects on photoluminescence, electron – phonon interaction and gas sensing property

1. Introduction

Over the past few years, rare earth (RE) based scheelite micro/nanostructured materials with well-defined morphology, tuneable size have attracted considerable passion of researchers in various applications, specifically in optoelectronic devices such as solid-state lasers, fluorescent lamps, optical sensors, scintillators, light-emitting diode, fiber optic communication, biological labeling etc. due to their unique optical features of intense emission, narrow band, high quantum yield, easy tuneability of emission wavelength, excellent thermal and chemical stability, improved electro-optical conversion etc. [1 – 3]**.** Among them, alkali RE - binary molybdates with generic formula $A^{I}Ln^{III}(MoO_4)_2$ (A = alkali metal, Ln = RE lanthanide), in which Mo^{6+} and Ln^{3+} are embedded in the lattice of A^{+} exhibit high potency as optically active material, ascribed to strong 5d – 4f transition of Ln^{3+}, particularly in diode-pumped solid state [4, 5]. It has been recognized that 5d – 4f transition of Ln^{3+} highly depends on symmetry of the unit cell, hence extensive research works have carried out to modulate 5d – 4f transition related optical emission. As an example, Cheng *et al*. has investigated influence of Li/Ag on the luminescence

properties of Eu^{3+} in $Li_{1-x}Ag_xLu(MoO_4)_2:Eu^{3+}$ [6], while Song *et al.* has explored red emission from Eu^{3+} doped $AgGd(MoO_4)_2$ [7]. Strongest integrated emission intensity and high color purity, observed in $LiEu(MoO_4)_2$ among all $AEu(MoO_4)_2$ (A = Li^+, Na^+ and K^+), has been ascribed higher faster charge transfer due to shortened and covalent Li – O bond in comparison with Na or K counterpart [8]**.** It has been noted in literature that most of the conventional techniques to prepare scheelite materials such as top seed solution growth, modified Czochralski method, solid-state reaction, Pechini, sol – gel, microwave etc. requires high temperature (~ 1000^oC) along with long reaction time leading to the formation in agglomerated form with high grain size and irregular morphology [9]. However, recent studies depicts close correlation exists between the morphology factors like shape, size, exposure facets, dimensionality, hierarchy and local crystal field which leads parity law and consequently optical emission, hence abundant efforts have been devoted to explore different micro/nanostructure of $ALn(MoO_4)_2$ to have improved optical emission. Among different strategies, organic additive assisted hydrothermal is widely accepted technique to produce various micro/nanostructure. As reference, Liu *et al.* has reported preparation of uniform tetragonal microspindles and nanoplates using ethylenediaminetetraacetic acid (EDTA-2Na) surfactant [10], while microrod, microcuboids and microflower have been obtained *via* PVP ligand based synthesis technique [11]. Zheng *et al.* had synthesized cotton-shaped 3D flower-like morphology using trisodium citrate assisted method [12]; whilst, uniform spherical nanoparticles have been achieved from cetyltrimethyl ammonium bromide (CTAB) assisted hydrothermal method [13]. Though a series of $ALn(MoO_4)_2$ type scheelite materials like $NaLa(MoO_4)_2$, $NaY(MoO_4)_2$, $NaYb(MoO_4)_2$, $NaTb(MoO_4)_2$, $NaGd(MoO_4)_2$, $NaEu(MoO_4)_2$ etc. have been synthesized and investigated; nevertheless, no report exists on the trisodium citrate (Na_3Cit) assisted

hydrothermal synthesis of $NaCe(MoO_4)_2$ in optoelectronic and gas sensing application.

In this manuscript, we report for the first time about an efficient trisodium citrate assisted hydrothermal technique to synthesis $NaCe(MoO_4)_2$ truncated octahedral nanostructure. Herein, it may be stated that previously we had got triclinic phase of $NaCe(WO_4)_2$ of irregular shape *via* CTAB assisted hydrothermal technique; but presently we have obtained tetragonal phase of $NaCe(MoO_4)_2$ with truncated octahedral shape. From our previous works, it is to mention that intrinsic defects in the form of vacancies, and / interstitial (O, Mo, Ce and Na) form are inherent of synthesis protocol and condition [14-16]. Thus, central to functionality of $NaCe(MoO_4)_2$ as optical active material is the accurate depiction of their local structure, specifically defects. Herein, defects of the as-prepared truncated octahedral $NaCe(MoO_4)_2$ have been thoroughly analysed and correlated with optical emissions, whilst our study reveals that $NaCe(MoO_4)_2$ contains O mono- and divacancy (V_O and $2V_O$), which lead formation of CeO_7 and CeO_6 acting as active luminous centres for blue and green emissions. It is worth noting that O vacancies often get diffused and accumulated at the surface of the nanostructure, wherein they act as electron trapping centers. They are often transferred to the surface adsorbed molecular O_2 leading formation of O_2^- which in consequences facilitates gas sensing property [17]. However, it has been identified that local environment of the emissive centers plays a crucial role during adsorption of particular gas; hence selectivity depends on local environment at the nanostructure's surface. Though vast researches have been carried out on optical properties of scheelite materials, but report on gas sensing property is very limited. Only a few authors mentioned gas sensing property of scheelites i.e. Lin *et al.* reported oxygen vacancy induced gas sensing activity of $NaBi(MoO_4)_2$ nanomaterials [18], while our previous studies demonstrate that triclinic $NaCe(WO_4)_2$ selectively sense NH_3 [19]. Herein, we have identified acetone sensing by our synthesized

$NaCe(WO_4)_2$ nanostructures. To the best of our knowledge, there is the first report on O vacancy induced gas sensing property of $NaCe(MoO_4)_2$. In addition, it is to mention that lattice deformation around O vacancy sites, caused by trapped electron, plays an important role in acetone sensing efficiencies, herein we have observed that $NaCe(MoO_4)_2$ nanostructure with lowest lattice deformation as expressed by electron – phonon coupling facilitates acetone sensing.

As there is no profound theoretical calculation on electronic structure of $NaCe(MoO_4)_2$, hence for better understanding, we have performed *ab initio* band structure calculation of $NaCe(MoO_4)_2$ which shows that Ce $5d_z^2$, $d_{x^2-y^2}$, d_{yz} orbitals provide to the 5d – 4f transition, resulting in the blue and green emissions from CeO_7 and CeO_6, formed due to V_O and $2V_O$. We have illustrated that electronic excitation involved MoO_4 tetrahedra and decay takes place within CeO_8 polyhedra, while $MoO_4 \rightarrow CeO_8$ charge transfer is mediated through $\nu_4(F_2)$ phonon mode. We have also identified that electron – phonon coupling plays a major role in this charge transfer process depending and is sensitive on defects. Herein, our study demonstrates that the use of surfactant trisodium citrate in this facile hydrothermal synthesis technique facilitates formation of $2V_O$ rather than V_O while former acts as an active site for acetone adsorption leading higher acetone sensitivity. Overall, it may be inferred that our synthesized truncated octahedra $NaCe(MoO_4)_2$ nanostructures can be potential for optoelectronic and sensing applications.

2. Experimental Section

2.1 Materials and synthesis

In order to prepare $NaCe(MoO_4)_2$ nanomaterials through typical hydrothermal method, 1.00 mmol (0.434 g) of cerium nitrate [$Ce(NO_3)_3.6H_2O$, Merck, Germany] and trisodium citrate [$Na_3Cit.2H_2O$, Merck, Germany] were mixed with 60 ml DI water, followed by 2 hours stirring at room temperature. Another

aqueous solution of 2.00 mmol (0.484 g) sodium molybdate [$Na_2MoO_4.H_2O$, Merck, Germany] in 20 ml DI water was added dropwise with the above solution. After vigorous stirring for 30 minutes, the resulting solution turned into pale yellow colour which was finally transferred to a Teflon autoclave for hydrothermal reaction at 180°C for 24 h. The final product was collected by centrifugation, followed by simultaneous washing with DI water and ethanol, overnight drying at 70°C and calcination at 800°C for 5 h in a muffle furnace. The synthesis was performed at different concentrations of $Na_3Cit.2H_2O$ (0.00, 0.50, 0.78, and 1.00 mmol i.e. 0.00, 0.147, 0.229, 0.294 g) to examine it's role on the final product and accordingly they were labelled as $NCMO_{0.00}$, $NCMO_{0.50}$, $NCMO_{0.78}$ and $NCMO_{1.00}$. The reaction procedure is schematically represented in Fig. A1, of APPENDIX-III.

2.2 Characterization and Gas sensing properties

X-ray diffraction (XRD) patterns, taken on Rigaku Ultima III powder diffractometer equipped with CuK_α radiation (λ= 1.54056 Å), were utilized to examine phase purity and other crystallographic informations through FullProf-based Rietveld refinement method. Experimental profiles were fitted with a suitable pseudo-Voigt analytical asymmetric function, while the background was fitted with a fourth-order polynomial function. Field emission scanning electron microscopy (FESEM: Hitachi S – 4800, operated at 5 kV) was used to inspect the morphology of the samples, while transmission electron microscope (TEM-2100 Plus Electronmicroscope, 200 kV) was adopted to obtain high resolution microscopic images and selected area electron diffraction (SAED). Raman spectra, taken on alpha 300 Witec with a 530 nm laser (power: 3 mW and spot size: 2 m) and Fourier transform infrared (IR) spectra, captured on IR Prestige, were utilized to examine short-range structural distortion. X-ray photoelectron spectra (XPS) were collected using the PHI Versa Probe III Scanning XPS Microprobe with Al K source. Optical properties of the as-prepared samples were investigated at room temperature using UV–Vis spectra

(JASCO V650) and photoluminescence spectra, recorded on FP-8300, JASCO consisting of 100 W Xe lamp.

Gas sensing property was examined using Taguchi type sensor module where a hollow cylindrical Al_2O_3 substrate having Pt electrodes was coated with thick slurry of NCMO nanostructured materials through drop casting method. Slurry was prepared by mixing the as-prepared samples with isopropyl alcohol as binder, while coated substrates were heated at 100^0C for 12 h to remove residual solvents. Ni-Cr wire was inserted through the hole of the substrate as heating element which provides the required temperature depending upon applied voltage across the wire. Gas cylinders balanced in air were used during measurement of the sensing performance on Agilent 34461A digital multimeter interfaced with data logger software.

2.3 Calculation of band structure and investigation of gas sensing mechanism using *ab initio* density functional theory

It is well-known that electronic band structure gives a theoretical insight about opto-electronic properties of any materials; hence we had computed spin-polarized band structure, density of states (DOS), partial DOS (pDOS), total DOS (TDOS) and projected DOS (PDOS) using VASP. Herein, plane-wave pseudo-potential (PAW) had been used, while Perdew-Burke-Ernzerh (PBE) exchange correlation and ultra-soft potential as basis set were considered. We employed the valence electrons of the respective atoms as follows: Na atom ($1s^2$ $2s^2$ $2p^6$ $3s^1$), Ce atom ($5s^2$ $5p^6$ $4f^1$ $5d^1$ $6s^2$), Mo atom ($4p^6$ $5s^2$ $4d^{10}$), and O atom ($2s^2$ $2p^4$). For this calculation, 5 × 5 × 7 Monkhorst - Pack k point were used as this allowed an accurate representation of the Brillouin zone and the electronic properties of the material. Prior to calculate band structure along $\Gamma \rightarrow X \rightarrow H_1 \rightarrow C \rightarrow H \rightarrow Y \rightarrow \Gamma$, structure was optimized with the lowest single point ground state energy by fixing cut-off energy at 520 eV while the convergence had been tested in between 220 and 620 eV. Herein, maximum atomic

displacement ~ 5×10^{-4} Å and stress ~ 0.02 GPa had been considered for this calculation. Each atom was exposed to a 0.01 eV Hellmann-Feynman force to ensure stable convergence, while EDIFF and force EDIFG parameters were adjusted to 10^{-6} eV and 10^{-3} eV, respectively to ensure high precision computational convergence.

In order gain theoretical insight about the influence of defect on gas sensing performance, we have calculated adsorption energies of acetone on the NCMO surface as shown in Fig. A2, APPENDIX-III. Herein, we have modelled tetragonal NCMO (112) surface with dimension of the supercell 7.573Å × 17.823Å × 32.422Å. The k-point mesh for this calculation has been optimized at 3×3×1, while thickness of the slab and the vacuum level are ~ 3 nm and 15 Å respectively. In these calculations, bottom half layers has been frozen, whereas top half layers with acetone as adsorbent have been set to relax. Presently, the adsorption energy has been calculated using eqn (1)

$$E_{ads} = E_{NCMO+acetone} - E_{NCMO} - E_{acetone} \quad (1)$$

where, $E_{NCMO+acetone}$, E_{NCMO} and $E_{acetone}$ represent total ground state energy of NCMO in combination with acetone molecule, bare NCMO and acetone gas respectively. In order to examine the influence of defects on the gas sensing activity, we have carried out the above calculation by removing one and two oxygen atoms at (112) surface of NCMO.

3. Result and discussion

3.1 Structural and morphological studies by XRD, FESEM and TEM

The powder XRD patterns of all the samples (Fig. 1) closely match with scheelite-type tetragonal NCMO with space group $I4_{1/a}$ (C_{4h}^6, ICDD Database No. 04-007-5489). Absence of any peak other than NCMO confirms phase purity of the synthesized nanostructures, while sharp diffraction peaks designate

good crystallinity. Herein, unit cell (from VESTA program on the basis crystallographic data, obtained from refinement) is represented in Fig. A3, while Table A1 of APPENDIX-III summarizes structural parameters e.g. lattice parameters, unit cell volume, bond length, bond angles, crystallite size, obtained through Rietveld refinement which was carried out till satisfactory convergence of χ^2, R_p and R_{wp} [20]. It has been realized from Fig. A3 that NCMO's unit cell comprises of Na and Ce atoms at 4b sites and they are coordinated to eight O atoms at 16f site *via* two different bond lengths producing (Na/Ce)O_8 polyhedra, while these polyhedrons are connected to MoO_4 tetrahedra with Mo at 4a site. Herein, unit cell volume, c – parameter, c/a ratio, Na/Ce-O bond lengths, Na/Ce-O-Mo and O-Mo-O bond angles except Mo – O bond length monotonically decrease from $NCMO_{0.00}$ to $NCMO_{1.00}$ indicating distortion of the unit cells. (Na/Ce)O_8 polyhedral (N) and MoO_4 tetrahedral (K) distortions, calculated from [21] $N = \frac{\alpha_{1(O-Mo-O)}}{\alpha_{2(O-Mo-O)}}$, where $\alpha_{1(O-Mo-O)}$ and $\alpha_{2(O-Mo-O)}$ denote two different bond angles and $K = \frac{d_{1(Na,Ce-O)}}{d_{2(Na,Ce-O)}}$, where $d_{1(Na,Ce-O)}$ and $d_{2(Na,Ce-O)}$ represent two different bond lengths, are found to be N ~ 1.011, 1.029, 1.043, 1.052 and K ~ 1.0587, 1.0827, 1.0838, 1.0842 for $NCMO_{0.00}$, $NCMO_{0.50}$, $NCMO_{0.78}$ and $NCMO_{1.00}$ respectively indicating predominant tetrahedral distortion in comparison with polyhedral distortion [22, 23]. According to previous studies, decrease of c/a is associated with charge confinement-induced short-range ordering due to partial substitution of Na^+ by Ce^{3+} where charge imbalance at 4b site mediated dipole – dipole interaction plays significant role [24]. In general, free carriers, ought to be kept electrical charge balance of O – deficient sample, are denoted by $0 \rightarrow Ce_{Na}^{m\bullet} + V_O^{n\bullet}$ [25] i.e. $V_O^{n\bullet}$s are expected to be associated with Ce occupancy > 0.5 at 4b sites, thus angular distortion in MoO_4 tetrahedra, enhancement Mo – O bond angles etc. are ascribed to O vacancy (V_O).

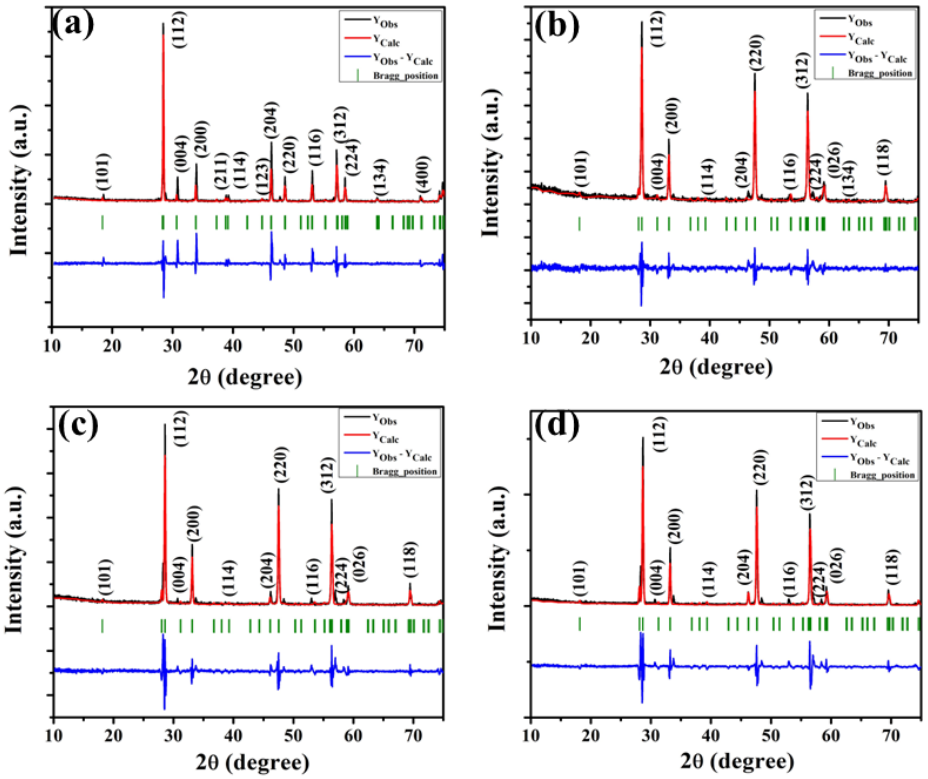

Fig. 1 XRD patterns of the $NaCe(MoO_4)_2$ samples (a) $NCMO_{0.00}$, (b) $NCMO_{0.50}$, (c) $NCMO_{0.78}$ and (d) $NCMO_{1.00}$ respectively.

FESEM images of the samples, synthesized at different Na_3Cit concentrations, are presented in Fig. 2 (a)-(d). It is noted that $NCMO_{0.00}$ possesses irregular shape (Fig. 2(a)), while a gradual transformation from irregular to truncated octahedral shape has been observed in case of samples $NCMO_{0.50}$, $NCMO_{0.78}$ and $NCMO_{1.00}$ (Fig. 2(b)-(d)) indicating that Na_3Cit has significant role during hydrothermal reaction to tune morphology. For better understanding about the shape of these microstructures, transmission electron microscopy (TEM) has been further employed. Fig. 2(e) depicts one TEM image of a typical sample (c.a. $NCMO_{1.00}$) that confirms truncated octahedral shape, while selected area diffraction (SAED) pattern (Fig. 2(f)) consists five diffraction spots corresponding to (112), (211), (123), (222) and (224) planes of tetragonal NCMO denoting crystalline character.

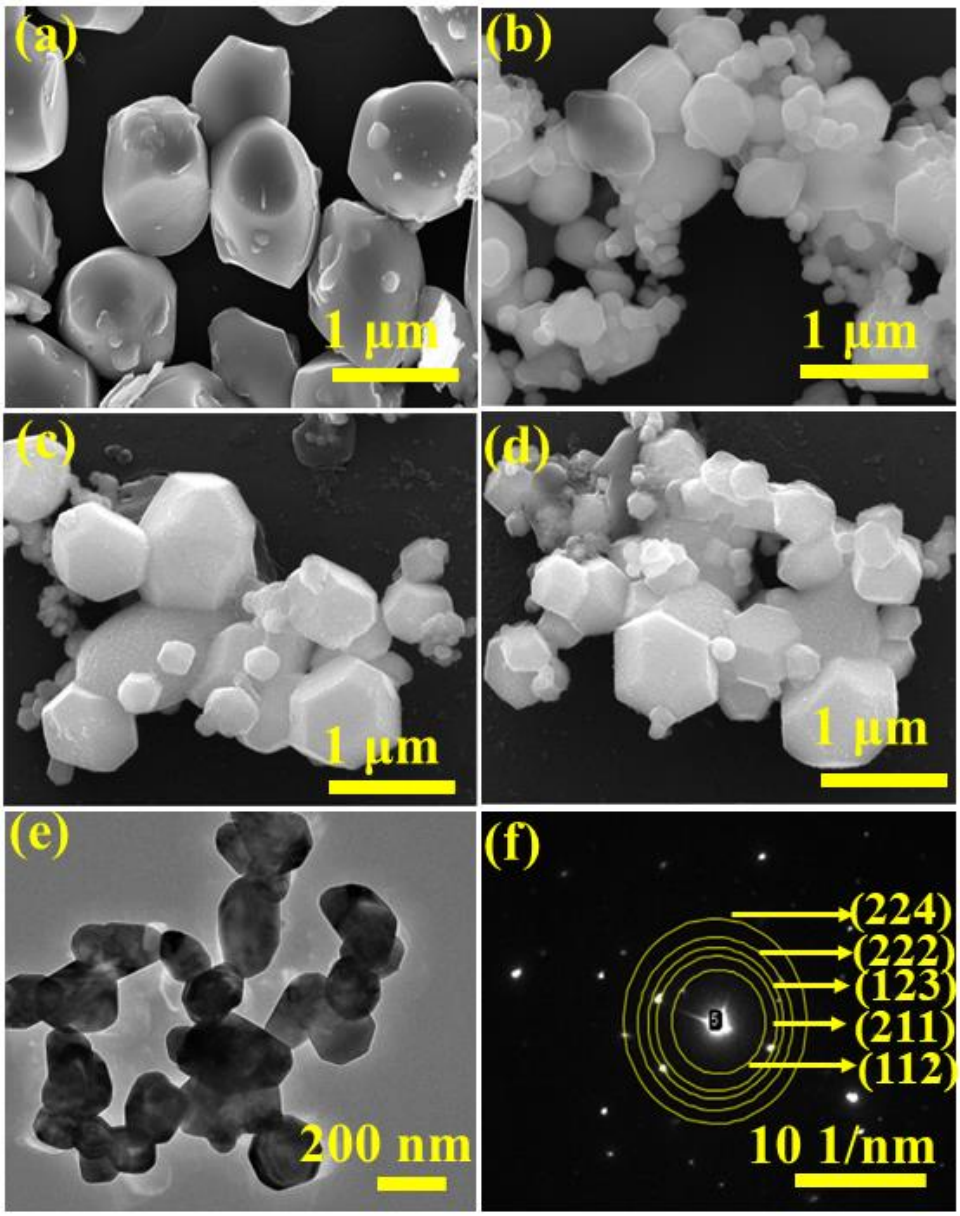

Fig. 2 FESEM images NCMO samples (a) $NCMO_{0.00}$, (b) $NCMO_{0.50}$, (c) $NCMO_{0.78}$ and (d) $NCMO_{1.00}$, (e) and (f) TEM image and SAED pattern of $NCMO_{1.00}$.

3.2 Investigations of local structure by FTIR, Raman and x-ray photoelectron spectroscopies

To understand the influence of V_O on short-range structural distortions within $(Na/Ce)O_8$ polyhedra and MoO_4 tetrahedra, we have taken FTIR and Raman

spectra of our synthesized samples. Various peaks in the absorption band (shown in Fig. A4, APPENDIX-III), measured in between 500 and 1000 cm^{-1}, are attributed to different active internal vibrations of MoO_4 tetrahedra. MoO_4 tetrahedra, in general, crystallize in either regular (Mo^RO_4) or distorted form (Mo^DO_4) due to V_O, while the vibration (Γ_{Td}) of the isolated Mo^RO_4 is represented by [26]:

$$\Gamma_{Td} = A_1 + E + 2F_2 \quad (2)$$

However, tetrahedra symmetry changes into S_4 in NCMO wherein IR active vibrational modes include $\nu_1(A_1)$, $\nu_2(E_1)$, $\nu_3(F_2)$, $\nu_4(F_2)$, one free rotation $\nu_{f.r.}(F_1)$ and one translation F_2. In contrast to Mo^RO_4, Mo^DO_4 having C_{2h}^6 space group exhibits four formula units per crystallographic unit cells with $2Mo(C_2)$, $4Mo(C_1)$, $4Ce(C_1)$ and $24O(C_1)$ symmetries of the atoms indicating splitting of the vibrational modes (c.a. $O \rightarrow Mo(C_1) \rightarrow O$ and $O \rightarrow Mo(C_2) \rightarrow O$) within Mo^DO_4 due to lower site symmetry [27]. Presently, two bands in between 650 – 749 and 750 – 1000 cm^{-1} are ascribed to $\nu_3(F_2)$ and $\nu_4(F_2)$, while the single peak at 670 cm^{-1} is assigned to $\nu_2(E_1)$ vibration. Careful deconvolution (shown in Fig. A5, APPENDIX-III) of $\nu_3(F_2)$ and $\nu_4(F_2)$ modes yields three peaks (c.a. 693, 705, 722 cm^{-1} and 813, 858, 909 cm^{-1}). As per bond length – stretching frequency correlation, prescribed by Hardcastle *et al.*, an increase in the bond length decreases vibrational frequency. Hence, Mo^DO_4 correspondences vibrational mode with lower energy, while high energized peaks are ascribed to Mo^RO_4 [28]. Therefore, peaks at 722 and 909 cm^{-1} are attributed to $\nu_3(F_2)$ and $\nu_4(F_2)$ modes of Mo^RO_4 respectively, while peaks at 693, 705 cm^{-1} and 813, 858 cm^{-1} correspondence $\nu_3(F_2)$ and $\nu_4(F_2)$ mode of vibration within Mo^DO_4 [27]. Mo^DO_4/ Mo^RO_4 ratio, calculated from area under the curve, is found to be 0.8, 1.0, 1.6 and 2.9 for $NCMO_{0.00}$, $NCMO_{0.50}$, $NCMO_{0.78}$ and $NCMO_{1.00}$ respectively indicating increase of tetrahedral distortion with increasing Na_3Cit and it corroborates with previous structural studies by XRD.

Raman spectra, taken upto the range of 1000 cm^{-1} at ambient temperature (Fig. A6, APPENDIX-III), consists of a peak at 463 cm^{-1} and three bands in between 64 – 231, 255 – 425 and 681 – 966 cm^{-1}. In general, Raman spectra of scheelite materials at Γ-point is expressed by

$$\Gamma = 3A_g + 5B_g + 5E_g \quad (3)$$

Where, non-degenerate A_g, B_g modes and doubly degenerate E_g mode corresponds various external and internal vibrations of MoO_4 and CeO_8 [26]. Peak in between 64 – 231 cm^{-1} corresponds to rotation and translation of MoO_4 tetrahedra and Na^+, Ce^{3+} respectively. Herein, the sharp peak is attributed to the external vibration of CeO_8 in well agreement with previous results [29], while bands are ascribed to internal bending of MoO_4 tetrahedra. After thorough examination, two peaks at 318 and 380 cm^{-1} are assigned to symmetric A_g bending and antisymmetric B_g bending vibrational modes of MoO_4 respectively [30]. While the peak at 463 cm^{-1} is assigned to antisymmetric A_g bending mode of MoO_4. The other two Raman peaks at 823 and 889 cm^{-1} are assigned to (O → Mo →O) antisymmetric stretching B_g and (O ←Mo → O) symmetric A_g mode of vibration [26, 31, 32]. Decrease in Raman intensity, observed with increasing Na_3Cit concentration, is believed to be related with increase of V_O and antisite defects corroborating XRD and FTIR studies [33, 34].

X-ray photoelectron spectroscopy (XPS), a well-known technique to investigate chemical state of elemental, has been adopted here to examine V_O associated changes in valance state of Na, Ce, Mo and O as they are highly sensitive to the local electronic environment. Herein, binding energy data of all elements were adjusted with respect to binding energy (~ 284.6 eV) of surface adsorbed atmospheric C 1s [19]. Survey scan (0 – 1100 eV) is presented in Fig. A7 of APPENDIX-III for all the synthesized samples, while high resolution spectra of Mo, Ce, and O are presented in Fig. A8, A9 and A10 of APPENDIX-

III respectively. Two peaks (c.a. 232.7 and 236.0 eV) of the XPS spectra of Mo are readily be ascribed to spin-orbit split $3d_{5/2}$ and $3d_{3/2}$ orbitals of Mo^{6+}, while careful deconvolution (Fig. A8(a)-(d), APPENDIX-III) reveals the presence of two peaks for two orbitals (c.a. 232.5, 232.9 eV for $3d_{5/2}$ and 235.7 and 236.2 eV for $3d_{3/2}$) and they designated as $Mo3d_{5/2}$(I), $Mo3d_{5/2}$(II) and $Mo3d_{3/2}$(I), $Mo3d_{3/2}$(II) respectively. Herein, we assign $Mo3d_{5/2}$(II) and $Mo3d_{3/2}$(II) to $Mo^{R}O_4$, while $Mo3d_{5/2}$(I) and $Mo3d_{3/2}$(I) correspondence to $Mo^{D}O_4$, while their difference can be assigned to V_O induced changes in electronegativity between Mo and O. In brief, electrons mostly are located on O due to its strong electronegativity and makes Mo – O bond significantly ionic, while V_O increases effective charge on Mo which in consequence increases electron concentration on Mo. Thus electron – electron repulsion on Mo reduces binding energies of the Mo $3d_{5/2}$ and $3d_{3/2}$ orbitals in $Mo^{D}O_4$. In this context, less energy difference between $3d_{5/2}$ and $3d_{3/2}$ in $Mo^{D}O_4$ with respect to $Mo^{R}O_4$ (c.a. 3.23 and 3.19 eV) which again indicates the influence local field, generated from V_O, on spin-orbit splitting. Weighted percentage of $Mo^{D}O_4$, calculated from the area under the curve, is found to be ~ 26, 32, 35 and 42% for $NCMO_{0.00}$, $NCMO_{0.50}$, $NCMO_{0.78}$ and $NCMO_{1.00}$ respectively which agrees well with previous finding of increasing $Mo^{D}O_4$. As illustrated in Fig. A9(a)-(d) of APPENDIX-III, two asymmetric peaks, observed in between 877 – 891 and 894 – 912 eV, are attributed to spin-orbit split $3d_{5/2}$ and $3d_{3/2}$ orbitals of Ce^{3+}. Similar to Mo orbitals, a careful deconvolution of the asymmetric $d_{5/2}$ peak yields three peaks at 882.0, 884.6, and 886.9 eV, designated $Ce3d_{5/2}$(I), $Ce3d_{5/2}$(II) and $Ce3d_{5/2}$(III), indicating presence of Ce with three different oxidation states. Herein, $Ce3d_{5/2}$(III) is assigned to Ce of regular CeO_8 polyhedra, while $Ce3d_{5/2}$(II) and $Ce3d_{5/2}$(I) denote Ce belonging to CeO_8 polyhedra with one and two oxygen vacancies (c.a. V_O and $2V_O$) and nomenclatured as CeO_7 and CeO_6 respectively. In this context, it may be stated that CeO_7 and CeO_6 correspond to deformed CeO_8 polyhedra with one and two nearby $Mo^{D}O_6$ and $Mo^{R}O_6$ subunits

(schematically shown in Fig. 3). Due to less difference of electronegativity between Ce and O, Ce – O bond is supposed to be more covalent; therefore, V_O has the predominant role on this covalence and on the binding energy of 3d orbitals. Herein, we have observed that V_O shortens Ce – O bond lengths from Rietveld analysis which in consequence increases electron – electron repulsion on the Ce site, thus the binding energy of 3d orbitals get decreased in distorted polyhedra [35]. The analysis showed that the weight percentage of Ce_a increases (~ 19, 23, 37, 41%) while there is a significant decrease in the weight percentage of Ce_b (~ 48, 46, 37, 26%) from $NCMO_{0.00}$ to $NCMO_{1.00}$. On the other hand, Ce_c remains almost unchanged for all samples (~30%). Therefore, it can be concluded that the concentration of CeO_6 increases, indicating more $2V_O$ at the cost of V_O i.e. there is a tendency of the formation of V_O cluster. XPS of O 1s displays asymmetric indicating presence of two different O species. A careful analysis reveals two O 1s peaks (Fig. A10, APPENDIX-III), measured at 530.6 and 532.4 eV eV, corresponding to lattice O and surface adsorbed O atom at V_O or $2V_O$ sites [36]. Increasing ratio of the area under the fitted curves illustrates that surface adsorbed O increases monotonically from $NCMO_{0.00}$ to $NCMO_{1.00}$ suggesting increasing V_O or $2V_O$.

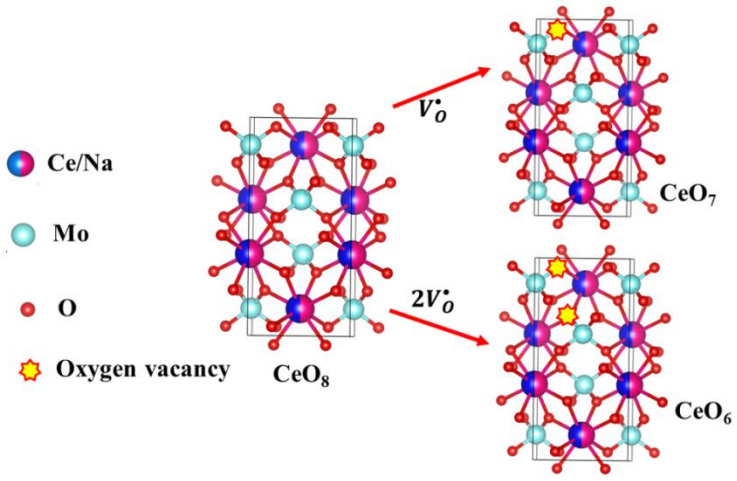

Fig. 3 Schematic diagram of oxygen vacancies of CeO_8 polyhedral unit.

3.3 Optical properties of the as-prepared NCMO samples by UV-Vis, photoluminescence spectroscopy

Optical band gap (E_g) is calculated to be ~ 3.07, 3.05, 3.02 and 2.99 eV for $NCMO_{0.00}$, $NCMO_{0.50}$, $NCMO_{0.78}$ and $NCMO_{1.00}$ from UV – Vis absorption spectra (shown in Fig. A11, APPENDIX-III). Very specifically, the variation can be understood as follows: our band structure calculation (discussed later) reveals that the valence band (VB) is made-up from hybridization between O – 2p and Mo – 4d orbitals, while the conduction band (CB) comprises of Mo – 4d, Ce – 4f and minute contribution from O – 2p orbitals. An V_O induced increase of Mo – O bond lengths (from Rietveld analyses) reduces overlapping between O – 2p and Mo – 4d orbitals, causing blue-shift of VB, which in consequence reduces E_g. Herein, all samples exhibit broad peak at 380 nm in photoluminescence excitation (PLE) spectra, monitored at emission wavelength λ_{em} = 531 nm (shown in Fig. A12, APPENDIX-III), while emission spectra, recorded in the visible region upon excitation wavelength λ_{ex} = 380 nm, are depicted in Fig. 4 (a)-(d). Presently, the peak in PLE spectra is assigned to the charge transfer (CT) absorption within MoO_4 tetrahedra in which O 2p electron goes into one of the empty Mo – 4d orbital [37]. Emission spectra have four distinct peaks in the blue (c.a. blue I, blue II, blue III) and green regions. Intense blue I peak has been noted at 440 nm (22,727 cm^{-1}), while relatively weak blue II, blue III and the prominent green peaks are measured at 462 nm (21,645 cm^{-1}), 488 nm (20,492 cm^{-1}) and 531 nm (18,832 cm^{-1}) respectively. The Stoke shift of the excitation and emission spectra is noted to be ~ 3588 cm^{-1} indicating that there may be reabsorption and interference among various emissions [38]. Although, understanding the emission spectrum from lanthanides is difficult due to several reasons including symmetry, crystal field surrounding the host crystal, anion polarizability, and covalence of the host crystal, however present emissions are typically believed to be 5d – 4f transition within Ce^{3+} [39]. As CT

band in PLE spectra involves O – 2p → Mo – 4d transition, while emissions are assigned to 5d – 4f transitions within Ce^{3+}, hence energy transfer from MoO_4 tetrahedra to Ce^{3+} is believed to occur here. In order to validate intra 5d – 4f transitions within CeO_8 polyhedron, we have calculated emission wavelength (λ in nm) using eqn (4) [40, 41]:

$$\frac{1}{\lambda} = \frac{Q^*}{hc}\left[1 - \left(\frac{V}{4}\right)^{\frac{1}{V}} 10^{\frac{-(nrE_a)}{80}}\right] \qquad (4)$$

where, Q*, V, 'n', E_a and 'r' represent the energy of 5d band edge of free Ce^{3+} ion (= 50,000 cm^{-1}), valance of the Ce^{3+}, number of anions in the immediate shell around Ce^{3+}, electron affinity of the atoms forming anions (~ 2.16 eV) and the difference between average bond length and radius of Ce^{3+} within CeO_8 polyhedra (1.03 Å). Very careful calculation yields λ ~ 449 nm, which closely matches with blue I emission. Previous studies indicate that V_O and $2V_O$ can significantly modify 5d – 4f transitions of lanthanide atoms and accordingly emission wavelength gets changed in CeO_7 and CeO_6 polyhedra. As an example, Sokolenko *et al.* [42] assigned green-red emission with WO_3•$\ddot{V}_O$ oxygen-deficient complexes, but Korzhik *et al*. ascribed green emission with WO_3 centres [43]. Considering CeO_7 and CeO_6 as V_O and $2V_O$ containing distorted CeO_8 polyhedra, we have calculated λ ~ 487 and 537 nm for intra-Ce^{3+} 5d – 4f transitions using eqn (4), those are in well-agreement with blue III and green emissions (schematically represented in Fig. A13, APPENDIX-III). For better understanding of the influence of V_O and $2V_O$ on these transitions, we have calculated shift of the centroid of d-orbitals (in eV) of Ce^{3+}, $\varepsilon_c(1, 3+, Ce^{3+})$, according to eqn (5) [44].

$$\varepsilon_c(1, 3+, Ce^{3+}) = 6.35 - E^C(1, 3+, Ce^{3+}) \qquad (5)$$

And it is found to be 5.91, 5.67 and 5.43 eV for CeO_8, CeO_7 and CeO_6 respectively. Therefore, red shift of the 5d – 4f transition is ascribed to reduce $\varepsilon_c(1, 3+, Ce^{3+})$ in CeO_7 and CeO_6 with reference to CeO_8. In order to validate blue II emission with crystal field splitted d-orbitals or not, we have

also calculated crystal field stabilization energy $\varepsilon_{cfs}\,(1,3+,\ Ce^{3+})$ using eqn (6)

$$\varepsilon_{cfs}\,(1,3+,\ Ce^{3+}) = \beta R_{av}^{-2} \qquad (6)$$

where, β = 1.35 × 10^9 pm^2 cm^{-1} for Ce^{3+} and $R_{av} = \frac{1}{N}\sum_{i=1}^{N}(R_i - 0.6\Delta R)$; R_i denotes individual bond lengths to the N coordinating anions in the un-relaxed lattice. We have obtained $\varepsilon_{cfs}\,(1,3+,Ce^{3+})$ ~ 2.16, 3.37 and 4.56 eV for CeO_8, CeO_7 and CeO_6 respectively indicating that splitting of d-orbitals of Ce^{3+} gradually increases from CeO_8 (~ 17,500 cm^{-1}) to CeO_6. Herein, we have noticed the difference between $^5D_0 - {}^2F_{5/2}$ and $^5D_0 - {}^2F_{7/2}$ transitions ~ 2,000 cm^{-1}, while blue I and blue II are differed by ~ 1082 cm^{-1}, hence blue II emission cannot be attributed to either $^5D_0 - {}^2F_{7/2}$ transition within CeO_8 polyhedra or 5d orbital splitted transition. Given that $2V_O$ gives two distinct $\varepsilon_c(1,3+,\ Ce^{3+})$ within CeO_6 according to our DFT calculations, thus we ascribe blue II emission with other $\varepsilon_c(1,3+,\ Ce^{3+})$ (discussed later). It will be interesting to note from Fig. 4(e) that intensities of green and blue II gradually increase from $NCMO_{0.00}$ to $NCMO_{1.00}$, due to increase of $2V_O$ i.e. CeO_6 which agrees well with our FTIR, XPS results giving that $Na_3Cit.2H_2O$ has a predominant role to tune oxygen vacancy, especially $2V_O$ in NCMO nanostructures. Herein, CeO_7 and CeO_6 related emission can also be intuitively understood from Kröger-Vink notation as follows: release of electrons into host matrix results V_O and $2V_O$ into ionised defects states (c.a. $V_O^{\bullet}$ and $2V_O^{\bullet}$) that can be represented by eqn (7) and (8)

$$[CeO_8]^x + \left[CeO_7 \bullet V_O^X\right] \rightarrow [CeO_8]' + [CeO_7 \bullet V_O^{\bullet}] \qquad (7)$$

$$[CeO_8]^x + \left[CeO_6 \bullet 2V_O^X\right] \rightarrow [CeO_8]'' + [CeO_6 \bullet 2V_O^{\bullet}] \qquad (8)$$

Where $[CeO_8]'$ and $[CeO_8]''$ are electron donors, while $[CeO_7 \bullet V_O^{\bullet}]$ and $[CeO_6 \bullet 2V_O^{\bullet}]$ act as electron acceptor giving emission. Here, we ascribe $[CeO_8]'$ for blue III, while $[CeO_8]''$ for and blue I, green emissions. In general, emission related to trivalent lanthanide exhibits weak electron – phonon coupling, mostly

giving one-phonon induced side band. Presently, a careful monitoring of green emission reveals presence of a phonon side band (PSB) at 516 nm with phonon energy 930 cm^{-1} which closely is related with $\nu_4(F_2)$ phonon of Mo^RO_4, thus it can be inferred that MoO_4 tetrahedra to Ce^{3+} (within CeO_6 polyhedra) charge transfer process is associated with $\nu_4(F_2)$ phonon mode. In this context, Huang – Rhys (S) factor [45], the indicator of electron – phonon coupling has been calculated according to eqns (9) and (10):

$$S = {}^{I_{PSB}}/_{I_{ZP}} \qquad (9)$$

$${}^{I_{1P}}/_{I_{ZP}} = \frac{W_1(S,<m>)}{W_0(S,<m>)} = \begin{cases} S < 1 + m >, p \geq 0 \\ S < m >, p < 0 \end{cases} \qquad (10)$$

Where, I_{PSB}, I_{ZP} and I_{1P} are the integrated intensities of the PSB, zero phonon line and one phonon line. As this emission includes a single phonon ($p \geq 0$ in eqn (10)), and considering $^5D_0$- $^2F_{5/2}$ transition purely dipolar, we may write I_{PSB}= I_{1P}. In addition, $< 1 + m >$ can also be considered as 1 due to higher phonon energy at room temperature. Therefore, S – factor has been calculated to 0.098, 0.077, 0.032 and 0.039 for four respective samples. This decrease of the S – factor may be ascribed to increasing distortion in the lattice structure and crystal field due to V_O, $2V_O$ which weaken the electron – phonon coupling strength in NCMO nanostructures.

Commission International De I'Eclairage (CIE) coordinate (Fig. 4(f)), calculated to be (0.180, 0.149), (0.180, 0.147), (0.170, 158) and (0.172, 0.148) of respective $NCMO_{0.00}$, $NCMO_{0.50}$, $NCMO_{0.78}$ and $NCMO_{1.00}$ samples, are well spread around blue region of the visible spectrum, indicating color purity (CP) of the NCMO samples [46]. We have also validated CP using eqn (11) [47,48]:

$$CP = \frac{\sqrt{(x-x_i)^2+(y-y_i)^2}}{\sqrt{(x_d-x_i)^2+(y_d-y_i)^2}} \times 100\% \qquad (11)$$

where (x, y) denotes the phosphor's color coordinates; (x_i, y_i) is the 1931 CIE Standard Source's illuminant point, with color coordinates of (0.3101, 0.3162); and (x_d, y_d) is the dominant wavelength's color coordinates. Herein, outstanding

CP ~ 90 – 94% has been observed for the samples indicating that NCMO can be good candidate for light emitting application. Correlated colour temperature (CCT), calculated from the McCamy's relation [49]:

$$CCT = 449n^3 + 3525n^2 + 6823.3n + 5520.3 \qquad (12)$$

where $n = \frac{(x-0.3320)}{(0.1858-y)}$ and (x, y) represents the chromaticity co-ordinates, is as ~ 7819K, 7630K, 7715K and 7854K for sample $NCMO_{0.00}$, $NCMO_{0.50}$, $NCMO_{0.78}$ and $NCMO_{1.00}$ respectively. High CCT indicates that NCMO can be used for cold lighting.

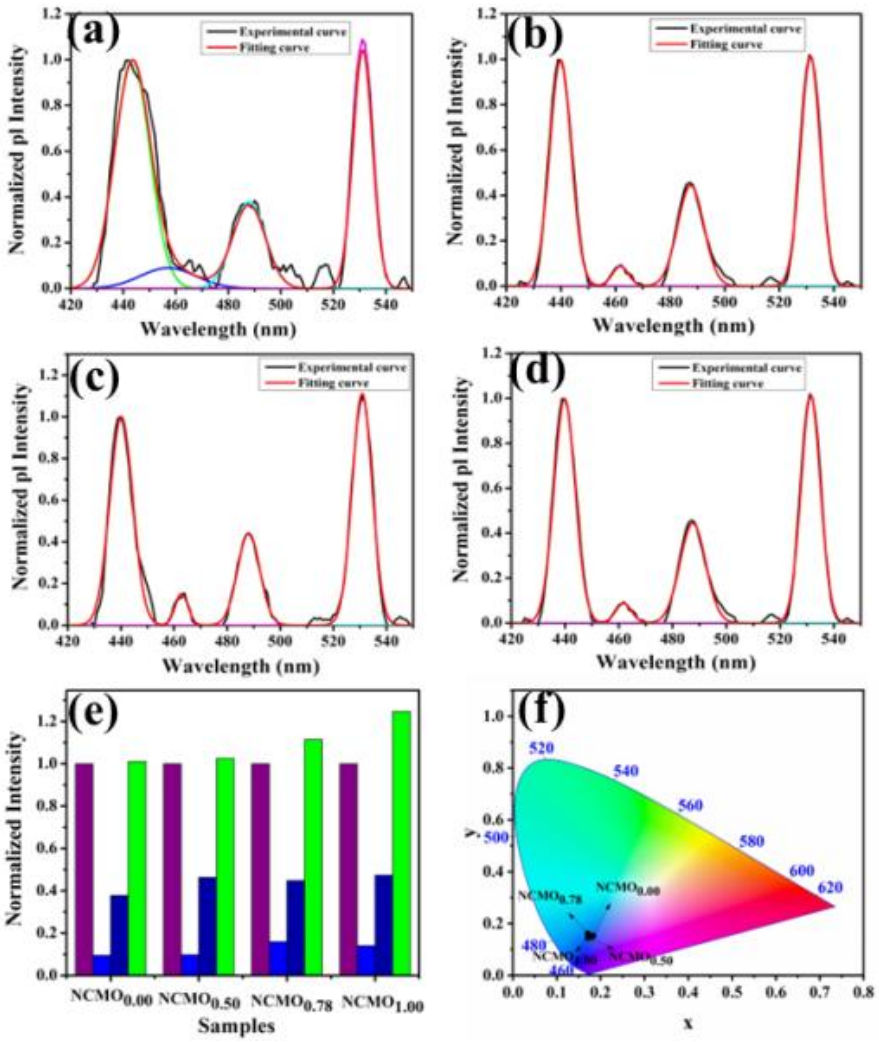

Fig. 4 Photoluminescence spectra of (a) $NCMO_{0.00}$, (b) $NCMO_{0.50}$, (c) $NCMO_{0.78}$ and (d) $NCMO_{1.00}$ respectively (e) Normalized PL intensity ratio of emission wavelengths (f) The CIE chromaticity diagram of the NCMO phosphors.

3.4 Investigations of gas sensing properties of NCMO nanostructures

Gas sensing property of any metal oxide nanostructures mostly involved solid-gas interfacial reaction mechanism where adsorption and desorption of targeted gas molecules on the surface of these nanostructures lead to a significant change in resistance, which is the basis for gas detection. Oxygen vacancies on the surface of the oxide nanostructures provide active sites for chemisorbed oxygen, described by $O_2(gas) + e^- \leftrightarrow O_2^-(ads)$, which in consequence increase the adsorption capacity of target the gas molecules, hence sensing efficiency gets improved significantly [50-53]**.** As our previous investigation show that NCMO samples contain V_O and $2V_O$ which may adsorb oxygen which in consequence may introduce gas sensing activity within NCMO. In this regard, a careful literature survey illustrates that the following redox reactions take between nanostructure and acetone (CH_3COCH_3), ethanol (C_2H_5OH), ammonia (NH_3), methanol (CH_3OH), formaldehyde (HCHO) place in the presence of $O_2^-(ads)$.

$$CH_3COCH_3(gas) + 8O_2^-(ads) \leftrightarrow 3H_2O(gas) + 3CO_2(gas) + 8e^- \quad (13)$$

$$CH_3CH_2OH(gas) + O_2^-(ads) \leftrightarrow 2H_2O(gas) + C_2H_2O + 2e^- \quad (14)$$

$$4NH_3(gas) + 3O_2^-(ads) \leftrightarrow 6H_2O(gas) + 2N_2(gas) + 3e^- \quad (15)$$

$$CH_3OH(gas) + O_2^-(ads) \leftrightarrow 2H_2O(gas) + CO(gas) + 2e^- \quad (16)$$

$$HCHO(gas) + O_2^-(ads) \leftrightarrow H_2O(gas) + CO_2(gas) + 2e^- \quad (17)$$

From previous studies, we have noticed that our synthesized samples contain $[CeO_8]'$ and $[CeO_8]''$ as electron donors. Therefore, it can be predicted that electrons from $[CeO_8]'$ and $[CeO_8]''$ may be transported to the chemisorbed O_2 molecule which will generate $O_2^-(ads)$ on the surface of NCMO nanostructures. Hence, NCMO nanostructures may have sensing property. In order to validate gas sensing ability of our synthesized NCMO nanostructures as proof of concept, we have carried out a series of sensing measurements using $NCMO_{0.00}$,

$NCMO_{0.50}$, $NCMO_{0.78}$ and $NCMO_{1.00}$ as resistive sensor probe against NH_3, acetone, ethanol methanol and formaldehyde at different operating temperatures in the range 200°C – 450°C at an interval of 50°C. In this regard, through studies illustrate optimum operating temperature ~ 300°C for all samples (shown in Fig. 5(a) and they are highly selective against CH_3COCH_3 (presented in Fig. 5(b)). In this context, it may be stated that selectivity was examined by exposing the sensor probe to 5.0 ppm of target analyte gases including CH_3COCH_3, C_2H_5OH, NH_3, CH_3OH, and HCHO. It can also be noted from the Fig. A14 (a) of APPENDIX-III that CH_3COCH_3 sensitivity (tested within 1.0 – 100.0 ppm) initially increases with increase in acetone concentration, then gradually slows down and tends to saturate at higher acetone concentration for all samples. It would be very interesting to note that the sensitivity monotonically increases from $NCMO_{0.00}$ to $NCMO_{1.00}$ giving highest sensitivity for $NCMO_{1.00}$, whereas sensitivity to other interfering gases ($\frac{R_{gas}}{R_{air}} < 1.2$) are very less in comparison with CH_3COCH_3. To understand the gas adsorption process on the surface, particularly to understand the influence of V_O and $2V_O$ on the sensing efficiency, we have fitted the response data with Freundlich adsorption isotherm as given in eqn (18) and (19).

$$S_g = 1 + aC_g{}^b \qquad (18)$$

$$\text{i.e. } \log(S_g - 1) = a + b \log(C_g) \qquad (19)$$

where, S_g and C_g represent sensitivity and concentration of the analyte gas, and 'a', 'b' are constants those depend on the electrical charge of the species and stoichiometry of the reactions on the surface of the sensing probe. It has been identified previously that 'b' is highly sensitive to the surface adsorbed O species, specifically $b \leq 0.5$ in case of O^{2-} adsorption, while $b \approx 1.0$ for O^- [54]. As displayed in Fig. 5(c), linear regressions have been observed for all samples according to eqn (19) and from slope of the curve, we have obtained b ~ 0.423, 0.279, 0.088, 0.053 for $NCMO_{1.00}$, $NCMO_{0.78}$, $NCMO_{0.50}$ and

$NCMO_{0.00}$ respectively. Hence, it may be stated that $2V_O$ rather than V_O acts as an active for O^{2-} which facilitates CH_3COCH_3 adsorption. We have also evaluated dynamic sensing response of $NCMO_{1.00}$ based sensor at 300°C in the presence of CH_3COCH_3 within the concentration range of 1.0 – 100.0 ppm (shown in Fig. 5(d)). As presented in Fig. 5(d), our measurements demonstrate sensitivity ~ 1.86, 2.81, 4.95, 6.21 and 6.89 in the presence of 1.0, 5.0, 10.0, 50.0 and 100.0 ppm of CH_3COCH_3. Fig. A14 (b) of APPENDIX-III shows continuous response and recovery curve for six consecutive cycles (at 5.0 ppm of CH_3COCH_3) and most notably the response value is almost same for all cycles (error $\leq 2\%$) indicating excellent reproducibility of $NCMO_{1.00}$ as sensor probe. The dynamic response curves of $NCMO_{0.00}$, $NCMO_{0.50}$, $NCMO_{0.78}$ based sensors at 300°C in the presence of CH_3COCH_3 are shown in Fig. A14 (c-e) of APPENDIX-III. The response and recovery time (Fig. 5(e)), measured at 1.0 ppm CH_3COCH_3, are found to be ~ 1.5s/33.8s indicating very fast response of $NCMO_{1.00}$ as sensing probe. In order to validate long-term stability of $NCMO_{1.00}$ as sensor probe, we have tested the sensing response for over 90 days at an interval of 10 day (Fig. 5(f)), while no significant drift has been observed indicating reliability of $NCMO_{1.00}$ as sensor probe.

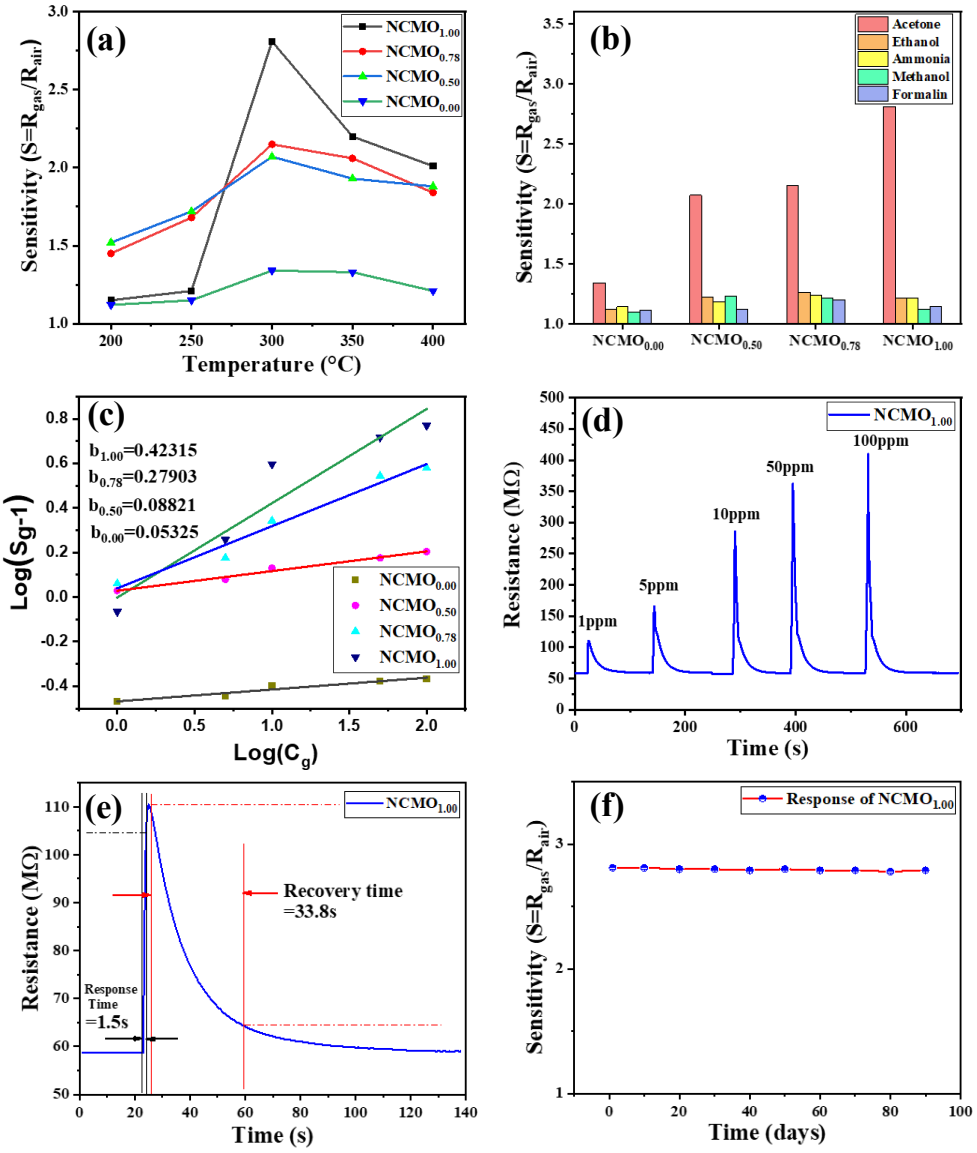

Fig. 5 (a) Temperature calibration curve of $NCMO_{0.00}$, $NCMO_{0.50}$, $NCMO_{0.78}$ and $NCMO_{1.00}$, respectively. (b) Selectivity of $NCMO_{0.00}$, $NCMO_{0.50}$, $NCMO_{0.78}$ and $NCMO_{1.00}$ sensors measured at 300°C operating temperature. (c) Linear fitting of logarithm of sensitivity and logarithm of acetone concentration data of all samples. (d) Dynamic acetone response curve of $NCMO_{1.00}$ sensor to acetone concentration from 1 – 100 ppm at 300°C. (e) Response and recovery time of $NCMO_{1.00}$ based sensor for 1 ppm acetone at 300°C. (f) Long term stability of $NCMO_{1.00}$ based sensor in 1 ppm acetone sensing measured over 90 days.

3.5 Density functional theory (DFT) calculation of NCMO

In order to validate V_O and $2V_O$ associated optical emissions and sensing activity, we have calculated the electronic band structure, total density of states (TDOS), and angular momentum projected partial density of states (PDOS) using ab initio density functional theory (DFT) that provides valuable insights about energy levels and electronic states, which can help to explain its luminescent behaviour. Herein, we have calculated band structure along several high symmetry k-points within the Brillouin zone. In this calculation, we have removed one and two O atoms from the NCMO unit cell to mimic CeO_7 (c.a. V_O) and CeO_6 ($2V_O$) and their associated optical transitions. Prior to calculate electronic band structure, we have optimized unit cell of pure NCMO and obtained lattice parameters a = b ~ 5.355 and c ~ 11.611Å, Na/Ce – O, Mo-O lengths ~ 2.453 and 1.806 Å respectively in well agreement experimental results proving the accuracy of our calculations, specifically choice of exchange correlation, pseudopotential. Herein, top of the valence band maxima (VBM) is set to zero as reference for other calculations. It appears from Fig. 6(a) that NCMO is an indirect bandgap material (E_g ~ 3.23 eV) having spin – unpolarized VBM and spin – polarized conduction band minima (CBM) at Γ– and X– point respectively. Curvature of the VBM is observed to be low, indicating a comparatively high effective hole mass, while CBM has a high curvature suggesting low effective mass of electron which is beneficial for high mobility of electrons. TDOS (shown in Fig. 6(b)) and PDOS contribution of O, Mo, Ce and Na (shown in Fig. A15(c)-(f), APPENDIX-III) demonstrates that the upper part of the VB is primarily composed of O – $2p_x$, $2p_y$, and $2p_z$ orbitals and with very little contributions from Mo – $2p_x$, $2p_y$, and $2p_z$ giving low curvature. Whilst, lower part of VB originates from predominant hybridization between Mo – $4d_{xy}$, $4d_{xz}$, $4d_z^2$ and O – $2p_x$, $2p_y$, and $2p_z$ orbitals, wherein $4d_x^2$ and $4d_{yz}$ contribute insignificantly. We have noticed almost no contribution from Ce – 4f and Na – 3s orbitals to VB. CBM comprises of between spin

polarized (c.a. up – spin) Ce – $4f_z^3$, $4f_{xz}^2$ and $4f_y{}^3{}_x{}^2$ orbitals, among which most predominant contribution comes from $4f_{xz}^2$, hybridized with O – $2p_x$, $2p_y$, $2p_z$ orbitals giving higher curvature in comparison with VBM, while upper portion of the CB is made of Mo – $4d_z^2$, $4d_x^2$. Thus, it may be stated that MoO_4 tetrahedra mostly construct VB, while CB is predominantly contributed from CeO_8 polyhedra and band-to-band transition includes Mo ↔ Ce charge transfer process.

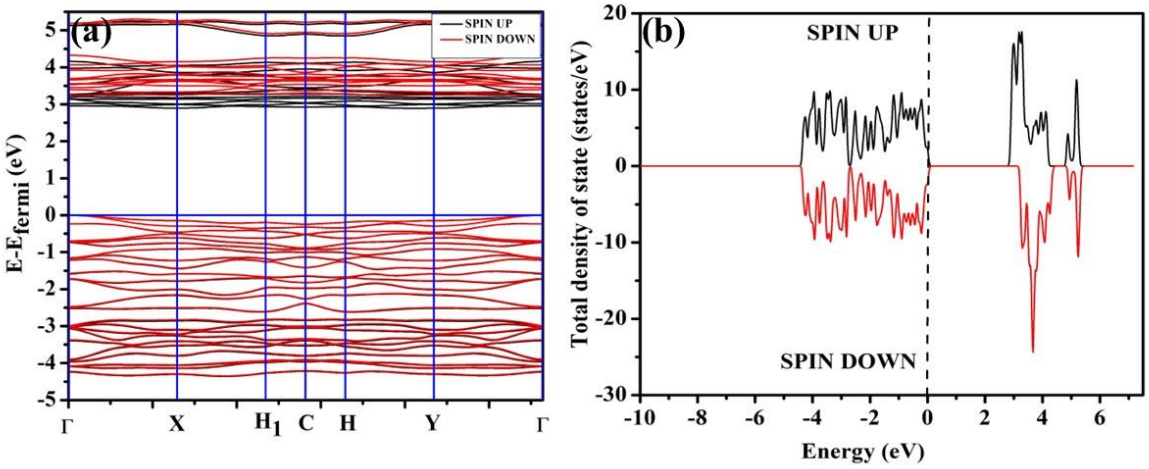

Fig. 6 (a) Band structure and (b) spin polarised TDOS of NCMO.

Band structures, TDOS and PDOS of $V_O^{\bullet}$ and $2V_O^{\bullet}$ contained NCMO samples, designated as NCMO – $V_O^{\bullet}$ and NCMO – $2V_O^{\bullet}$, are represented in Fig. A16 and A17 of APPENDIX-III respectively. Notably, both VBM and CBM (shown in Fig. A16(a), APPENDIX-III) of NCMO – $V_O^{\bullet}$ remains unchanged, while in case of NCMO – $2V_O^{\bullet}$, CBM band has shifted into Γ – point (shown in Fig. A16(a), APPENDIX-III) indicating transformation from indirect to direct E_g nature of NCMO. Herein, we have noticed E_g ~ 3.01 and 2.95 eV for NCMO – $V_O^{\bullet}$ and NCMO – $2V_O^{\bullet}$ suggesting decrease of E_g due to $V_O^{\bullet}$ and $2V_O^{\bullet}$. Thus, monotonic decrease of experimentally measured E_g from $NCMO_{0.00}$ to $NCMO_{1.00}$ is believed to be due to increasing V_O and $2V_O$ corroborating XPS studies. Herein, reduction of E_g can be understood as follows: TDOS (Fig. A16(b) and A17(b),

APPENDIX-III) and PDOS (Fig. A16(c)-(f) and Fig. A17(c)-(f), APPENDIX-III) calculations show that VB width decreases in NCMO – $2V_O^{\bullet}$ due to more localization of O 2p orbitals, while curvature increases in NCMO – $V_O^{\bullet}$ and NCMO – $2V_O^{\bullet}$, attributed to enhanced overlapping between Ce – $4f_{zx}^2$, $4f_{xz}^2$, $4f_{yz}$, $4f_{xyz}$ and O – $2p_x$, $2p_y$, $2p_z$ orbitals due to decrease of Ce – O bond lengths in CeO_8 polyhedra indicating higher carrier mobility. Further analysis of the TDOS and PDOS reveals that the contribution from Ce – $5d_{xy}$ and $5d_{xz}$ increases to CB in NCMO – $V_O^{\bullet}$ and NCMO – $2V_O^{\bullet}$. Defect state at 2.44 eV above valance band in NCMO – $V_O^{\bullet}$ has been assigned to Ce – $5d_z^2$, whilst these defects are found at 2.26 and 2.40 eV above in NCMO – $2V_O^{\bullet}$ due to Ce – $5d_z^2$ and Ce – $5d_x^2$ respectively. Therefore, it can be stated that blue III emission originates from Ce $5d_z^2 \rightarrow$ 4f transitions in CeO_7 polyhedra, while the blue II and green emissions are attributed to Ce $5d_z^2 \rightarrow$ 4f and Ce $5d_x^2 \rightarrow$ 4f transitions in CeO_6 polyhedra, respectively as schematically presented in Fig. 7.

For the calculation of the adsorption energies of NCMO, NCMO – $V_O^{\bullet}$ and NCMO – $2V_O^{\bullet}$ system using eqn (1), we found the energies listed in Table A2, APPENDIX-III. E_{ads}(eV) represents the adsorption energies of pristine NCMO, NCMO – $V_O^{\bullet}$, NCMO – $2V_O^{\bullet}$ system and found that $E_{ads} < 0$ indicating the adsorption processes involved in these systems are thermodynamically stable and exothermic, meaning that they release energy during the adsorption process. Additionally, the increasing negative value of NCMO – $V_O^{\bullet}$ and NCMO – $2V_O^{\bullet}$ suggest that the presence of active sites (oxygen vacancies) on the NCMO surface, which create localized electron-rich sites enabling strong interactions occurring between the adsorbate (acetone molecule) and the adsorbent (NCMO) surface [55]. Our experimental results showed that $NCMO_{1.00}$ exhibits best sensing results (Fig. 5) than other samples due to more oxygen vacancies as demonstrated from FTIR, Raman and XPS study which corroborates with theoretical results.

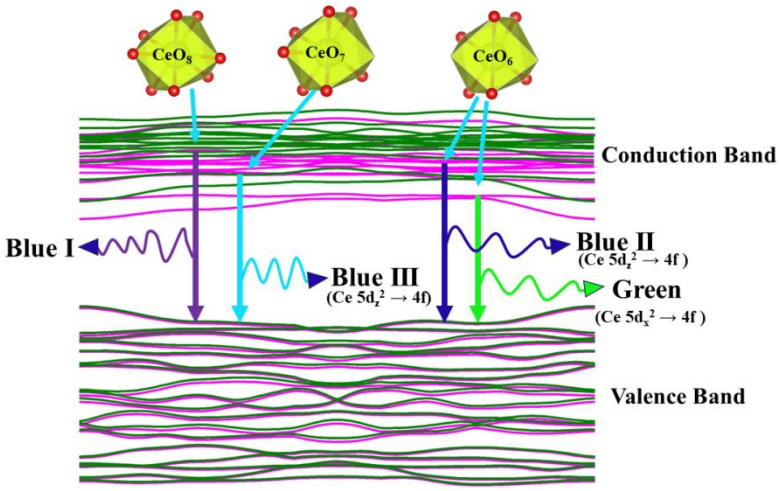

Fig. 7 Schematic picture of luminescent transitions within different CeO_8 polyhedra involving different orbitals.

4. Conclusion

In summary, the study reports the synthesis and characterization of oxygen-deficient NCMO materials, which exhibit intense blue I, green emissions and comparatively low intense blue II, blue III emissions. These emissions are attributed to the 5d → 4f transitions of Ce in different CeO_8 polyhedral configurations. The study also identifies the gas sensing properties of NCMO, which is attributed to oxygen vacancies related to CeO_7 and CeO_6. The valence and conduction bands of NCMO comprise O - 2p and O - 2p, Ce - 5d orbitals respectively and are highly sensitive to oxygen vacancies, making them potentially useful for tuning optical and gas sensing applications. The results suggest that NCMO may be a promising material for light-emitting and gas sensing applications.

APPENDIX-III

Table A1: Refined structural parameters and the reliability factors from the Rietveld fitting of NCMO samples.

Properties		$NCMO_{0.00}$	$NCMO_{0.50}$	$NCMO_{0.78}$	$NCMO_{1.00}$
Lattice parameter (A^0)	a=b	5.412(8)	5.404(2)	5.404(2)	5.398(9)
	c	11.569(2)	11.487(5)	11.478(5)	11.440(4)
Unit cell volume $(A^0)^3$		338.931(10)	335.755(3)	335.209(2)	333.518(2)
Bond length (A^0)	Na/Ce-O	2.5143(14) 2.3748(7)	2.497(4) 2.3062(4)	2.467(8) 2.2762(8)	2.448(4) 2.2578(3)
	Mo-O	1.772(17)	1.784(5)	1.786(5)	1.789(5)
Bond angle (in degree)	Na/Ce-O-Na/Ce	102.842(4)	102.033(10)	101.996(9)	102.008(9)
	Na/Ce-O-Mo	133.820(3)	133.244(7)	133.238(7)	133.226(6)
	O-Mo-O	107.397(4)	106.587(10)	106.550(9)	106.532(9)
Crystallite size (nm)		71.20	92.00	107.70	91.40
R_p (%)		14.10	12.10	16.20	15.00
R_{wp} (%)		18.80	18.20	17.60	18.40
R_{exp} (%)		8.77	14.60	13.40	10.80
χ^2		3.57	2.29	3.53	3.29

Table A2: Calculated energy (from DFT) for Acetone adsorption of NCMO samples

System	$E_{NCMO + acetone}$ (eV)	E_{NCMO} (eV)	$E_{acetone}$ (eV)	E_{ads} (eV)	No of atom	E_{ads} (eV)/at

					(NCMO + acetone)	om
NCMO	-195.666	-97.069	67.592	-166.189	33	-5.030
NCMO – $V_O^{\bullet}$	-186.202	-87.194	67.592	-166.600	32	-5.206
NCMO – $2V_O^{\bullet}$	-196.614	-77.141	67.592	-187.065	31	-6.030

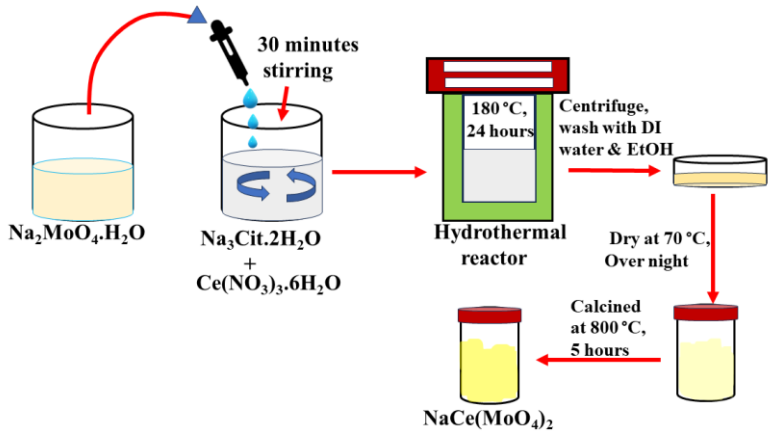

Fig. A1 Schematic representation of reaction procedure.

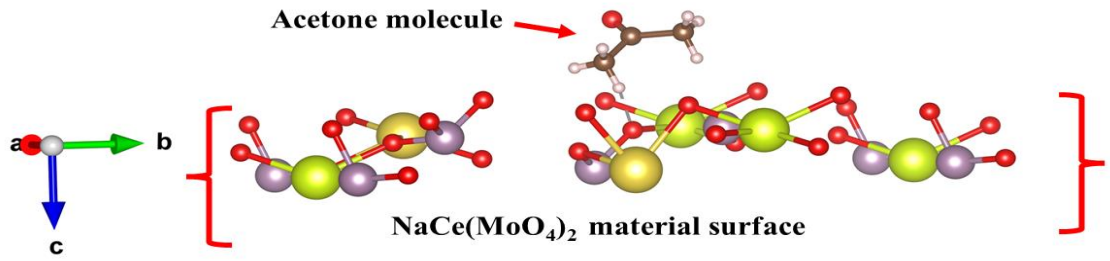

Fig. A2 Atomic structure of acetone molecule adsorption on NCMO (112) surface.

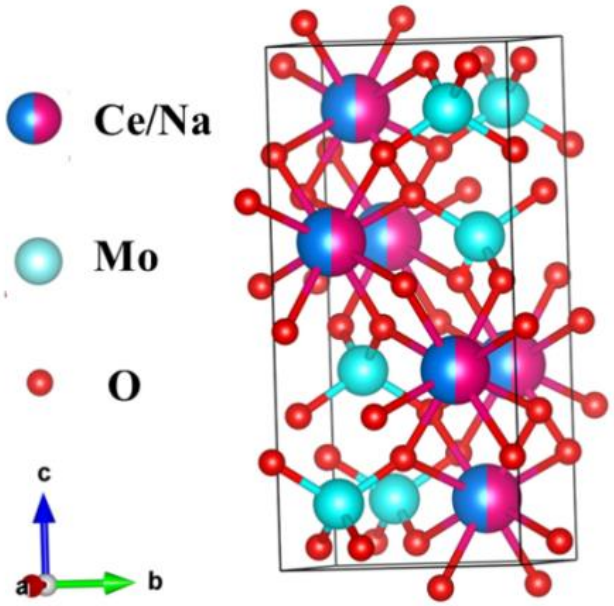

Fig. A3 Structure of the NCMO (Tetragonal) nanostructure.

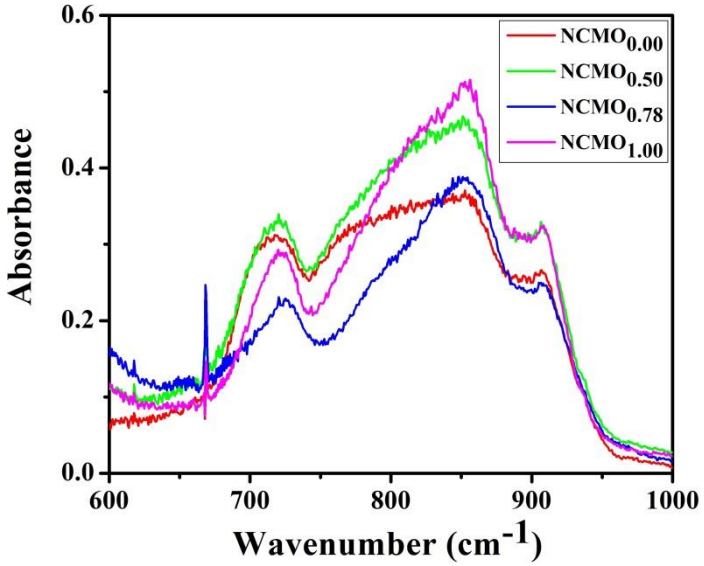

Fig. A4 FTIR spectra of NCMO nanostructures.

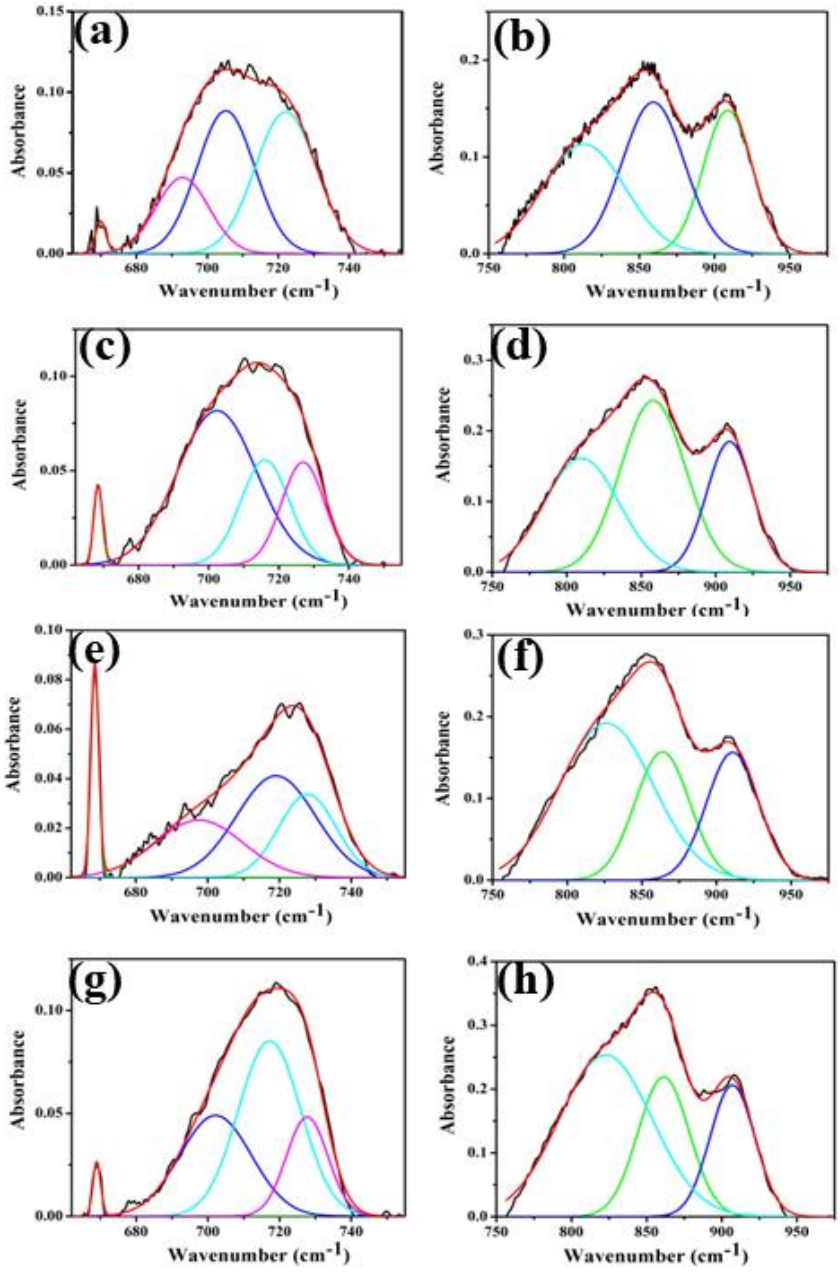

Fig. A5 Deconvoluted FTIR bands 660-750 and 750-960 of $NCMO_{0.00}$ (a, b), $NCMO_{0.50}$ (c, d), $NCMO_{0.78}$ (e, f) and $NCMO_{1.00}$ (g, h) respectively.

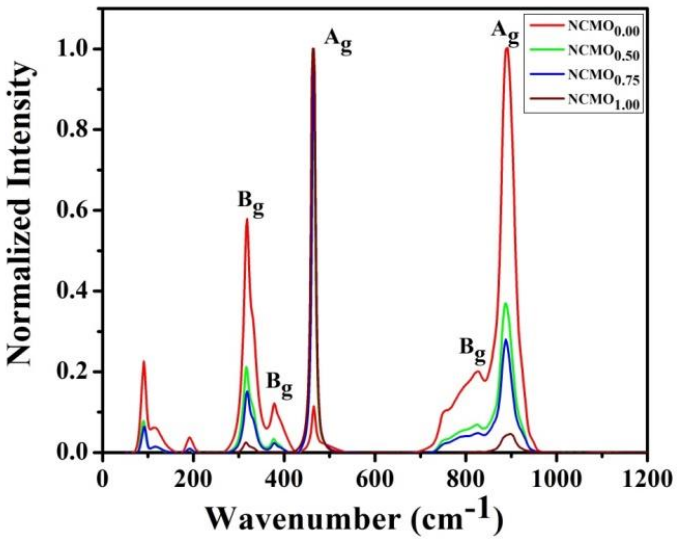

Fig. A6 Raman spectra of NCMO nanostructures.

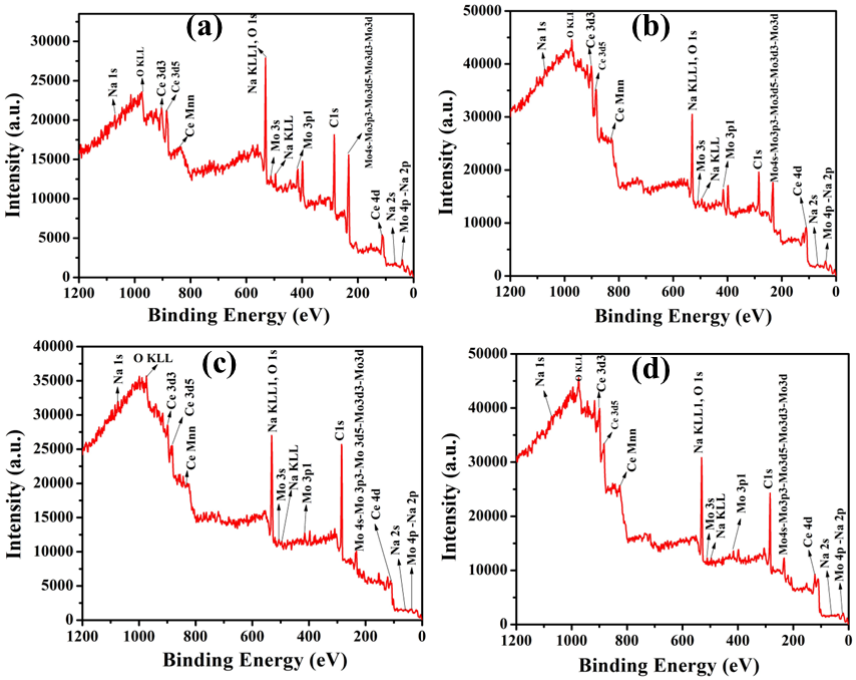

Fig. A7 XPS wide spectrum of Ce-3d, W-4f, O-1s, Na-1s of (a) $NCMO_{0.00}$, (b) $NCMO_{0.50}$, (c) $NCMO_{0.78}$ and (d) $NCMO_{1.00}$ respectively.

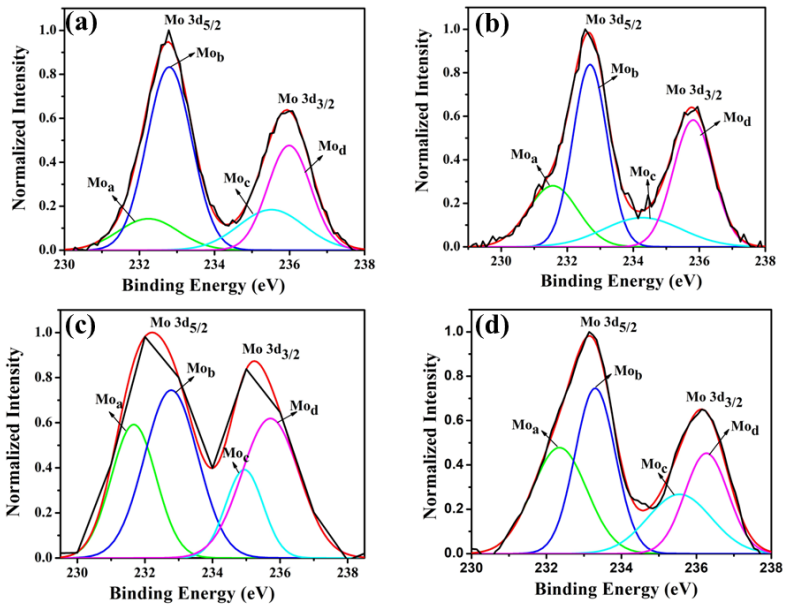

Fig. A8 XPS Mo 3d of (a) $NCMO_{0.00}$, (b) $NCMO_{0.50}$, (c) $NCMO_{0.78}$ and (d) $NCMO_{1.00}$ respectively.

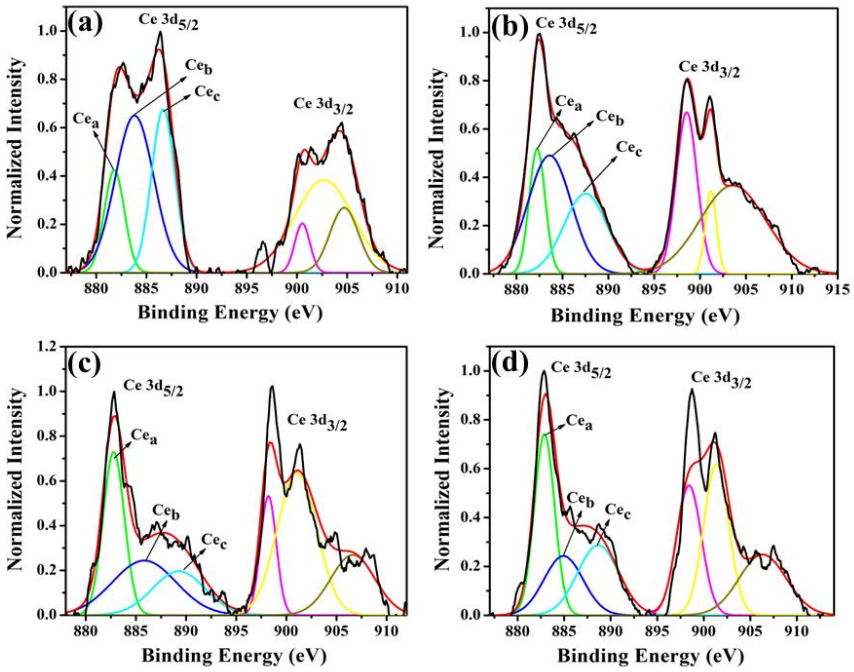

Fig. A9 XPS Ce 3d core level spectra of (a) $NCMO_{0.00}$, (b) $NCMO_{0.50}$, (c) $NCMO_{0.78}$ and (d) $NCMO_{1.00}$ respectively.

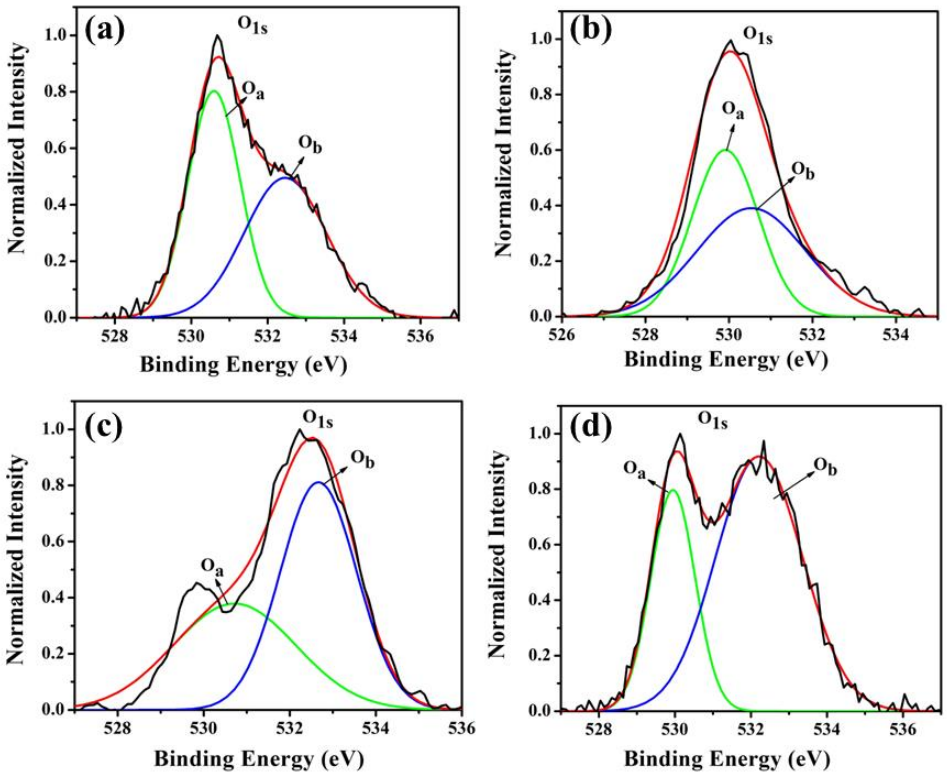

Fig. A10 XPS O1s core level spectra of (a) $NCMO_{0.00}$, (b) $NCMO_{0.50}$, (c) $NCMO_{0.78}$ and (d) $NCMO_{1.00}$ respectively.

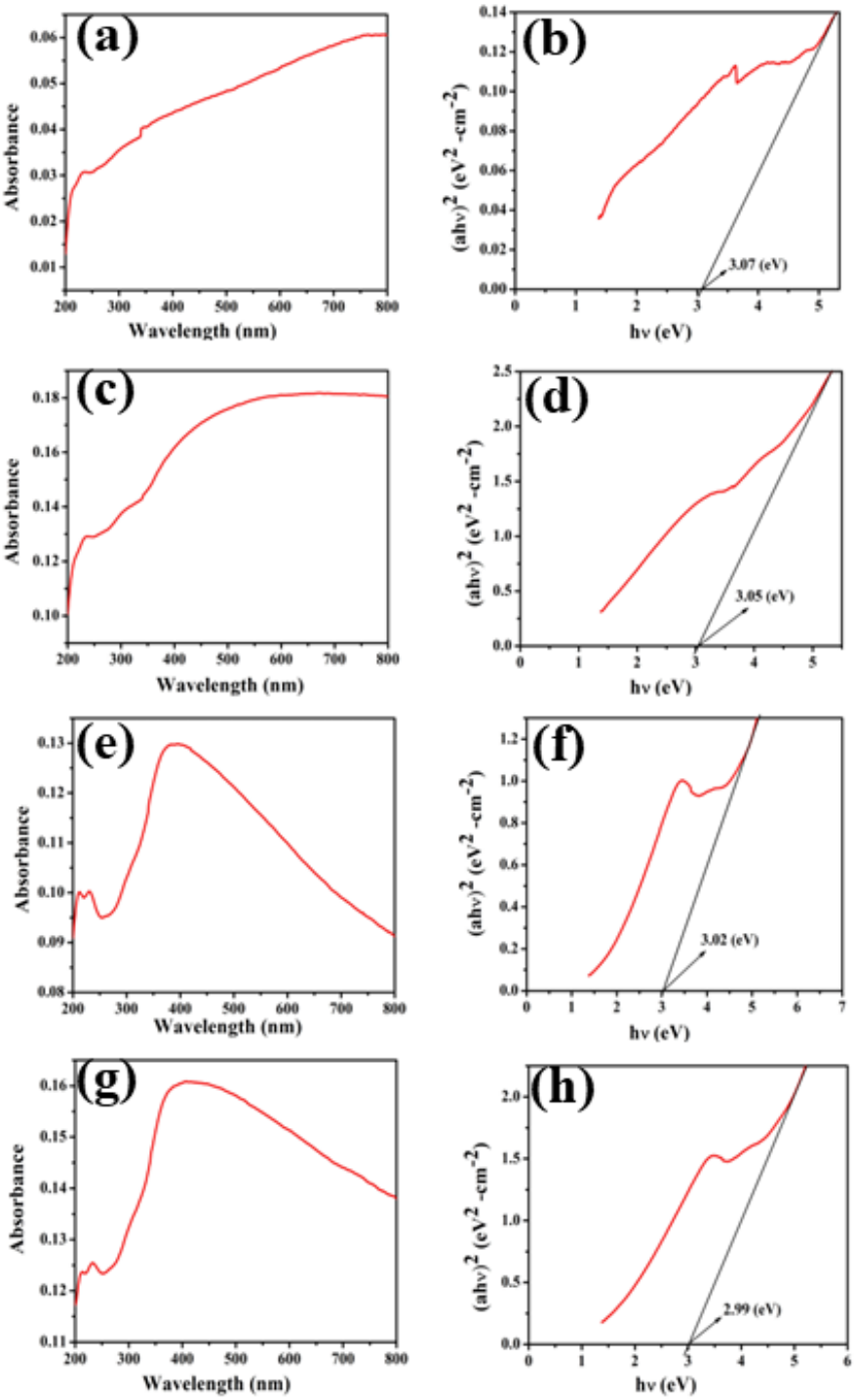

Fig. A11 UV spectra and corresponding band gap of (a, b) $NCMO_{0.00}$, (c, d) $NCMO_{0.50}$, (e, f) $NCMO_{0.78}$ and (g, h) $NCMO_{1.00}$ respectively.

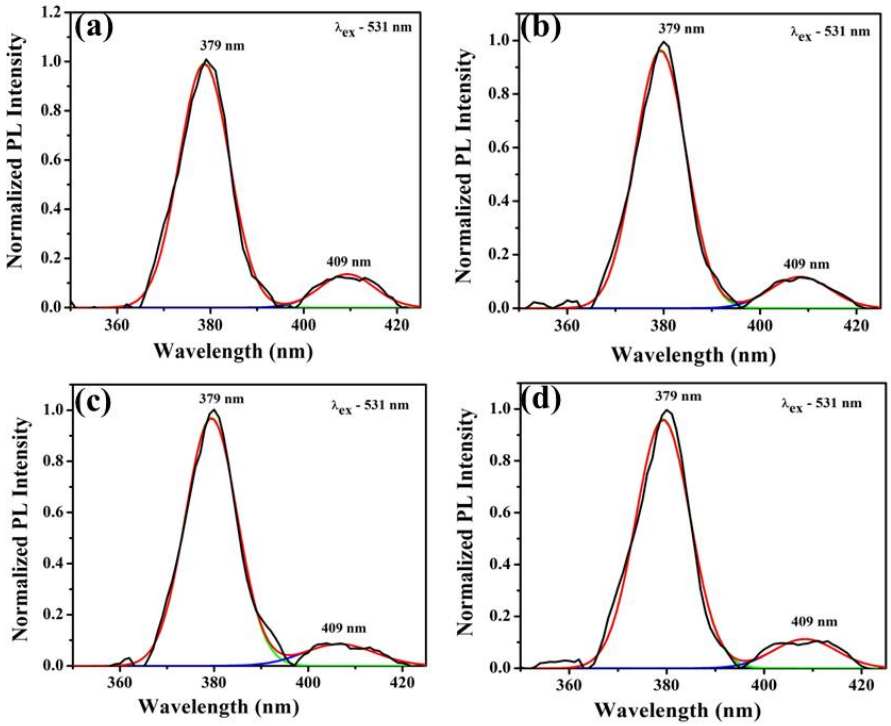

Fig. A12 PLE spectra of (a) $NCMO_{0.00}$, (b) $NCMO_{0.50}$, (c) $NCMO_{0.78}$ and (d) $NCMO_{1.00}$ respectively.

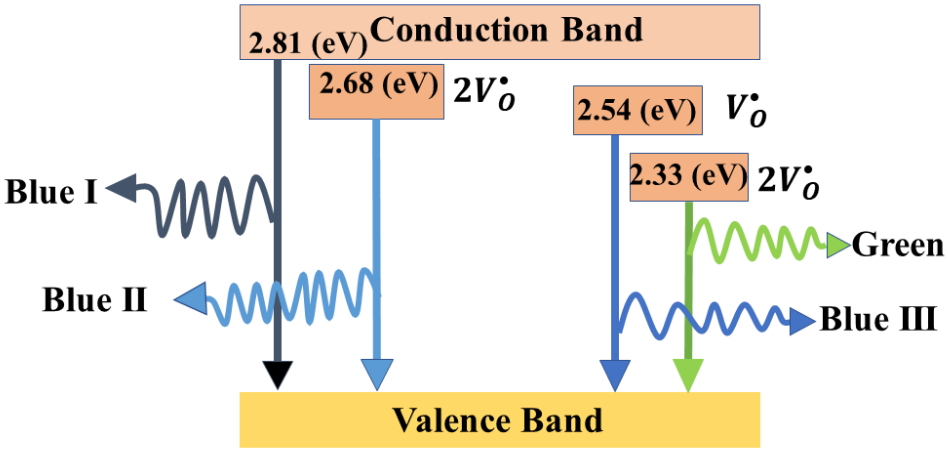

Fig. A13 Schematic representation of luminescent transitions of NCMO.

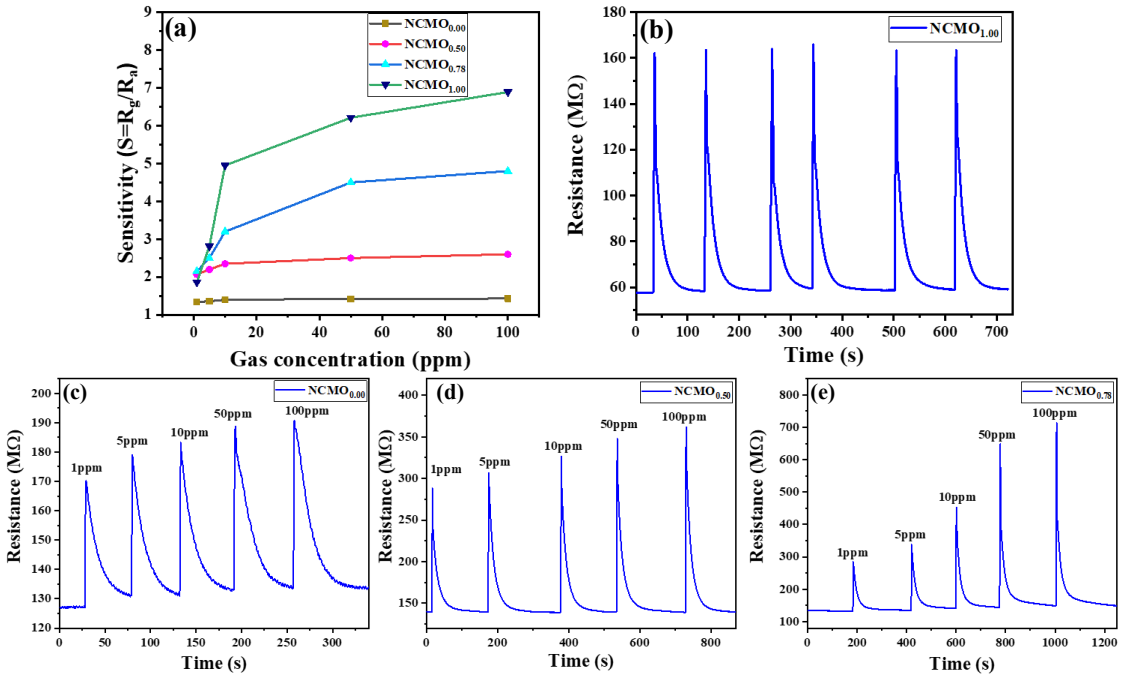

Fig. A14 (a) Sensitivity vs acetone concentration (1-100 ppm) curve for $NCMO_{0.00}$, $NCMO_{0.50}$, $NCMO_{0.78}$ and $NCMO_{1.00}$ at 300°C, (b) Cyclic response-recovery curves of $NCMO_{1.00}$ sensor to 5 ppm acetone for six consecutive cycles of measurement at 300°C. Dynamic acetone response curve of (c) $NCMO_{0.00}$, (d) $NCMO_{0.50}$ and (e) $NCMO_{0.78}$ sensor to acetone concentration from 1 – 100 ppm at 300°C, respectively.

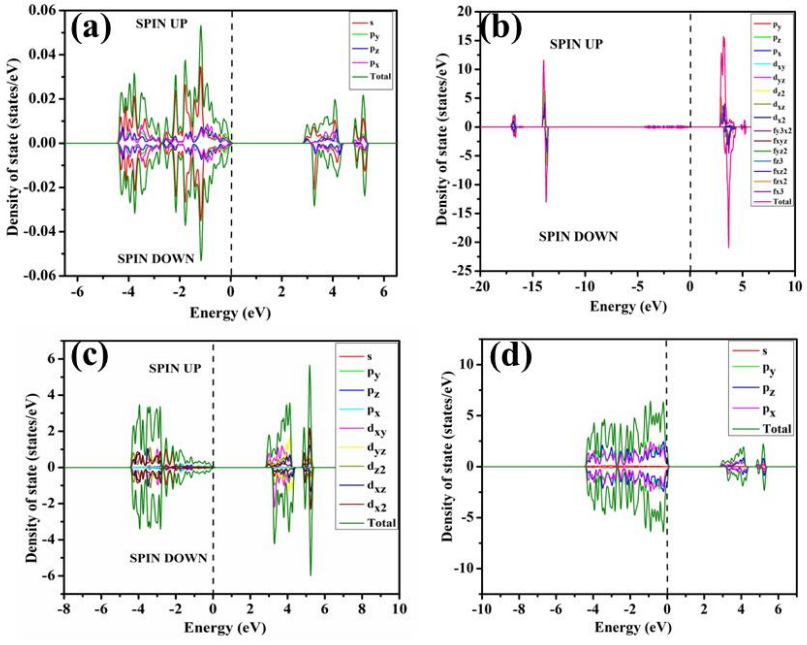

Fig. A15 PDOS of (a) Na, (b) Ce, (c) Mo and (d) O of NCMO.

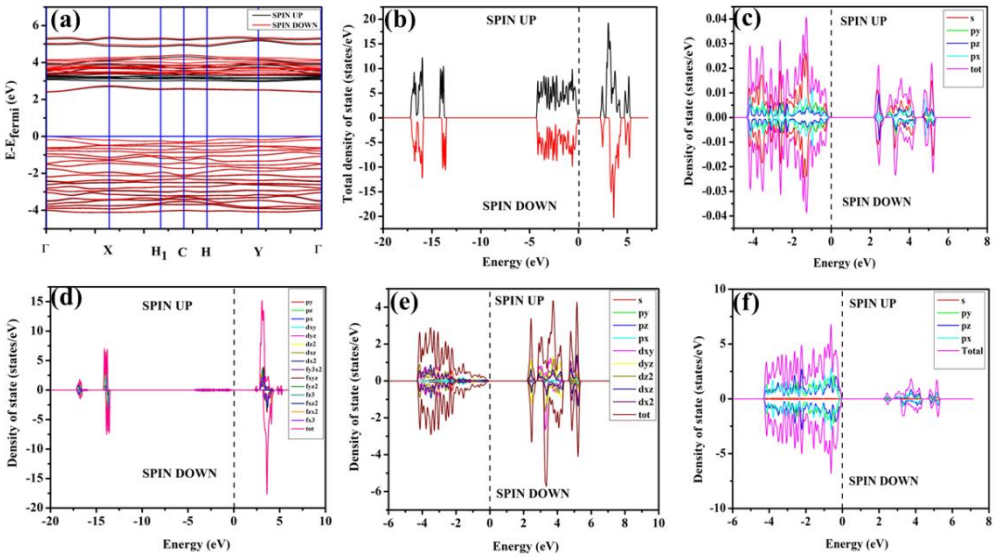

Fig. A16 (a) Band structure and (b) spin polarised TDOS and PDOS of (c) Na, (d) Ce, (e) Mo and (f) O of NCMO – $V_O^{\bullet}$.

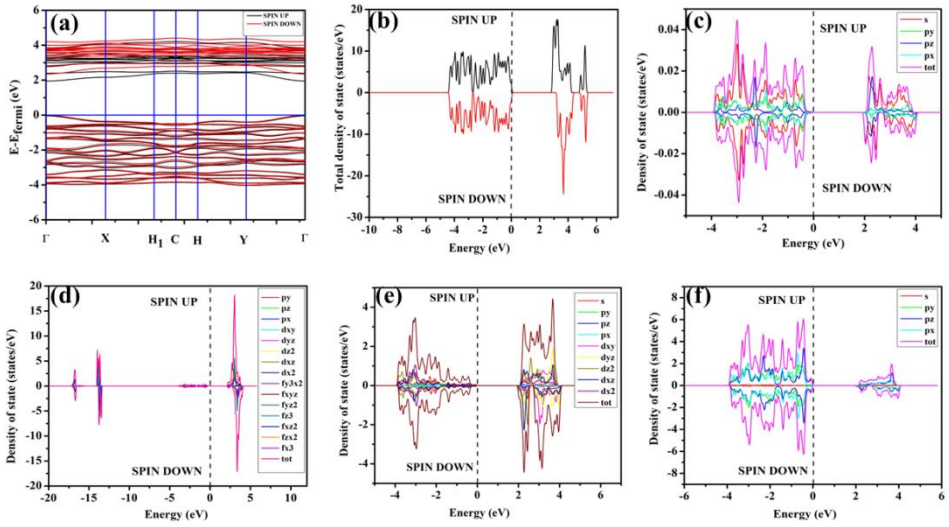

Fig. A17 (a) Band structure and (b) spin polarised TDOS and PDOS of (c) Na, (d) Ce, (e) Mo and (f) O of NCMO – $2V_O^{\bullet}$.

References

1) B. Glorieux, V. Jubera, A. Apheceixborde and A. Garcia, Sol. State. Sci., 2011, **13**, 460-467.

2) H. Yang, F. Peng, Q. Zhang, W. Liu, D. Sun, Y. Zhao and X., Wei, Opt. Mater., 2013, **35**, 2338-2342.

3) J.R. de Moraes, S.L. Baldochi, L.D.R.L. Soares, V.L. Mazzocchi, C.B.R. Parente and L.C. Courrol, Mater. Res. Bull., 2012, **47**, 744-749.

4) Z. Xu, S. Li, Q. Meng, X. Wang, Q. Zhu and J.G. Li, J. Alloys and Compd., 2020, **830**, 154676.

5) J. Kim, Inorg. Chem., 2017, **56**, 8078-8086.

6) F. Cheng, Z. Xia, M.S. Molokeev and X. Jing, Dalton Trans., 2015, **44**, 18078-18089.

7) J. Song, Y. Du, L. Xu, H. Wei, D. He and H. Jiao, J. Am. Ceram. Soc., 2014, **97**, 1442-1449.

8) A. Sarapulova, D. Mikhailova, A. Senyshyn and H. Ehrenberg, J. Solid State Chem., 2009, **182**, 3262-3268.

9) L.S. Cavalcante, J.C. Sczancoski, R.L. Tranquilin, M.R. Joya, P.S. Pizani, J.A. Varela and E. Longo, J. Phys. Chem. Solids, 2008, **69**, 2674-2680.

10) X. Liu, W. Hou, X. Yang and J. Liang, CrystEngComm., 2014, **16**, 1268-1276.

11) S. Huang, D. Wang, C. Li, L. Wang, X. Zhang, Y. Wan and P. Yang, CrystEngComm., 2012, **14**, 2235-2244.

12) Y. Tian, B. Chen, R. Hua, N. Yu, B. Liu, J. Sun, L. Cheng, H. Zhong, X. Li, J. Zhang and B. Tian, CrystEngComm., 2012, **14**, 1760-1769.

13) Z. Wang, Y. Li, Q. Jiang, H. Zeng, Z. Ci and L. Sun, J. Mater. Chem. C, 2014, **2**, 4495-4501.

14) S. Das, U.K. Ghorai, R. Dey, C.K. Ghosh and M. Pal, New J. Chem., 2022, **46**, 17585-17595.

15) S. Das, U.K. Ghorai, R. Dey, C.K. Ghosh and M. Pal, Phys.Chem.Chem. Phys., 2017, **19**, 22995-23006.

16) B. Ding, H. Qian, C. Han, J. Zhang, S.E. Lindquist, B. Wei and Z. Tang, J. Phys. Chem. C, 2014, **118**, 25633-25642.

17) R. Fernández-Climent, S. Giménez and M. García-Tecedor, Sustain. Energy Fuels, 2020, **4**, 5916-5926.

18) Z. Lin, M. Xu, Y. Hong, X. Wang and P. Fu, Mater. Lett., 2016, **168**, 72-75.

19) N. Haldar, T. Mondal, T. Das, D. Sarkar, M. Pal and C.K. Ghosh, CrystEngComm. 2023, **25**, 3514-3527.

20) W.R. Liu, C.W. Yeh, C.H. Huang, C.C. Lin, Y.C. Chiu, Y.T. Yeh and R.S. Liu, J. Mater. Chem., 2011, **21**, 3740-3744.

21) L.S. Cavalcante, F.M.C. Batista, M.A.P. Almeida, A.C. Rabelo, I.C. Nogueira, N.C. Batista, J.A. Varela, M.R.M.C. Santos, E. Longo and E.M.S. Li, RSC Adv., 2012, **2**, 6438-6454.

22) G.M. Kuzmicheva, A.V. Eremin, V.B. Rybakov, K.A. Subbotin and E.V. Zharikov, Russ. J. Inorg. Chem., 2009, **54**, 854-863.

23) R.L. Andrews, A.M. Heyns and P.M. Woodward, Dalton Trans., 2015, **44**, 10700-10707.

24) L. Li, Y. Su and G. Li, Appl. Phys. Lett., 2007, **90**, 054105.

25) G.M. Kuz'Micheva, I.A. Kaurova, V.B. Rybakov, P.A. Eistrikh-Geller, E.V. Zharikov, D.A. Lis and K.A. Subbotin, CrystEngComm., 2016, **18**, 2921-2928.

26) J.V.B. Moura, G.S. Pinheiro, J.V. Silveira, P.T.C. Freire, B.C. Viana and C. Luz-Lima, J. Phys. Chem. Solid, 2017, **111**, 258-265.

27) Z. Xu, P. Du, Q. Zhu, X. Li, X. Sun and J.G. Li, Dalton Trans., 2021, **50**, 17703-17715.

28) J.A. Horsley, I.E. Wachs, J.M. Brown, G.H. Via and F.D. Hardcastle, J. Phys. Chem., 1987, **91**, 4014-4020.

29) B.P. Singh and R.A. Singh, New J. Chem., 2015, **39**, 4494-4507.

30) F.F. Wu, D. Zhou, C. Du, S.K. Sun, L.X. Pang, B.B. Jin, Z.M. Qi, J. Varghese, Q. Li and X.Q. Zhang, J. Mater. Chem. C, 2021, **9**, 9962-9971.

31) Z. Zhao, Z. Sui, X. Wei, J. Zuo, X. Zhang, R. Dai, Z. Zhang and Z. Ding, CrystEngComm., 2015, **17**, 7905-7914.

32) J. Victor Barbosa Moura, A. Amison Gomes de Souza, P. de Tarso Cavalcante Freire, C. da Luz Lima and T. Mielle Brito Ferreira Oliveira, Int. J. Appl. Ceram. Technol., 2021, **18**, 615-621.

33) Y. Xiong, B. Wang, H. Zhuang, X. Jiang, G. Ma, Y. Yi, W. Hu and Y. Zhou, RSC Adv., 2014, **4**, 36738-36741.

34) N. Dirany, E. McRae and M. Arab, CrystEngComm., 2017, **19**, 5008-5021.

35) S. Mandal, C.K. Ghosh, D. Sarkar, U.N. Maiti and K.K. Chattopadhyay, Sol. State sci., 2010, **12**, 1803-1808.

36) T. Thomas, N. Jayababu, J. Shruthi, A. Mathew, A. Cerdán-Pasarán, J.A. Hernández-Magallanes, K.C. Sanal and R. Reshmi, Thin Solid Films, 2021, **722**, 138575.

37) A.I. Becerro, M. Allix, M. Laguna, D. González-Mancebo, C. Genevois, A. Caballero, G. Lozano, N.O. Núñez and M. Ocaña, J. Mater. Chem. C, 2018, **6**, 12830-12840.

38) R. Xiao, N. Guo, X. Lv, Q. Ma, B. Shao and R. Ouyang, Dalton Trans., 2022, **51**, 15484-15495.

39) G. Li, Y. Tian, Y. Zhao and J. Lin, Chem. Soc. Rev., 2015, **44**, 8688-8713.

40) Y. Zhu, Y. Liang, M. Zhang, M. Tong, G. Li and S. Wang, RSC Adv., 2015, **5**, 98350-98360.

41) L.G. Van Uitert, J. Lumin., 1984, **29**, 1-9.

42) E.V. Sokolenko, V.M. Zhukovskii, E.S. Buyanova and Y.A., Krasnobaev, Inorg. Mater., 1998, **34**, 499-502.

43) M.V. Korzhik, V.B. Pavlenko, T.N. Timoschenko, V.A. Katchanov, A.V. Singovskii, A.N. Annenkov, V.A. Ligun, I.M. Solskii and J.P. Peigneux, physica status solidi (a), 1996, **154**, 779-788.

44) A. Lecointre, A. Bessière, A.J.J. Bos, P. Dorenbos, B. Viana and S. Jacquart, J. Phys. Chem. C, 2011, **115**, 4217-4227.

45) J. Raha, N. Haldar and C.K. Ghosh, Appl. Phys. A, 2021, **127**, 1-8.

46) S. Das, C.K. Ghosh, R. Dey and M. Pal, RSC adv., 2016, **6**, 236-244.

47) Y. Shi, Y. Wen, M. Que, G. Zhu, and Y. Wang, Dalton Trans., 2014, **43**, 2418-2423.

48) Q. Wang, G. Zhu, Y. Li and Y. Wang, Opt. Mater., 2015, **42**, 385-389.

49) M. Rai, G. Kaur, S. K. Singh, S. B. Rai, Dalton Trans., 2015, **44**, 6184**.**

50) Z. Wang, X. Qiu, W. Xi, M. Tang, J. Liu, H. Jiang and L. Sun, Sen. Act. B Chem., 2021, **345**, 130417.

51) Z. Wang, X. Qiu, W. Xi, M. Tang, J. Liu, H. Jiang and L. Sun, Sen. Act. B Chem., 2023, **376**, 132936.

52) T. Das, S. Das, M. Karmakar, S. Chakraborty, D. Saha and M. Pal, Sen. Act. B. Chem. 2020, **325**, 128765.

53) T. Das, S. Mojumder, S. Chakraborty, D. Saha and M. Pal Appl. Surf. Sci. 2022, **602**, 154340.

54) Z. Wang, J. Xue, D. Han and F. Gu, ACS Appl. Mater. Interfaces, 2015, **7**, 308-317.

55) M. Ali, N. Amrane and N. Tit, Results Phys., 2020, **16**, 102907.

Chapter 6

Influence of alkali metal ion on the defect induced photoluminescence property of double tungstate compounds $ACe(WO_4)_2$ (A = Li, Na, K): Experimental and *ab initio* theoretical study

1. Introduction

Double tungstate compounds have garnered significant attention due to their intriguing optical and electronic properties, making them promising candidates for various technological applications. In recent years, there has been significant interest in rare earth-based double tungstate scheelite materials due to their unique optical characteristics, such as high luminescence quantum efficiency, narrow line width and excellent thermal stability [1-3].These materials exhibit UV absorption and emit visible light, making them well-suited for applications like phosphorescent materials, luminescent diodes and optical fibers etc [4,5]. Among these compounds, $ACe(WO_4)_2$ (where A = Li, Na, K) has emerged as a subject of intense research, owing to its unique defect-induced photoluminescence properties. The incorporation of alkali metal ions (Li^+, Na^+, K^+) into the crystal lattice of $ACe(WO_4)_2$ introduces defects that lead to distinct optical characteristics, opening new avenues for the design of advanced optoelectronic devices. Understanding this impact is vital for tailoring optical properties to specific applications. A recent study by Shimemura et al. focused on $ACe(WO_4)_2$ materials, where A represents Li^+, Na^+, and K^+. While they investigated the emission properties, detailed photoluminescence information was lacking [6].In another report, Shimemura et al. discussed $LiCe(WO_4)_2$ as a

fluorescent material, considering combined luminescence of Ce^{3+} and WO_4^{2-} [7]. The photoluminescence properties of materials have gained prominence due to their applications in various fields, ranging from lighting and displays to sensors and lasers. $ACe(WO_4)_2$ compounds, with their intriguing luminescent behavior, offer a versatile platform for tailoring and optimizing photoluminescence emissions. These emissions are primarily attributed to the interaction between 4f and 5d electron orbitals of Ce^{3+} ions within the crystal lattice. The manipulation of these emissions through controlled defect engineering, particularly the introduction of oxygen vacancies (V_O), provides an innovative approach to enhance the luminescence efficiency and tune the emission colors.

In this context, the present study delves into the intricate relationship between alkali metal ions, defect-induced photoluminescence, and crystal structure in $ACe(WO_4)_2$ compounds. By systematically investigating the impact of Li^+, Na^+, and K^+ ions on the defect formation and subsequent photoluminescence properties, valuable insights can be gained into the underlying mechanisms governing these phenomena. Through a combination of experimental characterization techniques and advanced theoretical modeling, a comprehensive understanding of the defect-induced photoluminescence behavior in $ACe(WO_4)_2$ compounds can be achieved. The insights garnered from this research not only contribute to the fundamental understanding of defect engineering in double tungstate materials but also pave the way for the development of novel optoelectronic devices with tailored luminescent properties.

This article presents the hydrothermal synthesis of scheelite-type $LiCe(WO_4)_2$ and $KCe(WO_4)_2$ using tri-sodium citrate as an organic additive. It examines the impact of alkali metal ions on crystal structure distortion and optical properties of $ACe(WO_4)_2$ (A = Li, Na, K). As per literature, there is no report on *ab initio*

band structures of $ACe(WO_4)_2$ clusters are employed to elucidate photoluminescence properties. This study provides insights into electronic and optical properties of $ACe(WO_4)_2$ and informs the development of new materials with tailored optical attributes.

2. Experimental section

2.1 Materials and synthesis

Scheelite-type $ACe(WO_4)_2$ (A = Li, Na, K) materials were synthesized using a conventional hydrothermal method. To prepare $Li/Na/KCe(WO_4)_2$, 0.17 mmol (0.074 g) of Cerium nitrate [$Ce(NO_3)_3 \cdot 6H_2O$, Merck, Germany] and 0.17 mmol (0.044 g) of trisodium citrate dihydrate ($Na_3Cit \cdot 2H_2O$, Sigma Aldrich) were dissolved in 60 ml of deionized (DI) water at room temperature. The initially transparent solution turned milky white. Another 20 ml of an aqueous solution containing 0.34 mmol (0.089 g) of lithium tungstate ($Li_2WO_4 \cdot H_2O$, Merck, Germany) or 0.112 g of sodium tungstate ($Na_2WO_4 \cdot H_2O$, Merck, Germany) or 0.111 g of potassium tungstate ($K_2WO_4 \cdot 2H_2O$, Merck, Germany) was added dropwise over 30 minutes with continuous magnetic stirring, maintaining the pH of the reaction medium at 7. Subsequently, the solution was transferred into a Teflon autoclave and maintained at 180°C for 24 hours. After cooling to room temperature, the resulting product was collected via centrifugation and subsequently washed with DI water and ethanol. The washed product was then dried at 70°C for 10 hours, followed by calcination at 800°C for 5 hours to obtain the powdered final product. Thus, materials with different alkali metal sources (Li, Na, K) were synthesized, and the resulting samples were designated as LCWO, NCWO, and KCWO respectively.

2.2 Measurement and Characterization

Various analytical techniques were employed to investigate the properties of the material. X-ray diffraction (XRD) was utilized to extract structural and

microstructural refinement parameters via the least-squares method. The Rigaku Ultima III powder diffractometer from Japan, equipped with CuK_α radiation (λ = 1.5404 Å), was employed for recording XRD patterns. The experimental profiles were fitted using the most appropriate pseudo-Voigt analytical function, accounting for asymmetry. A fourth-order polynomial function was applied to fit the background of each pattern. The sample morphology was examined using a field emission scanning electron microscope (FESEM; Hitachi S - 4800) operating at 5 kV. Raman spectra were analyzed using the Alpha 300 instrument from Wintec, with a 530 nm laser (3 mW output and a 2 m spot size). Infrared spectra, ranging from 400 to 4000 cm^{-1}, were recorded using the IR Prestige. X-ray photoelectron spectra (XPS) were collected through the PHI Versa Probe III Scanning XPS Microprobe with Al K source. UV-Vis absorption spectra were measured using a UV-Vis spectrophotometer (V-630, JASCO). Photoluminescence emission spectra were obtained using an FP-8300, JASCO, equipped with a 100W Xe lamp, and measurements were conducted at room temperature. The outcomes derived from these techniques hold the potential to optimize material synthesis and customize properties to suit specific applications.

2.3 Ab-Initio Density Functional Theory:

To compute the spin-polarized electronic band structure, projected density of states (PDOS), and total density of states (TDOS) for multiple atoms, the VASP simulation software was employed utilizing the plane-wave pseudopotential (PAW) method. The basis set utilized was the Perdew-Burke-Ernzerhof (PBE) exchange correlation ultra-soft potentials. The considered atoms included Li ($1s^2\ 2s^1$), Na ($1s^2\ 2s^2\ 2p^6\ 3s^1$), K ($3s^2\ 3p^6\ 4s^1$), Ce ($5s^2\ 5p^6\ 4f^1\ 5d^1\ 6s^2$), W ($5p^6\ 6s^2\ 5d^{10}$), and O ($2s^2\ 2p^4$). The supercell structure with the lowest single-point ground state energy was optimized using a 4 x 4 x 4 Monkhorst-Pack k-point grid. Subsequently, the band structure was calculated along symmetry points Γ

to X, X to H1, H1 to C, C to H, H to Y, Y to Γ, and Γ to C. A plane wave cutoff energy of 520 eV was chosen, and convergence energy was achieved within the range of 220 to 620 eV. To ensure accuracy, maximum atomic displacement and stress were constrained at $5x10^{-4}$ and 0.02 GPa, respectively. Each atom was subjected to a 0.01 eV Hellmann-Feynman force. For precise computational convergence, the EDIFF and force EDIFG parameters were set to 10^{-6} eV and 10^{-3} eV, respectively. This information aids in comprehending atomic behavior within diverse materials and can guide the design of materials possessing specific electronic properties.

3. Result and discussion

3.1 Phase and crystal structure analyses of the samples by XRD, FESEM, TEM

The obtained X-ray diffraction (XRD) patterns of $ACe(WO_4)_2$ materials are presented in Figure 1(a-c). These patterns closely resemble those of the triclinic scheelite-type material (ICSD card: 200520, space group: P-1(2)) [8]. The absence of additional peaks verifies the phase purity of the samples, and a strong agreement between observed and calculated XRD patterns via Rietveld refinement is evident. The refinement process was pursued until R_p, R_{wp}, R_{exp}, and χ^2 converged within acceptable ranges [9]. Detailed structural refinement information is available in Table A1 and A2 of APPENDIX-IV. The refinement reveals that W, Ce, and A atoms form a cage-like structure connected by O atoms. Ce atoms establish regular CeO_8 polyhedra, A atoms form AO_4 tetrahedra, and W atoms create WO_6 octahedra with 8, 4, and 6 coordinated O atoms, respectively. Each AO_4 shares an edge with WO_6 octahedra and links to CeO_8 polyhedra through O atoms. Schematic representations of the triclinic unit cell of ACWO are depicted in Figure 1(d)-(f). Rietveld analyses additionally indicate that W atoms possess inversion symmetry, resulting in edge-sharing octahedra forming W_4O_{16} as a tetramer via W_2O_2 bridged O atoms. The lattice

parameters, unit cell volume, A-O, Ce-O, and W-O bond lengths, as well as A-O-W, Ce-O-W, and O-Ce-O bond angles, decrease in LCWO and KCWO compared to NCWO unit cells, indicating distortion of the unit cells. This trend can be attributed to the ionic radius of Na^{+} (r = 0.99Å, CN = 4), which is closest to that of Ce^{3+} (r = 1.14Å, CN = 8), compared to the ionic radius of Li^{+} (r = 0.59Å, CN = 4) and K^{+} (r = 1.37Å, CN = 4). As a result, the crystal compactness is most significant in NCWO while both LCWO and KCWO show abnormal lattice distortion. The degree of CeO_8 polyhedron distortion (K) is quantified as ~1.066, 1.046, and 1.082 for LCWO, NCWO, and KCWO using the relation $K = \frac{d1(Ce-O)}{d2(Ce-O)}$, where d_1(Ce-O) and d_2(Ce-O) represent different bond lengths. Similarly, WO_6 octahedron distortion (N) is assessed as ~1.132, 1.095, and 1.285 using the relation $N = \frac{\alpha1(O-W-O)}{\alpha2(O-W-O)}$, where α_1(O-W-O) and α_2(O-W-O) denote distinct bond angles, affirming greater V_O-induced distortion in LCWO and KCWO compared to NCWO [10]. Furthermore, a reduction in the c/a ratio in NCWO relative to LCWO and KCWO indicates the influence of dipole-dipole interactions on short-range disorder attributed to charge entrapment at the V_O site [11].

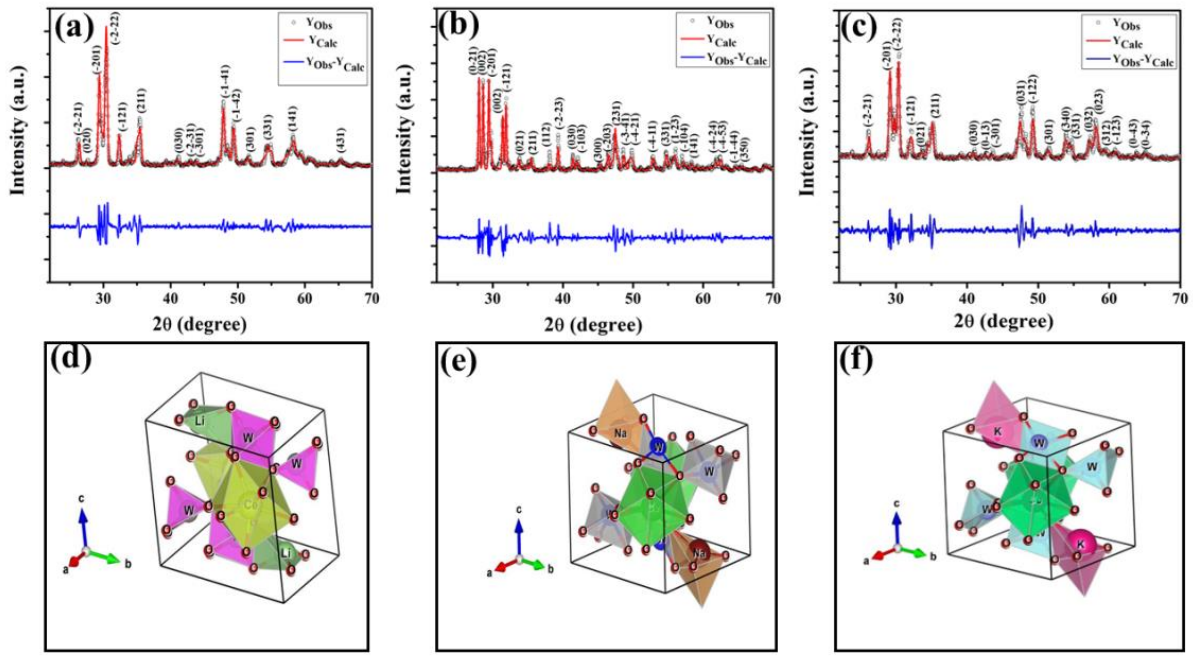

Figure 1: XRD patterns (a, b, c) and triclinic unit cell's structure (d, e, f) of LCWO, NCWO, KCWO respectively.

The morphologies of the ACWO samples are depicted in Figure 2(a-c), revealing an agglomerated form. This suggests that particles have clustered together due to the effects of calcination at high temperature (800°C). To gain more insights into the precise shape and size of the particles, further analysis was conducted using transmission electron microscopy (TEM). Upon TEM examination, the samples exhibited irregular shapes and sizes (Figure 3(a), (d), (g)) for LCWO, NCWO, and KCWO, respectively. High-resolution TEM (HRTEM) images allowed for the determination of d-spacing values, which were found to be 0.176 nm for LCWO, 0.142 nm for NCWO, and 0.263 nm for KCWO (Figure 3(b), (e), and (h)). These d-spacing values correspond to the (301), (350), and (021) planes of LCWO, NCWO, and KCWO, respectively. Notably, these results are consistent with the X-ray diffraction (XRD) data presented in Figure 1(a-c). Figure 3(c), (f), and (i) illustrate the selected area electron diffraction (SAED) patterns of LCWO, NCWO, and KCWO samples, respectively, derived from the TEM images. The diffraction spots represented

by white points in these patterns correspond to specific crystal planes. Importantly, these diffraction spots (Figure 3(c), (f), (i)) align well with the XRD data shown in Figure 1(a-c). The HRTEM images along with their corresponding d-spacing measurements support the crystallographic properties of LCWO, NCWO, and KCWO samples. These observations validate the structural characteristics of the materials under investigation.

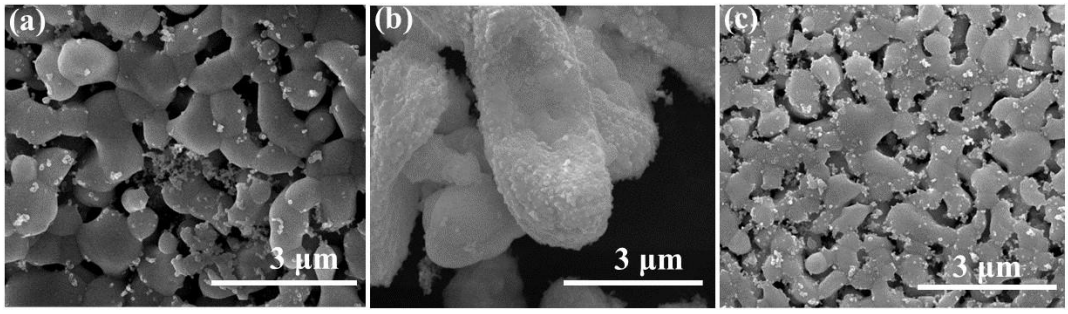

Figure 2: (a)-(c) FESEM image of LCWO, NCWO, KCWO respectively.

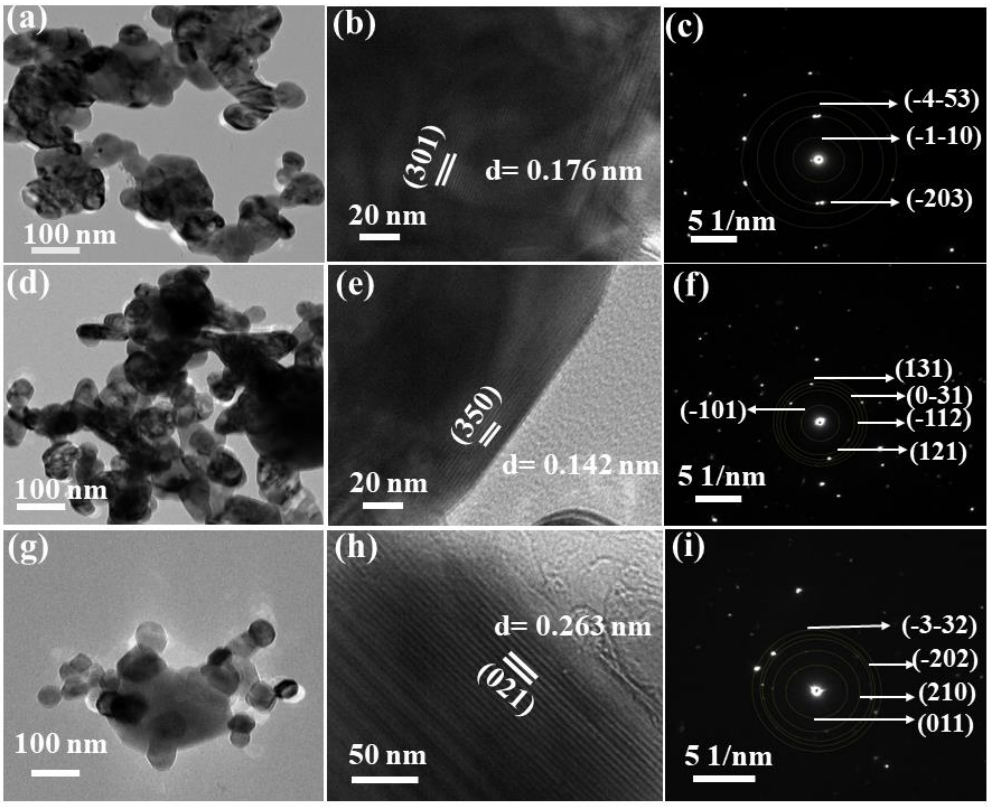

Figure 3: TEM image, HRTEM image and corresponding SAED pattern of LCWO (a)-(c), NCWO (d)-(f), KCWO (g)-(i) respectively.

3.2 Investigations of defects in ACWO nanostructures by FTIR, Raman and x-ray photoelectron spectroscopies

FTIR and Raman spectra serve as analytical techniques to assess structural distortions in terms of vibrational frequencies. In the context of materials like ACWO, these techniques offer insights into crystal structure and the presence of defects, such as vacancies (V_O). The FTIR spectrum of ACWO manifests four absorption bands (Figure A1, APPENDIX-IV), corresponding to internal vibrations of the WO_6 octahedron. Within the W^RO_6 structure, tungsten ions occupy the center of regular octahedra formed by six oxygen ions with 2i site symmetry. Group theory dictates that the symmetry modes can be expressed as $\Gamma_{Oh}= 36A_u$.

The emergence of an oxygen vacancy within the lattice can lead to a distorted octahedral structure, specifically the W^DO_6 octahedron. This introduces a reduction in lattice symmetry, subsequently affecting the vibrational frequencies of the system. The detailed deconvolution of FTIR bands is provided in the electronic supplementary information (Table A3, APPENDIX-IV). Deconvolution of two bands (780 – 920 and 673 – 715 cm^{-1}) in the FTIR spectra reveals the peaks at 679, 693, 697, 797, 823, 868 cm^{-1} for NCWO. Peaks at 697 and 868 cm^{-1} correspond to the stretching vibration (→ O → W → O →) of W^DO_6 and W^RO_6 octahedra respectively. Other deconvoluted peaks align with the asymmetric stretching of two-oxygen bridged W_2O_2 in W^RO_6 and W^DO_6 octahedra [12,13**].**

This blue shift in the FTIR spectrum of LCWO and KCWO signifies defects introduced into the crystal lattice, leading to alterations in the local chemical environment of atoms or molecules within the material. The peaks at 733 and 748 cm^{-1} for NCWO, correspond to W – O bending vibration of W^DO_6 and W^RO_6 respectively (Figure 4). Similarly a blue shift is also observed for LCWO and KCWO. [14]. However, that peak shifting alone may not be sufficient to

fully characterize a material's defects. Weighted percentage calculation from area under the curves indicates W^DO_6 ~ 44%, 30%, and 48% for LCWO, NCWO, and KCWO respectively. A noticeable blue shift is observed in LCWO and KCWO, indicating more pronounced V_O in those samples than in NCWO. The W^DO_6/ W^RO_6 ratios stand at 0.785, 0.428, and 0.923 for LCWO, NCWO, and KCWO respectively, indicating greater octahedral distortion in LCWO and KCWO compared to NCWO.

The Raman spectrum of NCWO exhibits peaks at 338, 389, 463, and 534 cm^{-1}, aligning with the vibrational motion of WO_6 octahedra and W_2O_2 units (Figure 5). The peak at 463 cm^{-1} is attributed to the A_g symmetric stretching mode of the W_2O_2 unit. The remaining peaks correspond to asymmetric and symmetric bending vibrations of O-W-O within the A_g mode, along with the asymmetric stretching mode of the W_2O_2 unit [14,15]. Furthermore, the relatively lower intensity of Raman peaks observed in KCWO and LCWO compared to NCWO can be attributed to symmetry disruption caused by an increased presence of oxygen vacancies and antisite defects [16].

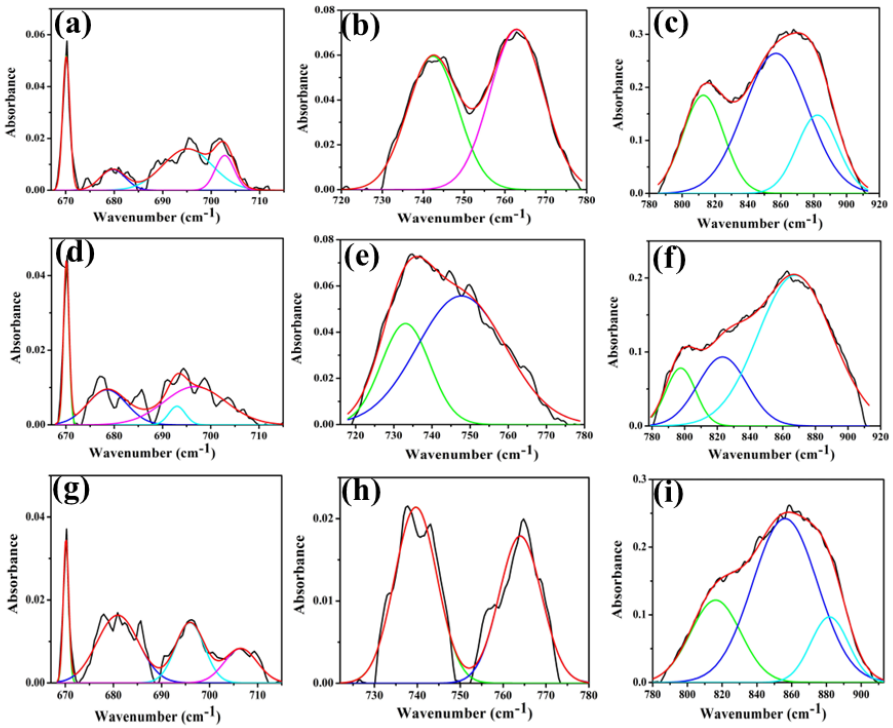

Figure 4: (a) Deconvoluted curves of the FTIR bands 660 – 717, 718-777 and 778 – 910 cm^{-1} of LCWO (a, b, c), NCWO (d, e, f) and KCWO (g, h, i) respectively.

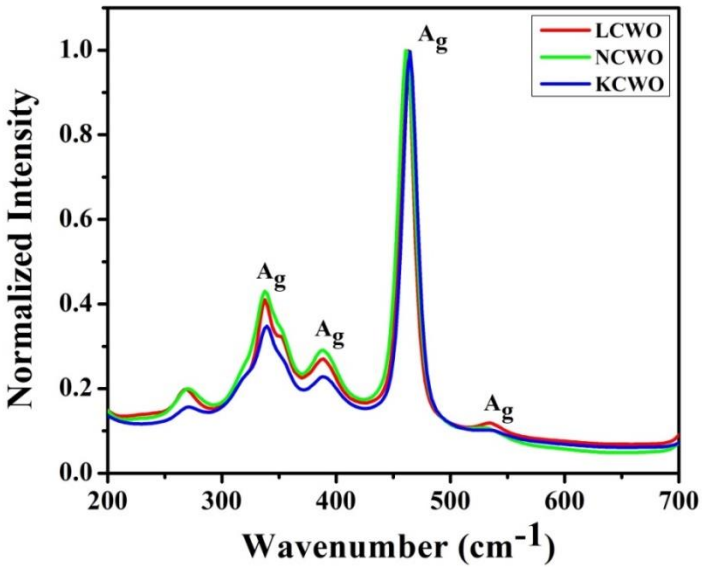

Figure 5: Raman spectra of ACWO nanostructures.

XPS analysis was undertaken to delve into the chemical states of Li, Na, K, Ce, W, and O, aiming to enhance comprehension of V_O-induced disorder effects on material electronic structure. The obtained XPS data for all elements were adjusted to account for the C1s peak attributed to adventitious carbon on the sample surface due to atmospheric exposure [17]. This C1s peak carries a binding energy of 284.6 eV. The survey scan (Figure A2 of APPENDIX-IV) encompasses core binding energies of Li, Na, K, Ce, W, and O within the energy range of 0 to 1100 eV. This scan aids in identifying chemical states present in the samples. Further, high-resolution spectra of W, Ce, and O from all samples are illustrated in Figure 6. These spectra offer detailed insights into the electronic structure of these materials, particularly highlighting changes prompted by the presence of V_O-induced disorder.

Figures 6(a), (b), and (c) reveal two asymmetric peaks in XPS spectra at 35.4 and 37.4 eV, originating from spin-orbit splitted $4f_{7/2}$ and $4f_{5/2}$ orbitals of W^{6+}. Deconvolution of these spectra results in four peaks, W_a, W_b, W_c, and W_d, corresponding to diverse electronic states of W. W_a and W_c associate with W^DO_6, while W_b and W_d signify W^RO_6. The electronegativity disparity between W and O suggests an ionic W-O bond. The presence of V_O heightens the effective charge on W, inducing electron-electron repulsion and reducing binding energies of the $4f_{7/2}$ and $4f_{5/2}$ states in W^DO_6. Estimated W^DO_6 percentages are higher in LCWO (~43%) and KCWO (~45%) compared to NCWO (~26%), aligning with FTIR findings. In Figures 6(d), (e), and (f), two asymmetric peaks within the ranges 877 – 891 eV and 895 – 910 eV manifest in Ce 3d spectra. Deconvolution of the $3d_{5/2}$ peak yields three peaks, Ce_a, Ce_b, and Ce_c, associated with distinct Ce electronic environments. Ce_c corresponds to CeO_8, while Ce_a and Ce_b relate to CeO_7 and CeO_6, containing V_O and $2V_O$, respectively. Analysis of Ce spectra demonstrates V_O's impact, shortening Ce-O bond lengths and heightening electron-electron repulsion at the Ce site, thereby

lowering binding energies of $3d_{5/2}$ and $3d_{3/2}$ orbitals [18]. Scrutinizing the data indicates a reduction in Ce_a weight percentage in NCWO (~21%) compared to LCWO (~34%) and KCWO (~40%), implying V_O suppression in NCWO. XPS analysis of O 1s manifests an asymmetric peak. Deconvolution of this spectrum yields one peak at 530.6 eV, attributed to lattice oxygen within Ce-O-Ce bonds in the crystal structure. Another peak at 532.4 eV corresponds to chemisorbed oxygen linked to oxygen vacancies. Notably, the area under the peak at 532.4 eV is greater in LCWO and KCWO compared to NCWO, signifying a higher oxygen vacancy amount in those samples than in NCWO.

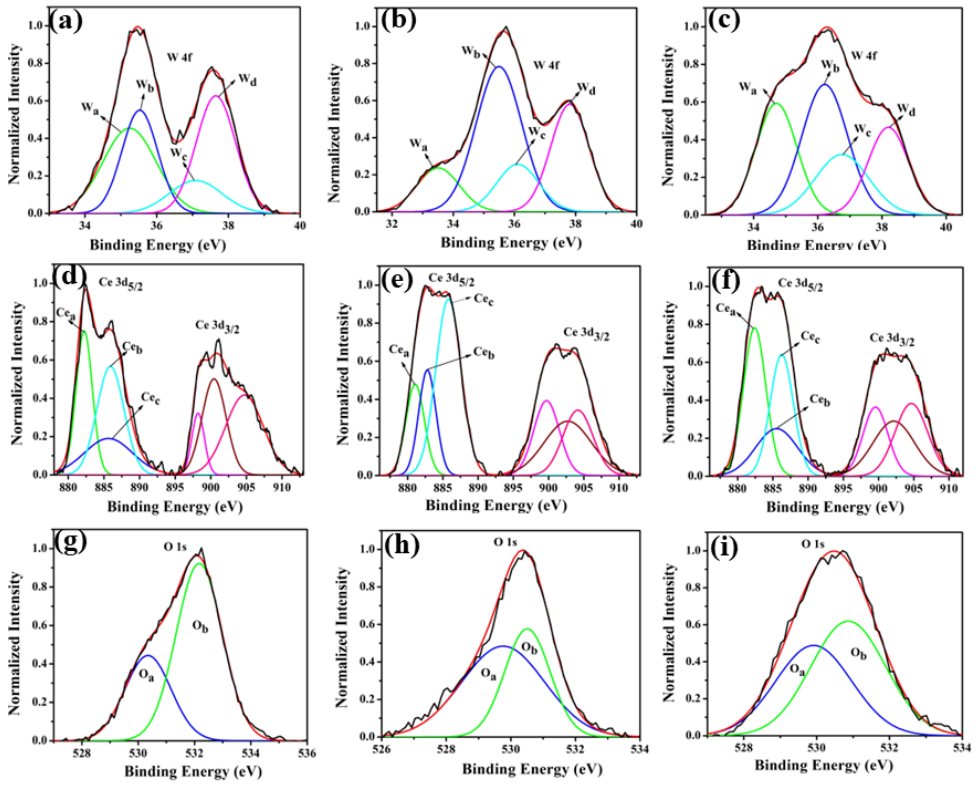

Figure 6: (a, b, c) XPS W4f, (d, e, f) XPS Ce 3d, (g, h, i) XPS O1s core level spectra of LCWO, NCWO, KCWO respectively.

3.3 Optical properties of the as-prepared ACWO samples by UV-Vis, photoluminescence spectroscopy

The UV-Vis absorption spectra of ACWO materials reveal an optical band gap of approximately 3.10 eV for LCWO, 3.14 eV for NCWO, and 3.06 eV for KCWO (depicted in Figure A3, APPENDIX-IV). The valence band (VB) of ACWO consists of O 2p – W 5d hybridization, while the conduction band (CB) of ACWO comprises W- 5d, Ce- 4f, and a minor contribution of O-2p, as indicated by a DFT-based *ab initio* calculation (discussed later) [19]. A broad peak at 380 nm is observed in the photoluminescence excitation (PLE) spectra for ACWO samples when monitored at an emission wavelength of 531 nm (Figure A4, APPENDIX-IV). Furthermore, the emission spectra recorded in the visible region with an excitation wavelength of 380 nm are illustrated in Figure 7(a)-(d). The 380 nm peak in the PLE spectra is attributed to charge transfer (CT) absorption within WO_6 octahedra. This absorption process involves electronic charge transfer between different atomic species, specifically between O-2p and W-5d within the WO_6 octahedra. The emission spectra in the visible region upon excitation at 380 nm likely correspond to the relaxation of excited states formed during the CT absorption process. The luminescence characteristics of the samples are displayed in Figures 7(a), (b), and (c), revealing four peaks in the visible region upon excitation at 380 nm. A prominent peak is observed at 439 nm (blue I, 22,779 cm^{-1}), followed by two peaks in the blue region at 462 nm (blue II, 21,645 cm^{-1}) and 487 nm (blue III, 20,533 cm^{-1}), along with a green emission at 531 nm (green, 18,832 cm^{-1}). Previous studies have proposed that emissions from scheelite materials are largely due to 5d to 4f transitions within rare earth elements. However, the precise mechanism remains debated due to factors such as crystal field, polarizability, etc., significantly affecting emission characteristics [20].

To comprehend the emission wavelength (λ) based on the 5d – 4f transition of Ce^{3+} within a regular CeO_8 polyhedron, we have employed a relationship provided by van Uitert et al. [21]:

$$\frac{1}{\lambda} = \frac{Q^*}{hc}\left[1 - \left(\frac{V}{4}\right)^{\frac{1}{V}} 10^{\frac{-(nrE_a)}{80}}\right] \qquad (1)$$

where, Q* represents the energy of 5d band edge of free Ce^{3+} ion (= 50000 cm^{-1}), V is the valance of the Ce^{3+}, 'n' is the number of anions in the immediate shell around Ce^{3+}, E_a is electron affinity of the atoms forming anions and 'r' is defined as the difference between average bond length and radius of anion of CeO_8 polyhedra (1.03Å). We have calculated wavelength ~ 437 nm is highly corroborating with our experimental blue I emission at 439 nm.

By using equation (1) with CeO_7 and CeO_6 configurations, it was calculated that the emission wavelengths for these configurations are approximately 470 nm and 522 nm, respectively. These values match well with the experimentally observed blue III and green emissions (as shown in Figure 7). It is believed that V_O defects alter the energy of the 5d orbitals of Ce^{3+} in CeO_7 and CeO_6, resulting in different emissions. To further understand this, the crystal field stabilization energy and centroid shift of the d-orbitals (ε_c (1, 3 +, A)) of Ce^{3+} in different CeO_8 polyhedra were calculated using Dorenbos's equation (2) and (3) [22]**:**

$$\varepsilon_{cfs}(1, 3+, A) = \beta R_{av}^{-2} \qquad (2)$$

$$\varepsilon_c (1, 3 +, A) = 6.35 - E^C (1, 3 +, A) \text{ eV}. \qquad (3)$$

where, β = 1.35 × 109 pm^2 cm^{-1} for Ce^{3+} and $R_{av} = \frac{1}{N}\sum_{i=1}^{N}(R_i - 0.6\Delta R)$; R_i denotes bond lengths to the N coordinating anions in distorted lattice.

The calculated values of $\varepsilon_c(1,3+, Ce^{3+})$ for CeO_8, CeO_7, and CeO_6 are approximately 5.94, 5.66, and 5.41 eV for LCWO, 5.93, 5.69, and 5.46 eV for NCWO, and 5.92, 5.62, and 5.35 eV for KCWO, respectively. Furthermore, the values of $\varepsilon_{cfs}\,(1,3+,Ce^{3+})$ are in the order of 2.06, 3.44, and 4.69 eV for LCWO, 2.01, 3.30, and 4.42 eV for NCWO, and 2.16, 3.62, and 4.99 eV for KCWO, respectively. It was also determined that the difference between the $^5D_0$ – $^2F_{5/2}$ and $^5D_0$ – $^2F_{7/2}$ transitions is approximately 2,000 cm^{-1}. The emissions labelled as "blue I" and "blue II" exhibit a distinct energy difference of around 1134 cm^{-1}. This disparity suggests that these emissions have different energy levels, indicating that the "blue II" emission cannot be attributed to the $^5D_0$ – $^2F_{7/2}$ transition within CeO_8 polyhedra or a 5d orbital split transition. This implies that the origin of the "blue II" emission differs from these known transitions. The presence of two distinct $\varepsilon_c(1,3+, Ce^{3+})$ states within CeO_6 units are associated with the existence of two vacancy oxygen (V_O) defects (discussed later in DFT calculation). An intriguing finding is that the centroid shift $\varepsilon_c(1,3+, Ce^{3+})$ value of CeO_7 and CeO_6 is observed to decrease, indicating presence of more oxygen vacancies in KCWO and LCWO compared to NCWO. This suggests that V_O defects significantly influence the values of ε_{cfs} and ε_c, consequently determining the emission wavelength (λ) for the 5d – 4f transition within CeO_7 and CeO_6.

The formation of V_O and $2V_O$ defects can be comprehended through the Kröger-Vink notation, which delineates the relationship between defects and stoichiometry in ionic crystals. Electrons are released into the host matrix, leading to the creation of ionized defect states $V_O^{\bullet}$ and $2V_O^{\bullet}$ which can be represented by equations 4(a) and (b):

$$[CeO_8]^x + \left[CeO_7 \bullet V_O^X\right] \rightarrow [CeO_8]' + [CeO_7 \bullet V_O^{\bullet}] \qquad 4(a)$$

$$[CeO_8]^x + \left[CeO_6 \bullet 2V_O^X\right] \rightarrow [CeO_8]'' + [CeO_6 \bullet 2V_O^{\bullet}] \qquad 4(b)$$

where $[CeO_8]'$ and $[CeO_8]''$ denote electron donors and $[CeO_7 \bullet V_O^{\bullet}]$ and $[CeO_6 \bullet 2V_O^{\bullet}]$ are the electron acceptors those exhibit blue III and green emission.

Additionally, the luminescent intensity demonstrates variations with the presence of Li^+, Na^+, and K^+ ions. Specifically, NCWO exhibits the strongest intensity for blue III and green emissions, whereas LCWO and KCWO display relatively weaker intensity for these emissions. It is suggested that the presence of A^+ ions affects the lattice parameters, thereby influencing the crystal field that surrounds the rare earth ions [23]. In our study, it is evident that the alkali metal ions do not alter the shape and peak position of the photoluminescence (PL) spectra; rather, they solely affect the luminescence intensity. It has been previously confirmed that NCWO exhibits reduced lattice distortion compared to LCWO and KCWO. This reduction in lattice distortion is associated with an increase in luminescence intensity in NCWO compared to both LCWO and KCWO [24,25]. The estimated Commission Internationale de l'Eclairage (CIE) coordinates are (0.179, 0.148), (0.181, 0.149), and (0.178, 0.148) for LCWO, NCWO, and KCWO, respectively, indicating a blue emission. However, the variations in the coordinates are attributed to different contributions from blue II and III emissions. According to equation (5), the color purity is calculated to be approximately 91% for all samples.

$$\text{Color purity} = \frac{\sqrt{(x-x_i)^2+(y-y_i)^2}}{\sqrt{(x_d-x_i)^2+(y_d-y_i)^2}} \times 100\% \qquad (5)$$

where (x, y) represents the color coordinates of the phosphor; (x_i, y_i) is the illuminant point of the 1931 CIE Standard Source with the colour coordinates of (0.3101, 0.3162); (x_d, y_d) refers to colour coordinates of the dominant wavelength and the correlated colour temperatures (CCTs) have been calculated from McCamy's relation as given in equation (6) [26], and it was found that (CCTs)~ 7763, 7803 and 7784K for LCWO, NCWO and KCWO respectively.

$$CCT = 449n^3 + 3525n^2 + 6823.3n + 5520.3 \quad (6)$$

where $n = \frac{(x-0.3320)}{(0.1858-y)}$ and (x, y) represents the chromaticity co-ordinates. Hence, it may be stated that ACWO materials are excellent for blue lightening.

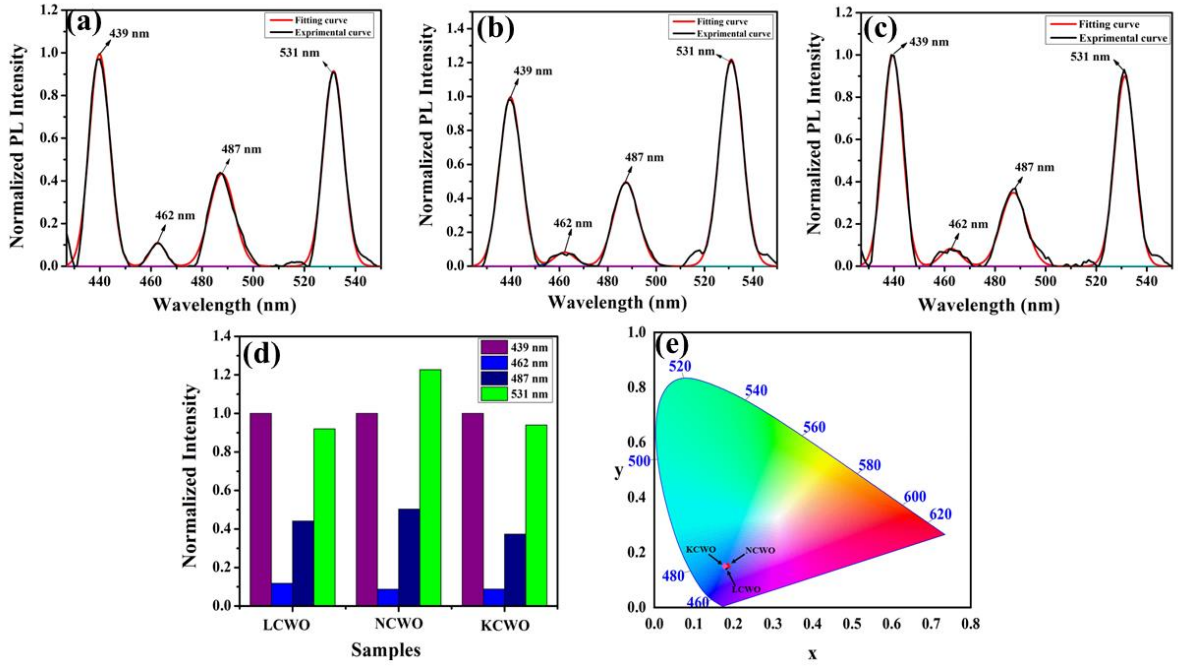

Figure 7: Photoluminescence spectra of (a) LCWO, (b) NCWO and (c) KCWO respectively. (d) Normalized PL intensity ratio of emission wavelengths (e) The CIE chromaticity diagram of the ACWO.

Density functional theory (DFT) calculation of ACWO

In our study, *ab-initio* density functional theory was employed to investigate the electronic properties and optical emissions induced by vacancies (V_O, $2V_O$) in ACWO materials. We performed calculations on the electronic band structure, total density of states (TDOS), and angular momentum projected partial densities of states (PDOS) for both pure ACWO and structurally distorted ACWO models containing V_O and $2V_O$. These models were created by removing oxygen atoms to mimic the CeO_7 (V_O) and CeO_6 ($2V_O$) structures. Through optimization of the ACWO unit cell, we determined lattice parameters

and bond lengths consistent with experimental results, providing confidence in the accuracy of our calculations. To begin, we set the top of the valence band maxima (VBM) to zero in all calculations. ACWO exhibited behavior as an indirect band material, with energy gaps (E_g) approximately 3.19 eV, 3.14 eV, and 3.15 eV for LCWO, NCWO, and KCWO, respectively, at the Γ – and X – points (depicted in Figure 8(a), 9(a), and 10(a)). While the conduction band minimum (CBM) showed spin polarization, the valence band maximum (VBM) remained spin-unpolarized. These calculated band gap values closely matched experimental values, attesting to the accuracy of our calculations (as illustrated in Figure A3, APPENDIX-IV). The pronounced curvature at CBM implied a low effective electron mass, suggesting high electron mobility within ACWO and a longer mean free path for electrons. Conversely, the curvature at VBM was comparatively low, indicating a higher effective hole mass.

By analyzing the PDOS of A, Ce, W, and O atoms (depicted in Figures 8(b-f), 9(b-f), and 10(b-f)), we determined that the upper portion of the valence band is predominantly influenced by O - $2p_x$, $2p_y$, and $2p_z$ orbitals, with additional contributions from W - $2p_x$, $2p_y$, and $2p_z$ orbitals, resulting in minimal curvature. The lower part of the valence band was primarily hybridized with W - $5d_{xz}$, $5d_{xy}$, $5d_{yz}$, $5d_z^2$, and O - $2p_x$, $2p_y$, and $2p_z$ orbitals. Contributions from Li - 2s, Na - 3s, K - 4s, and Ce - 4f orbitals were absent in ACWO samples for valence band formation. Within the CBM, spin-up Ce - $4f_z^3$, $4f_{zx}^2$, $4f_{xz}^2$, and $4f_x^3$ orbitals were dominant in LCWO, while spin-down Ce - $4f_z^3$, $4f_{zx}^2$, $4f_{xz}^2$, and $4f_x^3$ orbitals were prevalent in NCWO and KCWO samples. These orbitals were hybridized with O - $2p_x$, $2p_y$, and $2p_z$ orbitals, resulting in heightened curvature within the conduction band. The upper layer of the CB was composed of W - $4d_{xy}$, $4d_{xz}$, and $4d_z^2$ orbitals. Based on our findings, we concluded that the valence band is mainly constructed by WO_6 octahedra, while both CeO_8 polyhedra and WO_6 octahedra contribute to the conduction band in ACWO

materials. This insight led us to affirm that the band-to-band optical transitions occur through a Ce ↔ O charge transfer process.

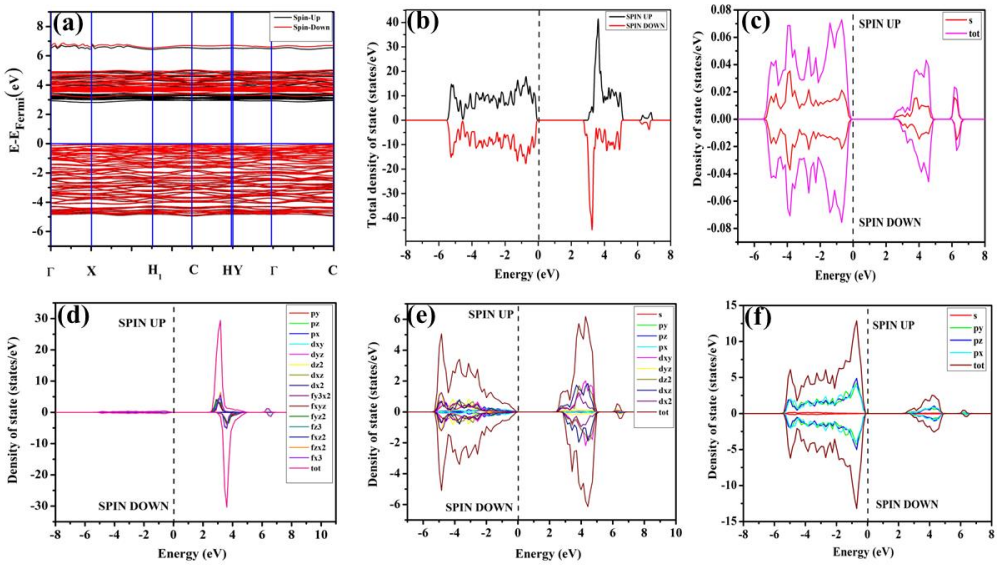

Figure 8: (a) Band structure and (b) spin polarised TDOS and PDOS of (c) Li, (d) Ce, (e) W and (f) O of pristine - LCWO.

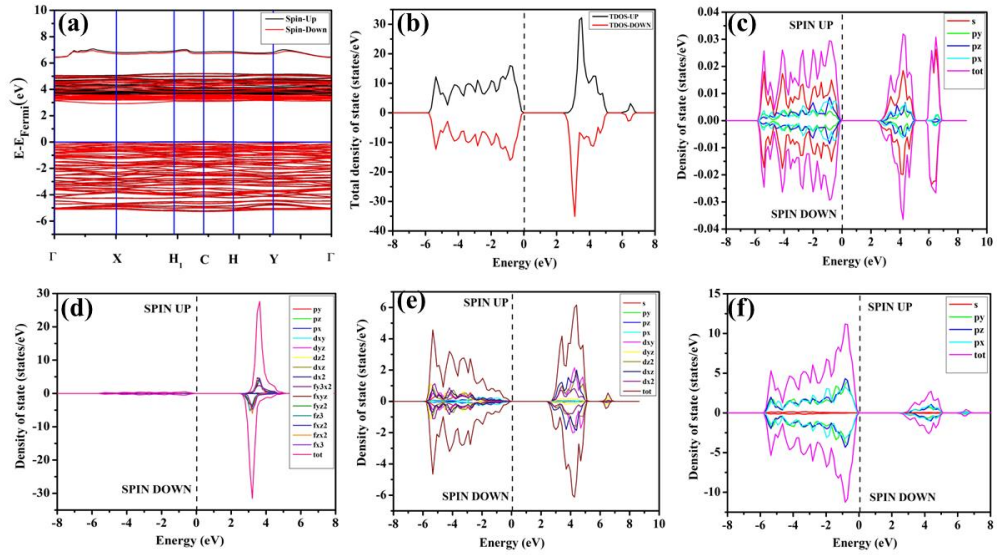

Figure 9: (a) Band structure and (b) spin polarised TDOS and PDOS of (c) Na, (d) Ce, (e) W and (f) O of pristine - NCWO.

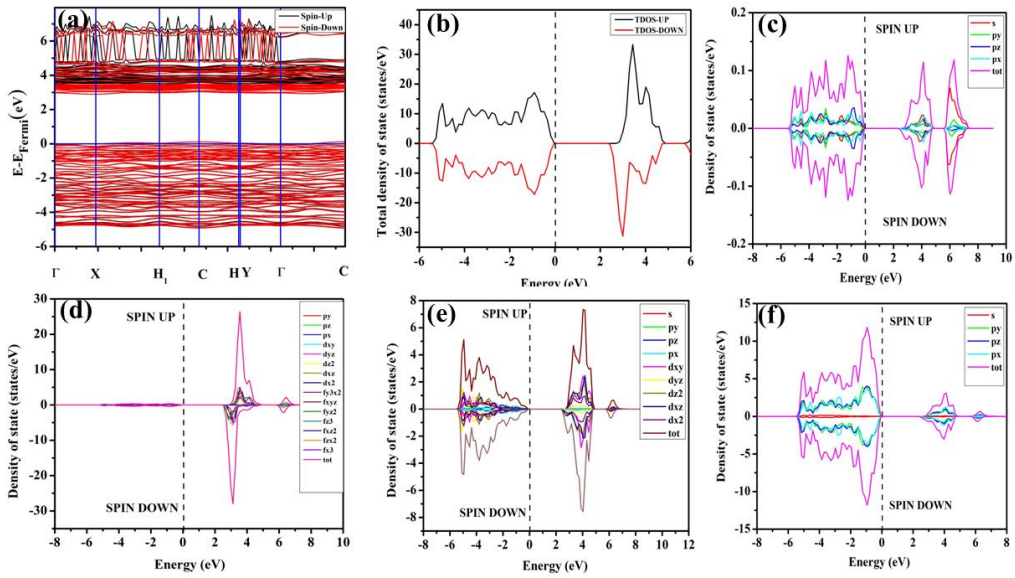

Figure 10: (a) Band structure and (b) spin polarised TDOS and PDOS of (c) K, (d) Ce, (e) W and (f) O of pristine - KCWO.

The band structures, total densities of states (TDOS), and angular momentum projected partial densities of states (PDOS) for ACWO samples induced by $V_O^{\bullet}$ and $2V_O^{\bullet}$, denoted as ACWO – $V_O^{\bullet}$ and ACWO – $2V_O^{\bullet}$, have been depicted in Figure (A5, A6, and A7) and Figure (A8, A9, and A10) of APPENDIX-IV respectively. In these figures, it is evident that the valence band maximum (VBM) of ACWO – $V_O^{\bullet}$ remains unaltered at the Γ-point, while that of ACWO – $2V_O^{\bullet}$ shifts to the X-point. Similarly, the conduction band minimum (CBM) remains constant at the Γ-point for ACWO – $V_O^{\bullet}$, whereas it shifts along the Γ – X line for ACWO – $2V_O^{\bullet}$. The calculated energy gaps (E_g) for ACWO with $V_O^{\bullet}$ and $2V_O^{\bullet}$ are (2.95 and 2.87), (2.99 and 2.97), and (3.00 and 2.96) eV for LCWO, NCWO, and KCWO, respectively. These results are presented in Figure A5(a), A6(a), and A7(a) of APPENDIX-IV. The TDOS (Figure A5(b), A6(b), A7(b), A8(b), A9(b), and A10(b)) and PDOS (Figure A5(c)-(f), A6(c)-(f), A7(c)-(f), A8(c)-(f), A9(c)-(f), and A10(c)-(f)) calculations revealed that the valence band width decreased in ACWO – $2V_O^{\bullet}$ due to increased localization of O-2p orbitals. This led to an enhanced curvature in both ACWO – $V_O^{\bullet}$ and

ACWO – $2V_O^{\bullet}$. This behaviour was attributed to an increased overlap between Ce - $4f_z^3$, $4f_{zx}^2$, $4f_{xz}^2$, $4f_x^3$ and O - $2p_x$, $2p_y$, $2p_z$ orbitals, resulting from a reduction in Ce - O bond lengths within CeO_8 polyhedra. These modifications have the potential to influence carrier mobility through oxygen vacancies.

Further analysis indicated that LCWO – $2V_O^{\bullet}$ exhibited energy gaps of (2.10, 2.81) eV above VBM, NCWO – $2V_O^{\bullet}$ displayed energy gaps of (2.14, 2.92) eV above VBM, and KCWO – $2V_O^{\bullet}$ demonstrated energy gaps of (2.21, 2.94) eV above VBM. In contrast, LCWO – $V_O^{\bullet}$ exhibited a defect state at 2.45 eV, NCWO – $V_O^{\bullet}$ at 2.31 eV, and KCWO – $V_O^{\bullet}$ at 2.38 eV above VBM. Through a meticulous examination of TDOS and PDOS, it was deduced that the Ce - $5d_{xz}$, $5d_{x^2-y^2}$, $5d_{xy}$, and $5d_{yz}$ orbitals played a pivotal role in the emission properties of ACWO samples containing $V_O^{\bullet}$ and $2V_O^{\bullet}$. A comprehensive list of the orbitals involved in different emissions stemming from diverse deformed structures of CeO_8 polyhedra is provided in Table A5 of APPENDIX-IV and schematically represented in Figure 11.

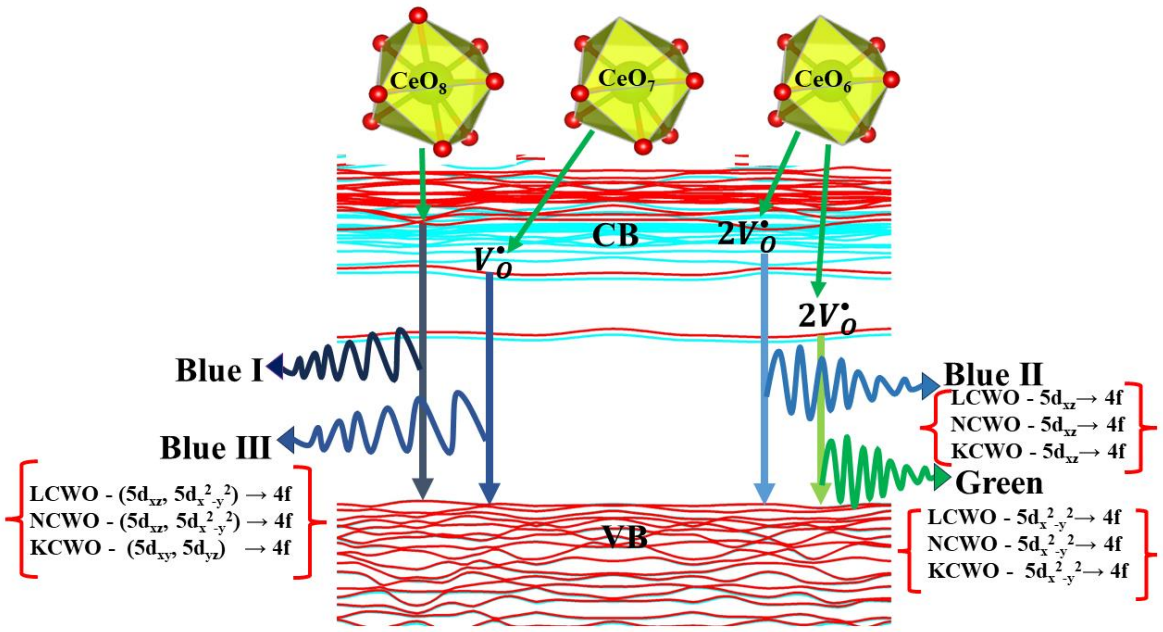

Figure 11: Schematic representation of photoluminescence transitions of ACWO nanomaterial involving different orbitals.

Conclusions

Pristine ACWO (A = Li, Na, K) clusters were synthesized using a trisodium citrate-assisted hydrothermal method. Notably, as per literature, there is no report on the synthesis procedure for LCWO and KCWO via hydrothermal methods, along with the characterization of their emission properties. These properties reveal pronounced blue I and green emissions, alongside relatively weaker blue II and blue III emissions. Through comprehensive experimental and theoretical investigations, we have demonstrated that all these transitions, occurring within distinct configurations of CeO_8 polyhedra, are linked to the Ce 5d → 4f transition. In particular, CeO_8 and CeO_7 configurations exhibit blue I and blue III emissions, while the CeO_6 configuration emits blue II and green colors. This observation suggests that ACWO holds promise as a material suitable for blue light-emitting diodes (LEDs). Our calculations underscore the sensitivity of the O - 2p and O - 2p – Ce - 5d orbitals, which constitute the valence and conduction bands, to defect states. These characteristics can be exploited to finely tune the electrical properties of ACWO. In essence, this research contributes to a deeper comprehension of the optoelectronic traits of pristine $ACe(WO_4)_2$ and its oxygen vacancy content. This understanding has implications for the potential applications of $ACe(WO_4)_2$, particularly in the domain of optoelectronic devices such as LEDs.

APPENDIX-IV

Table A1: Coordination environment of triclinic ACWO nanostructures.

Coordinates atoms	x	y	z	Occupancy	Site occupancy	symmetry
Li1/Na1/K1	0.2815	0.7733	0.1567	1.0	1a	1
Li2/Na2/K2	0.7184	0.2266	0.8432	1.0	1a	1
Ce1	0.1740	0.2878	0.4547	1.0	1a	1
Ce2	0.2860	0.7121	0.5452	1.0	1a	1
O1	0.1823	0.3500	0.7987	1.0	1a	1

O2	0.8176	0.6500	0.2012	1.0	1a	1
O3	0.4619	0.6413	0.2627	1.0	1a	1
O4	0.5380	0.4586	0.7372	1.0	1a	1
O5	0.8659	0.0119	0.1955	1.0	1a	1
O6	0.1340	0.9880	0.8044	1.0	1a	1
O7	0.7074	0.0107	0.4898	1.0	1a	1
O8	0.2925	0.9893	0.5101	1.0	1a	1
O9	0.1740	0.6339	0.5530	1.0	1a	1
O10	0.8259	0.3660	0.4469	1.0	1a	1
O11	0.4847	0.8316	0.0074	1.0	1a	1
O12	0.5152	0.1683	0.9925	1.0	1a	1
O13	0.0578	0.3132	0.1062	1.0	1a	1
O14	0.9421	0.6868	0.8937	1.0	1a	1
O15	0.3906	0.1712	0.2675	1.0	1a	1
O16	0.6093	0.8287	0.7324	1.0	1a	1
W1	0.2753	0.2990	0.0396	1.0	1a	1
W2	0.7246	0.7009	0.9603	1.0	1a	1
W3	0.6569	0.1086	0.2887	1.0	1a	1
W4	0.3430	0.8913	0.7112	1.0	1a	1

Table A2: Refined structural parameters and the reliability factors from Rietveld refinement of ACWO nanostructures.

Properties		**LCWO**	**NCWO**	**KCWO**
Lattice parameter (A^0)	a	7.082(7)	7.499(5)	7.061(4)
	b	8.009(10)	8.254(6)	8.011(5)
	c	7.405(8)	7.058(5)	7.445(4)
	α	114.341	113.441	114.122
	β	116.476	115.151	116.991
	γ	90.258	91.462	90.285
Unit cell volume $(A^0)^3$		333.343(6)	352.753(4)	333.032(3)
Bond length (A^0)	A-O	2.413(4)	2.503(4)	2.408(2)
	Ce-O	2.410(18), 2.569(14)	2.521(14), 2.636(12)	2.394(10), 2.590(7)
	W-O	1.919(4)	1.978(4)	1.916(5)
Bond angle (in degree)	A-O-W	92.280(3)	93.269(18)	92.541(12)
	A-O-Ce	114.613(19)	114.606(17)	114.334(11)
	O-Ce-O	74.790(3)	74.800(7)	74.650(13)
	Ce-O-W	145.346(18)	145.402(3)	145.208(8)

	O-A-O	69.283(3)	66.861(4)	69.272(12)
	O-W-O	89.614(13)	87.290(5)	89.600(5)
R_p (%)		10.5	12.8	13.9
R_{wp} (%)		15.5	16.2	17.3
R_{exp} (%)		10.2	10.3	10.3
χ^2		2.80	2.51	2.82

Table A3: The details of the deconvolution of the FTIR bands of ACWO nanostructures.

Samples	Peak position (cm^{-1})		Area (cm^2)	FWHM	χ^2
LCWO	660 – 718	670	0.097	1.761	2.10
		679	0.052	6.188	
		695	0.203	11.938	
		702	0.065	4.608	
	718-780	742	0.926	14.634	2.30
		762	1.179	15.532	
	780 – 910	812	5.781	29.355	2.70
		857	12.933	46.013	
		882	4.594	29.232	
NCWO	660 – 718	670	0.061	1.347	2.22
		678	0.094	9.493	
		693	0.021	4.076	
		697	0.164	15.086	
	718-780	733	0.695	14.939	3.20
		747	1.619	27.337	

	780 – 910	797	1.795	21.575	2.42
		823	3.520	35.468	
		867	11.595	53.496	
KCWO	660 – 718	670	0.048	1.323	3.70
		681	0.175	10.116	
		696	0.108	7.053	
		706	0.071	8.035	
	718-780	740	0.264	11.615	3.40
		764	0.220	11.566	
	780 – 910	816	4.412	34.078	1.97
		856	11.339	43.998	
		882	2.626	25.473	

Table A4: Lattice parameters of ACWO nanostructures from DFT calculation.

Lattice parameter (Å)	LCWO	NCWO	KCWO
a	7.110	7.115	7.760
b	7.430	7.348	7.571
c	7.535	7.271	7.577
A-O	2.06	2.32	2.79
Ce-O	2.45	2.38	2.35
W-O	1.82	1.80	1.82

Table A5: The contributed orbitals for different emissions of ACWO nanostructures from defect states (DFT).

Transitions	LCWO	NCWO	KCWO	Deformed structure of CeO_8

Blue II ($2V_O$)	$5d_{xz} \rightarrow 4f$	$5d_{xz} \rightarrow 4f$	$5d_{xz} \rightarrow 4f$	CeO_6
Blue III (V_O)	$(5d_{xz}, 5d_{x^2-y^2}) \rightarrow 4f$	$(5d_{xz}, 5d_{x^2-y^2}) \rightarrow 4f$	$(5d_{xy}, 5d_{yz}) \rightarrow 4f$	CeO_7
Green ($2V_O$)	$5d_{x^2-y^2} \rightarrow 4f$	$5d_{x^2-y^2} \rightarrow 4f$	$5d_{x^2-y^2} \rightarrow 4f$	CeO_6

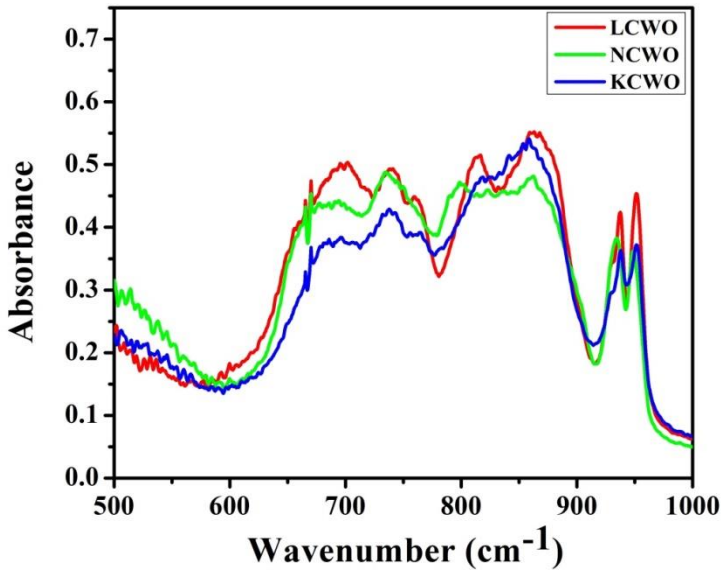

Figure A1: FTIR of ACWO nanostructures.

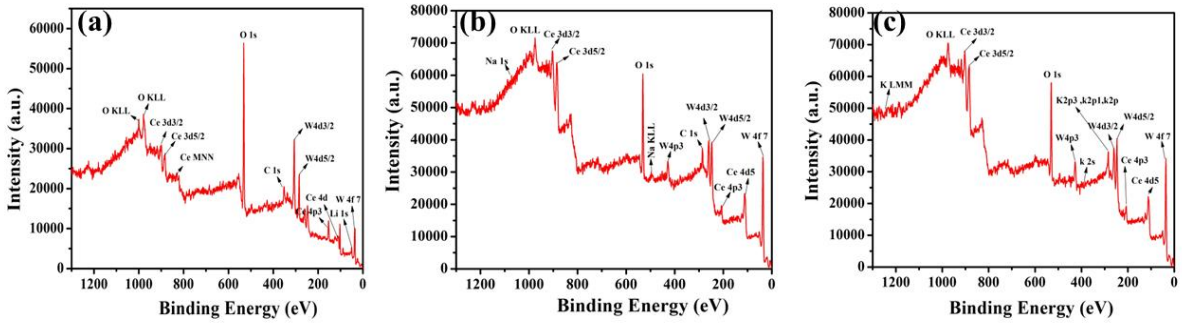

Figure A2: XPS wide spectrum of (a)LCWO, (b)NCWO and (c)KCWO respectively.

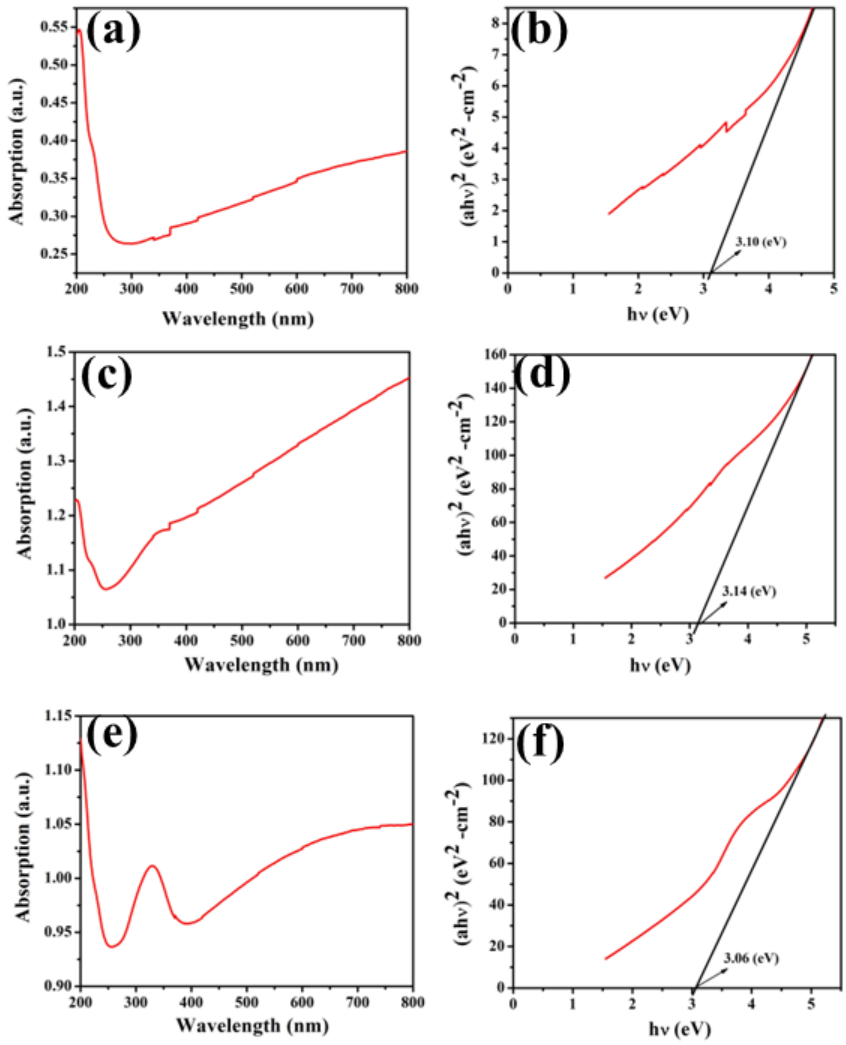

Figure A3: UV spectra and corresponding band gaps for (a, b) LCWO, (c, d) NCWO and (e, f) KCWO respectively.

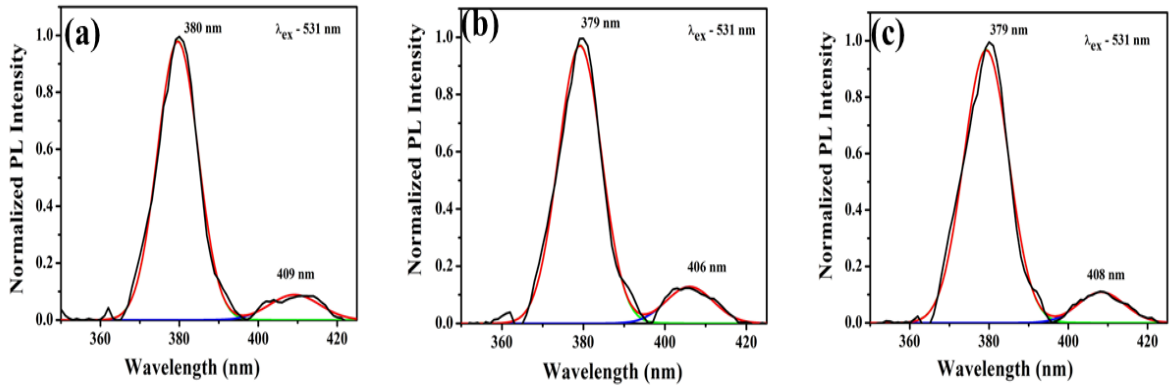

Figure A4: PLE spectra for (a)LCWO, (b)NCWO and (c)KCWO respectively.

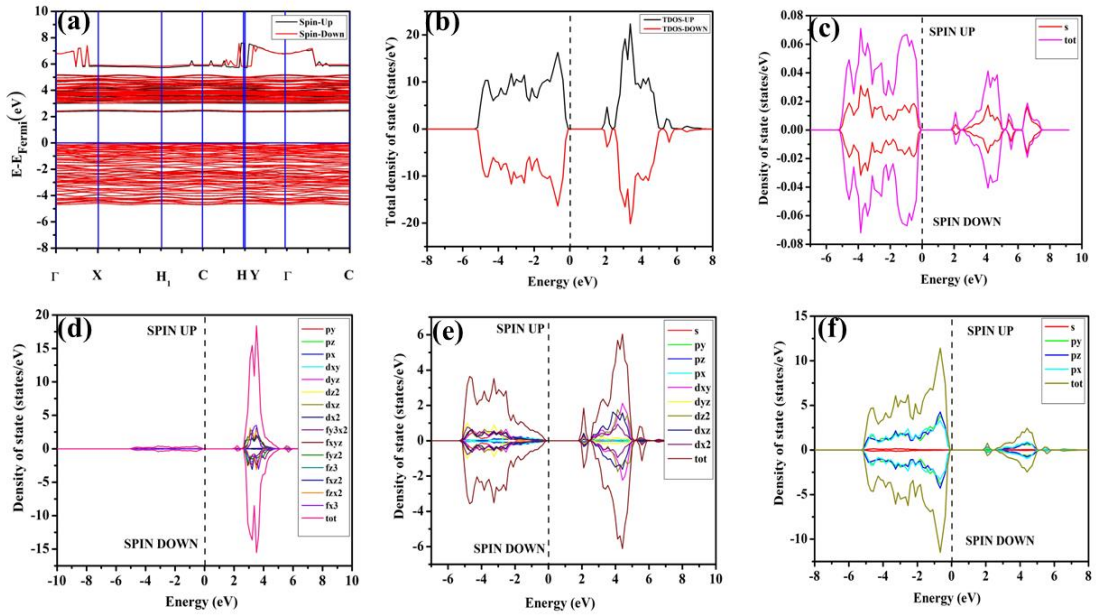

Figure A5: (a) Band structure and (b) spin polarised TDOS and PDOS of (c) Li, (d) Ce, (e) W and (f) O of LCWO – $V_O^{\bullet}$.

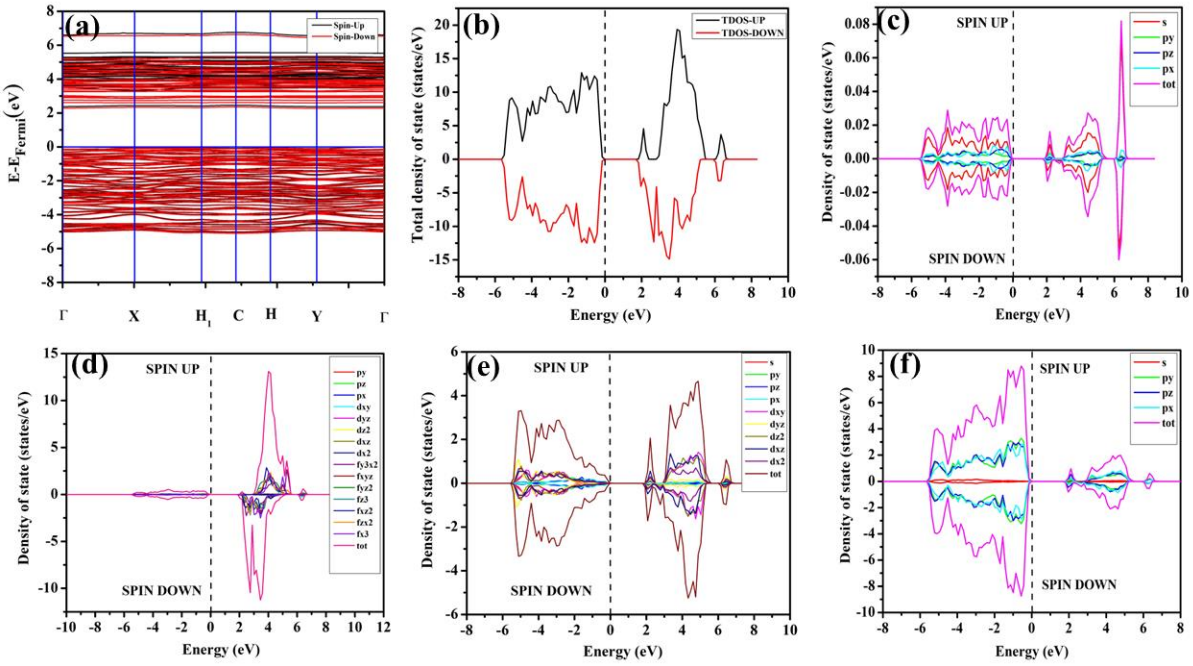

Figure A6: (a) Band structure and (b) spin polarised TDOS and PDOS of (c) Na, (d) Ce, (e) W and (f) O of NCWO – $V_O^{\bullet}$.

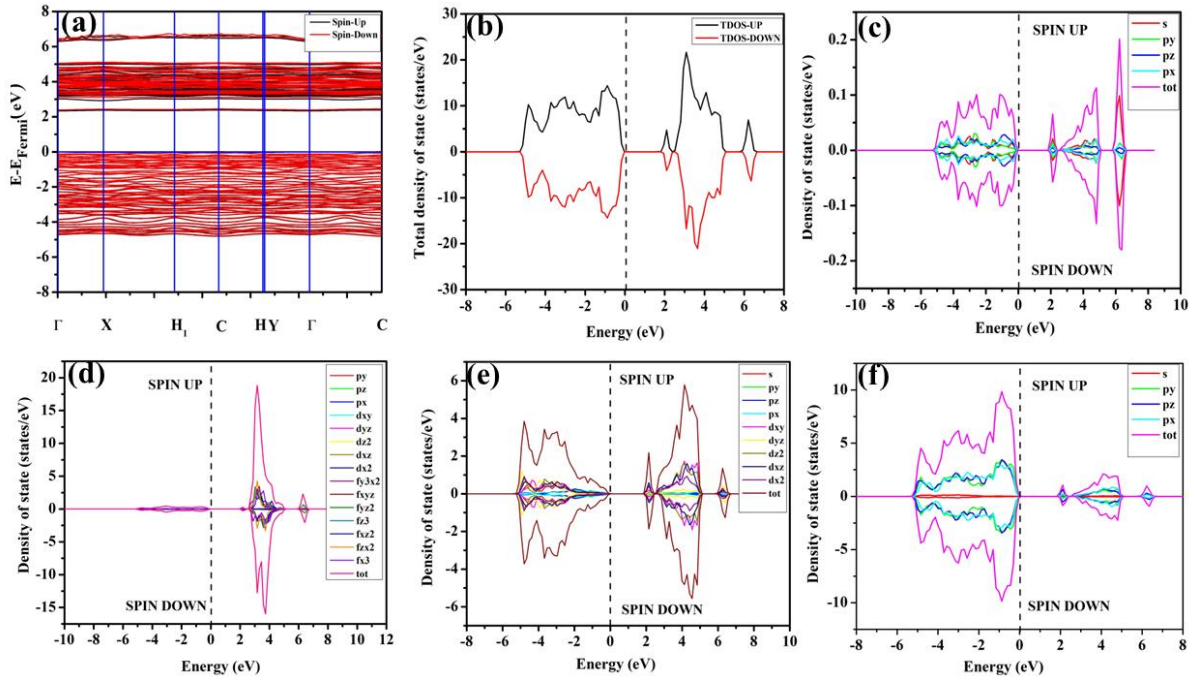

Figure A7: (a) Band structure and (b) spin polarised TDOS and PDOS of (c) K, (d) Ce, (e) W and (f) O of KCWO – $V_O^{\bullet}$.

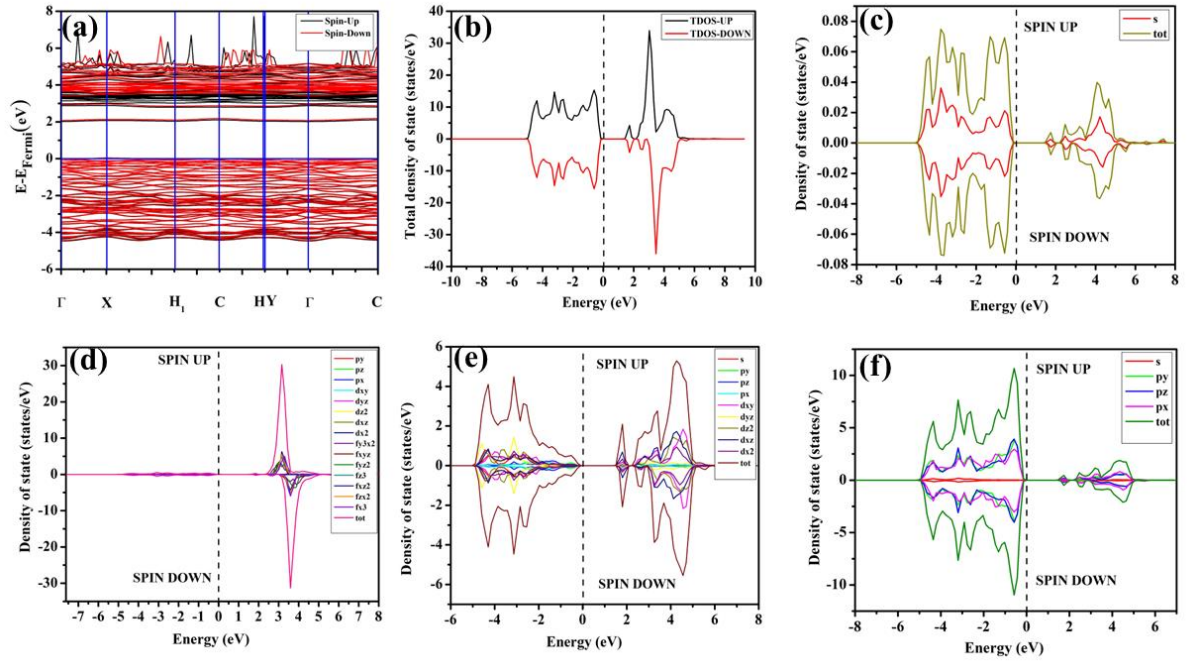

Figure A8: (a) Band structure and (b) spin polarised TDOS and PDOS of (c) Li, (d) Ce, (e) W and (f) O of LCWO – $2V_O^{\bullet}$.

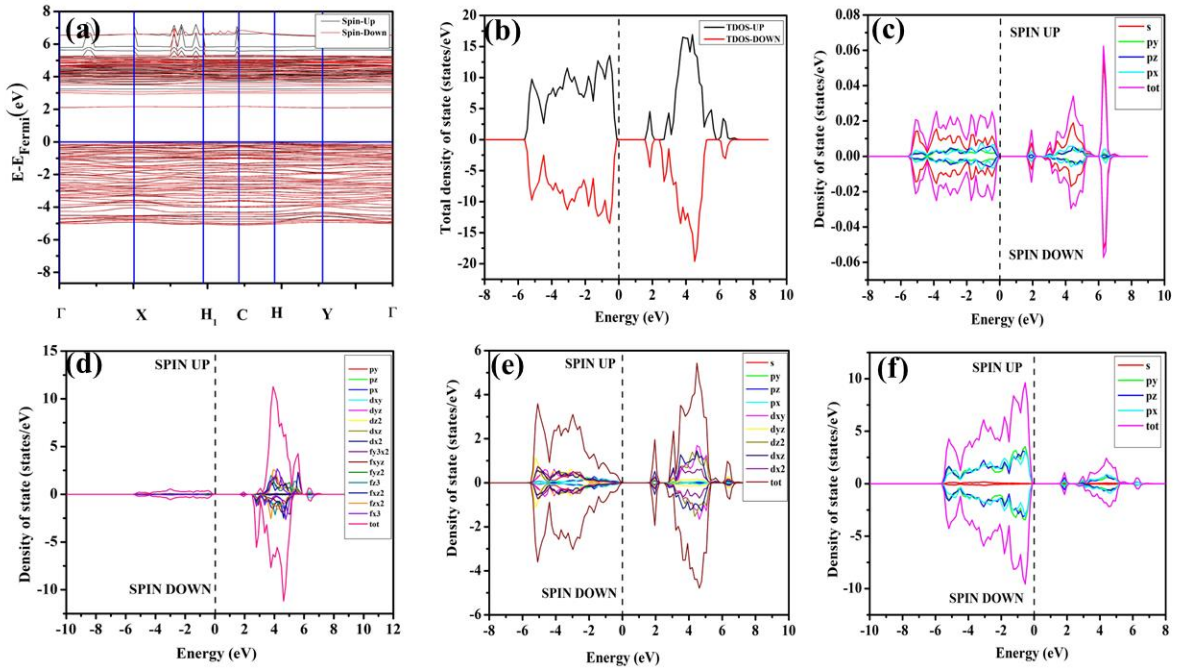

Figure A9: (a) Band structure and (b) spin polarised TDOS and PDOS of (c) Na, (d) Ce, (e) W and (f) O of NCWO – $2V_O^{\bullet}$.

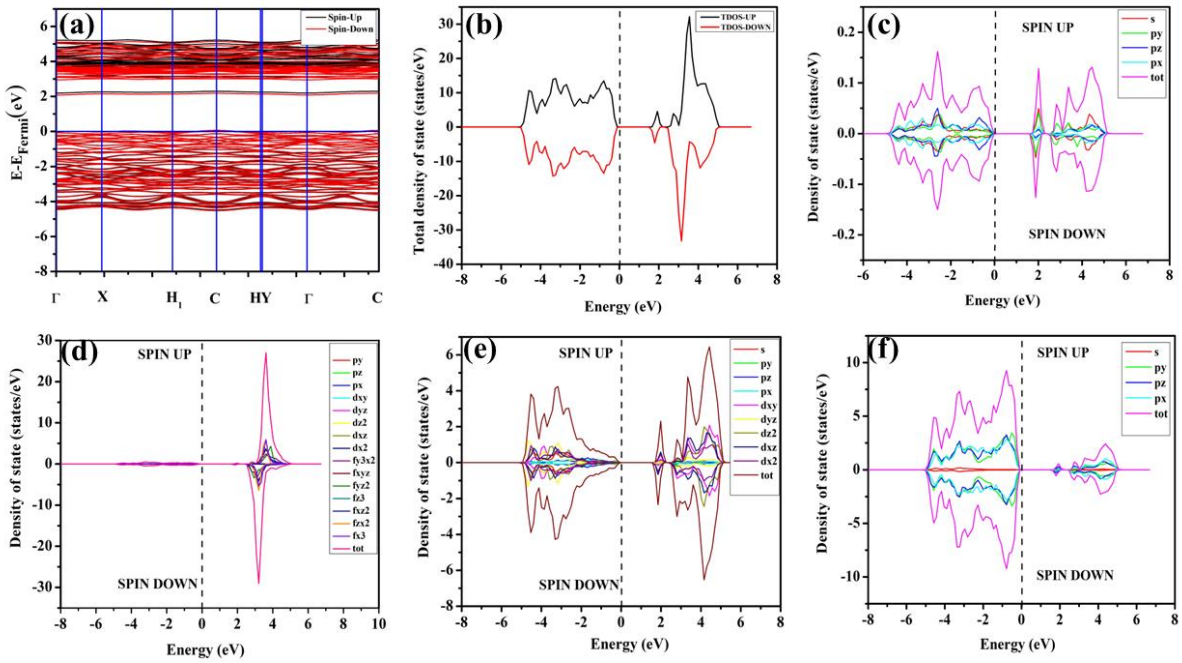

Figure A10: (a) Band structure and (b) spin polarised TDOS and PDOS of (c) K, (d) Ce, (e) W and (f) O of KCWO – $2V_O^{\bullet}$.

References

1. Jena, P., Gupta, S.K., Natarajan, V., Sahu, M., Satyanarayana, N. and Venkateswarlu, M., 2015. Structural characterization and photoluminescence properties of sol–gel derived nanocrystalline $BaMoO_4$: Dy^{3+}. *Journal of Luminescence*, *158*, pp.203-210.

2. Chiu, C.H., Wang, M.F., Lee, C.S. and Chen, T.M., 2007. Structural, spectroscopic and photoluminescence studies of $LiEu(WO_4)_2$− x (MoO_4) x as a near-UV convertible phosphor. *Journal of Solid State Chemistry*, *180*(2), pp.619-627.

3. Garg, N., Mishra, A.K., Poswal, H.K., Tyagi, A.K. and Sharma, S.M., 2015. High pressure phase transitions in scheelite structured fluoride: ErLiF4. *Journal of Solid State Chemistry*, *229*, pp.164-172.

4. Schwung, S., Rytz, D., Heying, B., Rodewald, U.C., Niehaus, O., Enseling, D., Jüstel, T. and Pöttgen, R., 2015. The crystal structure and luminescence quenching of poly-and single-crystalline KYW_2O_8 : Tb^{3+}. *Journal of Luminescence*, *166*, pp.289-294.

5. de Moraes, J.R., Baldochi, S.L., Soares, L.D.R.L., Mazzocchi, V.L., Parente, C.B.R. and Courrol, L.C., 2012. Growth, structural and optical characterizations of Li La $_{(1-\ x)}$ Eu $_{x}$ $(WO_4)_2$ single-crystalline fibers by the micro-pulling-down method. *Materials Research Bulletin*, *47*(3), pp.744-749.

6. Shimemura, T., Sawaguchi, N. and Sasaki, M., 2017. Structure and light emission of scheelite-type ACe $(WO_4)_2$ (A= Li, Na, or K). *Journal of the Ceramic Society of Japan*, *125*(3), pp.150-154.

7. Shimemura, T., Sawaguchi, N. and Sasaki, M., 2017. Structure and light emission of scheelite-type ACe $(WO_4)_2$ (A= Li, Na, or K). *Journal of the Ceramic Society of Japan*, *125*(3), pp.150-154.

8. Munirathnappa, A.K., Dwibedi, D., Hester, J., Barpanda, P., Swain, D., Narayana, C. and Sundaram, N.G., 2018. In Situ Neutron Diffraction Studies of LiCe $(WO_4)_2$ Polymorphs: Phase Transition and Structure–Property Correlation. *The Journal of Physical Chemistry C*, *123*(2), pp.1041-1049.

9. Liu, W.R., Yeh, C.W., Huang, C.H., Lin, C.C., Chiu, Y.C., Yeh, Y.T. and Liu, R.S., 2011. (Ba, Sr) Y_2 Si_2 Al_2 O_2 N_5: Eu^{2+}: a novel near-ultraviolet converting green phosphor for white light-emitting diodes. *Journal of Materials Chemistry*, *21*(11), pp.3740-3744.

10. Kuzmicheva, G.M., Eremin, A.V., Rybakov, V.B., Subbotin, K.A. and Zharikov, E.V., 2009. Structural features of phases $(Na_{0.5}$ $R_{0.5})$ MO_4 and $(Na_{0.5}$ $R_{0.5})$ MO_4: R′ (R= Gd, La; R′= Er, Tm, Yb; M= W, Mo) of the scheelite family. *Russian Journal of Inorganic Chemistry*, *54*, pp.854-863.

11. Li, L., Su, Y. and Li, G., 2007. Size-induced symmetric enhancement and its relevance to photoluminescence of scheelite $CaWO_4$ nanocrystals. *Applied physics letters*, *90*(5).

12. Gancheva, M., Naydenov, A., Iordanova, R., Nihtianova, D. and Stefanov, P., 2015. Mechanochemically assisted solid state synthesis, characterization, and catalytic properties of $MgWO_4$. *Journal of Materials Science*, *50*, pp.3447-3456.

13. Ahmad, A.H. and Arof, A.K., 2004. XRD, conductivity and FTIR studies on LiI-Li_2 WO_4 - Li_3 PO_4 prepared by low temperature sintering. *Ionics*, *10*, pp.200-205.

14. Macalik, L., Hanuza, J. and Kaminskii, A.A., 2000. Polarized Raman spectra of the oriented NaY $(WO_4)_2$ and KY $(WO_4)_2$ single crystals. *Journal of Molecular Structure*, *555*(1-3), pp.289-297.

15. Jayaraman, A., Sharma, S.K. and Wang, S.Y., 1998. Raman studies of some alkali metal–lanthanide double tungstates at high pressures. *Journal of Raman spectroscopy*, *29*(4), pp.305-312.

16. Dirany, N., McRae, E. and Arab, M., 2017. Morphological and structural investigation of $SrWO_4$ microcrystals in relationship with the electrical impedance properties. *CrystEngComm*, *19*(34), pp.5008-5021.

17. Haldar, N., Mondal, T., Das, T., Sarkar, D., Pal, M. and Ghosh, C.K., 2023. Hydrothermal synthesis of defect-induced pristine α-NaCe $(WO_4)_2$: a novel material for solid state lighting and gas sensing. *CrystEngComm*.

18. Mandal, S., Ghosh, C.K., Sarkar, D., Maiti, U.N. and Chattopadhyay, K.K., 2010. X-ray photoelectron spectroscopic investigation on the elemental chemical shifts in multiferroic $BiFeO_3$ and its valence band structure. *Solid state sciences*, *12*(10), pp.1803-1808.

19. Cavalcante, L.S., Batista, F.M.C., Almeida, M.A.P., Rabelo, A.C., Nogueira, I.C., Batista, N.C., Varela, J.A., Santos, M.R.M.C., Longo, E. and Li, M.S., 2012. Structural refinement, growth process, photoluminescence and photocatalytic properties of $(Ba_{1-x}\ Pr_{2x/3})\ WO_4$ crystals synthesized by the coprecipitation method. *Rsc Advances*, *2*(16), pp.6438-6454.

20. Li, G., Tian, Y., Zhao, Y. and Lin, J., 2015. Recent progress in luminescence tuning of Ce^{3+} and Eu^{2+}-activated phosphors for pc-WLEDs. *Chemical Society Reviews*, *44*(23), pp.8688-8713.

21. Van Uitert, L.G., 1984. An empirical relation fitting the position in energy of the lower d-band edge for Eu^{2+} or Ce^{3+} in various compounds. *Journal of Luminescence*, *29*(1), pp.1-9.

22. Lecointre, A., Bessière, A., Bos, A.J.J., Dorenbos, P., Viana, B. and Jacquart, S., 2011. Designing a red persistent luminescence phosphor: the example of

YPO_4: Pr^{3+}, Ln^{3+} (Ln= Nd, Er, Ho, Dy). *The Journal of Physical Chemistry C*, *115*(10), pp.4217-4227.

23. Singh, A.K., Singh, S.K. and Rai, S.B., 2014. Role of Li+ ion in the luminescence enhancement of lanthanide ions: favorable modifications in host matrices. *RSC advances*, *4*(51), pp.27039-27061.

24. Ran, W., Noh, H.M., Park, S.H., Moon, B.K., Jeong, J.H., Kim, J.H. and Shi, J., 2018. Break the interacting bridge between Eu^{3+} ions in the 3D network structure of $CdMoO_4$: Eu^{3+} bright red emission phosphor. *Scientific reports*, *8*(1), p.5936.

25. Li, X., Yang, Z., Guan, L., Guo, J., Wang, Y. and Guo, Q., 2009. Synthesis and luminescent properties of $CaMoO_4$: Tb^{3+}, R^+ (Li^+, Na^+, K^+). *Journal of Alloys and Compounds*, *478*(1-2), pp.684-686.

26. Rai, M., Kaur, G., Singh, S.K. and Rai, S.B., 2015. Probing a new approach for warm white light generation in lanthanide doped nanophosphors. *Dalton Transactions*, *44*(13), pp.6184-6192.

Chapter 7

Overall conclusions and future prospect

The present work has made significant strides in the synthesis and characterization of phase-pure rare earth-based scheelite materials using an energy-efficient and cost-effective chemical route. Several key findings and accomplishments have emerged from this research, which have profound implications for both the scientific community and potential technological applications.

1. **Oxygen Defect-Induced Tuned Optical Properties:** One of the standout achievements of this study is the successful synthesis of phase-pure rare earth-based shylleeite materials with oxygen defects, including V_O and $2V_O$. These defects have been reported for the first time in this material, and they play a pivotal role in tuning the optical properties. This discovery opens up exciting possibilities for applications in solid-state lighting due to the materials' unique optical properties, as well as in gas sensing applications. The potential for advanced lighting technologies and sensitive gas detection is highly promising.

2. **Versatile Nanoparticle Engineering:** The research showcases the versatility of the synthesis method by using different organic additives to achieve various shapes and sizes of nanoparticles. This capability is a significant asset for tailoring materials to specific applications and requirements. It underscores the adaptability of rare earth-based scheelite materials for diverse technological needs.

3. **Novel Hydrothermal Techniques:** The study's utilization of hydrothermal techniques with different organic additives has resulted in the formation of various nanostructures. While some of these nano powders initially exhibited spherical shapes, the subsequent high-temperature calcination caused them to form agglomerate structures. This understanding of nanostructure formation processes is valuable for further optimizing synthesis methods.

4. **Experimental Evidence for Tuned Photoluminescence:** Perhaps one of the most groundbreaking contributions of this research is the provision of experimental evidence for tuning photoluminescent properties within these nano

powders. The elucidation of the mechanisms behind these photoluminescent properties offers a deeper understanding of the materials and highlights their potential for solid-state lighting and gas sensing applications.

5. **Exploration of Alkali Metal Ions and Crystal Compactness:** The study delves into the influence of alkali metal ions on the photoluminescence behavior of alkali rare earth-based sheelite materials (ACWO) and critically examines the crystal compactness of these nanostructures. These investigations further expand our knowledge of the factors impacting the properties of these materials.

6. **Band Structure Calculations:** The incorporation of band structure calculations using *ab-initio* density functional theory provides a theoretical framework for understanding the photoluminescence characteristics observed in the materials. This computational approach enhances our comprehension of the underlying physics and chemistry governing the materials' behavior.

In conclusion, this research has made substantial progress in the field of rare earth-based scheelite materials, with a particular emphasis on their optical properties and potential applications in solid-state lighting and gas sensing. While many significant achievements have been made, it is clear that further research is essential to fully harness the potential of these materials.

Future prospects include optimizing synthesis methods, exploring additional applications, and advancing our understanding of the underlying science. The combination of experimental evidence and theoretical insights presented in this work sets the stage for exciting future developments in the field of advanced materials science and technology. Here are detailed future prospects for these materials:

1. **Solid-State Lighting Revolution:** Scheelite materials have emerged as potential game-changers in the field of solid-state lighting. The future may bring more efficient and cost-effective light-emitting diodes (LEDs) and lighting devices based on these materials. The prospects include:

- Improved efficiency and brightness of scheelite-based LEDs.
- Enhanced color tunability for dynamic lighting applications.
- Longer lifespans and reduced energy consumption in lighting systems.
- Integration into displays, automotive lighting, and general illumination.

2. **Energy-Efficient Displays:** Scheelite materials may revolutionize display technologies. Future developments could lead to:

- High-resolution, energy-efficient displays for smartphones, tablets, and TVs.
- Increased color accuracy and vibrancy in displays.
- Flexible and transparent display applications.
- Enhanced outdoor visibility due to high brightness.

3. **Quantum Technologies:** Scheelite materials, with their rare earth ions, hold great promise for quantum technologies. The future may see:

- Development of quantum memory devices based on scheelite materials.
- Advances in quantum cryptography and secure communication.
- Quantum computing applications utilizing scheelite's unique properties.

4. **Environmental Sensors:** The sensitivity of scheelite materials to various gases and environmental factors opens doors to advanced environmental sensing technologies. Future prospects include:

- Highly sensitive and selective gas sensors for pollution monitoring.
- Compact and portable environmental monitoring devices.
- Real-time air quality monitoring for smart cities and indoor spaces.

5. **Advanced Photonics:** Scheelite materials offer excellent optical properties for photonics applications. Future developments may involve:

- Faster data transmission in optical communication networks.
- Miniaturized and efficient photonic devices.
- Integration into emerging technologies like Li-Fi (light-based wireless communication).

6. **Sustainable Energy:** Scheelite materials can contribute to green energy solutions. Future prospects include:

- Integration into highly efficient solar cells for renewable energy generation.
- Enhanced photocatalytic materials for water purification and pollutant degradation.
- Development of energy-efficient lighting for reduced electricity consumption.

7. **Multifunctional Devices:** Scheelite materials' unique combination of properties makes them suitable for multifunctional devices. Future innovations could include:

- Integrated devices combining lighting, sensing, and data processing capabilities.
- Smart sensors and actuators for Internet of Things (IoT) applications.

8. **Materials Science Advancements:** Ongoing research in materials science and nanotechnology may lead to:

- Tailored scheelite-based materials with specific properties for diverse applications.
- Discovery of new scheelite-like compounds with even more exciting properties.

9. **Collaborative Research:** The future of alkali rare earth-based scheelite materials will likely involve interdisciplinary collaboration. Researchers from materials science, physics, chemistry, and engineering may work together to unlock new applications and optimize existing ones.

The future prospects for alkali rare earth-based scheelite materials are diverse and promising. Their unique properties position them as key players in industries ranging from lighting and displays to quantum technologies and environmental monitoring. Continued research, innovation, and collaboration across disciplines will drive the development of groundbreaking applications and technologies using these materials.

PhD Thesis

ORIGINALITY REPORT

1 %

SIMILARITY INDEX

PRIMARY SOURCES

1	Tanmoy Mondal, Nibedita Haldar, Biplab Paul, Chandan Kumar Ghosh. "Morphology controllable synthesis of GdOF nanocrystals and application in theranostic purpose", Materials Today: Proceedings, 2022 Crossref	285 words — 1%

EXCLUDE QUOTES ON

EXCLUDE BIBLIOGRAPHY ON

EXCLUDE SOURCES < 1%

EXCLUDE MATCHES < 10 WORDS

Nibedita Haldar
29.09.2023

29/09/2023
Dr. Chandan Kumar Ghosh
Assistant Professor
School of Materials Science
& Nanotechnology,
Jadavpur University
Kolkata - 700 032